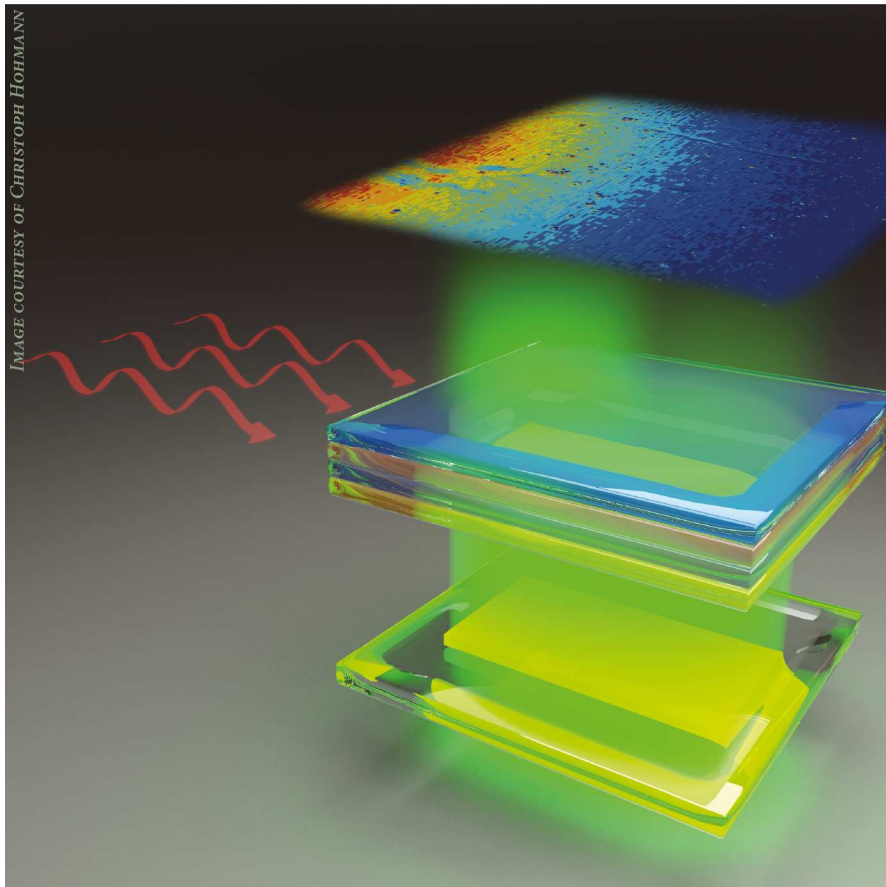Dissertation zur Erlangung des Doktorgrades

der Fakultät für Chemie und Pharmazie

der Ludwig-Maximilians-Universität München

STIMULI-RESPONSIVE PHOTONIC CRYSTAL SENSORS: TOWARDS AN INTEGRATED ELECTROPHOTONIC DETECTION PLATFORM

Ida Pavlichenko
aus
Baku, Aserbaidschan

2014

ERKLÄRUNG

Diese Dissertation wurde im Sinne von § 7 der Promotionsordnung vom 28. November 2011 von Frau Prof. Dr. Bettina Lotsch betreut.

EIDESSTATTLICHE VERSICHERUNG

Diese Dissertation wurde eigenständig und ohne unerlaubte Hilfe erarbeitet.

München, 14.08.2014

....

(Ida Pavlichenko)

Dissertation eingereicht am   14.08.2014

1. Gutachterin: Prof. Dr. Bettina Lotsch

2. Gutachter: Prof. Dr. Paolo Lugli

Mündliche Prüfung am   16.09.2014

Посвящается моим родителям

ACKNOWLEDGMENTS

The past four years spent in Munich have been a truly amazing experience for me. My PhD journey couldn't have been so exciting without all the incredible people I met on my way.

First and foremost I would like to thank my supervisor Professor Bettina Lotsch, whom I admire not only as a successful researcher, but also as a strong and talented woman, and a source of inspiration. Bettina, thank you for your brilliant ideas and advice, late night discussions, curiosity, and most importantly, freedom to choose the research directions. Thank you for your contagious and never-ending perfectionism, which surely made me a better scientist. Above all, I appreciate your moral support and personal approach in the hardest times of my PhD, Thank you for your patience. You were the best "Doktormutter" I can imagine to myself.

Secondly, this thesis could not have become true without the input of my collaborators Professor Paolo Lugli and Professor Giuseppe Scarpa. I was very lucky to join the OLED-Photonic crystal-OPD hybrid project from the very beginning of my PhD. Thank you for all the fruitful discussions, paper corrections and precious ideas. I will always remember our meetings and your invaluable suggestions.

I thank particularly the members of my examination committee for finding time to read my thesis: Prof. Thomas Bein, Prof. Christina Scheu, Prof. Achim Hartschuh, Prof. Andreas Kornath. I specially thank Prof. Paolo Lugli for providing the evaluation of the PhD thesis.

My big thank you goes to Dr. Armin Exner, with whom we were working hard on our "baby" – the PC-based sensing platform. Armin, I wish you good luck in your future projects. Thanks to Yoshiyuki Fukuda, Ellen Broda and Prof. Bräuchle for a possibility to realize my "bio-dream". I must thank all my practical students, who performed a massive part of this work: Gerald Derondeau, Alena Folger, Peter Zehetmaier, Katalin Szendrei, Maria Hoyer, Johannes Mannsperger and Anna Katharina Hatz. I must admit that I have also learned a lot from you, my students. Thank you for your excellent performance.

My dear Lotsch group, without you my time in Munich and Stuttgart would not have been so amazing! Thank you for a warm welcome and for all the fun activities together. Anna, Erik, Hongji, Albi, Katha, Basti, you are the best lab neighbours I could wish to myself. You were always helpful and ready to discuss interesting scientific and nonscientific phenomena. Lotsch group has helped me to learn German faster and dive into the German lifestyle. Thanks also to Stephans, Dan, Chris, Claudia and Linus for nice conversations. My "fan" message is also addressed to Erwin, who supported me with fun videos and chocolates during the times I had to stay late in the lab. Anna R.,

I learned a lot from you, and you are a great friend. I thank both Schnick and Johrendt groups for a nice time together.

I would like to thank specially Wolfgang Wünschheim and Thomas Müller for the technical support, Catrin Löhnert for providing the labs with fresh coffee and Olga Lorenz for the kind help with the paperwork. Furthermore, I thank a lot Viola Duppel, Steffen Schmidt and Christian Minke for the assistance with the SEM analisys, Dr. Konuma for the XPS investigation. Claudia Kamella, your help with administrative problems was invaluable. I thank the members of the Bein group for the technical assistance with the ellipsometer and tensiometer, as well as the Baumeister group for their help with the realization of my "bio-project".

I thank the managing team of the IDK NanoBiotechnology Fellowship, especially, Marilena Pinto, for helping me to settle down in Germany. And the managing team of CeNS and NIM for their great help during these years. Birgit and Peter, thank you for a great year at NIM, I had a lot fun being a Student Representative, thanks also to the NIM Student Board 2013. Criss, thank you for the beautiful images!

Thanks to all my German (stemming from IDK and IMPRS), Italian, Australian, Russian (especially Vasilisa, Maria, Anna, Daria, Alex and Alex) and other international friends and for their support and great time together in Munich and elsewhere.

My life in Munich would not be as wonderful and meaningful without the dear Asano family, who provided me with good mood, advice, shelter and delicious food. Carmen and Akihiro thank you very much! I thank the Goldovsky family for helping me to get settled in Munich.

I would like to especially thank my both beloved families for their moral support during all these years. I am what I am only because of your tremendous work. I will always cherish your love and devotion. Knowing you are always by my side even at a long distance keeps me going.

Finally, I would like to thank my husband Shoh for his endless support, patience and love. His devotion and tireless correction were of great importance to me during the writing phase. It is his sense of humor, care and ability to find solutions fast that made this thesis see the daylight. Thank you for always being there for me, Shoh!

Whence is that Nature doth nothing in vain; and whence arises all that

Order and Beauty which we see in the World?

Sir Isaac Newton
"Opticks: or, A treatise of the reflections, refractions, inflections and colours of light"

TABLE OF CONTENTS

1. INTRODUCTION

The development of novel sensing techniques is driven by an ever-increasing demand for compact and sensitive platforms with a fast response to external physical, chemical or biological stimuli. Since last two decades, photonic crystals have conquered a place on the podium of existing sensing schemes and gained interest from various scientific communities (as can be seen in the bibliometric citation analysis in the Figure 1.1). Owing to their unique synergic combination of well-defined optical and structural properties and a wide range of chemical functionalities, photonic crystals provide great potential for the development of new multifunctional optical devices. The introduction to this thesis will focus on the basic concepts underlying the optical and sensing properties of photonic crystals. Special attention will be drawn to the properties of one-dimensional photonic crystals. Furthermore, the current progress and applications of titania- and silica-based porous multilayers will be discussed. Additionally, the key concepts fundamental for the operation of (in)organic light emitting devices and photodetectors will be briefly emphasized. Finally, this introduction will close with the objectives of this thesis.
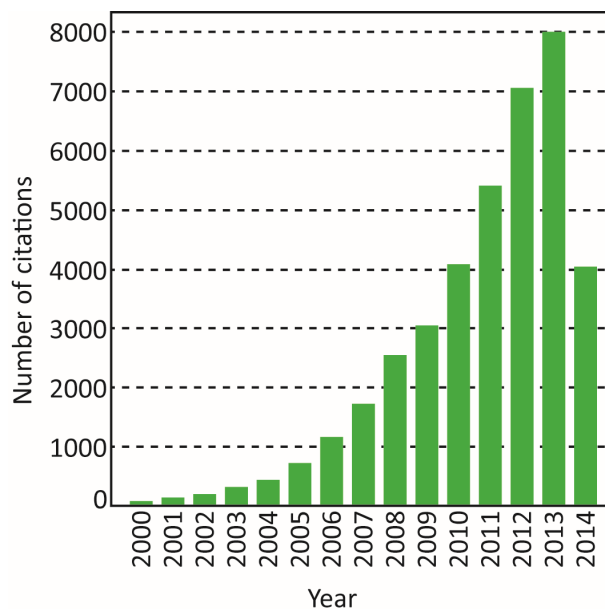
Figure 1.1. Number of citations per year based on the search of the topic "photonic crystal sensors" in the Web of Science™ database. Accessed on May 20, 2014.

1.1. PHOTONIC CRYSTALS

In 1887, Lord Rayleigh published one of his first manuscripts about the optical properties of the medium "endowed with periodic structure",[1] thus opening doors towards a new era in the research of light. It took 100 years until in 1987, Yablonovitch[2] and John[3] independently published two milestone papers describing a new kind of artificial material able to control and manipulate the motion of photons and thus sparkling the creation of a new paradigm in the design of the optical devices. Soon after, in 1989, Yablonovitch suggested the name for the novel optical materials – "the photonic crystals" – and introduced the term "the photonic band gap" for characterizing their optical properties.[4]

Photonic crystals (PCs) are periodic arrangements of materials with different refractive indices, which can create a range of "forbidden" frequencies for the photons called the photonic band gap (PBG).[5,6] The materials are engineered such that the incident photons with energies lying within the photonic band gap cannot propagate through the PC. Thus, photonic crystals are able to "mold" the properties of photons in a similar way that semiconductor crystals affect the properties of the electrons in a crystal lattice.[7] Photonic crystals can be fabricated with periodicity in one (1D), two (2D), or three (3D)[8] dimensions as shown in Figure 1.2.[9]
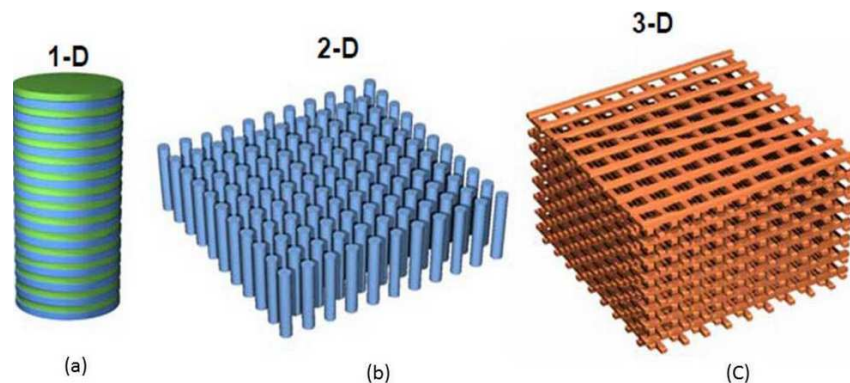
Figure 1.2. Schematic examples of a) one-, b) two- and c) three-dimensional crystals. Reproduced with permission.[10]

The photonic band structure of the periodic dielectric materials can be obtained from the Maxwell equations (see Equations 1.1).[7] The Equations 1.1 are written for macroscopic, isotropic, transparent and lossless media without free charges and currents:

$$\nabla \cdot \vec{H}(\vec{r},t) = 0 \qquad \nabla \times \vec{E}(\vec{r},t) + \mu_0 \frac{\partial \vec{H}(\vec{r},t)}{\partial t} = 0$$

$$\nabla \cdot \left[\varepsilon(\vec{r})\vec{E}(\vec{r},t)\right] = 0 \quad \nabla \times \vec{H}(\vec{r},t) - \varepsilon_0 \varepsilon(\vec{r}) \frac{\partial \vec{E}(\vec{r},t)}{\partial t} = 0 \qquad (1.1)$$

where $\vec{E}$, $\vec{H}$ are the macroscopic electric and magnetic fields, μ_0 is the vacuum permeability, ε_0 is the vacuum permittivity, $\varepsilon(\vec{r})$ is the dielectric function. Note that the constants μ_0 and ε_0 can be combined to obtain the speed of light in vacuum: $c = 1/\sqrt{\mu_0 \varepsilon_0}$. By expanding the fields into a set of harmonic modes: $\vec{H}(\vec{r},t) = \vec{H}(\vec{r})e^{-i\omega t}$ and $\vec{E}(\vec{r},t) = \vec{E}(\vec{r})e^{-i\omega t}$, and inserting them into the Equations 1.1, one obtains the "master" equation for $\vec{H}(\vec{r})$ (1.2):[5]

$$\nabla \times \left(\frac{1}{\varepsilon(\vec{r})} \nabla \times \vec{H}(\vec{r}) \right) = \left(\frac{\omega}{c} \right)^2 \vec{H}(\vec{r}). \qquad (1.2)$$

The solutions for $\vec{H}(\vec{r})$ and ω are determined by the symmetry properties of the $\varepsilon(\vec{r})$. If $\varepsilon(\vec{r})$ is perfectly periodic (in the case of perfect photonic crystals), the solutions can be characterized by a wavevector $\vec{k}$ and a band index n.[5] In this case the $\vec{H}(\vec{r})$ can be written in the Bloch form, $\vec{H}_{\vec{k}}(\vec{r}) = e^{i\vec{k}\vec{r}}\vec{u}_{\vec{k}}(\vec{r})$, and then be inserted into Equation 1.2 to find the solutions. The region of all allowed wavevectors is called a Brillouin zone, and the collection of all solutions is termed a band structure.[11] The photonic band structures of the 1D, 2D and 3D photonic crystals from Figure 1.2 are presented in Figure 1.3. Notably, similarly to doping of semiconductor crystals, by introducing defects (point or line defects, or both) in these periodic structures, one can disrupt the periodicity of the PBG material, thus allowing for the localization or guiding of light in the PBG region, which is the basis for the design of PC based optical devices.[12,13] For calculating the band structure and field distribution, a variety of numerical methods can be employed: Plane wave expansion, finite element and finite-difference time-domain (FDTD) methods, and others.[14,15]

The intriguing optical properties of photonic crystals have stirred the development of novel applications in the field of telecommunication[16], optical fibers[17,18] and switches[19,20], displays,[21] and inks.[22,23] The miniaturization of photonic integrated circuits to a scale comparable to the wavelength of light can open

new doors for future optical networks and optical computing.[24] Furthermore, the use of functional materials that behave as active chemo-/biocomponent layers open up an interesting new route for sensing.[25,26,27] The sensing approach is based on the utilization of 1D, 2D and 3D PCs as tunable optical structures capable of changing their refractive properties (or lattice constant), when in contact with an analyte of interest or when exposed to external stimuli such as electrical[28] and magnetic actuation,[29] mechanical strain,[30] pH,[31] etc.[32,33,34] Favorably, photonic crystal surfaces can be modified to provide functions that are used in biochemical and cell-based assays for label-free biosensing.[35,36,37]
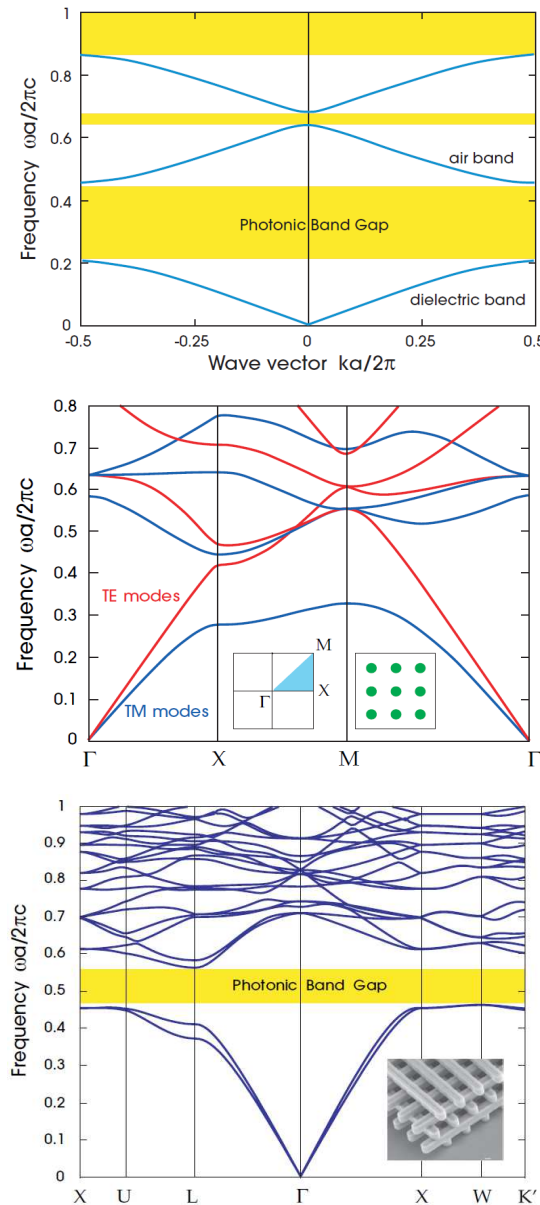
Figure 1.3. The photonic band structure for (top) a multilayer film (shown schematically in Figure 1.2a) with lattice constant *a* and dielectric constants of layers ε_1= 13 and ε_2 = 13, with the respective thicknesses of 0.2*a* and 0.8*a*, (middle) a square array of dielectric columns (ε = 8.9) embedded in air (shown in Figure 1.2b), (bottom) the

lowest bands of the woodpile structure (see the inset and Figure 1.2c) with ε = 13 logs in air. Reproduced with permission.[10]

1.2. ONE-DIMENSIONAL PHOTONIC CRYSTALS

One-dimensional photonic crystals (1D PCs), also known as (distributed) Bragg reflectors, Bragg mirrors or Bragg stacks (BSs), − the simplest photonic architectures, in which the periodicity of the dielectric constant exists in only one dimension − have attracted significant attention recently.[38,39] 1D PCs consist of periodically alternating layers of high and low refractive index (RI) dielectric materials (as schematically shown in Figure 1.2a).[40] Interference of light reflected at the interfaces of the dielectric layers leads to strong reflections in a well-defined wavelength range − the photonic band gap (see Figure 1.4a).
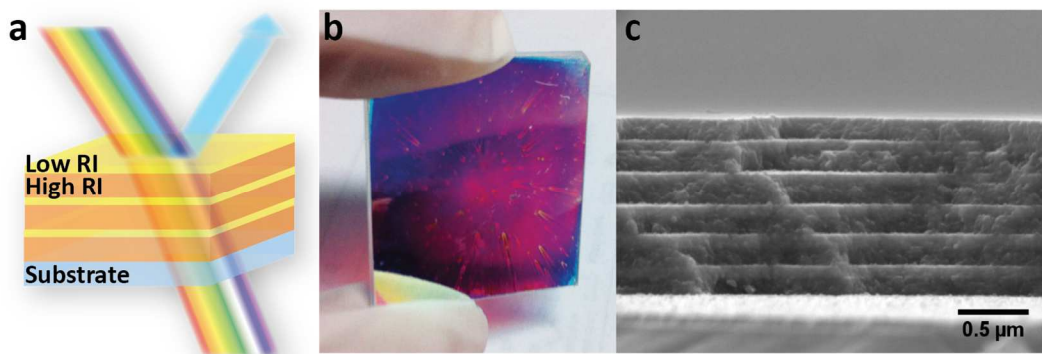
Figure 1.4. a) Schematic demonstration of blue light reflection from the multilayer structure composed of alternating layers of high and low refractive index (RI) dielectric materials, b) 1D PC obtained by spin-coating nanoparticle TiO_2 and SiO_2 suspensions, c) scanning electron microscopy (SEM) image of the photonic crystal shown in Figure 1.4b.

If the band gap of a PC lies within the visible light spectrum, one can observe an intense coloration in a stack comprised of inherently colorless materials; this phenomenon is also called a "structural" coloration. Brilliant structural colors that arise from optical interference of 1D PC structures can be often seen in Nature.[41] The examples include nacre in shells of molluscs,[42] eye of the California fishery squid,[43] elytra of the Japanese jewel beetle,[44] wings of Madagascan sunset moth[45] (see Figure 1.5a-b), stripes of Paradise whiptail fish,[46] and others.[47]
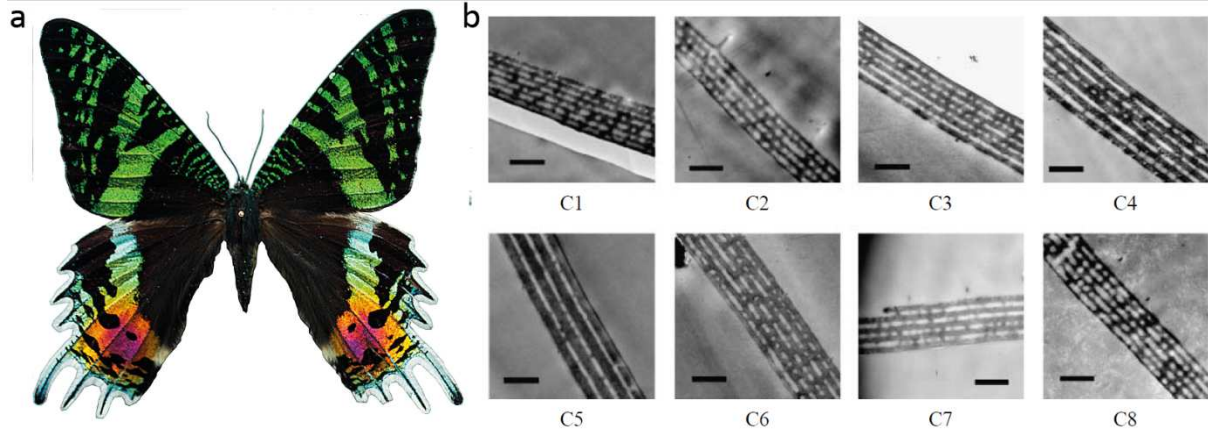
Figure 1.5. a) Madagascan sunset moth from dorsal view. The areas on the wings with different colours were investigated by means of transmission electron microscopy: b) the longitudinal cross section of the iridescent cover scales of the eight areas named from C1 to C8. Scale bar, 1 mm. ©Royal Society Publishing 2008. Reproduced with permission.[45]

To describe the opttical properties of the 1D PC, consider the central wavelength of the stop band, λ , of a structure composed of a periodic stack of materials, which can be predicted by Bragg-Snell's law:[25]

$$m\lambda = 2d\sqrt{n_{eff}^2 - \sin^2\theta}, \quad (1.3)$$

where *m* is the diffraction order, θ is the angle of incidence, and n_{eff} is the effective refractive index of the bilayer comprising the stack. As can be seen from Equation 1.3, different colors are observed at different angles of observation. This challenge can be solved without the need of a complete band-gap structure as demonstrated with the omnidirectional Bragg reflectors with high refractive-index contrast constituent layers.[48]

At normal incidence Equation 1.3 transforms into Equation 1.4:[38]

$$m\lambda = 2(n_H h_H + n_L h_L), \quad (1.4)$$

where n_H, n_L, h_H and h_L are the respective refractive indices and thicknesses of the high- (H) and low- (L) RI materials. As can be seen from Equation 1.4, the position of the stop band can be modulated by varying the optical thickness (the product of RI and physical thickness) of the layers. If one of the 1D PC materials exhibits a change in either RI or in the physical dimensions[49], when exposed to external stimuli, the 1D PC can act as a transducer with an optical read-out, as shown in Figure 1.6.

The intensity of the reflectance band of the 1D PC in air is given by Equation 1.5:[50]

$$R = \left(\frac{1-Y}{1+Y}\right)^2 \times 100\%, \, Y = \left(\frac{n_H}{n_L}\right)^{N-1} \frac{n_H^2}{n_s}, \quad (1.5)$$

where n_H, n_L, h_H and h_L are the respective refractive indices and thicknesses of the high- (H) and low- (L) RI materials, n_s is the RI of the substrate, and N is the number of bilayers in the stack. As can be seen from the Equation 1.5, the reflectivity of the BS increases at larger RI contrast (n_H/n_L) and upon increasing the number of bilayers in the BS.
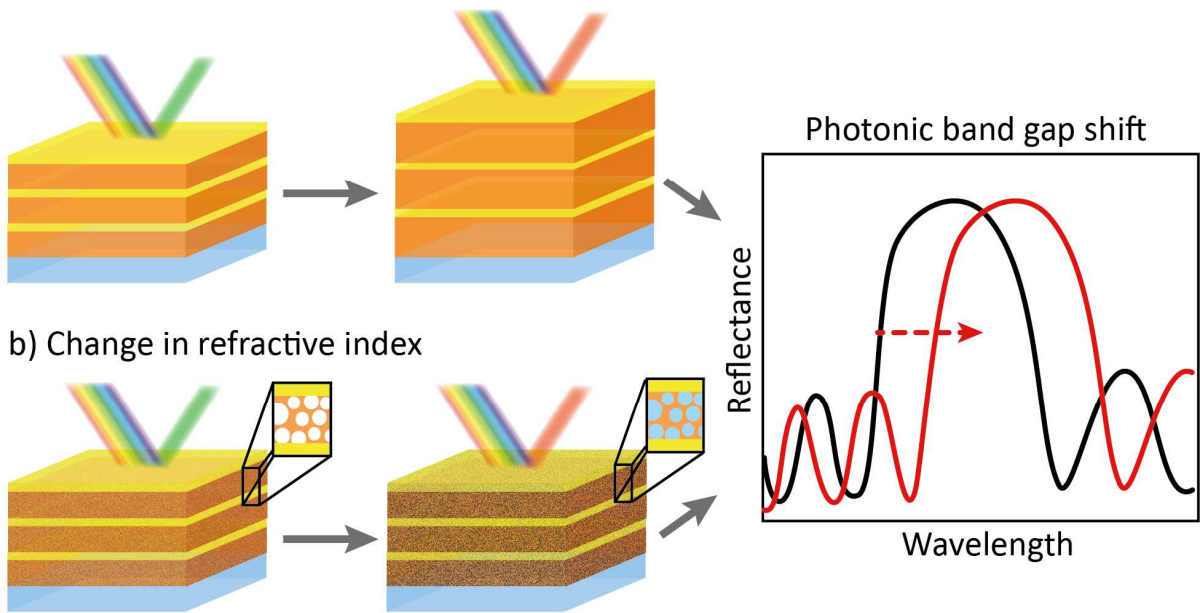
Figure 1.6. Photonic stop band tuning *via* optical thickness modulation. Schematic illustration of effect a) physical thickness tuning and b) refractive index change (e.g. by the infiltration of the pores of a 1D PC).

The reflectivity and transmittance of 1D PCs can be calculated through a transfer matrix method.[50] Figure 1.7a shows the calculated reflectivity for an ideal multilayer with a varying number of layers under normal incidence, in the case when the difference in the refractive indices between the two layers is very small, which is a typical case for polymeric materials.[41] Figure 1.7b depicts the reflection spectrum of the multilayer with a high refractive index contrast of the materials. In this case, the maximum reflectivity is reached with only a few layers. Figures 1.8a and 1.8b show the calculated results for a non-ideal multilayer corresponding to Figures 1.7a and 1.7b, respectively, in which the ratio of the optical path length in the layer with a higher refractive index decreases, while the sum of the optical path lengths is

kept constant. Figure 1.8a depicts that the peak reflectivity decreases with increasing asymmetry, while the bandwidth slightly decreases; at the same time, the peak position shifts toward shorter wavelengths. Similar behaviour is observed in Figure 1.8b.
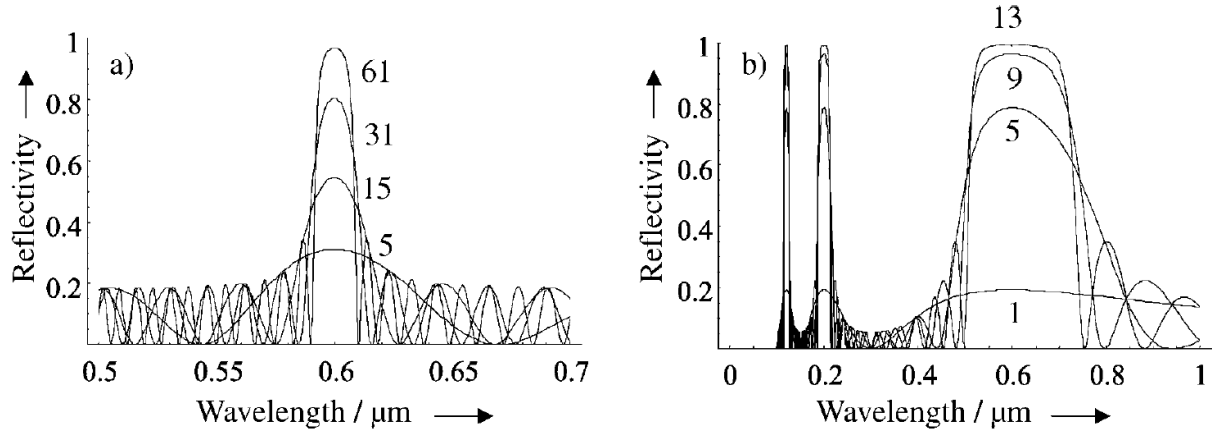
Figure 1. 7. Reflectivity from a multilayer with various numbers of layers. a) The difference of the refractive indices for the two layers is small; n_L =1.55 and n_H =1.60. b) A large refractive index difference; n_H =1.6 and n_L =1.0. The thickness of each layer is set to satisfy an ideal multilayer and the total optical path length of the sum of layers is set to 0.25 mm. © 2005 Wiley-VCH Verlag GmbH&Co. Reproduced with permission.[41]
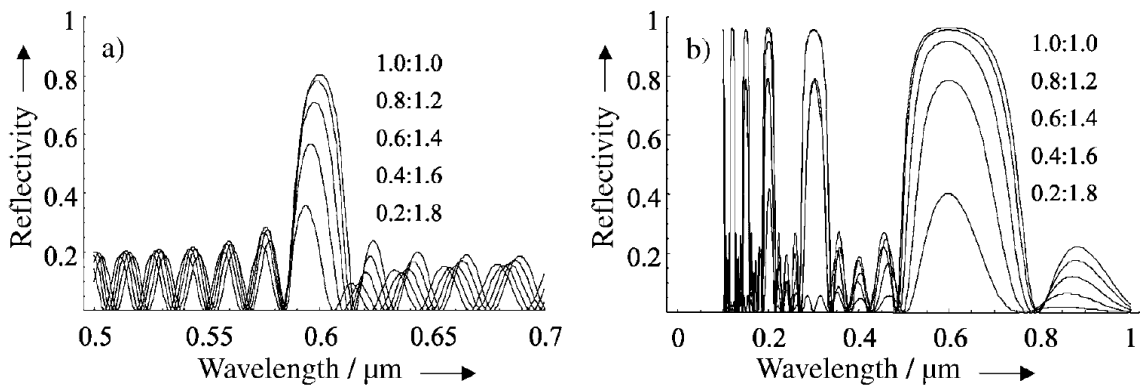
Figure 1. 8. Reflectivity from a nonideal multilayer corresponding to Figure 1.7. a) A small difference in the refractive index and b) a large difference. The total optical path length is set to take a constant value of 0.25 mm, while the ratio of the optical path lengths for the layers is varied as indicated in the Figure. © 2005 Wiley-VCH Verlag GmbH&Co. Reproduced with permission.[41]

The advantage of one-dimensional photonic crystals lies in the wide range of materials available that can be deposited as multilayers, the possibility to accurately control the optical properties of the periodic ensemble, the fact that high structural and optical quality can be obtained, and in the ease of functionalization and their integration in devices. Favorably, there is a plethora of processing methods for producing 1D photonic crystals including thermal evaporation, reactive sputtering, pulsed laser

deposition, chemical vapour deposition,[49] spin-, dip- and spray-coating[51], cut-and-stack technique,[52] photolithography and sol–gel chemistry.[53,54]

1.2.1. SILICA/TITANIA ONE-DIMENSIONAL PHOTONIC CRYSTALS FOR SENSING APPLICATIONS

1D PCs (or Bragg stacks) composed of TiO_2/SiO_2 multilayers were studied extensively during the past years due to the variety of captivating properties such systems offer.[38,39,55] Titanium dioxide is a well-investigated optical material with high RI (= 1.8–2.5), possessing a high chemical stability, low toxicity, and photocatalytic properties when illuminated with ultraviolet light.[56] TiO_2 together with SiO_2 – the low-RI material (= 1.3-1.45) – bode well for the fabrication of highly-reflective multilayers due to a high refractive index contrast between these two materials.

Among the first, Choi *et al.* discussed the structural coloration of mesoporous Bragg stacks (see Figure 1.9) fabricated by alternating spin-coating and calcination of mesoporous TiO_2 and SiO_2 layers.[60] They noted reversible sensitivity of the BS' optical properties to the adsorption and desorption of analytes, such as alcohols and alkanes. Further investigation of the sorption properties of the multilayered stacks of mesoporous thin films obtained by using evaporation-induced self-assembly (EISA)[57] with varying framework compositions, pore sizes, and pore structure revealed that the optical response can be tuned through the selective introduction of functional groups in the multilayer scaffold.[58,59,60] Moreover, the *in situ* ellipsometric analysis of adsorption/desorption behavior of mesoporous single film, bilayer and multilayer systems shows that the optical response to the analyte's relative pressure change depends not only on the pore size and chemical affinity of the material to the analyte, but also on the interaction between neighboring layers, pore accessibility and interconnectivity between different pore size systems.[61]

Thereupon, attention was drawn to another class of porous TiO_2/SiO_2 multilayers – *nanoparticle-based silica/titania 1D PCs*. Wu *et al.* observed structural color in TiO_2 and SiO_2 nanoparticle-based BSs assembled by polyelectrolyte-assisted layer-by-layer (LbL) deposition with subsequent calcination of the layers.[63] The LbL technique was further optimized for the deposition of all-nanoparticle thin film coatings in the absence of a polymer.[64,51] The resulting multilayers showed superhydrophilicity (antifogging), antireflection and self-cleaning properties – such coatings may play a significant role in a

wide variety of optical technologies (e. g. flat-panel displays for electronics, solar-cell collectors and others) by reducing reflective losses at interfaces. Lee *et al.* showed that by adjusting the pH of the TiO_2 and SiO_2 nanoparticle suspensions it was possible to vary the average bilayer thickness of multilayers as well as the porosity and chemical composition.[65]
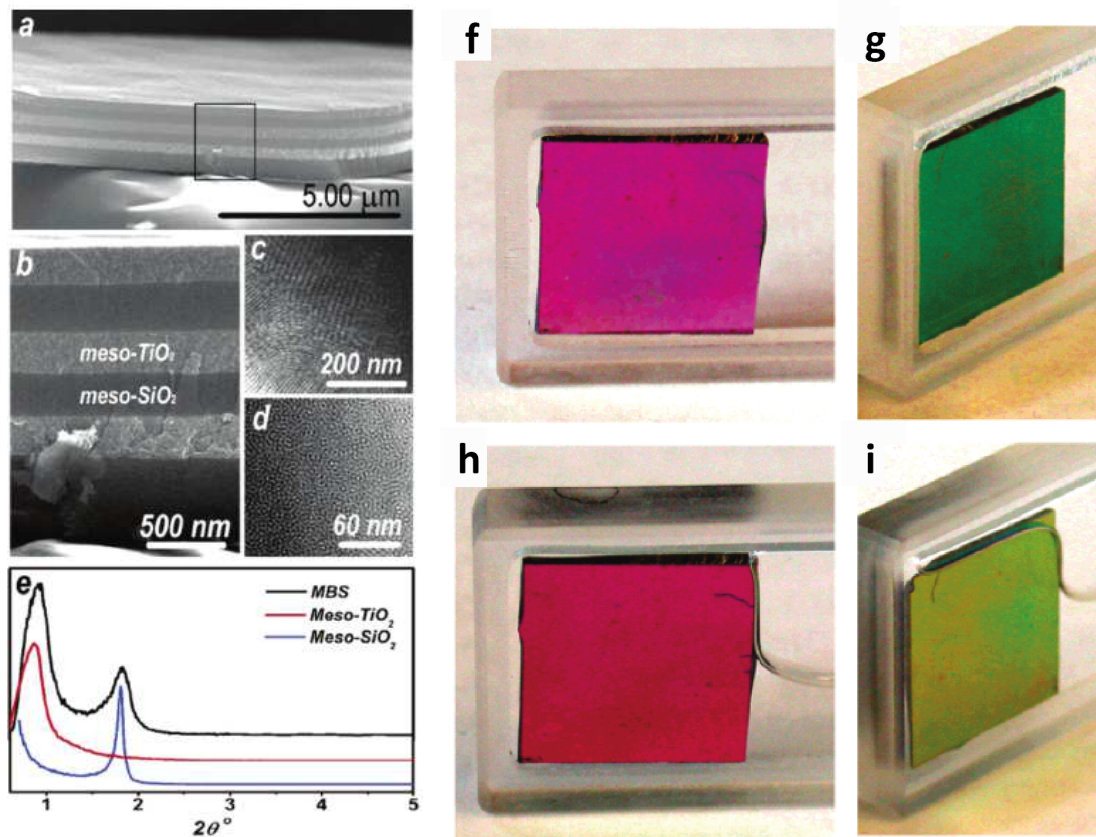
Figure 1.9. a,b) High-resolution SEM images of a mesoporous (meso-) TiO_2/SiO_2 Bragg stack. Scanning transmission electron microscopy images displaying the pore architecture of c) meso-TiO_2 and d) meso-SiO_2 and e) small-angle XRD pattern of a meso-TiO_2/SiO_2 Bragg stack compared to those of single meso-TiO_2 and SiO_2 layers. Four-layer meso-TiO_2/SiO_2 Bragg stack in air (f and g) and in ethanol (h and i) observed from different viewing angles. © American Chemical Society (2006). Reproduced with permission.[62]

Likewise, a "bottom-up" assembly of Bragg stacks by spin-coating of TiO_2 and SiO_2 precursors allows for fabricating 1D PCs with high optical quality (see an example of a spin-coated TiO_2/SiO_2 1D PC in Figure 1.4b,c).[66] Bragg stacks built from TiO_2/SiO_2 *nanoparticle (NP)* multilayers demonstrated great potential in chemical vapor and liquid detection.[39,67] Colodrero *et al.* studied the optical properties of various spin-coated NP-based 1D PCs versus changes in the ambient vapor pressure and discussed the sorption properties of the constituent layers.[68] As was mentioned in Section 1.1, promising opportunities for analyte sensing arise from the use of defect layers that break the periodicity of a PC, and create allowed photonic modes in the band gap. In their study Colodrero *et al.* showed also that sharp dips

within the reflectance spectrum, corresponding to the band gap, provide an excellent possibility to precisely monitor the peak shifts induced by vapor adsorption (see Figure 1.10).[68] A next captivating application for the NP-based TiO_2/SiO_2 1D PCs was demonstrated by Bonifacio *et al.*, who were able to make a highly specific *photonic nose* by using an array of mesoporous Bragg stacks functionalized with different surface groups that selectively adsorbed various vapors to different degrees.[69,70] By using the digital-color image principal-component analysis the photonic nose could identify different classes and types of molecular species and also discriminate several pathogenic bacteria strains.
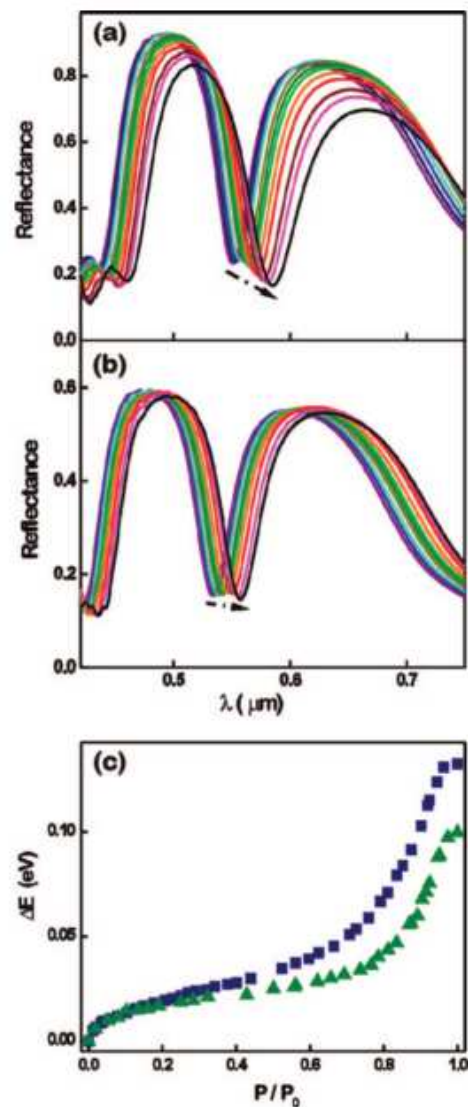
Figure 1.10. Optical response of the multilayer structure with a planar defect after being exposed to different partial pressures of a) isopropanol and b) water vapors. (c) Evolution of the position of the reflectance dip corresponding to the defect state within the bandgap for different partial pressures of isopropanol (blue squares) and water (green triangles). © American Chemical Society 2008. Reproduced with permission.[68]

Nanoparticle-based porous 1D PCs attracted interest in the field of dye-sensitized solar cells (DSSCs). 1D PCs can substantially enhance its power-conversion efficiency by means of localizing optical modes within the dye-sensitized electrode at photonic bandgap frequencies (see Figure 1.11a).[71] Its porous structure enables the electrolyte to flow through it and soak the electrode without interfering with the charge transport through the solar cell. With a thickness in the micrometer range, the PC is able to localize incident light within the nanocrystal-dyed TiO_2 electrode (see Figure 1.11b and c) in a desired wavelength range. Average power conversion efficiencies of DSSCs can be improved to between 15 and 30% of the reference value attained for standard electrodes.
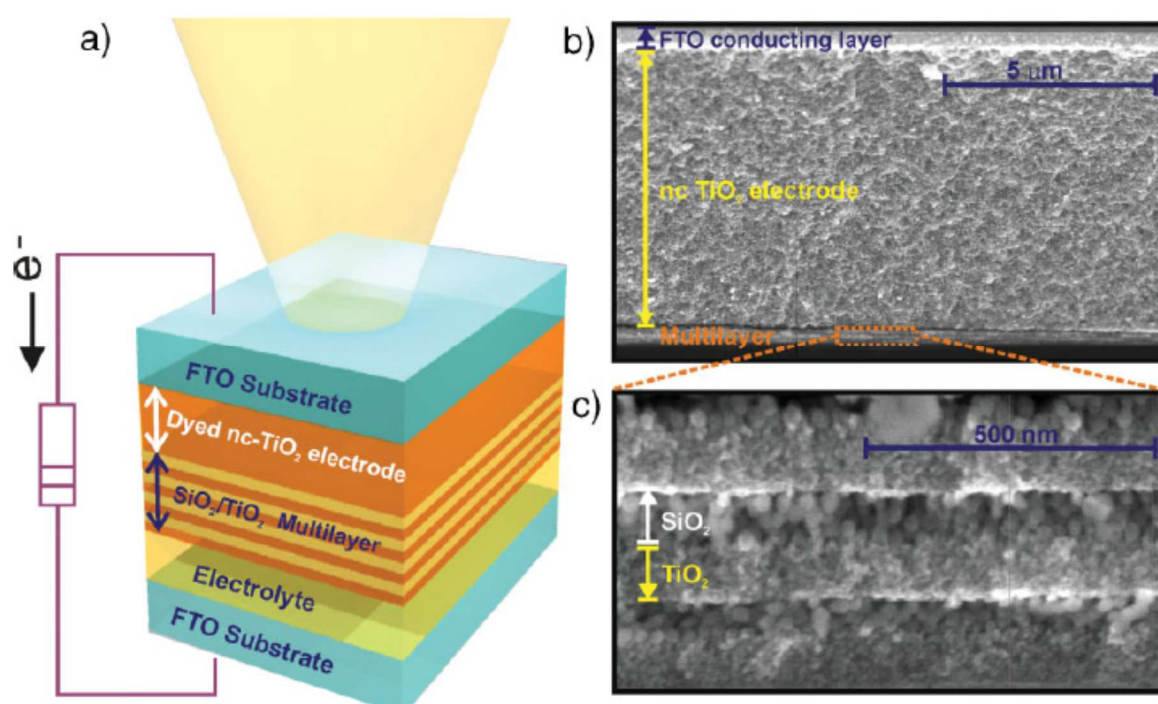
Figure 1.11. Design and microstructure of a dye-sensitized solar cell coupled to a porous nanoparticle-based 1D PC. a) Scheme of the solar cell based on the 1D PC illuminated by a light beam. b) SEM image showing a cross-section of a dye-sensitized nanocrystal TiO_2 electrode onto which a TiO_2/SiO_2 NP-based 1D PC has been deposited (bottom of the image). c) Magnified view of the silica (spherical particles) and titania (smaller crystallites) layers composing the 1D PC. © 2009 Wiley-VCH Verlag GmbH&Co. Reproduced with permission.[71]

Infiltrating the PCs with polymers provides routes to obtaining flexible Bragg stacks (see Figure 1.12).[72] Flexible Bragg stacks can serve as protectve multilayers for the prevention of UV degradation of food and beverage, storage of cosmetics, or, generically, as adaptable coatings for a variety of UV sensitive

environments (e.g. human skin). This new approach is an alternative to the current technology for shielding that is based on the inclusion of UV-absorbers into a liquid or solid matrix.
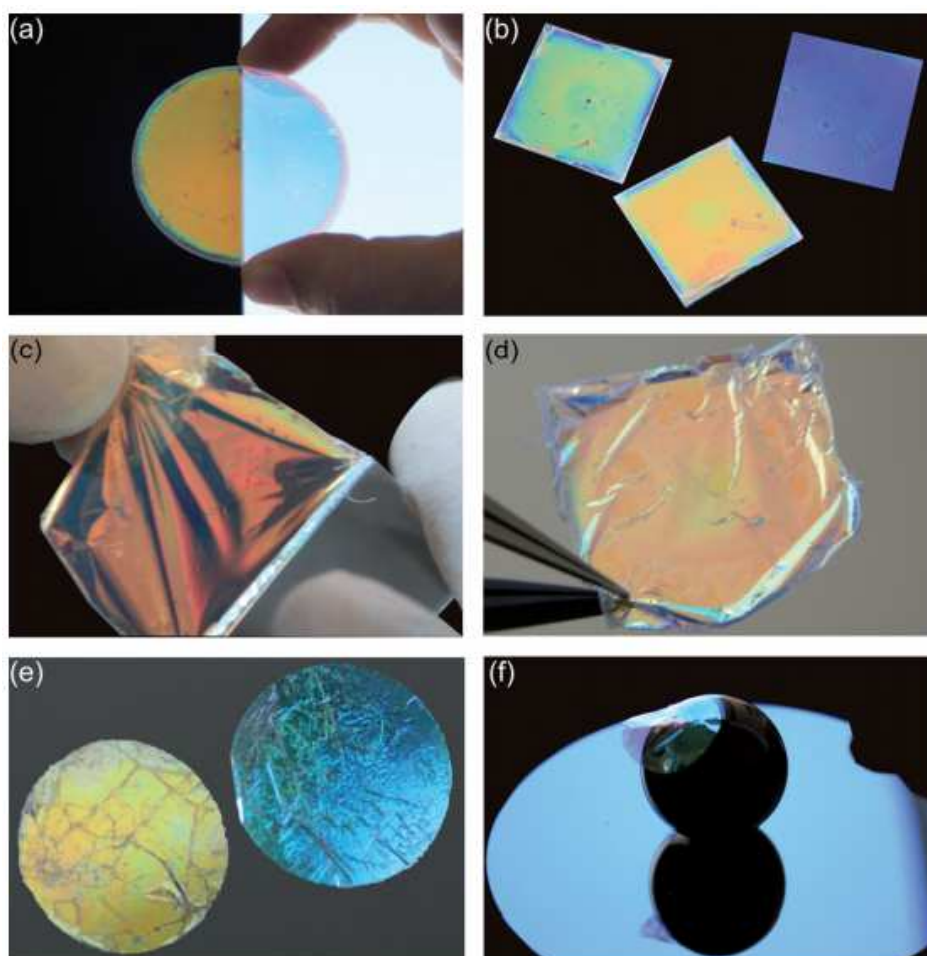
Figure 1.12. (a) A twelve layer nanoparticle based 1D PC deposited on a circular glass and infiltrated with polycarbonate. (b) 1D PC of different lattice parameters deposited on different square Si and glass substrates and infiltrated with polycarbonate. (c) A picture taken while peeling off a polycarbonate infiltrated 1D PC previously deposited on glass. (d) The flexible Bragg mirror shown in (c) being put in conformal contact with the flat surface of a Si wafer. (e) Different round cuts of flexible Bragg mirrors of different lattice parameters deposited on Si wafers. (f) A circularly cut 1D PC film being put in conformal contact with a black painted sphere. ©2011 The Royal Society of Chemistry. Reproduced with permission.[72]

1.3. INORGANIC AND ORGANIC OPTOELECTRONIC DEVICES

Optoelectronics is a research field investigating the interaction between light and electrical materials. Optoelectronic devices play a key role in various applications in everyday life including lighting, optical

telecommunications, data storage, solar cells, and others. Among the many examples of optoelectronic devices are the inorganic and organic light emitting diodes (LEDs and OLEDs) and photodetectors.

1.3.1. INORGANIC SEMICONDUCTOR LIGHT-EMITTING DIODES

Inorganic semiconductor light emitting diodes (LEDs) are the light sources that provide a direct non-thermal transfer of electrical energy into light based on the effect of electroluminescence (EL).[73] LEDs has been foreseen as an "ultimate lamp" for the future,[74] and are being increasingly used in general illumination, display backlight technologies, communications, medical services, signage and others.[75,76] The advantages of LEDs include a longer lifetime (up to 50,000 h), better thermal management than conventional lighting sources (e.g. fluorescent lamps and incandescent lamps), ultra-high-speed response time (microsecond-level on–off switching), wider range of controllable color temperatures (4500 K -12,000 K) and wider operating temperature range (-20 °C to 85 °C).[77]

An LED consists of two compounds called *p-type semiconductor*s and *n-type semiconductor*s, which are placed in a direct contact, forming an active region called a *p-n junction*. When a p–n junction is biased in the forward direction, electrons in the n-junction move to the boundary layer into the p-junction, and holes are injected from the p-junction across the active layer into the n-junction.[77] The active region of an ideal LED emits one photon for every electron injected. The internal quantum efficiency is defined as the number of photons emitted from an active region per second divided by the number of electrons injected into the LED per second. The light extraction efficiency is defined as the number of photons emitted into free space per second divided by the number of photons emitted from the active region per second.[73] The external quantum efficiency is the ratio between the number of photons emitted into free space per second and the number of electrons injected into the LED per second. Notably, the extraction efficiency in LEDs can be enhanced through the use of photonic crystals.[78]

A cross-sectional side view of an LED is shown in Figure 1.13. An LED package mounted on a printed circuit board is composed of a housing, encapsulant, die, bond wires, die attach, lead frames, metal heat slug, and solder joints.[77] The die is a compound semiconductor; the common materials for a die include GaAs, AlGaAs, GaAsP, GaP, AlN, AlGaN, GaN, InGaN and others.[79] LEDs range from a narrow spectral band emitting light (red, yellow, green, blue, *etc.*), to a wider spectral band light of white, with a different distribution of luminous intensity spectra and shades depending on color mixing and package design. Every LED color is represented by unique *x–y* coordinates, as shown in the CIE (Commission

Internationale De L'eclairage (International Commission on Illumination)) 1931 chromaticity diagram (Figure 1.14). [73]
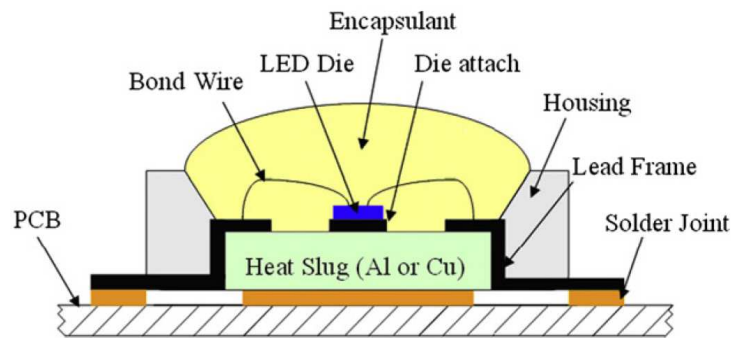
Figure 1.13. LED package assembled with printed circuit board (PCB). ©2011 Elsevier Ltd. Reprinted with permission.[77]
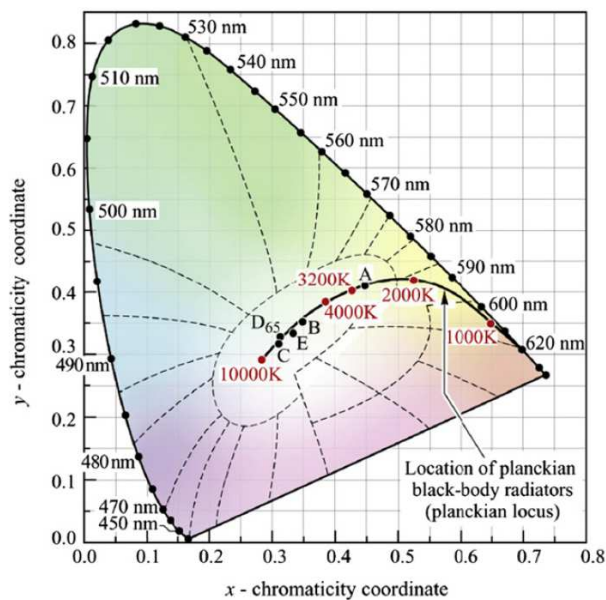
Figure 1. 14. CIE 1931 chromaticity diagram. © Cambridge University Press. Reprinted with permission.[73]

There are three major degradation mechanisms in LEDs: semiconductor-, interconnect- and package-related ones.[77] Semiconductor–related failure mechanisms include defect and dislocation generation and movement, die cracking, dopant diffusion, and electron migration; interconnect-related ones are electrical bond wire fatigue, electrical contact interdiffusion, and electrostatic discharge; and package-related ones include carbonization of the encapsulant, delamination, encapsulant yellowing, lens cracking, phosphor thermal quenching, and solder joint fatigue. The development of more reliable LEDs is of crucial importance for the optoelectronic applications.

1.3.2. ORGANIC LIGHT-EMITTING DIODES

In contrast to their inorganic counterparts (see Section 1.3.1), organic light-emitting diodes (OLEDs) are flat and thin large-area light sources.[80] A composition of a typical three-layer OLED is schematically displayed in Figure 1.15. The positively biased anode is required in order to inject holes into the hole transport layer. Similarly, electrons are injected from the cathode into the electron transport layer. The emission layer may comprise one or more dyes emitting light in different regions of the visible spectrum.
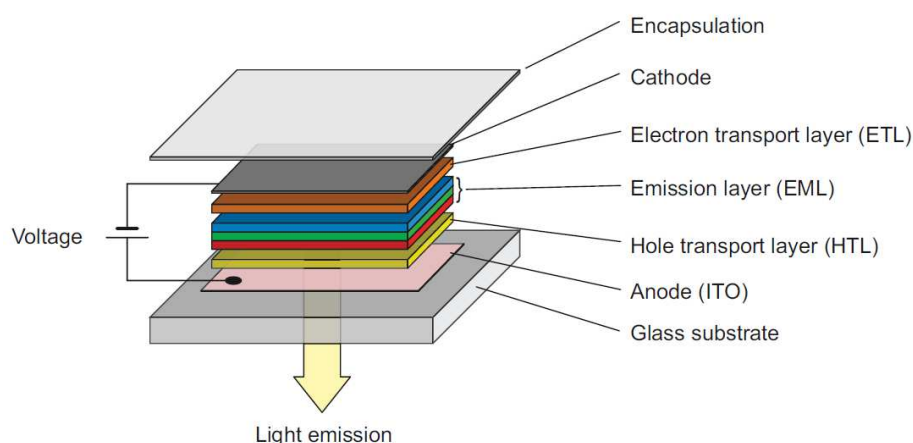
Figure. 1.15. Simplified illustration of a three-layer OLED stack. © 2012 WILEY-VCH Verlag GmbH. Reprinted with permission.[80]

When discussing the properties of organic LEDs, it is common to use the concepts derived from inorganic semiconductor physics. However, one should be aware of the peculiarities and differences of organic semiconductors to their inorganic counterparts. Since most polymeric or low-molecular weight materials used in OLEDs form disordered amorphous films without a macroscopic crystal lattice, it is not possible to simply adopt mechanisms developed for semiconductor crystals.[81] In comparison to the inorganic-based LEDs, the charge transport is not a coherent motion in well-defined bands, but rather a stochastic process of hopping between localized states. Excitations are localized on either individual molecules or a few monomeric units of a polymer chain and usually have a large exciton binding energy of several tenths of an eV. Also, impurities usually act as traps rather than as sources of extrinsic mobile charge carriers.

As shown schematically in Figure 1.16 EL in organic materials requires several steps, including the injection, transport, capture and radiative recombination of positive and negative charge carriers inside

an organic layer with suitable energy gap to yield visible light output.[81] For simplicity, the spatial variation of the molecular energy levels is drawn in a band-like fashion, however, one has to keep in mind that these organic semiconductors are disordered materials without a well-defined band structure.
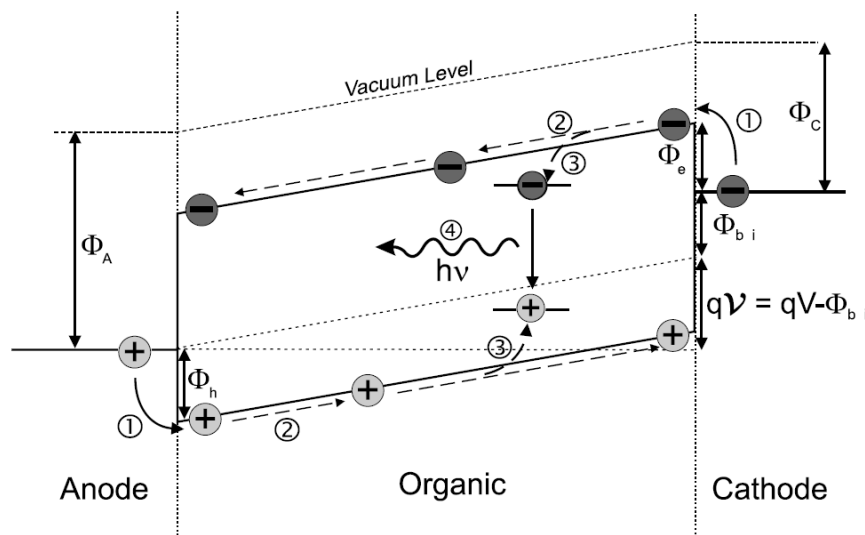
Figure 1.16. Basic steps of EL: (1) charge carrier injection, (2) charge carrier transport, (3) exciton formation, (4) radiative exciton decay. Φ_A is the anode workfunction, Φ_C is the cathode workfunction, Φ_H is the hole injection barrier, Φ_e is the electron injection barrier, Φ_{bi} is the built-in potential, V - applied voltage, v is the effective voltage across the organic layer, q - elementary charge. © 2001Elsevier Science B.V. Reprinted with permission.[81]

The development of OLEDs has been propelled by the synthetic progress in the realm of tailor-made functional organic materials that can be processed into well-controlled thin films.[82] Typically, the materials for OLED include small molecules, like organometallic chelates (e. g. tris(8-hydroxyquinolinato)aluminium (Alq3)), fluorescent and phosphorescent dyes and conjugated dendrimers, or conjugated polymers, like poly(p-phenylenevinylenes), polythiophenes (e. g. P3HT), poly(3,4-ethylenedioxythiophene) polystyrene sulfonate (PEDOT:PSS) mixture and others.[82]

1.3.3. PHOTODIODE DETECTORS

Photodiodes operate by absorption of photons or charged particles and generate a flow of current in an external circuit, proportional to the incident power. A scheme of a typical photodetector is shown in Figure 1.17. When a photon of sufficient energy strikes the diode, it creates an electron-hole pair. The behavior of a photodiode depends on the fate of photogenerated carriers that can either be collected at

electrodes (holes at the anode and electrons at the cathode) or can undergo recombination before collection.[83]
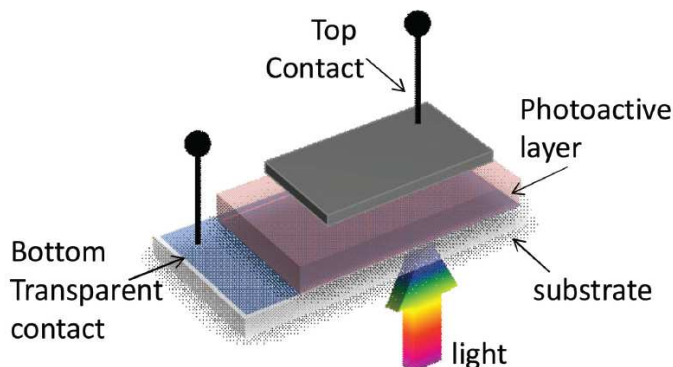
Figure 1. 17. Typical configuration of a photodetector with vertical topology in which with the light window entrance is on the bottom. © 2013 WILEY-VCH Verlag GmbH & Co. Reproduced with permission.[83]

One of the important characteristics of a photodiode is the responsivity – a measure of the sensitivity to light, defined as the ratio of the photocurrent to the incident light power at a given wavelength. It varies with the wavelength of the incident light as well as applied reverse bias and temperature.[84] Responsivity increases slightly with applied reverse bias due to improved charge collection efficiency in the photodiode. Also, there are responsivity variations due to change in temperature. Another parameter is the dark current - the current through the photodiode in the absence of light, when it is operated in photoconductive mode, which includes photocurrent generated by background radiation and the saturation current of the semiconductor junction. Dark current must be accounted for by calibration if a photodiode is used to make an accurate optical power measurement, and it is also a source of noise when a photodiode is used in an optical communication system. A commonly adopted figure of merit to quantify the limit of what can be detected due to the presence of noise is the noise equivalent power (NEP), defined as the signal optical power yielding a signal-to-noise ratio equal to 1.[83]

Optoelectronics properties of organic semiconductors make them interesting candidates for applications in the field of light signal detection. Organic optoelectronic materials have attracted particular attention since the discovery of conducting polymers in the 1970s.[85] Photodetectors based on organic semiconductors are proposed to afford devices with low-cost, light-weight, high efficiency and high environmental benignity, which are important for organic optoelectronic devices and circuits.[86] Solution-processability of organic photodetectors allows a straightforward combination with other

materials, including inorganic ones, without increasing cost and process complexity significantly compared with conventional crystalline semiconductors.[87]

1.4. OBJECTIVES

As shown in Chapter 1, recent progress in the realm of "smart" 1D photonic structures has paved the way to the realization of a variety of novel optical sensing motifs. Typically, optical sensing in such systems was realized *via* tracking the behavior of the photonic band gap – a characteristic spectral region allowing for the modulation of the transmission/reflection properties of PCs – by means of a spectrophotometer or a naked eye. For practical use, however, it is favorable that the sensor is integrated into a platform that converts the optical (spectral) response into an electrical signal *via* a transduction scheme with a high sensitivity and a noncomplex read-out. Therefore, the major objective of this thesis was to design and perform a bottom-up assembly of an integrated miniature detection platform featuring a facile electrophotonic read-out, which would be an alternative to a conventional spectrophotometric approach. Furthermore, the versatility and feasibility of this platform in multi-modal sensing was to be explored. The prototype detection platform was designed to serve three major realms of sensing: thermo-, chemo- and biosensing, as shown schematically in Figure 1.18.
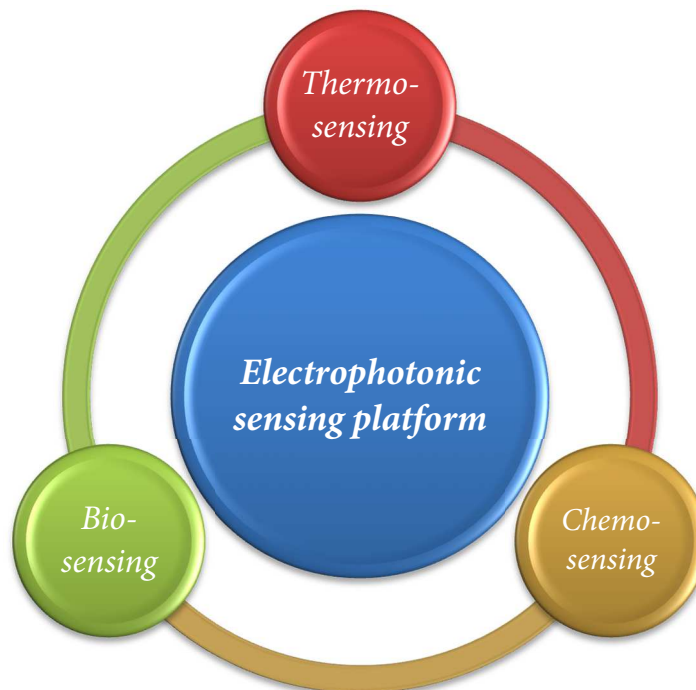
Figure 1.18. Schematic overview of the thesis objectives.

Thermal sensing

As was demonstrated in Section 1.2.1, TiO$_2$/SiO$_2$ multilayers represent an established class of photonic crystals for sensing applications, however, their thermo-optic properties were not previously studied. Therefore, TiO$_2$/SiO$_2$-based 1D PCs were chosen as the sensing elements for the prototype platform. The first goal was to investigate the thermo-optic response of TiO$_2$/SiO$_2$ with various morphologies, thicknesses and porosities to find the PC candidates with an optimal thermo-optic response, which was crucial for the further platform assembly. Then, the next goal was to integrate the optimized thermoresponsive tunable TiO$_2$/SiO$_2$ 1D PCs with various narrowband light emitting diodes for a proof-of-concept temperature sensing experiment.

Chemical sensing

The next objective was to design and realize an integrated all-in-one sensing platform, christened "electrophotonic nose", by combining chemo-responsive TiO$_2$/SiO$_2$ 1D PCs with a solution-processed spin-coated organic light-emitting diode and organic photodetector, and adding a polydimethylsiloxane fluidic chamber for the vapor and fluid sensing experiments. Additionally, a focus was placed on visualizing spatially resolved chemical diffusion in the multilayer system.

Biosensing

Finally, the objective was to demonstrate a non-invasive, real-time optical monitoring approach for evaluating the confluency and viability of various adhesive cell lines. To address this goal, two proof-of-concept experiments for monitoring the cell lysis (apoptosis) and cell growth were chosen.

1.5. BIBLIOGRAPHY

(1)   Rayleigh, Lord. *Philos. Mag. Ser. 5* **1887**, *24*, 145.

(2)   Yablonovitch, E. *Phys. Rev. Lett.* **1987**, *58*, 2059.

(3)   John, S. *Phys. Rev. Lett.* **1987**, *58*, 2486.

(4)   Yablonovitch, E.; Gmitter, T. *Phys. Rev. Lett.* **1989**, *63*, 1950.

(5)   Joannopoulos, J. D.; Villeneuve, P. R.; Fan, S. *Nature* **1997**, *386*, 143.

(6)   Sakoda, K. *Optical Properties of Photonic Crystals*; 2nd ed.; Springer Berlin Heidelberg, **2005**.

(7)   Joannopoulos J. D.; Johnson S. G.; Winn J.N.; Meade, R. D. *Photonic Crystals: Molding the Flow of Light*; 2nd ed.; Princeton University Press: Princeton, **2008**.

(8)   Moon, J. H.; Yang, S. *Chem. Rev.* **2010**, *110*, 547.

(9)   Inoue, K.; Ohtaka, K. *Photonic Crystals - Physics, Fabrication and Applications*; Springer Berlin Heidelberg, **2004**.

(10)   Robinson S.; Nakkeeran R. *Photonic Crystal Ring Resonator Based Optical Filters, Advances in Photonic Crystals,* Passaro V. (Ed.), InTech, **2013**.

(11)   Yablonovitch, E. *J. Opt. Soc. Am. B* **1993**, *10*, 283.

(12)   Smith, D. R.; Dalichaouch, R.; Kroll, N.; Schultz, S.; McCall, S. L.; Platzman, P. M. *J. Opt. Soc. Am. B* **1993**, *10*, 314.

(13)   Noda, S.; Chutinan, A.; Imada, M. *Nature* **2000**, *407*, 608–610.

(14)   Prather, D. W.; Sharkawy, A.; Shi, S.; Murakowski, J.; Garrett, S. *Photonic Crystals, Theory, Applications and Fabrication*; John Wiley & Sons, Inc., **2009**.

(15)   Vignéras, L. O. *Photonic Crystals - Introduction, Applications and Theory*; Massaro, A., Ed.; InTech, **2012**.

(16)   Deubel, M.; von Freymann, G.; Wegener, M.; Pereira, S.; Busch, K.; Soukoulis, C. M. *Nat. Mater.* **2004**, *3*, 444.

(17)   Russell, P. S. J. *J. Light. Technol.* **2006**, *24*, 4729.

(18)   Russell, P. S. J.; Hölzer, P.; Chang, W.; Abdolvand, A.; Travers, J. C. *Nat. Photonics* **2014**, *8*, 278.

(19)   Tanabe, T.; Notomi, M.; Mitsugi, S.; Shinya, A.; Kuramochi, E. *Appl. Phys. Lett.* **2005**, *87*, 151112.

(20)   Asakawa, K.; Sugimoto, Y.; Watanabe, Y.; Ozaki, N.; Mizutani, A.; Takata, Y.; Kitagawa, Y.; Ishikawa, H.; Ikeda, N.; Awazu, K. *New J. Phys.* **2006**, *8*, 208.

(21)   Kang, P.; Ogunbo, S. O.; Erickson, D. *Langmuir* **2011**, *27*, 9676.

(22)   Wang, M.; He, L.; Hu, Y.; Yin, Y. *J. Mater. Chem. C* **2013**, *1*, 6151.

(23)   Phillips, R. W.; Coombs, P. G.; Higgins, P. K.; Markantes, C. T. Polymeric Sheet Having Oriented Multilayer Interference Thin Film Flakes Therein, Product Using the Same and Method. *US5424119* A, **1995**.

(24)   McGurn, A. R. *Phys. B Condens. Matter* **2001**, *296*, 201.

(25)   Fenzl, C.; Hirsch, T.; Wolfbeis, O. S.. *Angew. Chem. Int. Ed. Engl.* **2014**, *53*, 3318.

(26)   Nair, R. V.; Vijaya, R. *Prog. Quantum Electron.* **2010**, *34*, 89.

(27)   Pacholski, C. *Sensors* **2013**, *13*, 4694.

(28)   Arsenault, A. C.; Puzzo, D. P.; Manners, I.; Ozin, G. A. *Nat. Photonics* **2007**, *1*, 468.

(29)   Ge, J.; He, L.; Goebl, J.; Yin, Y. *J. Am. Chem. Soc.* **2009**, *131*, 3484.

(30)   Arsenault, A. C.; Clark, T. J.; von Freymann, G.; Cademartiri, L.; Sapienza, R.; Bertolotti, J.; Vekris, E.; Wong, S.; Kitaev, V.; Manners, I.; Wang, R. Z.; John, S.;Wiersma, D.; Ozin G. A. *Nat. Mater.* **2006**, *5*, 179.

(31)   Li, C.; Lotsch, B. V. *Chem. Commun.* **2012**, *48*, 6169.

(32)   Ge, J.; Yin, Y. *Angew. Chem. Int. Ed.* **2011**, *50*, 1492.

(33)   Wang, H.; Zhang, K.-Q. *Sensors* **2013**, *13*, 4192.

(34)   Gallei, M.; Zahn, J. T.; Engelhardt, J.; Hellmann, G. P.; Rehahn, M. *Chem. Mater.* **2013**. 25 *(11),* 2309.

(35)   Shamah, S. M.; Cunningham, B. T. *Analyst* **2011**, *136*, 1090.

(36)   Choi, C. J.; Cunningham, B. T. *Lab Chip* **2006**, *6*, 1373.

(37)   Shafiee, H.; Lidstone, E. A.; Jahangir, M.; Inci, F.; Hanhauser, E.; Henrich, T. J.; Kuritzkes, D. R.; Cunningham, B. T.; Demirci, U. *Sci. Rep.* **2014**, *4*, 4116.

(38)   Bonifacio, L. D.; Lotsch, B. V.; Puzzo, D. P.; Scotognella, F.; Ozin, G. A. *Adv. Mater.* **2009**, *21*, 1641.

(39)   Calvo, M. E.; Colodrero, S.; Hidalgo, N.; Lozano, G.; López-López, C.; Sánchez-Sobrado, O.; Míguez, H. *Energy Environ. Sci.* **2011**, *4*, 4800.

(40)   Ozin, G. A.; André, A.; Ludovico, C. *Nanochemistry: A Chemical Approach to Nanomaterials*; The Royal Society of Chemistry, **2009**.

(41)   Kinoshita, S.; Yoshioka, S. *ChemPhysChem* **2005**, *6*, 1429.

(42)   Finnemore, A.; Cunha, P.; Shean, T.; Vignolini, S.; Guldin, S.; Oyen, M.; Steiner, U. *Nat. Commun.* **2012**, *3*, 966.

(43)   Holt, A. L.; Sweeney, A. M.; Johnsen, S.; Morse, D. E. *J. R. Soc. Interface* **2011**, *8*, 1386.

(44)   Schenk, F.; Wilts, B. D.; Stavenga, D. G. *Bioinspir. Biomim.* **2013**, *8*, 045002.

(45)   Yoshioka, S.; Nakano, T.; Nozue, Y.; Kinoshita, S. *J. R. Soc. Interface* **2008**, *5*, 457.

(46)   Mathger, L. M. *J. Exp. Biol.* **2003**, *206*, 3607.

(47)   Levy-Lior, A.; Shimoni, E.; Schwartz, O.; Gavish-Regev, E.; Oron, D.; Oxford, G.; Weiner, S.; Addadi, L. *Adv. Funct. Mater.* **2010**, *20*, 320.

(48)   Fink, Y. *Science* **1998**, *282*, 1679.

(49)   Karaman, M.; Kooi, S. E.; Gleason, K. K. *Chem. Mater.* **2008**, *20*, 2262.

(50)   Born, M.; Wolf, E. Principles of Optics: Electromagnetic Theory of Propagation, Interference and Diffraction of Light; Cambridge University Press, **1999.**

(51)   Nogueira, G. M.; Banerjee, D.; Cohen, R. E.; Rubner, M. F. *Langmuir* **2011**, *27*, 7860.

(52)   Kolle, M.; Zheng, B.; Gibbons, N.; Baumberg, J. J.; Steiner, U. *Opt. Express* **2010**, *18*, 4356.

(53)   Almeida, R. M.; Portal, S. *Curr. Opin. Solid State Mater. Sci.* **2003**, *7(2)*, 151.

(54)   Hinczewski, D. S.; Hinczewski, M.; Tepehan, F. Z.; Tepehan, G. G. *Sol. Energy Mater. Sol. Cells* **2005**, *87*, 181.

(55)   Colodrero, S.; Ocaña, M.; Míguez, H. *Langmuir* **2008**, *24*, 4430.

(56)   Macwan, D. P.; Dave, P. N.; Chaturvedi, S. *J. Mater. Sci.* **2011**, *46*, 3669.

(57)   Brinker, C. J.; Lu, Y.; Sellinger, A.; Fan, *Adv. Mater.* **1999**, *11*, 579.

(58)   Angelomé, P. C.; Fuertes, M. C.; Soler-Illia, G. J. A. A. *Adv. Mater.* **2006**, *18*, 2397.

(59)   Illia, G. S.; Fuertes, M. C.; Angelomé, P. C.; Marchi, M. C.; Troiani, H.; Luca, V.; Míguez, H. **2007**, ISSN 1518-0204.

(60)   Fuertes, M. C.; López-Alcaraz, F. J.; Marchi, M. C.; Troiani, H. E.; Luca, V.; Míguez, H.; Soler-Illia, G. J. A. A. *Adv. Funct. Mater.* **2007**, *17*, 1247.

(61)   Fuertes, M. C.; Colodrero, S.; Lozano, G.; Gonzalez-Elipe, A. R.; Grosso, D.; Boissiere, C.; Sanchez, C.; Soler-Illia, G. J. A. A.; Miguez, H. *J. Phys. Chem. C* **2008**, *112*, 3157.

(62)   Choi, S. Y.; Mamak, M.; von Freymann, G.; Chopra, N.; Ozin, G. A. *Nano Lett.* **2006**, *6*, 2456.

(63)   Wu, Z.; Lee, D.; Rubner, M.; Cohen, R. *Small* **2007**, *3*, 1467.

(64)   Lee, D.; Rubner, M. F.; Cohen, R. E. *Nano Lett.* **2006**, *6*, 2305.

(65)   Lee, D.; Omolade, D.; Cohen, R. E.; Rubner, M. F. *Chem. Mater.* **2007**, *19*, 1427.

(66)   Calvo, M. E.; Sánchez-Sobrado, O.; Colodrero, S.; Míguez, H. *Langmuir* **2009**, *25*, 2443.

(67)   Kobler, J.; Lotsch, B. V; Ozin, G. A.; Bein, T. *ACS Nano* **2009**, *3*, 1669.

(68)   Colodrero, S.; Ocaña, M.; González-Elipe, A. R.; Míguez, H. *Langmuir* **2008**, *24*, 9135.

(69)   Bonifacio, L. D.; Puzzo, D. P.; Breslav, S.; Willey, B. M.; McGeer, A.; Ozin, G. A. *Adv. Mater.* **2010**, *22*, 1351.

(70)   Bonifacio, L. D.; Ozin, G. A.; Arsenault, A. C. *Small* **2011**, *7*, 3153.

(71)   Colodrero, S.; Mihi, A.; Häggman, L.; Ocaña, M.; Boschloo, G.; Hagfeldt, A.; Míguez, H. *Adv. Mater.* **2009**, *21*, 764.

(72)   Calvo, M. E.; Sánchez Sobrado, O.; Lozano, G.; Míguez, H. *J. Mater. Chem.* **2009**, *19*, 3144.

(73)   Schubert, E. F. *Light-Emitting Diodes*; 2nd ed.; Cambridge University Press: New York, **2006**.

(74)   Holonyak, N. *Am. J. Phys.* **2000**, *68*, 864.

(75)   Steigerwald, D. A.; Bhat, J. C.; Collins, D.; Fletcher, R. M.; Holcomb, M. O.; Ludowise, M. J.; Martin, P. S.; Rudaz, S. L. *IEEE J. Sel. Top. Quantum Electron.* **2002**, *8*, 310.

(76)   Brañas, C.; Azcondo, F. J.; Alonso, J. M. *MRS Bull.* **2008**, *33*, 459.

(77)   Chang, M.-H.; Das, D.; Varde, P. V.; Pecht, M. *Microelectron. Reliab.* **2012**, *52*, 762.

(78)   Matioli, E.; Weisbuch, C. *J. Phys. D. Appl. Phys.* **2010**, *43*, 354005.

(79)   Craford, M. G.; Steranka, F. M. *Light-Emitting Diodes in Encyclopedia of Applied Physics*; Trigg, G. L., Ed.; VCH: Weinheim, **1994**.

(80)   Brütting, W.; Frischeisen, J.; Schmidt, T. D.; Scholz, B. J.; Mayr, C. *Phys. Status Solidi* **2013**, *210*, 44.

(81)   Brütting, W.; Berleb, S.; Mückl, A. G. *Org. Electron.* **2001**, *2*, 1.

(82)   Mitschke, U.; Bäuerle, P. *J. Mater. Chem.* **2000**, *10*, 1471.

(83)   Baeg, K.-J.; Binda, M.; Natali, D.; Caironi, M.; Noh, Y.-Y. *Adv. Mater.* **2013**, *25*, 4267.

(84)   *OSI Optoelectronics*, www.osioptoelectronics.com.

(85)   Shirakawa, H.; Louis, E. J.; MacDiarmid, A. G.; Chiang, C. K.; Heeger, A. J. *J. Chem. Soc. Chem. Commun.* **1977**, 578.

(86)   Dong, H.; Zhu, H.; Meng, Q.; Gong, X.; Hu, W. *Chem. Soc. Rev.* **2012**, *41*, 1754.

(87)   Baierl, D.; Pancheri, L.; Schmidt, M.; Stoppa, D.; Dalla Betta, G.-F.; Scarpa, G.; Lugli, P. A *Nat. Commun.* **2012**, *3*, 1175.

2. EXPERIMENTAL METHODS

2.1. ULTRAVIOLET-VISIBLE MICROSCOPE SPECTRO-PHOTOMETRY

Within the whole range of electromagnetic radiation, which is of interest to material scientists, ultraviolet (UV-) and visible (Vis-) spectroscopy inhabits only a very narrow wavelength region. However, this photon energy range is of great importance as it corresponds to the region of energy in which atoms and molecules undergo electronic transitions, and the interaction of the electromagnetic radiation in this (Vis-) range with matter affects their perceived color.[1] UV-Vis spectroscopy enables characterisation of optical properties of the materials by measuring their spectral transmittance (T) – the ratio of transmitted spectral flux ($\Phi_{\lambda t}$) to the incident one $\Phi_{\lambda i}$: $T = \Phi_{\lambda t}/\Phi_{\lambda i}$; reflectance (R) – the ratio of reflected spectral flux ($\Phi_{\lambda r}$) to the incident one: $R = \Phi_{\lambda r}/\Phi_{\lambda i}$; or absorbance (A) – the ratio of absorbed spectral flux ($\Phi_{\lambda a}$) to the incident one: $A = \Phi_{\lambda a}/\Phi_{\lambda i}$.[2]

For the spectral characterisation of microscopic samples a UV-visible-NIR microscope spectrophotometer can be used. The microscope spectrophotometer combines an optical (wide-field) microscope and an add-on miniature spectrometer as shown in Figure 2.1, and can be configured to measure the transmittance (transillumination mode) or the reflectance (epi-illumination) of the sample. The objective of the microscope (Figure 2.1 b) is used to collect the light from the sample (Figure 2.1 a) and transfer it through the optical fiber (Figure 2.1 c) to the spectrometer (Figure 2.1 d-e). The diagram in the Figure 2.1 f shows how light travels through the miniature spectrometer based on the asymmetrical crossed Czerny-Turner optical bench.[3] Light from the input fiber enters the optical bench through the connector (1) - the amount of light is being regulated by a slit (2) and the wavelength range is being restricted by the filter (3). The collimating mirror (4) focuses light entering the optical bench towards the grating (5) of the spectrometer, which then directs the diffracted light onto the focusing mirror (6). The focusing mirror then focuses the light onto the detector collection lens (7) and the CCD detector (8) equipped with the variable longpass order-sorting filters (9) a quartz window (10) to enhance the spectrometer's performance in the UV range. The CCD detector converts the optical signal to a digital signal.
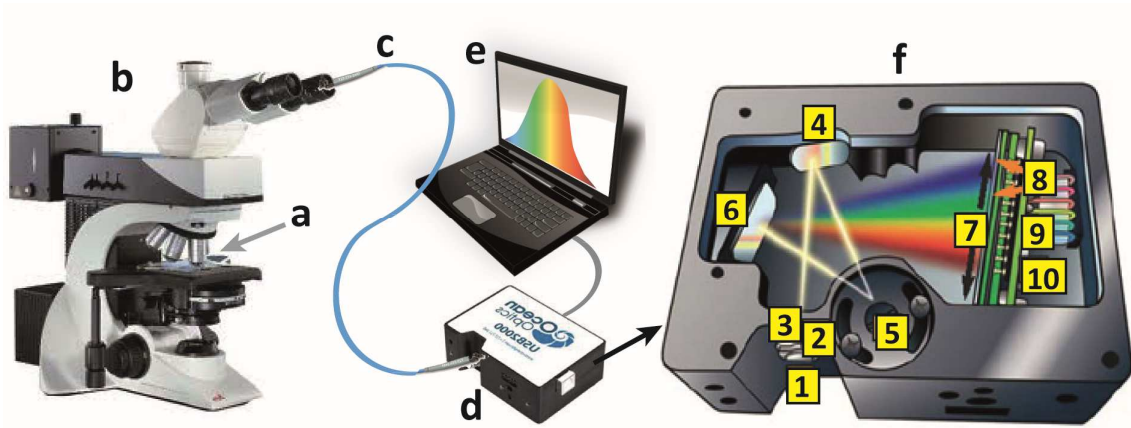
Figure 2.1. Investigation of the optical properties of the sample (a) performed by using the UV-VIS spectroscopic setup, based on the integration of a wide-field microscope (b) with an optical fiber (c), transferring the light signal to a miniature spectrometer (d) controlled by a computer (e). f) The schematic diagram illustrates the architecture of the optical bench and the light path in a miniature spectrophotometer USB2000+. © Ocean Optics, reproduced with permission.[4]

Using the setup shown in Figure 2.2, the transmittance $T(\lambda)$ of the sample relative to a standard substance (e. g. air) can be expressed by the Equation 2.2:

$$T(\lambda) = \frac{I_t(\lambda) - I_d(\lambda)}{I_r(\lambda) - I_d(\lambda)} \cdot 100\% \ , \quad (2.1)$$

where $I_t(\lambda)$ is the intensity of the light transmitted through the sample at wavelength λ, $I_d(\lambda)$ is the dark intensity at wavelength λ, $I_r(\lambda)$ is the reference intensity at wavelength λ. Similarly one can derive the specular reflectance relative to the reflection from a standard reference substance (e. g. highly reflective mirror).

One of the advantages of the suggested measurement route (see Figure 2.1) is that spectra can be acquired from microscopic sample areas (with micron-size features), which means that only small amounts of solid or liquid samples are required. UV-visible micro-spectrophotometry can also be used to map the spectral characteristics of samples with a high spatial resolution simultaneously with the image acquisition.

2.2. VARIABLE ANGLE SPECTROSCOPIC ELLIPSOMETRY
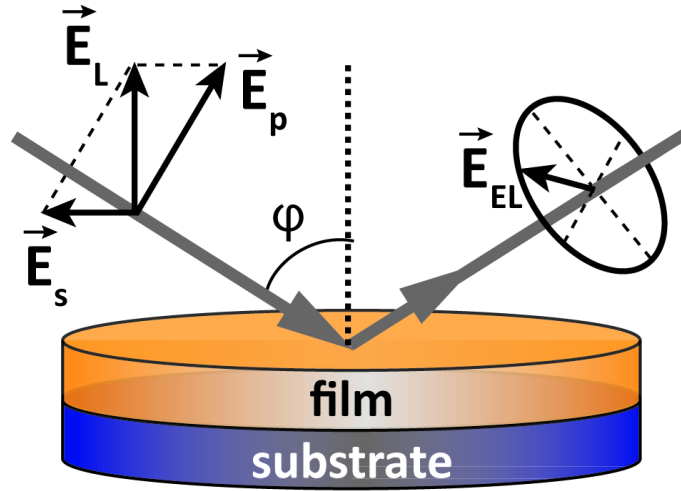
Figure 2.2. A sample ellipsometry measurement: The linearly polarized light $\vec{E}_L$ with both p- and s-components ($\vec{E}_p$ and $\vec{E}_s$) reflects from the film surface deposited on a substrate at an angle of incidence φ, and undergoes the amplitude and phase change for both p- and s- components becoming elliptically polarized ($\vec{E}_{EL}$).

In 1945, Rothen[5] has suggested an "apparatus designed to determine the thickness of films deposited on metal slides", which he christened the "ellipsometer". Ever since, ellipsometry became a powerful characterization technique able to provide invaluable information about the thickness (from sub-nanometer to a few microns), optical properties (refractive index, n, and extinction coefficient, k), homogeneity, roughness, doping concentration and crystallinity of bulk and thin film materials.[6] Ellipsometry represents a fast, non-destructive, and sensitive diagnostic method based on measuring a change in the polarisation of light after reflection from the material (or a stack of materials) of interest: dielectric, semiconductor, metal, superconductor, organic, biological coating, and composite materials.[7,8] To collect the ellipsometry data the following components are necessary: light source, polarization generator (polarizer, compensator or phase modulator), polarization analyzer, and detector. The ellipsometric measurement is expressed in terms of ellipsometric angles ψ (an amplitude ratio) and Δ (a phase difference), as shown in the Equation 2.1:[9]

$$\tan\psi \cdot e^{i\Delta} = \rho = \frac{r_p}{r_s} \qquad (2.1)$$

where ρ is a ratio of complex Fresnel reflection coefficients r_p and r_s of the sample for p- (parallel, i.e. in plane of incidence) and s- (perpendicular to the plane of incidence) polarized electric field

components ($\vec{E}_p$ and $\vec{E}_s$), as shown in Figure 2.2.[1] Variable-angle spectroscopic ellipsometry performs the measurement of ρ as a function of wavelength (in the wavelength range from 140 nm to 1700 nm) and angle of incidence ($0° \leq \varphi < 90°$) for an increased sensitivity to multiple film parameters.

Knowing ρ and φ enables the calculation of a complex pseudodielectric function $\langle \varepsilon \rangle$ of a bulk material (assuming the surface oxide and/or roughness effects are negligible) by using the Equation 2.2:[10]

$$\langle \varepsilon \rangle = (\langle n \rangle + i\langle k \rangle)^2 = \sin(\varphi)^2 \cdot \left[1 + \tan(\varphi)^2 \left(\frac{1-\rho}{1+\rho} \right)^2 \right] \quad (2.2)$$

In order to relate the measured parameters ψ and Δ with actual characteristics of the investigated region, such as thin film morphology and thickness, surface roughness or the dielectric functions of a film or the substrate, an optical model must be constructed, from which r_p and r_s are calculated.[11] Once the model has been chosen and the dielectric functions of the individual layers have been specified, the experimental ellipsometry data can then be optimally fitted to the model by using the regression analysis. For transparent materials the Cauchy dispersion model ($n(\lambda)$) is often used, see Equation 2.3: [12]

$$n(\lambda) = A + \frac{B}{\lambda^2} + \frac{C}{\lambda^4}, \quad (2.3)$$

in which A, B and C are the index optimization parameters, and λ is the measured wavelength. For the materials with absorption the Cauchy-Urbach dispersion model can be implemented by adding the dispersion Equation 2.4 to the classical Cauchy model:

$$k(\lambda) = \alpha \cdot e^{\beta \left(12400 \left(\frac{1}{\lambda} - \frac{1}{\gamma} \right) \right)}, \quad (2.4)$$

where α is the extinction coefficient amplitude, β is the exponent factor and γ is the characteristic band edge of the material. The mean squared error (MSE) estimator can be used to quantify the degree of correlation between the model and experimental spectra.

2.2.1. ELLIPSOMETRIC POROSIMETRY

---

[1] Note that because *the ratio* (ρ) is measured, no reference material is needed.

Spectroscopic ellipsometry can also be employed in a characterisation method called *ellipsometric porosimetry*, used for an *in situ* determination of the amount of analyte adsorbed/desorbed in/from the porous films.[13] This effective method for characterization of porosity, pore size distribution and specific surface area in porous films was first reported by Baklanov *et al.* in 2000.[14] The technique enables plotting the *physisoprtion isotherm* by analyzing the change of the refractive index (RI) of the film upon varying the partial pressure of a volatile analyte in a closed chamber, as can be seen in Figure 2.3.[15]
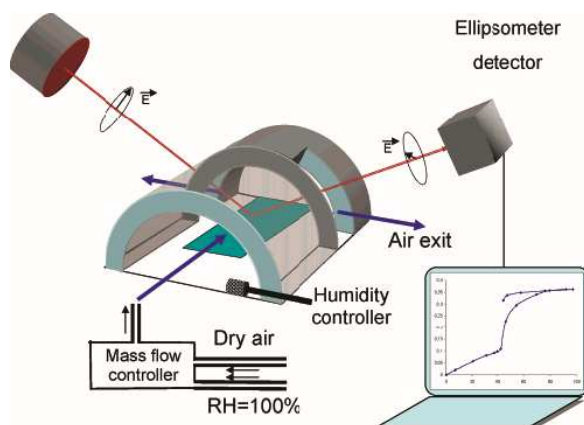
Figure 2.3. Scheme of the ellisometric porosimeter setup based on the coupling of a pressure-controlled chamber and a spectroscopic ellipsometer. ©American Chemical Society 2005. Reprinted with permission from ACS.[15]

According to the International Union of Pure and Applied Chemistry (IUPAC) classification,[16] there are six major types of physisorption isotherms, each typical for a certain class of materials depending on the interaction of the adsorptive and the adsorbent and on the adsorptive-adsorptive interactions, as shown in Figure 2.4. As designated by the IUPAC, pore sizes between 2 and 50 nm are termed *mesopores*, the pores with diameter ≤ 2 nm are called *micropores*, and the pores with diameter ≥ 50 nm are considered to be *macropores.*

Type I:	Microporous materials/chemisorption
Type II:	Non- or macroporous materials/ strong interaction between the adsorbate and adsorbent
Type III:	Non- or macroporous materials/ weak interaction between the adsorbate and adsorbent
Type IV:	Mesoporous materials/ strong interaction between the adsorbate and adsorbent
Type V:	Mesoporous materials/ weak interaction between the adsorbate and adsorbent
Type VI:	Nonporous, uniform materials/ layer-by-layer adsorption

Figure 2.4. Six major types of physisorption isotherms classified by the IUPAC and general examples of materials that are indicative for each of the isotherms. Reproduced after (15).

For the calculation of the pore size distribution of mesopores one should perform the analysis of the sorption hysteresis loop (see the isotherms of type IV and V in the Figure 2.4), which is observed due to the difference in the curvature radii of the menisci of the condensed liquid in the pore for the adsorption and desorption cycles.[14] The pore size determination is based on the Kelvin equation for the dependence of the relative pressure P/P_0 (the ratio of the vapour pressure to the equilibrium pressure of a flat liquid surface) on the meniscus curvature (see Equation 2.5):

$$\frac{1}{r_1} + \frac{1}{r_2} = -\frac{RT}{\mathcal{V}_L \cos\theta} \ln\left(\frac{P}{P_0}\right), \qquad (2.5)$$

where γ and V_L are the surface tension and the molar volume of the liquid, respectively, θ is the contact angle of the adsorptive, r_1 and r_2 are the principal curvature radii. Because the Kelvin equation does not take explicit account of the structure at the molecular level, it becomes inaccurate for small mesopores (≤ 50 Å) and is invalid for the description of the micropore size.[17]

For the determination of micropore size distribution one of the widely used approximations in ellipsometric porosimetry is the Dubinin-Raduchkevich model,[18] which allows for the calculation of such parameters as the micropore volume and the average pore size by using Equation 2.6:

$$W = W_0 e^{-\left[\frac{\left(RT \ln P_0/P\right)}{\beta E_0}\right]^2}, \qquad (2.6)$$

where W_0 is the micropore volume, β is the affinity coefficient, E_0 is the characteristic adsorption energy. The average pore size w_0 can be derived by using the formula $w_0 = K/E_0$ where $K \cong 12$ is a coefficient slightly changing depending on the product βE_0.

For the characterisation of film porosity by ellipsometric porosimetry, various effective medium approximations (Maxwell-Garnett theory,[19] Bruggeman,[20] Drude[21] and others[7]) can be used. One of the commonly used approximations is the Lorentz-Lorenz equation for the calculation of the relative film porosity V (Equation 2.7):

$$V = 1 - \left[\frac{\left(n_p^2 - 1\right)}{\left(n_p^2 + 2\right)}\right] \bigg/ \left[\frac{\left(n_s^2 - 1\right)}{\left(n_s^2 + 2\right)}\right], \qquad (2.7)$$

where n_s is the RI of the film skeleton and n_p is the measured RI of the porous film. If the pores are filled with the adsorbate with known RI (n_{ads}), the effective RI (n_{eff}) can by calculated with Equation 2.8:

$$\frac{n_{eff}^2 - 1}{n_{eff}^2 + 2} = V \frac{n_{ads}^2 - 1}{n_{ads}^2 + 2} + (1 - V) \frac{n_s^2 - 1}{n_s^2 + 2} \quad (2.8)$$

By combining Equations 2.7 and 2.8 one can obtain the following formula for the calculation of V (Equation 2.9):

$$V = \left(\frac{n_{eff}^2 - 1}{n_{eff}^2 + 2} - \frac{n_p^2 - 1}{n_p^2 + 2} \right) \Big/ \left(\frac{n_{ads}^2 - 1}{n_{ads}^2 + 2} \right), \quad (2.9)$$

which demonstrates that the value of the film skeleton RI (n_s) is not needed for the calculation of the porosity.

2.3. ATOMIC FORCE MICROSCOPY

Since its invention in 1986 by Binnig,[22] atomic force microscopy (AFM) has proved to be a powerful, multifunctional nanoscale tool opening up a variety of exciting new possibilities for nanobiotechnologists.[23] Primarily, AFM was developed to overcome the limitations of its predecessor, the scanning tunneling microscope (STM),[24] for imaging non-conducting samples. The principle of AFM is to probe the sample surface with a sharp tip (several μm long and ≈10 nm in diameter) located at the end of the cantilever (100-200 μm long) with a piconewton sensitivity. During the raster-scan the cantilever deflections, induced by the interaction forces between the tip and the sample surface, are being registered allowing to produce the surface topography map. The AFM cantilever can be deflected by the contribution from several microscopic surface-related forces.[25,26] The major role is played by the inter-atomic van der Waals force described by the Lennard-Jones potential (Equation 2.10):

$$U(d) = 4\varepsilon \left[\left(\frac{\sigma}{d} \right)^{12} - \left(\frac{\sigma}{d} \right)^6 \right], \quad (2.10)$$

where ε is the depth of the potential well, σ is the finite distance at which the inter-particle potential is zero, d is the distance between the particles. As can be seen from Equation 2.10 the van der Waals force acts repulsively when the cantilever tip is brought into contact with the surface. Another force acting during the AFM measurement is the cantilever force (F_z) given by Hook's law (Equation 2.11): [25]

$$F_z = -k \cdot z, \quad k = \frac{Eah^3}{4l^3}, \quad (2.11)$$

where z is the displacement of the cantilever, k is the spring constant, E is the Young's modulus, a is the cantilever width, h is the cantilever thickness, l is the cantilever length. Another, capillary, force appears, when water on the surface "pulls" the tip with strong force attraction of about 10^{-8} N.[25] The schematic illustration of the AFM experimental setup is presented in Figure 2.5. During the measurement the piezoelectric actuators in the XY scanning stage move the sample back and forth underneath the tip in order to scan the area with which the tip is interacting. The linear variable differential transformers (LVDT) integrated into the X-Y and Z piezo stages of the AFM are used for measuring the position of the stages by providing an output voltage proportional to the displacement. The deflection of the cantilever is detected by the change in the reflected light beam which is directed onto the segmented photodiode detector by a mirror.
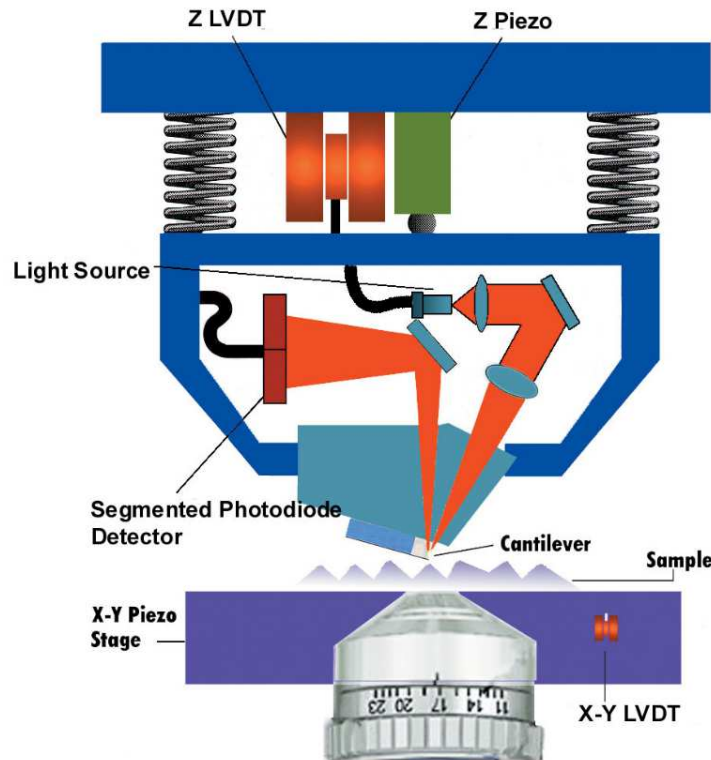
Figure 2.5. Scheme of the atomic force microscopy setup. © 2003-2004 Asylum Research, Inc. The cross-sectional view of the MFP-3D AFM head was reproduced with permission.[27]

The AFM can operate in three measurement modes: contact, intermittent (tapping) and non-contact.[28] In the contact (static) mode the cantilever tip is dragged across the surface of the sample. The dragging motion of the tip together with frictional and adhesive forces between the tip and the surface, can cause damage to both sample and probe and distort the image data. In the intermittent or tapping mode the cantilever is oscillating *near* its resonance frequency with a sufficient amplitude to prevent the tip from being trapped by adhesive meniscus forces from the top surface layer. In the third, non-contact mode, the cantilever is oscillating at resonant frequency and does not touch the surface to ensure minimal sample modification by the tip, and can allow achieving atomic resolution and direct imaging of chemical bonds in real space.[29]

The possibility to manipulate biological systems on the nanometer scale by means of AFM has garnered significant attention of the biophysical community.[30,31] AFM makes it possible to characterize biological cells and their components with a high resolution in real time and image surfaces in buffer solution with outstanding signal-to-noise ratio, offering a means of observing single biomolecules without the need for fixation or staining.[23]

2.4. FLUORESCENCE MICROSCOPY

Fluorescence is the property of some molecules to absorb light of a certain wavelength (from the ultraviolet or visible range), and emit light of a *longer* wavelength after a time interval called the fluorescence lifetime (typically on the order of nanoseconds).[32] A Jablonski diagram illustrates the electronic states of a fluorophore and the transitions between them (see Figure 2.6) during the fluorescence process:[33] A photon of energy $h\nu_{EX}$ absorbed by the molecule in the ground state (S_0) creates an excited electronic singlet state (S_2). The excited state exists for about 1–10 nanoseconds. During this time the energy of S_2 is partially dissipated, yielding a relaxed singlet excited state (S_1) from which fluorescence emission of a photon of energy $h\nu_{EM}$ originates. Due to dissipation $h\nu_{EX} < h\nu_{EM}$, therefore the emitted photon is of longer wavelength, than the excitation photon. As can be seen from the diagram in Figure 2.6, not all the molecules initially excited by absorption return to the ground state (S_0) by

fluorescence emission. There are other processes such as quenching, fluorescence resonance energy transfer and intersystem crossing depopulating S_1.
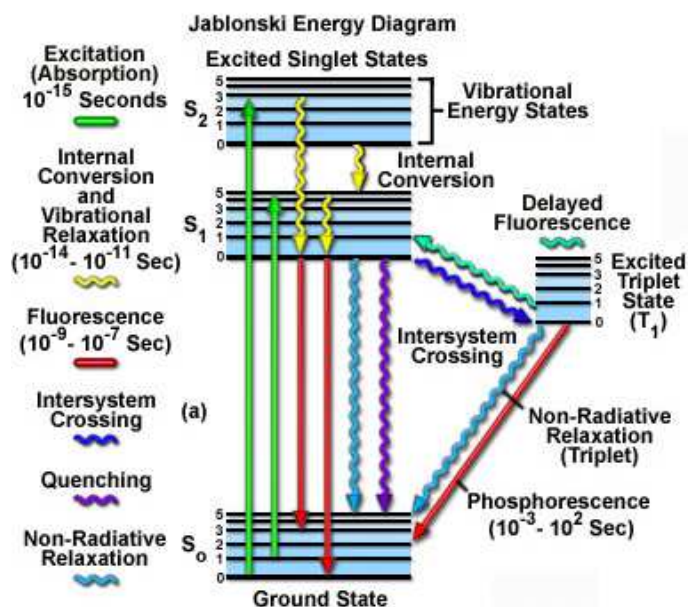
Figure 2.6. Jablonski diagram illustrating the electronic states of a molecule and the transitions between them. The states are arranged vertically by energy and grouped horizontally by spin multiplicity. Nonradiative transitions are indicated by wavy arrows and radiative transitions by straight arrows. ©Carl Zeiss Microscopy. Reproduced with permission.[34]

The difference in energies of the absorbed and emitted photons represented by ($h\nu_{EX}$ - $h\nu_{EM}$) called the Stokes shift (see Figure 2.7), is the critical property that makes fluorescence so powerful. In the fluorescence microscope excitation and emission can be separated by means of optical filter cubes. A filter cube consists of three coated glasses, namely an excitation filter, the dichromatic mirror and the emission filter. Both excitation and emission filters have distinct transmission curves that should not overlap to remove contributions of the excitation beam.
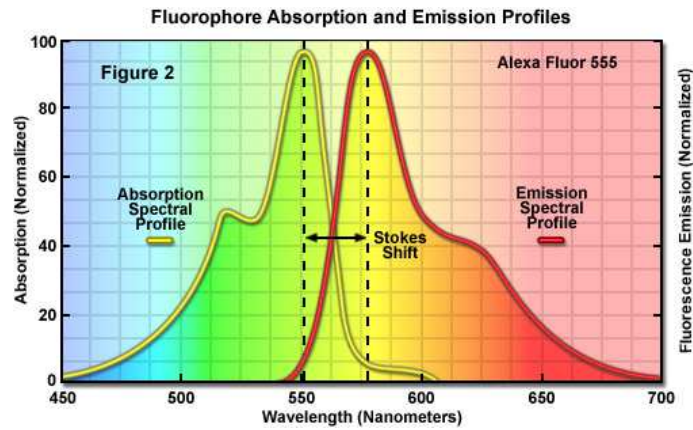
Figure 2.7. Demonstration of the Stokes shift between the absorption and the emission spectra of the fluorophore Alexa Fluor 555. ©Carl Zeiss Microscopy. Reproduced with permission.[34]

Most fluorescence microscopes are operated in the episcopic (epi-) illumination mode (illumination and detection from one side of the sample). The light path of a typical (epi-)fluorescence microscope is shown in Figure 2.8. A mercury arc lamp is commonly used as a light source for a range of excitation wavelengths. The illumination light passes the excitation filter, which ideally removes any other wavelengths and is directed by a dichromatic mirror to the objective focused to the sample. The specimen absorbs a part of the photons and emits Stokes-shifted (red-shifted) fluorescence light back into the objective. Only the correctly red-shifted light passes the emission filter to the ocular or detector.
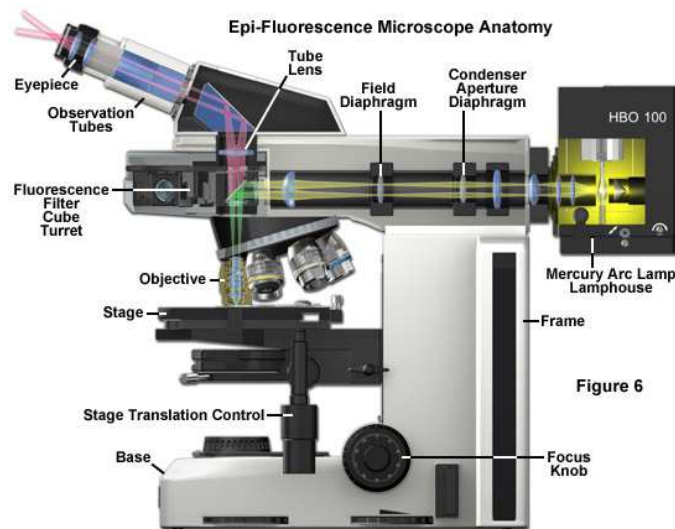
Figure 2.8. A cutaway diagram of an epi-fluorescence microscope. ©Carl Zeiss Microscopy. Reproduced with permission.[34]

In contrast to optical microscopy modes that are based on phase gradients, light absorption, and birefringence of the sample, fluorescence microscopy enables imaging of the distribution of a single molecular species based exclusively on the properties of fluorescence emission. By using fluorescence microscopy, the exact location of intracellular subunits labelled with various fluorophores can be examined, as well as their associated diffusion coefficients, transport characteristics, and interactions with other biomolecules.[34,35]

2.5. SCANNING ELECTRON MICROSCOPY

Scanning electron microscopy (SEM) is a versatile tool for the characterisation of the morphology and chemical composition of materials.[36] In comparison with the standard optical microscopy, the resolution of which is limited by diffraction to $\approx$ 200 nm (see Section 2.4), SEM can offer depths of field of several millimeters at low magnifications (x20-200) and a high spatial resolution of 1-10 nm.[37] The principle of SEM operation is shown in Figure 2.9. In a scanning electron microscope primary electrons are generated on the cathode represented by either thermionic (based on tungsten or lanthanum hexaboride filaments) or field (cold-cathode Schottky type) emission guns. The primary electrons are accelerated by an anode and then they are focused by condenser lenses to a diameter typically between 0.5 nm and 5 nm. The beam then passes through the scanning coils, which scan it in a raster pattern over the specimen surface.
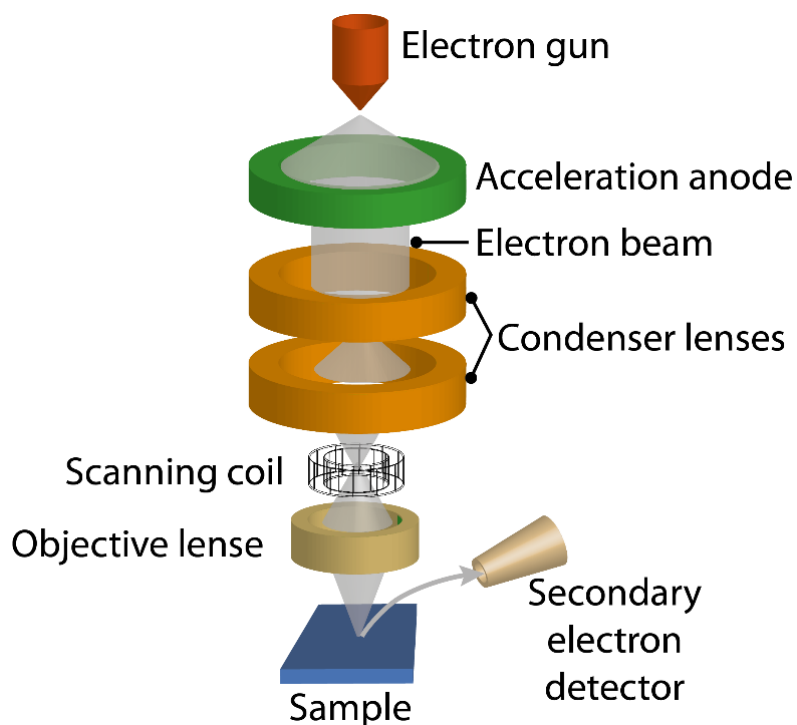
Figure 2.9. The principle of SEM operation.

Once the electron beam hits the sample surface a variety of processes can occur in a teardrop-shaped volume of the sample called the interaction volume, as shown in Figure 2.10. The size of the "interaction volume" depends on the electron's energy, the atomic number of the specimen and the specimen's density. Primary electrons hitting the surface can be reflected by elastic scattering or they can cause ionization of atoms in the surface resulting in the ejection of low-energy secondary electrons or Auger electrons, or induce the electromagnetic radiation (X-ray and cathodoluminescence).

The spatial resolution of the SEM depends on the size of the electron beam, which in turn depends on both the wavelength of the electrons and the electron-optical system that produces the scanning beam. The resolution is also limited by the size of the interaction volume, the volume of specimen material that interacts with the electron beam.
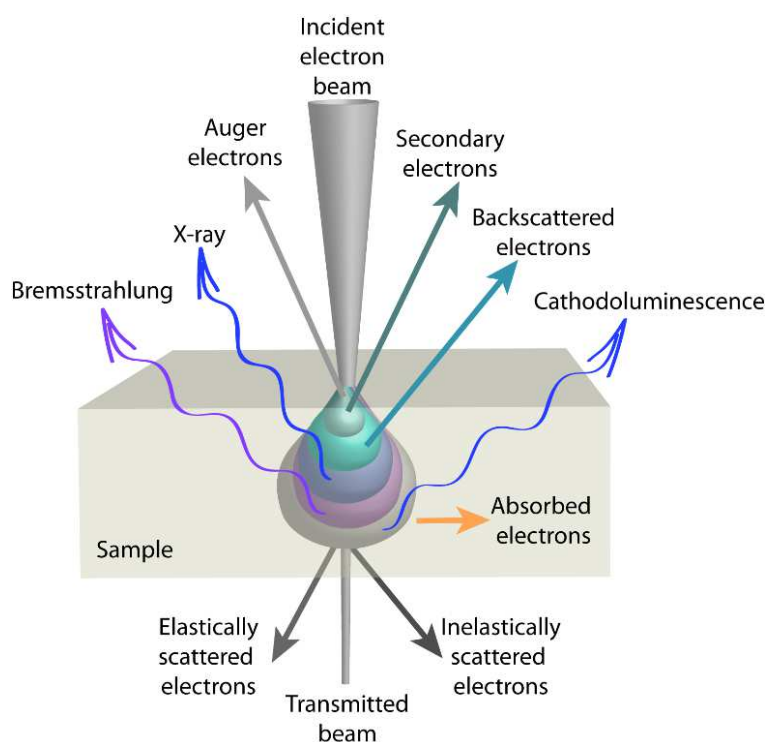
Figure 2.10. Interaction of an electron beam with a sample.

The secondary electron (SE) imaging is considered to be the most applicable method for producing the specimen's topography map. The explanation for this lies in the dependence of the number of SEs emitted from a surface on the incident angle of the electron beam. SEs are detected by a scintillator photomultiplier system, e.g. Everhart-Thornley detector (see Figure 2.9).[38] Another useful SEM method is the backscattered electron (BSE) imaging, which in addition provides the compositional information about the specimen.

2.6. X-RAY PHOTOELECTRON SPECTROSCOPY

X-ray photoelectron spectroscopy (XPS) is a powerful quantitative technique for establishing the elemental composition, chemical and electronic state of the few atomic layers at a surface of a material.[39] The method was developed by Siegbahn starting 1957, who referred to it as electron spectroscopy for chemical analysis (ESCA).[40,41] In an XPS experiment a sample is first placed in an ultra-high vacuum and then its surface is irradiated with an X-ray beam of known energy (typically Al Kα or Mg Kα radiation) that interacts with the inner electron shells of the sample atoms, thus generating photoelectrons with characteristic kinetic energies that escape from the top 1-10 nm of the surface.[42] The photoionization

process, during which the incident X-ray photon with energy of $h\nu$ (h is Planck's constant and ν is the frequency of the photon) ejects the photoelectron (e^-) from the surface atomic layers (the process is schematically shown in Figure 2.11 a), can be formulated as follows:

$$M + h\nu \rightarrow M^+ + e^-, \quad (2.12)$$
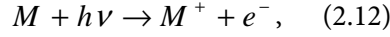
where M is the ground state species and M^+ is the ionized species.
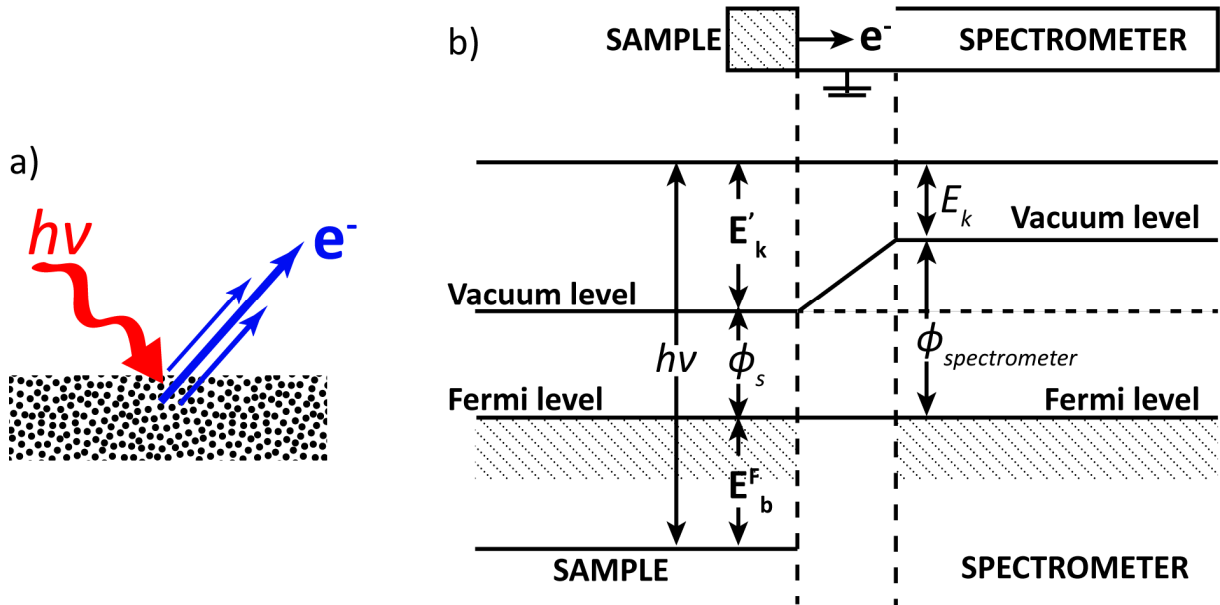
Figure 2.11. Schematic representation of a) the photoionization process and b) energy level diagram for the sample and the spectrometer, electrically connected to each other. Reproduced after ref. [43].

The prerequisites for an XPS experiment are: a) a monochromatic X-ray radiation source, b) an instrument which can separate the ejected electrons according to their kinetic energy, c) an electron energy analyser (spectrometer), and d) a high vacuum environment (to enable the emitted photoelectrons to be analysed without interference from gas phase collisions).[44] Figure 2.11b schematically depicts the energy levels for the solid sample which is in an electric contact with the spectrometer during the XPS measurement.[43] Based on the energy diagram in Figure 2.11b, the energy conservation law for photoelectrons can be written as the Equation 2.13:

$$h\nu = E_b^F + E_k^{'} + \phi_s, \quad (2.13)$$

where E_b^F is the binding energy of the electron relative to the Fermi level of the sample or the chemical potential of the electron, $E_k^{'}$ is the kinetic energy of the emitted electron directly after ejection, ϕ_s is the

work function of the solid material. As can be seen from Figure 2.11 b, the kinetic energy of the electron, E_k, measured by a spectrometer with the work function $\phi_{spectrometer}$ (note that the measured kinetic energy can have a different value from $E_k^{'}$), can be written as the Equation 2.14:

$$E_k = E_k^{'} + \phi_s - \phi_{spectrometer} \, . \quad (2.14)$$

Thus, by combining Equations 2.13 and 2.14 the binding energy of the electron relative to the Fermi level can be determined by using the following formula (see Equation 2.15):

$$E_b^F = h\nu - (E_k + \phi_{spectrometer}) \, , \quad (2.15)$$

note that the work function of the sample ϕ_s is no longer involved in the calculation.

In the XPS measurement, the kinetic energy spectrum of the escaped photoelectrons is measured: Each element gives rise to a characteristic set of peaks determined by the photon energy and the respective binding energies. The measured kinetic energy can be then directly recalculated into the binding energy spectrum associated with the different electron orbitals. XPS can be used for the analysis of all elements except hydrogen and helium.

2.7. POWDER X-RAY DIFFRACTION

Many crystalline solids cannot be fabricated in the form of single crystals of sufficient size and/or quality for the characterisation by means of single-crystal X-ray diffraction. To study the structural properties of various kinds of micro- and nano-crystalline materials it is therefore essential to obtain X-ray powder diffraction data.[45]

In 1912, Max von Laue discovered that crystals act as 3D diffraction gratings for X-rays with wavelengths similar to the interplanar spacing (d) in a crystal lattice.[46] The atoms in the crystal lattice can be visualized in all three directions by imaginary planes representing different periodic electron density distributions (see Figure 2.12); the planes can be described by a set of indices (Miller indices, *hkl*). For constructive interference, it is mandatory that the waves reflecting from the different planes satisfy the Bragg equation (2.16):

$$n\lambda = 2d_{hkl} \sin\theta \, , \quad (2.16)$$

where n is an integer determined by a given order, λ is a wavelength, and θ is the angle of the incident beam.[47]
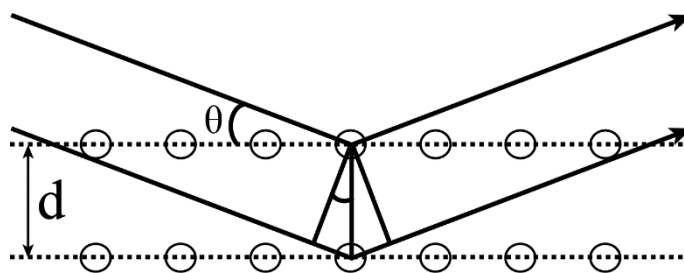
Figure 2.13. Schematic illustration of the Bragg diffraction.

During the measurement a collimated X-ray radiation is directed onto the sample. As the sample and detector are rotating, the intensity of the diffracted X-rays is recorded. When the geometry of the incident X-rays impinging on the sample satisfies Equation 2.16, constructive interference occurs and, thus, a peak in intensity is observed.

Powder X-ray diffraction provides information about the crystalline (coherently scattering) domains and allows for estimating the crystallite size. Regarding crystalline domains, one should not confuse the terms "particle size" and "crystallite size", as demonstrated in Figure 2.14: Figure 2.14a consists of one 10x10 nm^2 crystallite, whereas the 10x10 nm^2 agglomerate (or "particle", or "grain") in Figure 2.14b consists of several crystalline domains or crystallites. X-ray diffraction in the latter case will be sensitive to the sizes of the smaller single crystalline domains. Another example is shown in Figure 2.14c: A particle with the size of 12 nm consists of the crystallite (10 nm) coated by an amorphous layer. In such a case, the size of the crystalline domain, as determined by XRD, will be different from the "particle size" determined by electron microscopy or dynamic light scattering (see Section 2.8). In 1918, Scherrer suggested an Equation (2.17) relating the crystalline domain size with the line broadening in a diffraction pattern:[48]

$$L = \frac{k\lambda}{\beta \cos \theta}, \quad (2.17)$$

where L is the mean size of the ordered (crystalline) domains, k is the dimensionless Scherrer constant depending on the crystallite shape, λ is the wavelength, β is the integral line broadening (in radians), θ is the Bragg angle. The Scherrer approach assumes a homogeneous size of the crystalline domains and does not take into account the contribution of stress, strain, dislocations, twins or stacking faults.[47]
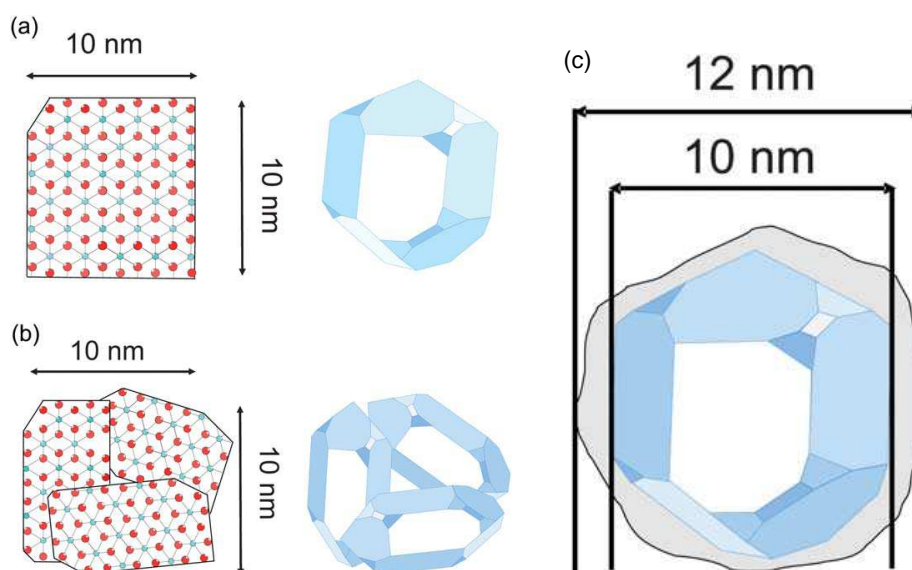
Figure 2.14. a) Single crystallite, b) three differently oriented crystallites forming an agglomerate, c) schematic illustration of a particle with overall size of 12 nm containing a crystalline core of 10 nm and an amorphous surface layer. ©Royal Society of Chemistry 2011. Reprinted with permission.[47]

2.8. DYNAMIC LIGHT SCATTERING

Dynamic light scattering (DLS), sometimes referred to as photon correlation spectroscopy, is a commonly used technique for measuring *in situ* the hydrodynamic sizes and size distributions (and sometimes the shapes) of particles in liquids.[49,50] DLS analyses the intensity of the monochromatic and coherent light scattered by the particles in the suspension as a function of time. The scattered intensity represents a stochastic signal due to the thermal (Brownian) motion of the particles. The intensity fluctuations can be related to the rate of diffusion of the particle through the solvent, described by the translational diffusion coefficient (D_t) expressed by the Stokes-Einstein equation (2.18):[51]

$$D_t = \frac{kT}{3\pi\eta d_H} , \quad (2.18)$$

where k is the Boltzmann constant, T is the absolute temperature, η is the viscosity of the solvent, and d_H is the hydrodynamic diameter of the particle. The equation 2.18 is valid only for spherical particles in a dilute dispersion. A stable known temperature is essential for the DLS measurement in order to assess the viscosity of a liquid.

To derive the translational diffusion coefficient from the rate of fluctuations of the scattered light signal, the second order time correlation function $g^{(2)}(\tau)$ of the scattered intensity $I(t)$ for the times t and $t + \tau$ is computed by using Equation 2.19:

$$g^{(2)}(\tau) = \frac{\langle I(t)I(t+\tau)\rangle}{\langle I(t)\rangle^2} \ . \quad (2.19)$$

The translational diffusion coefficient can be derived from the correlation function by using Equation 2.20:

$$g^{(2)}(\tau) = 1 + \gamma\left[\exp\left(-\vec{q}^2 D_t\right)\right]^2 , \quad (2.20)$$

where $\vec{q}$ is the scattering wavevector and γ is a constant determined by the specific experimental setup.[50]

2.9. MASS FLOW CONTROL OF VAPORS

For the realization of vapor sensing, in the studies described in this thesis, the mass flow of vapors was controlled by means of a system of mass flow controllers. More precisely, the technique used for vapor sensing experiments is based on a Controlled Evaporator Mixer (CEM)-Liquid Delivery System (LDS), which is depicted in Figure 2.15.[51, 52]

As can be seen from the Figure 2.15, the CEM-LDS contains three major components: a mass flow controller (MFC) for the carrier gas, a liquid flow controller (indicated as LIQUI-FLOW in Figure 2.15) for the liquid source and the controlled evaporator mixer which leads the mixture of two gases to the reaction chamber. The individual components of the platform are discussed in the following paragraphs.

Gas mass flow controller

A mass flow controller[51,53] is a closed-loop device that sets, measures, and controls the flow of a particular gas or liquid. The operating principle of an MFC is shown in Figure 2.16. The heart of the thermal mass flow meter/controller is the sensor that consists of a stainless steel capillary tube with resistance thermometer elements. A part of the gas flows through this bypass sensor, and is warmed up by heating elements. Consequently the measured temperatures T_1 and T_2 drift apart. The temperature difference ΔT is directly proportional to the mass flow through the sensor. In the main channel a laminar flow

element consisting of a stack of stainless steel discs with precision-etched flow channels is applied. The sensor output is proportional to the total mass flow rate.
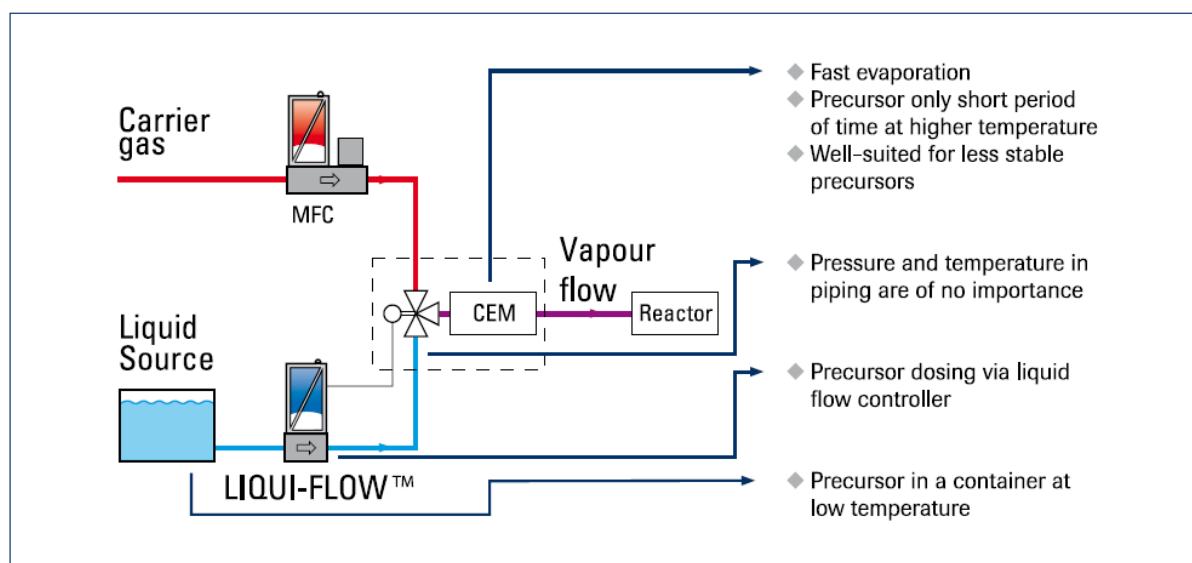
Figure 2.15. Scheme of the controlled evaporation mixing process and its capabilities. © Bronkhorst High-Tech, reproduced with permission.[51]

Liquid flow controller

The liquid flow controller (LFC)[53] consists of the same flow components found in traditional MFCs. The major difference is that each component must be designed to prevent the most prevalent problem with LFCs—bubble formation and retention. In an LFC, a liquid source can gain heat from the sensor tube, which operates at an elevated temperature, and from contact with the internal parts of a control valve if it is of a type that generates heat. The present design uses a vertically configured flow path that prevents retention of bubbles. The control valve is of a piezoelectric/diaphragm type, which has a much cooler operating temperature than other types of control valves and permits no liquid to enter the internal region of the valve.

Controlled evaporator mixer

The liquid, controlled by the liquid flow controller, is transported with a carrier gas into the evaporator-mixer where vaporization takes place. The heater can provide a vapor temperature between ambient and 200 °C. Fast response, high repeatability, good stability, and low working temperatures are the main advantages of the CEM liquid injection system.[52]

A collection of routines to calculate physical properties of gases and liquids, as well as the relative pressure and the concentration of the vapor is available at the FLUIDAT on the Net software.[54]
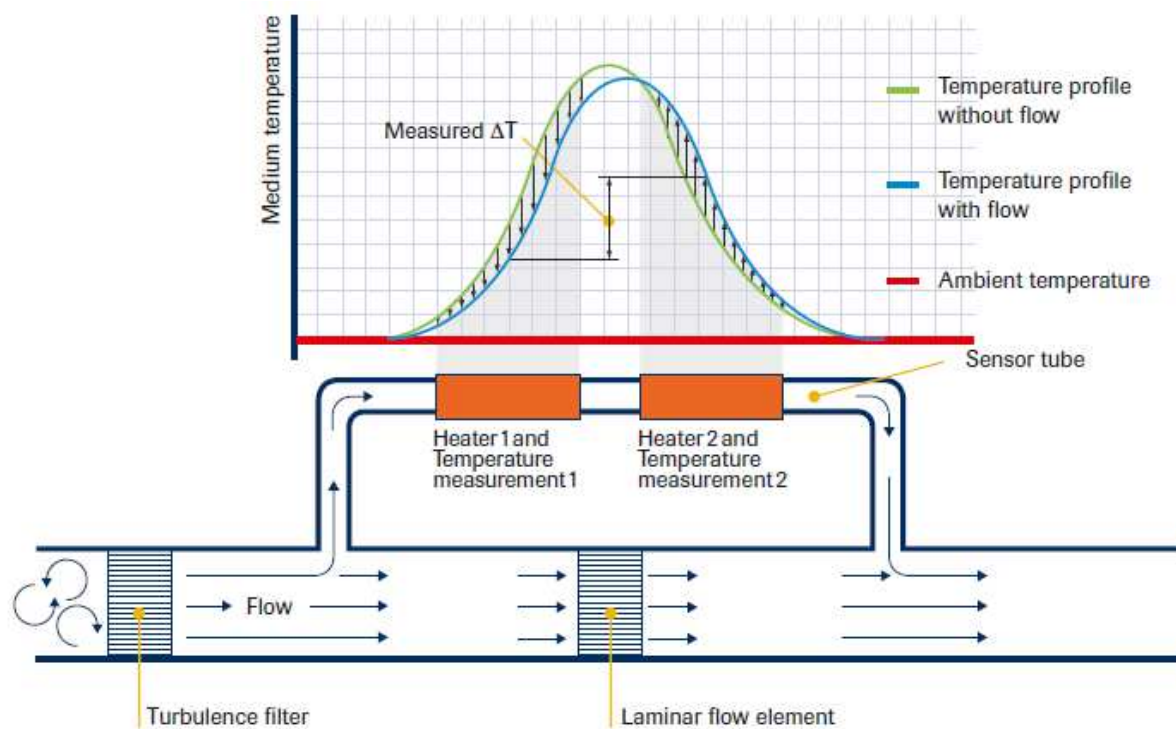
Figure 2.16. The operating principle of a MFC. © Bronkhorst High-Tech, reproduced with permission.[51]

2.10. BIBLIOGRAPHY

(1)   Perkampus, H.-H. *UV-VIS Spectroscopy and Its Applications*, Springer Berlin, Heidelberg, **1992**.

(2)   Bass, M.; Eric, W.; Van Stryland, D. R.; Williams, W. L. *Handbook of optics 2 . Devices , measurement , and properties*, 2nd ed., Vol. 2, McGraw-Hill, Inc, **1995**.

(3)   Lee, K.-S.; Thompson, K. P.; Rolland, J. P. *Opt. Express* **2010**, *18*, 23378.

(4)   Ocean Opticks, http://www.oceanoptics.com/.

(5)   Rothen, A. *Rev. Sci. Instrum.* **1945**, *16(2)*, 26.

(6)   Fujiwara, H. *Spectroscopic Ellipsometry*, John Wiley & Sons, Ltd., Chichester, **2007**.

(7)   Tompkins, H. G.; Eugene, I. A. *Handbook of ellipsometry*, William Andrew, Inc, **2005**.

(8)   J. A. Woollam Co., http://www.jawoollam.com/.

(9)   Woollam, J. A.; Snyder, P. G. *Mater. Sci. Eng. B* **1990**, *5*, 279.

(10)   Woollam, J. A.; Johs, B.; Herzinger, C.; Hilfiker, J.; Synowicki, R.; Bungay C. *Proc. SPIE CR72, Optical Metrology*, **1999**, 3.

(11)   Jellison, G. E. *Thin Solid Films* **1993**, *234*, 416.

(12)   Pavunny, S. P.; Thomas, R.; Katiyar, R. S. *ECS Trans.* **2012**, *45*, 219.

(13)   Baklanov, M.; Maex, K.; Green M. *Dielectric Films for Advanced Microelectronics*, John Wiley & Sons, Ltd., Chichester , **2007**.

(14)   Baklanov, M. R.; Mogilnikov, K. P.; Polovinkin, V. G.; Dultsev, F. N. *J. Vac. Sci. Technol. B Microelectron. Nanom. Struct.* **2000**, *18*, 1385.

(15)   Boissiere, C.; Grosso, D.; Lepoutre, S.; Nicole, L.; Bruneau, A. B.; Sanchez, C. *Langmuir* **2005**, *21*, 12362.

(16)   Sing, K.S.W.; Everett, D.H.; Haul, R. A. W.; Moscou, L.; Pierotti, R. A. J.; Rouquerol, Siemieniewska, T. *Pure Appl. Chem.* **1985**, *57*, 603.

(17)   Murray, K. L.; Seaton, N. A.; Day, M. A. *Langmuir* **1999**, *15*, 6728.

(18)   Nguyen, C.; Do, D. D. *Carbon,* **2001**, *39*, 1327.

(19)   Garnett, J. C. M. *Philos. Trans. R. Soc. A Math. Phys. Eng. Sci.* **1906**, *205*, 237.

(20)   Bruggeman, D. A. G. *Ann. Phys.* **1935**, *416*, 636.

(21)   Drude, P. *The Theory of Optics*, 3rd ed., Dover, London, **1959**.

(22)   Binnig, G., Quate, C. F. *Phys. Rev. Lett.* **1986**, *56*, 930.

(23)   Müller, D. J.; Dufrêne, Y. F. *Nat. Nanotechnol.* **2008**, *3*, 261.

(24)   Binnig, G.; Rohrer, H. *Surf. Sci.* **1983**, *126*, 236.

(25)   Smith, G. T. *Industrial Metrology*, Springer, London, **2002**.

(26)   Cappella, B.; Dietler, G. *Surf. Sci. Rep.* **1999**, *34*, 1.

(27)   Asylum Research, www.asylumresearch.com.

(28)   Bowen, W. R.; Hilal, N. *Atomic Force Microscopy in Process Engineering. An Introduction to AFM for Improved Processes and Products*, Elsevier Ltd, **2009**.

(29)   Gross, L.; Mohn, F.; Moll, N.; Liljeroth, P.; Meyer, G. *Science* **2009**, *325*, 1110.

(30)   Jalili, N.; Laxminarayana, K. *Mechatronics* **2004**, *14*, 907.

(31)   Evanko, D. *Nat. Methods* **2012**, *9*, 778.

(32)   Lichtman, J. W.; Conchello, J.-A. *Nat. Methods* **2005**, *2*, 910.

(33)   Lakowicz, J. *Principles of Fluorescence Spectroscopy*, Springer London, **2009**.

(34)   Carl Zeiss Microscopy, http://zeiss-campus.magnet.fsu.edu/articles/basics/fluorescence.html.

(35)   Yuste, R. *Nat. Methods* 2005, *2*, 902.

(36)   Goldstein, J., Newbury, D.E.; Joy**,** D.C.; Lyman, C.E.; Echlin, P.; Lifshin, E.; Sawyer, L.; Michael**,** J.R. *Scanning Electron Microscopy and X-ray Microanalysis*, 3rd ed., Springer US**, 2003**.

(37)   Weilie Zhou, Z. L. W. *Scanning Microscopy for Nanotechnology: Techniques and Applications*, Springer US, **2006**.

(38)   Everhart, T. E.; Thornley, R. F. M. *J. Sci. Instrum.* **1960**, *37*, 246.

(39)   Seah, M. P., *Vacuum* **1984**, *34*, 463.

(40)   Nordling, C.; Sokolowski, E.; Siegbahn, K. *Phys. Rev.* **1957**, *105*, 1676.

(41)   Siegbahn, K. *Phil Trans R Soc A* **1970**, *268*, 33.

(42)   Van der Heide, P. *X-Ray Photoelectron Spectroscopy*, John Wiley & Sons, Inc., Hoboken, **2011**.

(43)   Alford, T. L.; Feldman, L.C.; Mayer, J. W. *Fundamentals of Nanoscale Film Analysis*, Springer US, Boston, **2007**.

(44)   Wilson M. J. *Clay Mineralogy : Spectroscopic and Chemical Determinative methods,* Chapman & Hall, **1994**.

(45)   Harris, K. D. M.; Tremayne, M.; Kariuki, B. M. *Angew. Chem. Int. Ed. Engl.* **2001**, *40*, 1626.

(46)   Hammond, C. *The Basics of Crystallography and Diffraction*, 3rd ed., Oxford University Press, **2009**.

(47)   Weidenthaler, C. *Nanoscale* **2011**, *3*, 792–810.

(48)   Scherrer*,* P. *Nachr. Ges. Wiss. Goettingen, Math.-Phys. Kl.*, **1918**, *2*, 96.

(49)   Berne B. J.; Pecora R. *Dynamic Light Scattering: With Applications to Chemistry, Biology, and Physics*, Dover Publications, New York, **2000**.

(50)   Pecora, R. *J. Nanoparticle Res.* **2000**, *2*, 123.

(51)   Kaszuba, M.; McKnight, D.; Connah, M. T.; McNeil-Watson, F. K.; Nobbmann, U. *J. Nanoparticle Res.* **2007**, *10*, 823.

(51)   *Bronkhorst® High-Tech*, http://www.bronkhorst.com/en/.

(52)   Boer, H. J. Liquid-Injection System Based on Mass Flow Controllers. *Solid State Technol.* **1996**.

(53)   *Fundamentals of Mass Flow Control: Critical Terminology and Operation Principles for Gas and Liquid MFCs*; Advance Energy Ltd., Fort Collins, Colorado, **2005**.

(54)   FLUIDAT° on the Net, http://www.fluidat.com.

3. ONE-DIMENSIONAL PHOTONIC CRYSTALS

FOR THERMO-OPTIC SENSING

Stimuli-responsive one-dimensional photonic crystals (1D PCs), also known as Bragg stacks (BSs), represent a promising class of "smart" environmentally responsive nanostructures featuring "optically engineered" stimuli detection. 1D PCs have already gained recognition as sensitive, label-free colorimetric chemical and biological sensors. Aptly, these periodic multilayer nanostructures represent functional systems with an inherent response also to physical stimuli such as temperature and humidity changes. In chapter 3.1 the thermo-optic response of tunable thermo- and hygroresponsive nanoparticle-based TiO_2/SiO_2 1D PCs obtained by bottom-up assembly is reported. Next, in chapter 3.2 we discuss the impact of layer thickness, refractive index and thermo-optic coefficients of the employed materials on the thermo-optic tunabiliy of the 1D PCs, and put forward "design" criteria for thermoresponsive 1D PCs operating in the visible range of the optical spectrum. Finally, in chapter 3.3 we demonstrate the thermo-optic performance of the 1D PCs fabricated by different deposition methods and fabrication schemes, featuring various morphologies, and the response and recovery kinetics of the multilayer systems are analyzed. The trends revealed in this study are relevant for the development of sensitive photonic crystal temperature and humidity sensors.

3.1. HUMIDITY-ENHANCED THERMALLY TUNABLE TiO₂/SiO₂ BRAGG STACKS

Ida Pavlichenko*, Armin T. Exner*, Markus Guehl, Paolo Lugli, Giuseppe Scarpa, and Bettina V. Lotsch

* These two authors made an equal contribution

Abstract

Tunable, stimuli-responsive photonic crystals (PCs) have developed into a fast growing, interdisciplinary research field attracting attention from various scientific communities, such as photonics, sensing, and materials chemistry. Here, we propose a thermally tunable and environmentally responsive optical filter derived from nanoparticle-based TiO₂/SiO₂ one-dimensional photonic crystals, christened Bragg stacks (BSs). Photonic crystals with textural mesoporosity were obtained by bottom-up assembly based on sequential spin-coating suspensions of TiO₂ and SiO₂ nanoparticles on glass substrates. The mechanism of the BS thermal tunability is based on the thermo-optic effect, i.e., dependence of the refractive index on temperature. Notably, the optical response of the BS to temperature can be significantly enhanced by varying the relative humidity of the environment. Thus, the magnitude of the spectral shift increases more than fourfold from 4.4 to 21.9 nm with a change in relative humidity from 25% to 55% in the temperature range between 15 and 60 °C. Thus, humidity-enhanced thermal tuning causes shifts of the transmission spectra by up to −1.66 nm K⁻¹. The simulations of the wavelength shift based on the measurement of the effective thermo-optic coefficient of the individual TiO₂ and SiO₂ layers at ambient conditions closely correspond to the experimental values. Owing to their high inherent porosities and ease of fabrication, nanoparticle-based BSs offer a

great potential for the development of sensitive, label-free photonic crystal temperature and humidity sensors.

3.1.1. INTRODUCTION

Photonic crystal (PC) research has witnessed rapid progress over the past years, materializing in the development of photonic crystal building blocks for various optical systems, for example, in fiber-optic communication networks as wavelength-division and add–drop multiplexers, microelectro-mechanical systems (MEMS), infrared spectrometers, and color displays.[1-3] "Smart" photonic crystals further extend the range of applications toward environmentally responsive and, hence, *tunable* optical filters, as they are able to dynamically respond to external stimuli through optical thickness changes. An emerging area of applications of stimuli-responsive PCs is the development of label-free biological, chemical, and physical sensors.[4,5] The sensing approach is based on the utilization of PCs as tunable optical filters capable of changing their refractive properties when in contact with an analyte of interest or when exposed to external stimuli such as electric and magnetic fields, pH, etc. Thermo- and hygroresponsive PCs are of particular interest because of the increasing demand for compact, low-cost, and label-free temperature and humidity sensors.

1D PCs, christened Bragg stacks (BSs), are interference-based optical multilayer structures consisting of a periodic stack of layers of two different materials featuring high and low refractive indices (n), respectively. The periodicity of the dielectric lattice of the multilayer structure creates a periodic potential for photons in one dimension, such that photons with particular energies cannot propagate within the PC. The resulting photonic band gap, called stop band, gives rise to photons being reflected in a particular wavelength range, resulting in "structural color" as opposed to color originating from light absorption by chromophores.[6] The central wavelength of the stop band can be calculated by the Bragg–Snell law for normal incidence (Equation 3.1):

$$m\lambda = 2(n_H h_H + n_L h_L), \quad (3.1)$$

where m is the diffraction order and n_H, n_L, h_H, and h_L are the respective refractive indices and thicknesses of the high- (H) and low- (L) refractive index (RI) materials. Therefore, the position of the stop band can be modulated by varying the optical thickness (the product of RI and physical thickness) of the layers.[7]

One possible mechanism of color tuning is based on the thermo-optic effect (TOE), i.e., the dependence of the RI of a material on temperature. Titanium dioxide is an excellent optical coating material due to its high transparency above 350 nm and high RI (1.8–2.5). The thermo-optic coefficient (TOC) of titanium dioxide measured for coatings deposited by electron beam physical vapor deposition is negative and equal to -1.77×10^{-4} K^{-1} between 18 and 120 °C and -3.04×10^{-4} K^{-1} between 220 and 325 °C at 800 nm.[8] Xie *et al.*[9] compared the TOC of titanium dioxide films obtained by magnetron sputtering. The TOC of nonannealed films was found to be -1.21×10^{-4} K^{-1}, while values around -2.14×10^{-4} K^{-1} were reported for an annealed sample in the temperature range 31–105 °C at 632 nm. Measurements of TOCs of sol–gel-derived TiO$_2$ films have not yet been reported. In contrast, the thermo-optic coefficient of silicon dioxide is positive and ranges between 0.88×10^{-5} and 1.34×10^{-5} K^{-1}.[10] A change in RI due to the change of thickness is negligible since the thermal expansion coefficient (TEC) for both materials is on the order of 10^{-6} K^{-1}. The tuning mechanism based on the TOE has already been demonstrated on optical filters produced mainly by expensive deposition techniques such as sputtering, electron beam evaporation, or plasma-enhanced chemical vapor deposition. The tuning efficiency of a single amorphous Si cavity arranged between Si$_3$N$_4$/SiO$_2$ distributed Bragg reflectors (DBRs) was measured[11] to be 0.05 nm K^{-1}, whereas that of a polycrystalline (poly-)Si cavity in poly-Si/SiO$_2$ DBRs[12] was reported to be 0.07 nm K^{-1}. A similar approach demonstrated thermal tunability of the emission of conjugated polymers embedded in a microcavity between DBRs deposited by reactive electron beam evaporation.[13] The photoluminescence spectra of the polymers inside the cavity were tuned with an efficiency of -0.2 nm K^{-1}. A wavelength shift of 0.01 nm K^{-1} was verified for external-cavity DBR laser with a silica fiber Bragg grating.[14] The performance of thin-film optical filters in the presence of humid atmosphere has been a subject of interest in several studies.[15-21] The principal objective of these investigations was to determine the influence of water vapor exposure on the stability of the spectral characteristics of band-pass filters. Still, the effect of moisture adsorption and desorption as a function of temperature was not hitherto examined as a feasible mechanism for enhancement of the tuning efficiency of the thin film coatings.

The sol–gel method affords a relatively simple, fast, and low-cost synthetic pathway to produce nanoparticles for the assembly of 1D PCs with high optical and structural quality by spin-coating.[22,23] An intrinsic property of nanoparticle-based 1D PCs is the high porosity of the constituent layers, giving rise to versatile and multifunctional multilayer architectures which can be fabricated in a straightforward

manner. In particular, Bragg stacks built from TiO_2/SiO_2 nanoparticle multilayers have already demonstrated their great potential in chemical vapor and liquid detection.[24-30] An additional benefit of these systems stems from their self-cleaning properties provided by the photoactivity of TiO_2 particles under UV irradiation and the porosity-driven superwetting behavior ensuring the superhydrophilic properties of such BSs.[31] However, the impact of ambient conditions such as temperature and humidity on their optical response remains elusive. In this work we present a thermo- and hygrotunable optical filter and specifically point out the effect of ubiquitous humidity on the thermal response of photonic crystals. To the best of our knowledge, cross-correlation effects between temperature and ambient humidity in tunable 1D PCs have been largely neglected so far. We propose that exploiting them may offer great potential for the development of highly sensitive PC optical sensors featuring a humidity-enhanced temperature response and shed light on the fundamental aspects of the water-adsorption-induced colorimetric behavior of porous multilayer systems.

3.1.2. EXPERIMENTAL

Preparation of TiO₂ and SiO₂ suspensions

The suspension of TiO_2 nanoparticles was synthesized by the sol–gel hydrolysis of titanium(IV) ethoxide (6.25 mL, technical grade, Aldrich) in HNO_3 (0.1 M, 37.5 mL).[40] Titanium(IV) ethoxide was added dropwise to the acid at room temperature during vigorous stirring in a N_2 atmosphere. The mixture was then heated at 80 °C for 8 h. The subsequent sonication (Elmasonic S100/H, 37 kHz) of the sol allowed obtaining nanoparticles with a hydrodynamic diameter in the range between 7 and 15 nm. SiO_2 colloids (hydrodynamic diameter 6–10 nm) were purchased from Sigma-Aldrich (LUDOX SM-30, 30 wt % in H_2O) and diluted with distilled water using a ratio of 1:5. Particle size distribution of the precursor TiO_2 and SiO_2 suspensions was analyzed using dynamic light scattering photocorrelation spectroscopy (Malvern Nano ZS Zetasizer) at 20 °C. The crystalline nature of the TiO_2 powder calcined at 350 °C for 1 h was confirmed by X-ray diffraction (Bruker D8 Discover).

Bragg stack assembly

Thermoresponsive photonic crystals were assembled by sequential deposition of TiO_2 and SiO_2 suspensions on a clean ISO 8037/1 glass side (2.5×2.5 cm^2) previously activated by air plasma treatment (Femto, Diener Electronic). To improve the TiO2 film quality, 2.5 wt % of poly(ethylene glycol) (PEG, Mw = 8000 g mol^{-1}) was added for spin coating. Both suspensions were filtered using syringe filters (SPARTAN 13, 0.2 μm) to remove aggregates. Thin layers of TiO_2 and SiO_2 were produced by using the spin-coating technique (Laurell WS-650SZ-6NPP/LITE). The glass slides were covered by 200–250 μL of TiO_2 suspension and accelerated at 1500 rpm s^{-1} to final rotation speeds ranging from 2500 to 5500 rpm. The total spin-coating process for each layer was completed in 60 s. Afterward the sample was put into a muffle furnace (Nabertherm, L3/11/B810) for calcination at 350 °C for 30 min. The same procedure was applied to the deposition of the following layers until 8.5 TiO_2/SiO_2 bilayers were assembled. The single thin film thickness was characterized by spectroscopic ellipsometry (performed on a Woollam M200D variable angle ellipsometer in the entire spectral range of 190–1000 nm at angles of incidence of 65°, 70°, 75°) and profilometry (Dektak-150 Stylus profiler BRUKER AXS). To investigate the porosity of the layers an ellipsometric porosimetry setup was used. The RIs of the SiO_2 and TiO_2 single films were measured first with void pores and then with the pores filled with toluene. Scanning electron microscopy (JEOL JSM-6500F operating at an accelerating voltage of 4 kV) was used to examine the morphology of the BS cross section.

Thermo-optical analysis

To obtain transmission spectra of the Bragg stack in the range of 400–800 nm, we used a monochromator (Cornerstone260 1/4 m) with a high-pressure arc lamp as a light source and a 10×10 mm calibrated silicon detector connected to a digital lock-in amplifier (Merlin). The sample was mounted in the sample holder and placed before the detector in a closed chamber (the distances "monochromator-sample" and "sample-detector" were 8 and 12 cm, respectively). The temperature of the Bragg stack was varied by two Peltier elements that were placed onto the sample and arranged with a 4 mm gap in between to provide the optical axis. The PT100 temperature sensor was attached to the other side of the Bragg stack above the optical axis. Peltier elements and the temperature sensor were connected to a remote-controlled source meter. A software proportional integral controller regulated the heating and cooling of the Peltier elements. The measured deviation of the temperature during the measurement was less than 0.1 °C. For each temperature the sample was equilibrated for 60 s. We

changed the relative humidity (RH) or the environment by introducing the water vapor into the monochromator chamber. The RH was varied between 25% and 80%. To measure the TOC of the TiO_2 and SiO_2 thin films, we used a heating stage (Peltier element) mounted into the house of the ellipsometer. The measurement was done when the sample was equilibrated at the desired temperature. The temperature was varied from 12 to 60 °C.

3.1.3. RESULTS AND DISCUSSION

Bragg stack assembly and characterization

Bragg stacks were assembled by sequential spin-coating of stable colloidal suspensions of TiO_2 and SiO_2 nanoparticles. In order to enhance the layer stability and mutual layer adhesion, calcination steps at 350 °C for 30 min were added after depositing each individual layer. The scanning electron microscopy cross-sectional images of the Bragg stacks are shown in Figure 3.1.1.
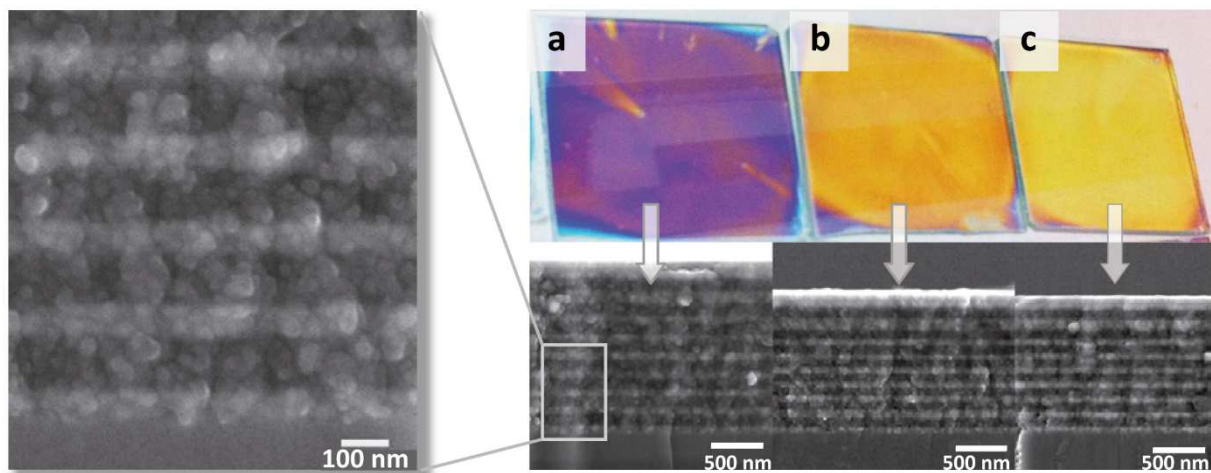
Figure 3.1.1. SEM images showing the relationship between the color of the TiO_2/SiO_2 Bragg stacks and the thickness of the layers spin-coated at (a) 2500, (b) 4500, and (c) 5500 rpm with an acceleration of 1500 rpm s^{-1}. Left: Magnification of the cross-section image in (a) to demonstrate the porous morphology of the layers.

The layers of TiO_2 and SiO_2 can be identified as bright (higher electron density) and dark stripes, respectively. Different "structural" colors of the PCs shown arise from variation of the lattice parameters resulting from different spin-coating rotation speeds. Information about the thickness of the layers can be derived from spectroscopic ellipsometry by fitting the experimentally obtained data to a Cauchy dispersion equation (see Table 3.1.1). An important observation is that the layers constituting the Bragg stack are porous. The porosity calculated by spectroscopic ellipsometry using the Lorentz–Lorenz

equation and toluene as adsorptive is 10% for TiO_2 and 25% for SiO_2.[32,33] The degree of porosity can be kept constant by strict control of the nanoparticle synthesis and calcination conditions. We confirmed the crystalline nature of the TiO_2 nanoparticles calcined at 350 °C by powder X-ray diffraction, which clearly shows the signature of the anatase polymorph (see Figure 8.1.1 in Appendix 8.1). The crystallite size of the TiO_2 nanoparticles derived from the Scherrer equation is around 6 nm, while dynamic light scattering (DLS) gives the number size distribution of the values for the hydrodynamic diameter between 7 and 15 nm (see Figure 8.1.2, in Appendix 8.1). The hydrodynamic diameter derived for the SiO_2 particles ranges between 6 and 10 nm.

Table 3.1.1. Dependence of the thickness of the layers in the Bragg stack on the rotation speed during spin-coating.

Rotation speed[a]	TiO_2 layer thickness[b]	SiO_2 layer thickness
[rpm]	[nm]	[nm]
2500	75 ± 3	118 ± 3
4500	60 ± 3	93 ± 2
5500	56 ± 3	80 ± 2

[a] **Acceleration 1500 rpm s⁻¹.**

[b] **Note that the thickness values are given after calcination of the layers for 30 min at 350 °C.**

Thermo-optical behavior

Figure 3.1.2 depicts a simplified scheme of the experimental setup and the general principle of temperature sensing with 1D PCs. To realize the temperature tuning, the BS, deposited on a transparent glass substrate, was placed on thermoelectric heaters and connected to a resistance thermometer (Pt100) capable of tracking the actual temperature. The BS was positioned between the monochromator and the detector such that the incident beam was normal to the surface of the sample (divergence angle ≈3°). Using this setup, the BS modifies the spectrum of the incident light as a function of temperature by acting as a thermoresponsive optical filter. We performed the thermo-optic experiments with the BS presented in Figure 3.1.1b, as it exhibited the highest optical quality and homogeneity. Transmission spectra were measured in the temperature region between 15 and 60 °C with steps of 2 °C between 15 and 25 °C, and with steps of 5 °C between 25 and 60 °C (Figure 3.1.3). The BS was thermally equilibrated

for 1 min before taking the measurement. The transmission of the substrate (98.5%) did not change during heating.
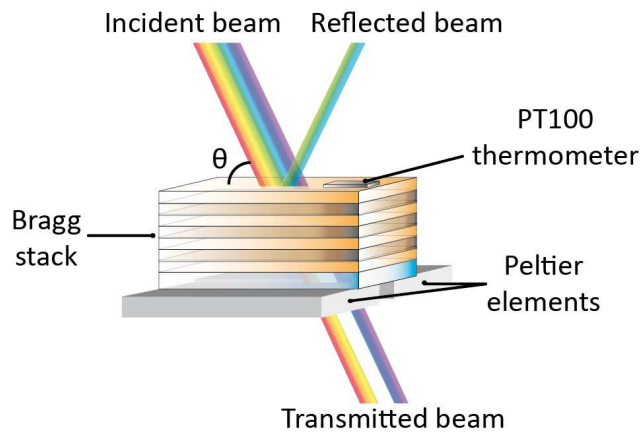

Figure 3.1.2. Schematic drawing of the experimental setup. The Bragg stack is deposited on a transparent glass substrate placed on thermoelectric heaters. The PT100 thermometer tracks the actual temperature. The Bragg stack acts like an optical filter for the incident beam resulting in the observation of the photonic stop band. In our experiment the beam hits the surface of the Bragg stack at an angle of $\theta = 90°$ (i.e., orthogonal incidence).

For a clear representation only the red edge of the photonic stop band between 480 and 580 nm is shown. In all experiments, we consistently observed a blue shift of the transmission spectra during heating, which was confirmed by taking measurements at different spots on the BS. The blue shift is fully consistent with the large, yet negative TOC of TiO_2 and the small positive TOC of SiO_2. Notably, however, the shifts observed were significantly larger than those expected to be induced by the thermo-optic effect with the literature values of TOCs reported for TiO_2 and SiO_2 and prognosticated to have less than 2 nm shift between 15 and 60 °C. In order to explore the nature of the observed enhancement effect further, the experiments were performed under ambient conditions (RT, 20 °C) with varying relative humidities (RH) of 25%, 45%, or 55%. Figure 3.1.3 outlines the impact of ambient RH on the temperature response of the BS. At a RH of 25%, the shift amounts to 4.4 ± 0.1 nm in the temperature range from 15 to 60 °C. For a RH of 45% the shift equals 16.1 ± 0.6 nm within the same temperature range. At a RH of 55%, a shift of 21.9 ± 1.7 nm is observed. The inherent porosity of nanoparticle Bragg stacks due to interparticle voids provides a quick response pathway to the humidity of ambient air. The change in temperature induces two parallel effects: a change of the refractive indices of the TiO_2 and SiO_2 layers due to the thermo-optic effect and a change in ambient humidity in the vicinity of the Bragg stack. Upon cooling the Bragg stack below RT, the RH close to the Bragg stack surface increases with respect to that of

ambient air, leading to adsorption of water into the pores of the BS. Likewise, heating gives rise to desorption of water from the Bragg stack. The capillary system of the interparticle pores facilitates penetration of water into the whole volume of the photonic crystal and diffusion throughout the mesopore system.[34] As the BS is cooled down, the effective refractive index of the material increases due to water adsorption, thus shifting the position of the stop band to the red. We observed the wavelength shift without a change in the transmission profile and intensity, which indicates that the adsorption/desorption effect occurs in the entire multilayer[15] and that there are no scattering losses due to water condensation on the surface of the BS. However, the Bragg stack should not be cooled down to temperatures lower than the dew point for the corresponding relative humidity of the environment. We also analyzed the possible influence of the thermal expansion on the tuning properties of the BS. According to the literature, the thermal expansion coefficients of nanocrystalline anatase (crystallite size ≈ 9 nm) and of silicon dioxide in air are 8.57×10^{-6} and 0.50×10^{-6} K^{-1}, respectively.[35,36] Using the given values, the increase in thickness amounts to approximately 0.02 nm for the 60 nm TiO_2 and 93 nm SiO_2 films in the studied range from 15 to 60 °C. This value has negligible effect on the RI change and at the same time slightly shifts the stop band position to longer wavelengths at higher temperatures, i.e., contrary to the shift based on the TOC (see Figure 8.1.3, in Appendix 8.1). We also investigated the behavior of the film thickness *in situ* at ambient conditions by means of spectroscopic ellipsometry to probe possible swelling of the inorganic layer due to water adsorption. According to the conducted measurements the thickness of the thin films does not change within the given temperature range, taking into account an error of 0.2 nm.

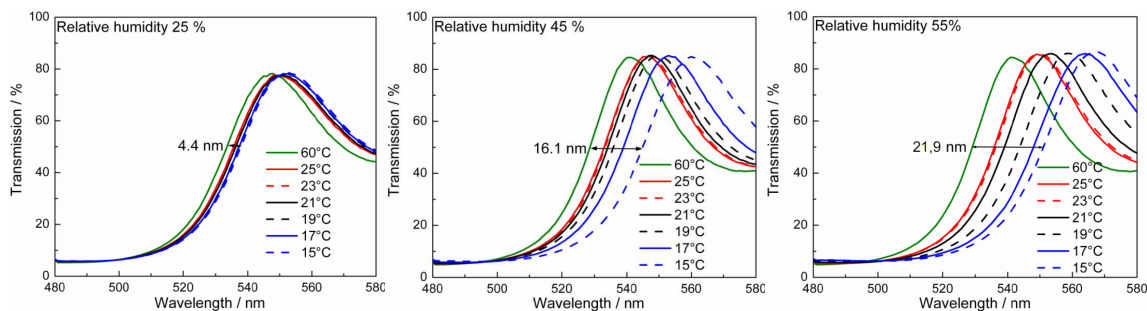**Figure 3.1.3.** Transmission spectra of the TiO_2/SiO_2 BS shown in Figure 3.1.1b, demonstrating the blue shift in the temperature range between 15 and 60 °C and at various relative humidities (RH): 25%, 45%, and 55%. The relative humidity was measured at 20 °C. Spectra between 25 and 60 °C are omitted for clarity. The black double arrow indicates the magnitude of the shift *in toto*.

In order to support the argument of humidity-based amplification of the temperature response, optical spectra of the Bragg stack at different humidities were recorded at constant temperature (Figure 3.1.4). This experiment was designed to determine the pure humidity response of the BS. To this end, the measurement setup was supplemented by a tubing that guided humid air onto the sample, the RH of which was controlled by blowing it through a water-filled bubbler. The stop band of the Bragg stack shifted to the red by 11 nm after increasing the RH from 40% to 80% at RT without scattering losses in transmission. Repeated cycling between these two RHs was fully reversible. This observation is in accord with the fact that the transmission curves of the BS taken at the same temperature, but different RHs (Figure 3.1.3), are red-shifted with respect to each other upon increasing RH.
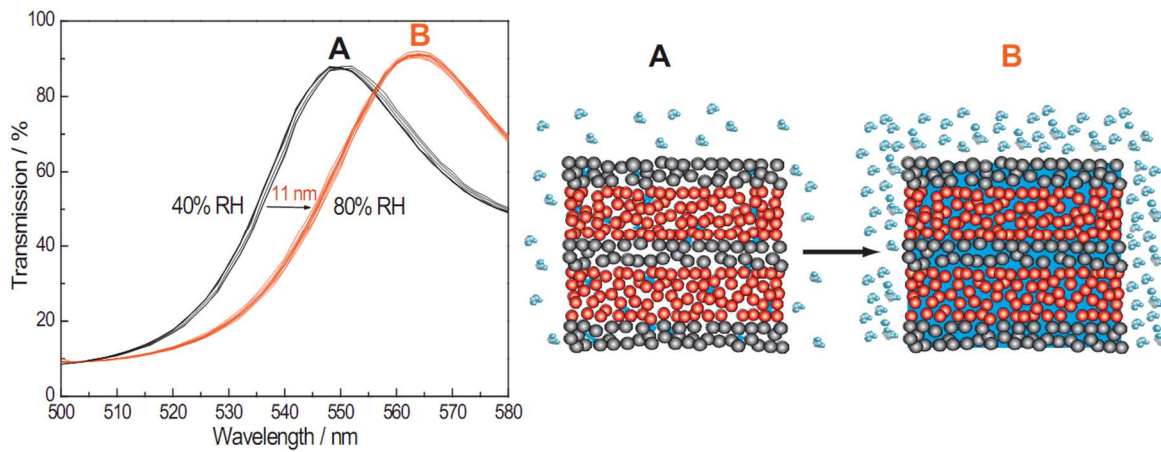
Figure 3.1.4. Effect of a change in humidity on the Bragg stack stop band position at constant temperature. Several cycles are shown to demonstrate the reversibility of the water adsorption and desorption. The black arrow indicates 11 nm red shift upon increasing RH from 40% (A) to 80% (B). The scheme on the left demonstrates the increase of the water content in the BS pore network upon augmenting the RH, which results in the enlargement of the effective refractive index of the layers.

From Figure 3.1.5 it becomes evident that the temperature response is nonlinear; i.e., increasingly larger shifts are observed at lower temperatures. We rationalize this finding by enhanced water adsorption into the pores as the dew point is approached, which maps the exponential behavior of the RH as a function of temperature (see Figure 8.1.4, in Appendix 8.1 for additional details). As the temperature is increased, water is increasingly desorbed from the pores such that above RT the shift is governed predominantly by the thermo-optic effect. We can therefore describe the thermal tuning of the Bragg stack as the superposition of the changes in temperature and the relative humidity during heating (cooling). The linear approximation of the temperature response in the range between 30 and 60 °C gives shifts of −0.05, −0.08, and −0.12 nm K^{-1} for 25%, 45%, and 55%, respectively. Below 30 °C we observe a nonlinear shift

behavior, showing steeper slopes of the shifts at higher humidities. The humidity-enhanced thermal tuning causes shifts of the transmission spectra by up to -1.93 nm K^{-1} as compared to 0.35 nm K^{-1} calculated for typical nonporous Si/SiO$_2$ BSs.[37] The observed optical response thus correlates with the dependence of the humidity on temperature for various dew points (see Figure 8.1.5, in Appendix 8.1). The dew points are 11 °C for ambient air at 55% RH, 7 °C for 45% RH, and 0 °C for 25% RH. Graph 8.1.4 evidences that the slope of the curves is significantly steeper below RT for all dew points and, notably, that upon temperature change from 20 to 10 °C the increase in humidity and hence optical shift is significantly larger for the 55% setting (dew point 11 °C) than for the 25% setting (dew point 0 °C), which corresponds well with our measurements.
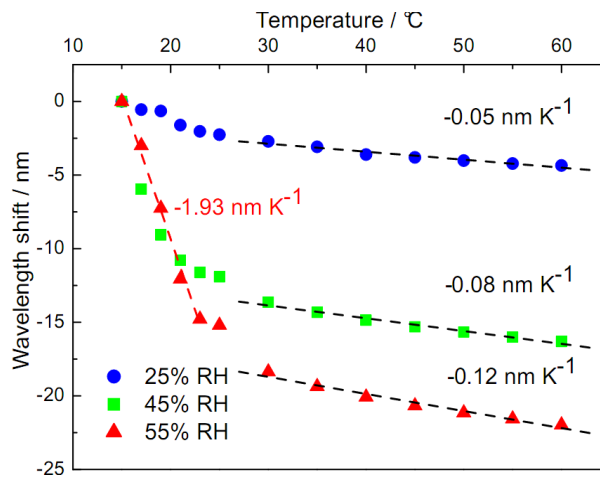
Figure 3.1.5. Wavelength shift as a function of temperature at different RHs. The shifts were obtained by extracting the wavelength values at 50% transmission from the spectra presented in Figure 3.1.3 for the temperatures between 15 and 60 °C at various RHs. The shifting behavior is strongly dependent on the RH. For temperatures above 30 °C the shift is linear. The linear approximation between 30 and 60 °C shows the rate of the shift being equal to -0.05, -0.09, and -0.12 nm K^{-1} for RHs 25%, 45%, and 55%, respectively. Below ≈30 °C we observe a nonlinear behavior of the shift, showing a higher slope of up to -1.93 nm K^{-1}.

In order to verify the experimental results, we carried out simulations of the transmission spectra with the program COMSOL Multiphysics 3.3 based on the experimental layer thicknesses and effective refractive indices of the respective layers.[38] To simulate the thermal behavior, the thermo-optic coefficients of TiO_2 and SiO_2 were required. Due to a lack of literature data on the TOC (dn/dT) for nanoparticle-based TiO_2 and SiO_2 films, we measured the dependence of the RI on temperature by spectroscopic ellipsometry at temperatures between 10 and 60 °C at 25% relative humidity (Figure 3.1.6).
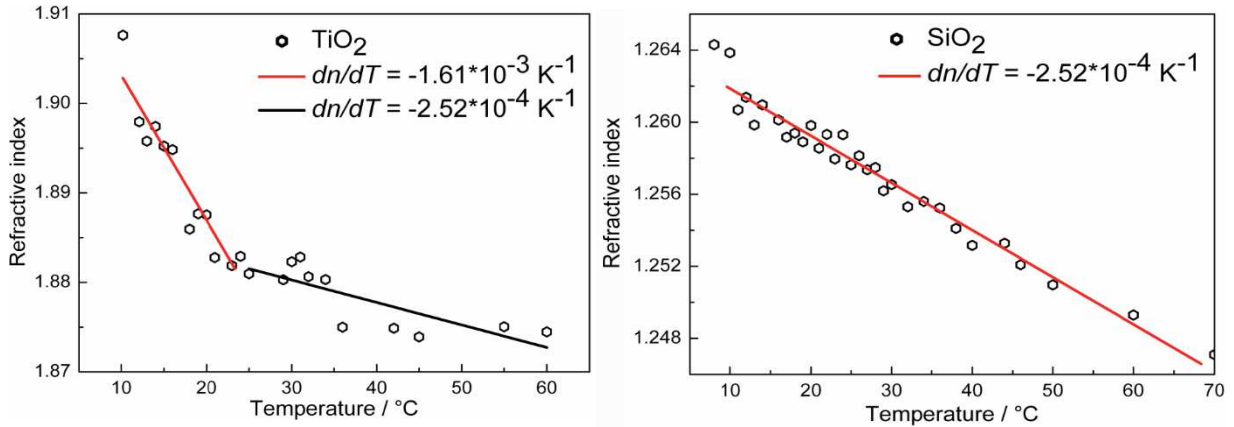
Figure 3.1.6. Dependence of the refractive index on the temperature for TiO_2 (66 nm) and SiO_2 (111 nm) single thin films measured by spectroscopic ellipsometry at RH 25%. The refractive index was determined at 530 nm.

The acquired data were fitted to the Cauchy dispersion equation for the visible wavelength region. The RI was determined at 530 nm. We observed a linear behavior of RI for SiO_2 between ≈12 and 60 °C. The effective TOC was determined to be -2.52×10^{-4} K^{-1}. Thus, in contrast to the majority of literature sources that report positive TOC values for silicon dioxide, we measured a negative trend in the refractive index change as a function of temperature. However, Müller *et al.* also observed a negative TOC of $-1.92 \times 10-5$ K^{-1} for SiO_2 in an intermediate buffer layer between Si substrate and metal oxide film and attributed such behavior to the difference in the TEC of the silicon substrate and amorphous silica.[39] According to the above-mentioned report, the temperature-induced extension of bulk silicon substrate causes stretching of the SiO_2 film, thus reducing the RI of the film. The TOC of SiO_2 determined in our study has a 13 times higher value, which can be explained by the additional influence of the previously described humidity effect. The TiO_2 film shows a nonlinear $n(T)$ behavior which can be approximated by two separate negative slopes switching around 30 °C. The region between 10 and 30 °C is described by $dn/dT = -1.61 \times 10^{-3}$ K^{-1}, whereas above 30 °C a lower TOC of -2.52×10^{-4} K^{-1} was

measured. We extracted the RIs corresponding to the respective temperatures and used them as input parameters for the simulations. The simulations of the wavelength shift based on the effective TOCs for single TiO_2 and SiO_2 films at ambient conditions essentially reproduce the experimental values for the BSs measured at the same RH of 25% (Figure 3.1.7). The shift determined from the simulations is nonlinear and equal to 2.4 nm between 15 and 25 °C, which confirms the experimentally measured shift of 2.5 nm in the same temperature range. The overall shift of 5.8 nm between 15 and 60 °C is also in close agreement to the experimental value of 4.4 nm.
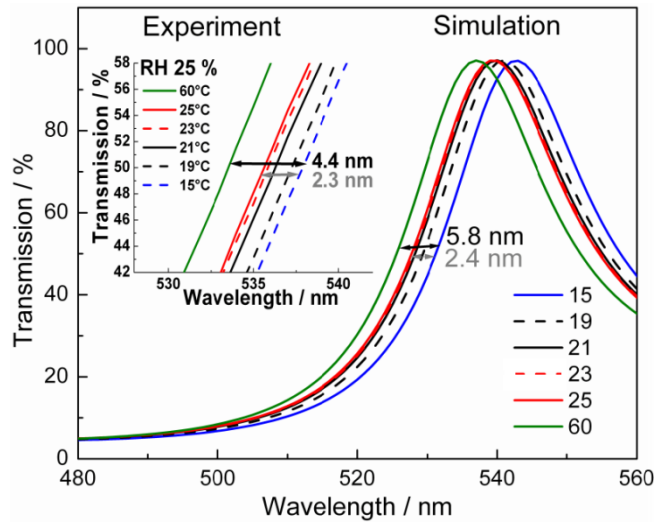
Figure 3.1.7. Correlation between the simulated and experimental transmission spectra at 25% RH. Simulations are based on the effective thermo-optic coefficients of the individual TiO_2 and SiO_2 layers determined by spectroscopic ellipsometry at 25% RH (see Figure 3.1.6).

3.1.4. CONCLUSIONS

We have presented a comprehensive study of the oftentimes neglected influence of ambient conditions on the thermal tunability of nanoparticle-based one-dimensional TiO_2/SiO_2 photonic crystals. Reversible tuning was achieved through the thermo-optic effect in the Bragg stack layer materials. Due to the porous nature of the multilayer, we observe spectral shifts of different magnitude at various relative humidities. Notably, the shift is significantly enhanced with increasing relative humidity of the environment, thereby amplifying the thermal response and, thus, sensitivity of the Bragg stack. The observed shifts range between 4.4 and 21.9 nm between 25% and 55% RH in the temperature range 15–60 °C. The temperature response is nonlinear at low temperatures and high humidities, whereas it approaches a linear behavior at increasing temperature as the impact of humidity decreases. The tuning efficiency during heating varies from -0.05 nm K^{-1} at 25% RH and -0.12 nm K^{-1} at 55% RH between 25

and 60 °C up to −1.93 nm K^{-1} at 55% RH between 15 and 25 °C. We assume that at lower temperatures (T < 30 °C) the shifting behavior is governed by a combination of water adsorption/desorption processes and the thermo-optic effect, whereas at higher temperatures (T > 30 °C) the shift is dominated by the thermo-optic effect and, thus, is essentially linear.

In summary, the detailed knowledge about the interplay between temperature- and humidity-based effects on the structural color of PCs facilitates the design of future PC architectures exhibiting decoupled temperature or humidity response, or coupled and hence enhanced temperature–humidity response. Along these lines, bottom-up assembly employing spin-coating of sol–gel nanoparticle suspensions can provide an easy-to-fabricate and low-cost route to creating highly responsive functional PCs with various degrees of porosity for further sensitivity enhancement.

3.1.5. BIBLIOGRAPHY

(1) Bechtold T.; Rudnyi E. B.; Korvink J. G. *Fast Simulation of Electro-Thermal MEMS. Efficient Dynamic Compact Models;* H. Fujita, D. Liepmann, Eds.; Springer –Verlag: Berlin, Heidelberg, Germany **2007,** 65-67.

(2) Yu, K.; Park, N. *Proc. of SPIE* **2005**, *6021*, 60212R.

(3) Lammel, G.; Schweizer, S.; Renaud, P. *14th IEEE Int. Conf. On MEMS* **2001**, 578-581.

(4) Ge, J.; Yin, Y. *Angew. Chem. Int. Ed.* **2011**, *50*, 1492.

(5) Nair, R.V.; Vijaya, R. *Prog. Quant. Electron.* **2010**, *34*, 189.

(6)   Joannopoulos J. D.; Johnson S. G.; Winn J. N.; Meade R. D. *Photonic crystals: molding the flow of light*; Princeton University Press: Princeton, NJ **2008**, 2nd ed., 44-65.

(7)   Bonifacio, L.D.; Lotsch, B.V.; Puzzo, D.P.; Scotognella, F.; Ozin, G.A. *Adv. Mater.* **2009,** *21***,** 1641.

(8)   Gülşen, G.; Inci, M. N. *Opt. Mater.* **2002**, *18*, 373.

(9)   Xie, H; Ng, F. L.; Zeng, X. T. *Thin Solid Films* **2009**, *517*, 5066.

(10)   Ghosh, G. *Non-Cryst. J. Solids* **1995**, *189*, 191.

(11)   Hohlfeld, D.; Zappe, H. *J. Opt. A: Pure Appl. Opt.* **2004**, *6*, 504.

(12)   Hohlfeld, D.; Epmeier, M.; Zappe, H. *Sensors Actuat. A* **2003***, 103*, 93.

(13)   Regoliosi, P.; Guehl, M.; Scarpa, G.; Lugli, P.; Persano, L.; Del Carro, P.; Camposeo, A.; Cingolani, R.; Pisignano, D.; Bietti, S.; Grilli E.; Guzzi *M. Appl. Phys. Lett.* **2008,** *92*, 253.

(14)   Beregovski, Y.; Hennig, O.; Fallahi, M.; Guzman, F.; Clemens, R.; Mendes, S.; Peyghambarian*, N. Sensors Actuat B* **1998***, 53,* 116.

(15)   Pellicori, S. F.; Hettich, H. L. *Appl. Optics* **1988**, *27*, 3061.

(16)   Saxe, S. G.; Messerly, M. J.; Bovard, B.; DeSandre, L.; Van Milligen, F. J.; Macleod, H. A. *Appl Optics* **1984**, *23*, 3633.

(17)   Hirsch, E. H. *J. Phys. D: Appl. Phys.* **1980**, *13*, 2081.

(18)   Macleod, H. A.; Richmond, D. *Thin Solid Films* **1976**, *37*, 163.

(19)   Pulker, H. K. *Appl Optics* **1979**, *18,* 1969.

(20)   Gibson, D. R; Lissberger, P. H. *Appl. Optics* **1983**, *22*, 269.

(21)   Brunsting, A.; Kheiri, M. A.; Simonaitis, D. F.; Dosmann, A. J. *Appl. Optics* **1986**, *25*, 3235.

(22)   Colodrero, S.; Ocana, M.; Míguez, H. *Langmuir* **2008**, *24*, 4430.

(23)   Chen, K. M.; Sparks, A.W.; Luan, H. C.; Lim, D. R.; Wada, K.; Kimerlinga, L. C. *Appl. Phys. Lett.* **1999**, *75*, 3805.

(24)   Choi, S. Y.; Mamak, M.; von Freymann, G.; Chopra, N.; Ozin, G. A. *Nano Lett.* **2006**, *6*, 2456.

(25)   Kobler, J.; Lotsch, B. V.; Ozin, G. A.; Bein, T. *ACS Nano* **2009,** *3***,** 1669.

(26)   Lee, D.; Rubner, M. F.; Cohen R. E. *Nano Lett.* **2006**, *6*, 2305.

(27)   S. Colodrero, M. Ocaña, A.R. Gonzailez-Elipe, H. Míguez, *Langmuir* **2008**, *24*, 9135.

(28)   Calvo, M.E.; Colodrero, S; Rojas, C. T.; Ocaña, M.; Anta, J. A.; Míguez, H. *Adv. Funct. Mater* **2008**, *18*, 2708.

(29)   Fuertes, M. C.; Colodrero, S.; Lozano, G.; Gonzalez-Elipe, A. R.; Grosso, D.; Boissiere, C.; Sanchez, C.; Soler-Illia, G. J. A. A.; Míguez, H. *J. Phys. Chem. C* **2008**, *112,* 3157.

(30)   Fuertes, M. C.; Lopez–Alcaraz, F. J.; Marchi, M. C.; Troiani, H. E. Luca, V. Míguez, H. Soler-Illia, G. J. A. A. *Adv. Funct. Mater.* **2007**, *17*, 1247.

(31)   Wu, Z.; Lee, D.; Rubner, M.; Cohen, R. E. *Small* **2007**, *3*, 1445.

(32)   Baklanov, M. R.; Mogilnikov, K. P. *Microelectron. Eng.* **2002**, *64*, 335.

(33)   Eslava, S.; Baklanov, M. R.; Kirschhock, C. E. A.; Iacopi, F.; Aldea, S.; Maex, K.; Martens, J. A. *Langmuir* **2007**, *23*, 12811.

(34)   Puzzo, D. P.; Bonifacio, L. D.; Oreopoulos, J.; Yip, C. M.; Manners, I.; Ozin G. A. *J. Mater. Chem.* **2009**, *19*, 3500.

(35)   Jagtap, N.; Bhagwat, M.; Awati, P.; Ramaswamy, V. *Thermochim Acta* **2005**, *427*, 37.

(36)   Tada, H.; Kumpel, A. E.; Lathrop, R. E.; Slanina, J. B.; Nieva, P.; Zavracky, P.; Miaoulis, I. N.; Wong, P. Y. *J Appl. Phys* **2000**, *87*, 4189.

(37)   Banerjee*,* A. *PIER Letters* **2009**, *11*, 129.

(38)   The COMSOL *Multiphysics* Version 3.3 *simulation software:* http://www.comsol.com/.

(39)   Wiechmann, S.; Müller, J. *Thin Solid Films* **2009,** *517,* 6847.

(40)   Lotsch, B. V.; Ozin, G. A. *ACS Nano* **2008**, *2*, 2065.

3.2. TUNABLE THERMORESPONSIVE TiO$_2$/SiO$_2$ BRAGG STACKS BASED ON SOL−GEL FABRICATION METHODS

Ida Pavlichenko*, Armin T. Exner*, Paolo Lugli, Giuseppe Scarpa, and Bettina V. Lotsch

* These two authors made an equal contribution

Abstract

Thermoresponsive TiO$_2$/SiO$_2$ one-dimensional photonic crystals (Bragg stacks) fabricated *via* sol–gel processing methods represent a promising class of environmentally responsive nanostructures featuring optically encoded temperature and humidity detection. The thermo-optic response of the layer materials is amplified by their inherent porosity owing to adsorption/desorption of ambient humidity into the mesoporous multilayer structure. Based on a comprehensive analysis of the impact of layer thickness, refractive index and thermo-optic coefficient on the stop band position, and width of various Bragg stack architectures, design criteria for thermoresponsive Bragg stacks operating in the visible range of the optical spectrum are put forward. A large and well-defined thermo-optic signature is expected for material combinations featuring individually high thermo-optic coefficients with the same sign or allowing for large changes in the effective refractive indices due to water adsorption in the porous layers reinforcing the thermo-optic response, as observed in the TiO$_2$/SiO$_2$ couple. Important practical aspects of the performance of thermoresponsive Bragg stacks are addressed, including the hysteresis properties of TiO$_2$/SiO$_2$ Bragg stacks during multiple heating/cooling cycles, as well as response and recovery times (~2–4 s) of the multilayer system during external changes in ambient humidity.

3.2.1. INTRODUCTION

One-dimensional photonic crystals (1D PCs), also known as Bragg stacks (BSs), have recently demonstrated potential for various technological applications such as chemical, physical, and biological sensing, photovoltaics, distributed feedback lasers, radiation shielding, and many others.[1-5] 1D PCs represent a class of multilayer structures possessing a periodic modulation of the refractive index (RI) in one dimension, giving rise to a photonic band gap (stop band) and hence structural color.[6] The position and width of the stop band are determined by the periodic dielectric structure and can be tuned by external stimuli inducing changes in the optical thickness of the layers, that is, RI or physical thickness.[7] A wide arsenal of fabrication methods and numerous combinations of organic and inorganic materials together with surface functionalization and morphology tuning opens up new avenues to the design of simple, yet versatile sensing devices.[8,9] For the fabrication of 1D PCs, the sol–gel process has proven a valuable strategy as it enables a relatively simple, fast, and low-cost synthetic pathway to produce dense, nanoparticle (NP)-based or ordered mesoporous thin films with excellent compositional control and homogeneity facilitating the fabrication of uniform crystalline layers. Properties such as thickness, pore size, and surface area of the film can be tailored by the control of sol–gel processing and deposition parameters.[10,11] Along these lines, several deposition methods for the assembly of 1D PCs with high optical and structural quality have been reported, namely, dip-, spin-, and spray-coating methods, as well as layer-by-layer (LbL) assembly protocols that allow for the deposition of multilayer thin films on various substrates in a more facile and cost-efficient manner as compared to physical deposition techniques such as electron beam evaporation or sputter deposition.[12,13,14]

BSs composed of TiO_2/SiO_2 multilayers were studied most extensively during the past years due to the variety of intriguing properties such systems offer. Titanium dioxide is an excellent optical material with high RI (= 1.9–2.5), possessing a high chemical stability and low toxicity.[15] Owing to its ultraviolet induced photocatalytic properties, TiO_2 is used for the degradation of organic pollutants and exhibits fairly good antibacterial activity.[16] Thin film BSs exhibiting structural color have, for instance, been fabricated by means of a LbL deposition process[17,18] or by spin-coating from NP dispersions.[19,20] Colodrero et al. (2008)[21] carried out a comprehensive study on the optical properties of various NP-based 1D PCs versus changes in the ambient vapor pressure and discussed the sorption properties of the constituent layers. Further captivating possibilities, including the fabrication of flexible NP-based Bragg

mirrors, embedding of gold NPs into the BS for plasmonic applications and many others were demonstrated recently.[22,23] Owing to the intrinsic porosity of sol–gel-processed NP-based multilayers, they are more sensitive toward various analytes and hence possess excellent morphologies for sensing applications.

Apart from various analyte sensing schemes realized with NP-based TiO_2/SiO_2 BSs owing to their inherent porosity, the thermo-optic properties of TiO_2 render multilayer systems involving TiO_2 layers interesting candidates for temperature sensing applications. A comprehensive description of the most common technologies and a review of materials frequently used for the fabrication of thermo-optic switches have been provided by Coppola et al. (2011).[24] However, the authors do not consider the utilization of 1D porous PCs consisting of materials with a high thermo-optic coefficient (TOC) (e.g. TiO_2) as potential systems for thermo-optic tuning. The TOC of titanium dioxide measured for coatings deposited by electron beam deposition is negative and equal to -1.77 x 10^{-4} K^{-1} between 18°C and 120°C and corresponds to -3.04 x 10^{-4} K^{-1} between 220°C and 325°C at 800 nm.[25] The TOC of silicon dioxide is positive with a value around 1 x 10^{-5} K^{-1}.[26] The thermo-optic response of TiO_2/SiO_2 BSs was recently studied by Pavlichenko et al. (2012).[27] The authors observed enhancement of the thermal shift induced by ambient humidity, which is adsorbed into the porous layer architecture due to capillary condensation. Nanostructured TiO_2 films lend themselves particularly well for humidity-enhanced temperature tuning due to the high exposed surface area and facilitated water adsorption into the pore system owing to the photo-activated self-cleaning properties of TiO_2 surfaces.[28-30] While the stability, and hence performance, of optical filters is reduced by the influence of ambient humidity,[31] the thermo-optic response can be greatly enhanced by the presence of humidity. Therefore, NP-based BSs represent a versatile detection platform featuring a convenient and compact optical readout system.

In this article, we elaborate on different aspects pertaining to the temperature and humidity responses of BSs based on a label-free optical readout. The design of periodic multilayer architectures by both experiment and simulations will be outlined based on various design criteria, such as sensitivity and response kinetics. We also discuss important practical aspects of the performance of thermoresponsive BSs including the hysteresis properties of the multilayer system during multiple heating/cooling cycles and the response and recovery times during external changes in ambient humidity.

3.2.2. METHODS

Preparation of TiO₂ and SiO₂ suspensions

The suspension of TiO_2 NPs was synthesized as in Lotsch and Ozin (2008).[32] Sonication (37 kHz, S100H; Elmasonic) of the suspension allows obtaining NPs with a hydrodynamic diameter in the range between 7 and 15 nm. SiO_2 colloids were purchased from Sigma-Aldrich (LUDOX SM-30 (size of 7–10 nm), 30 wt% in H_2O and (LUDOX TMA (size of 15–30 nm), 34 wt% in H_2O). Particle size distribution of the precursor TiO_2 and SiO_2 suspensions was analyzed using dynamic light-scattering photocorrelation spectroscopy (Zetasizer Nano ZS; Malvern) at 20°C. The anatase modification of the TiO_2 powder calcined at 350°C for 1 h was confirmed by X-ray diffraction (D8 DISCOVER; Bruker).

Bragg stack assembly

Thermoresponsive PCs were assembled by sequential deposition of TiO_2 and SiO_2 suspensions on a clean ISO 8037/1 glass slide (2.5 x 2.5 cm²).[27] Thin layers of TiO_2 and SiO_2 were produced using the spin-coating technique (WS-650SZ6NPP/LITE; Laurell). The single thin film thickness and porosity were characterized by spectroscopic ellipsometry (performed on a Woollam M200D variable angle ellipsometer in the entire spectral range of 190–1000 nm at angles of incidence of 65°, 70°, and 75°). Scanning electron microscopy (JSM-6500F, JEOL, operating at an accelerating voltage of 2–5 kV) was used to examine the morphology of the BS cross section and flat surfaces.

Simulations

We carried out the simulations of the transmission spectra with the program COMSOL Multiphysics 3.3, radio frequency (RF) module in a two-dimensional (2D) in-plane transverse electric (TE) waves application mode. In the absence of external currents and sources, Maxwell's equations are represented in the following form (Equation (1))

$$\nabla \times \big(\nabla \times \boldsymbol{E(r)}\big) - n^2 k^2 \boldsymbol{E(r)} = 0\,, \quad (1)$$

where $\boldsymbol{E}$ is the electric field, n is the RI, and k is the free-space wave number. To model the TE waves propagating through the simulated 1D PC, drawn in a 2D geometry as a stack of rectangles with user-defined thicknesses, we switch to a scalar Equation (2) for the TE field component E_z

$$-\nabla \cdot \nabla \cdot E_z - n^2 k^2 E_z = 0 \,, \quad (2)$$

To avoid reflection at outer boundaries of the PC geometry, we selected the "matched boundary" conditions, and inside the geometry, we applied the "continuity" boundary condition to each boundary except for the one where the wave is entering the structure. To characterize the transmission coefficient, we calculated the S_{21} scattering parameter (for more details, see COMSOL Multiphysics, 2008). [33]

Optical response and hysteresis analysis

To obtain transmission spectra of the BS in the range of 400–800 nm, we used a monochromator (Cornerstone260 1/4 m; Newport) with a high pressure arc lamp as a light source and a 10 x 10-mm calibrated silicon detector connected to a digital lock-in amplifier (Merlin).[27] The temperature of the BS was varied by two Peltier elements, and the PT100 temperature sensor was attached to the other side of the BS above the optical axis. Peltier elements and the temperature sensor were connected to a remote-controlled source meter. A software proportional integral controller regulated the heating and cooling of the Peltier elements. The measured deviation of the temperature during the measurement was less than 0.1°C. For each temperature, the sample was equilibrated for 60 s.

For the hysteresis measurement, the sample was mounted on two Peltier elements as described for the spectral transmission measurements. A standard orange light-emitting diode (LED) (peak wavelength of 604 nm with angular divergence of the light beam of ~20°), sourced by a current of 5 mA, was chosen as a light source. The LED was equilibrated before the experiment for 30 min. The LED light beam passed through a monochromator set to the wavelength of 610 nm, to gain a narrower spectrum. For the temperature control, extra care has been taken such that the temperature was neither oscillating nor overshooting the set-point temperature. After the setpoint temperature was reached, the sample was equilibrated for another 60 s before the measurement was taken.

For the characterization of response time, we changed the RH of the environment (20%) by introducing water vapor onto the sample surface. The tubing with the nitrogen stream carrying the water vapor was mounted above the surface of the BS. The measured RH of the vapor was 70%; additionally, the valve located on the tubing allowed the instant turning off of the vapor stream. Time-dependent spectroscopy was performed by fiber optic spectrometer (USB2000+; Ocean Optics) integrated with an optical light microscope (DM2500 M; Leica).

3.2.3. RESULTS AND DISCUSSION
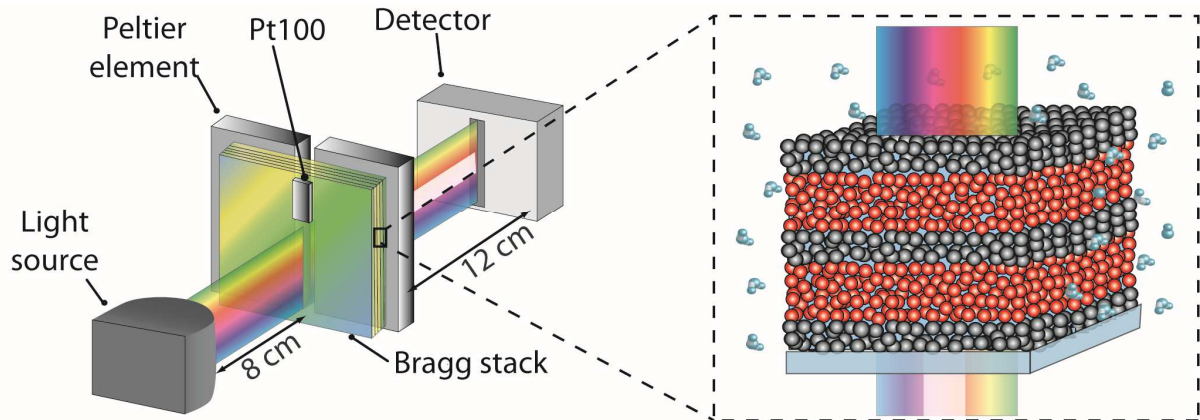
Scheme 3.2.1. (a) Schematic drawing of the experimental setup for humidity-enhanced temperature detection using a 1D PC. The Bragg stack acts as a tunable optical filter for the incident beam, resulting in the observation of the photonic stop band. (b) Enlarged schematic illustration of the Bragg stack in ambient conditions, showing the adsorption/desorption of the water vapor surrounding the BS into the textural pores of the network.

The experimental setup for the characterization of the thermo-optic behavior of NP-based porous BSs under environmental conditions is illustrated in Scheme 3.2.1. Temperature tuning of the BS, deposited on a transparent glass substrate, is realized through controlled heating/cooling by means of thermoelectric elements as demonstrated in Scheme 3.2.1(a). The BS, acting as a thermoresponsive optical filter, modifies the spectrum of the incident light as a function of temperature.[34,35] The porous nature of the NP-based multilayers facilitates condensation of ambient humidity in the vicinity of the BS into the pores, thus changing the effective RI of the system.[27]

This principle is demonstrated by monitoring the shift of the stop band of a 8.5-bilayer TiO_2 (50 nm)/SiO_2 (90 nm) BS upon heating under ambient conditions. Since in the previous studies,[27] we observed that the largest thermal shift enhancement occurs in the temperature region below 30°C, transmission spectra were measured in the temperature range between 15°C and 25°C with steps of 2°C. The BS was thermally equilibrated for 1 min before taking the measurement. We observed an enhanced blue shift of the transmission spectra during heating due to the combined effects of the thermo-optic RI change and water desorption from the pores of the BS. However, evidently, the temperature-induced shift of the "red" edge of the stop band is significantly larger (20 nm) than that of the "blue" edge (5 nm). Such asymmetric behavior will be rationalized by means of simulation of the stop band position and

width upon changing various geometric BS parameters (thickness of the layers) and material properties (RI) as discussed in the following (Figure 3.2.2).
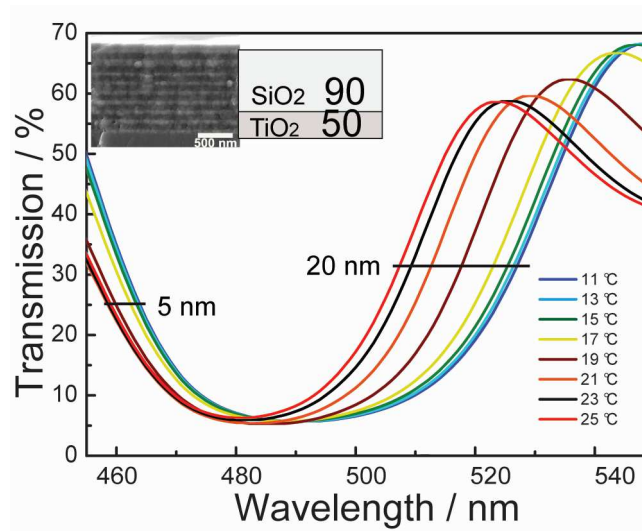
Figure 3.2.1. Transmission spectra of a 8.5-bilayer TiO_2 (50 nm)/SiO_2 (90 nm) BS demonstrating a significant blue shift of the stop band in the temperature range between 15°C and 25°C at ambient conditions. Black bars indicate the shift of the "red" edge (20 nm) and of the "blue" edge (5 nm) of the stop band. The cross-sectional SEM image of the BS is shown in the upper left corner; the scale bar is 500 nm.

In order to design BSs with suitable optical characteristics as well as sensitivity to ambient conditions, we demonstrate how thickness changes and independently RI changes of the low-RI and high-RI materials affect the position and width of the photonic stop band, based on well-established PC concepts.[6] Figure 3.2.2(a) and (b) shows the influence of the increase in layer thickness from 100 to 140 nm of the low-RI material SiO_2 (RI ≈ 1.3) and from 70 to 110 nm of the high-RI material TiO_2 (RI ≈ 1.9), respectively, for a 9-bilayer BS TiO_2/SiO_2 in increments of 2 nm. It can be seen that the change in layer thickness of one of the materials results in a shift of the stop band to longer wavelengths, consistent with an increase in optical thickness of a bilayer with increasing physical thickness, while the width of the stop band remains approximately constant. A different behavior is seen in Figure 3.2.2(c) and (d), which shows the influence of an increase in RI from 1.1 to 1.5 for SiO_2 and from 1.7 to 2.1 for TiO_2, respectively, while keeping the layer thicknesses constant: 90 nm for TiO_2 and 120 nm for SiO_2. Although only the RI of one material at a time is changed for clarity, the simulations show a substantial effect of changes in the RI on the position and width of the stop band. In general, a larger RI contrast between the two layer materials translates into a larger stop band width and vice versa. With increasing RI of SiO_2, the high energy ("blue") edge of the stop band shifts significantly, while the low energy ("red") edge of the stop

band is only slightly affected. In contrast, for changes in the RI of TiO_2, we observe a more significant shift of the "red" edge of the stop band, whereas the "blue" edge remains almost constant (Figure 3.2.2(d)). This observation can be generalized to arbitrary materials: a change in RI of the low-RI material predominantly affects the "blue" edge, and a change in RI of the high-RI material significantly affects the "red" edge of the stop band, owing to the localization of the electromagnetic field in the high-dielectric material at the red edge of the stop band, and vice versa.[36] Consequently, two conclusions can be drawn: first, even minute changes in the RIs of the layers at constant layer thickness have a major impact on the position, especially the width of the stop band. This generally translates into a high sensitivity to processes changing the effective RI of one or both of the layers, such as the adsorption of ambient humidity into a porous material,[27] as evidenced by using NP-based layers with a high degree of textural porosity (note that by textural porosity, we refer to the porosity arising from intra-aggregate/interparticle voids in the film, i.e. from the spaces formed by interparticle contacts). Second, a BS sensing element may distinguish between a disproportionate change of the RIs of the two different layer materials, for instance, if one layer material shows a significantly larger porosity or TOC than the other layer material, leading to substantial changes in the RI contrast and hence the width of the stop band. Therefore, we may conclude that the observation of the asymmetrical shift for the BS in Figure 3.2.1 is consistent with the earlier simulations (Figure 3.2.2), indicating that the magnitude of the wavelength shift is larger for the "red" edge of the stop band due to the chosen wavelength scale. In addition, however, it can be seen that the width of the stop band in Figure 3.2.1 slightly decreases with increasing temperature, thus suggesting a disproportionate change of the RIs of the two different layer materials. The observed narrowing is in agreement with the scenario represented in Figure 3.2.2(d), indicating that the RI of TiO_2 changes more significantly than that of SiO_2 owing to larger amounts of physisorbed water in the more hydrophilic TiO_2 layers and a larger TOC of TiO_2.
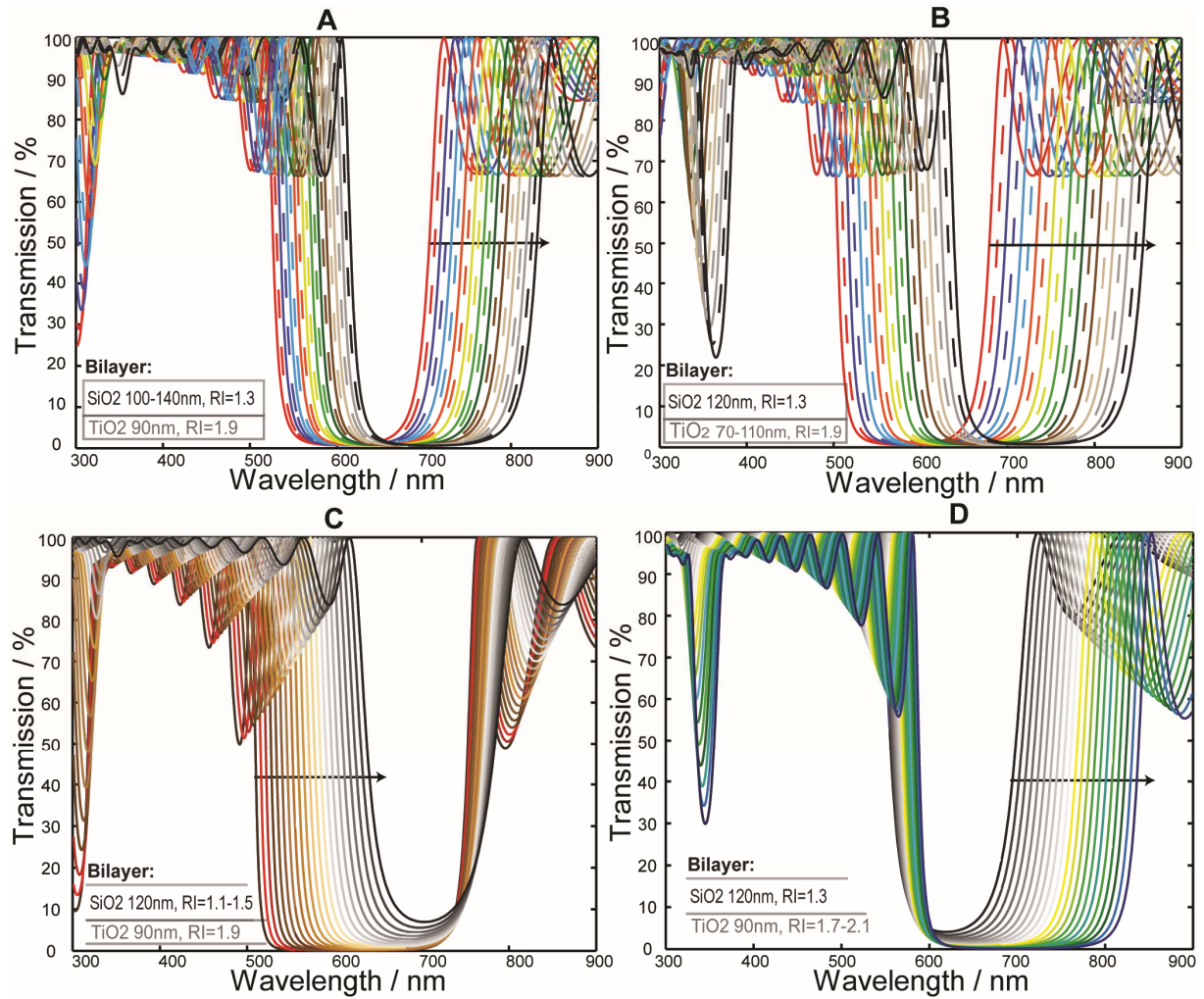
Figure 3.2.2. Simulated transmission spectra of a BS with 9-bilayer BSs, starting with the TiO_2 layer, and consisting of various combinations of (a) TiO_2 layers of 90 nm/RI = 1.9 and SiO2 layers with RI = 1.3 and thicknesses varying from 100 to 140 nm. (b) TiO_2 layers with RI = 1.9 and thicknesses varying from 70 to 110 nm, and SiO_2 layers of 120 nm/RI = 1.3. (c) TiO_2 layers of 90 nm/RI = 1.9 and SiO_2 layers of 120 nm with RI varying from 1.1 to 1.5. (d) TiO_2 layers of 90 nm with RI varying from 1.7 to 2.1, and SiO_2 layers of 120 nm/RI = 1.3. The black arrow indicates the direction of the stop band shift as the layer thickness or RI increases.

The basic design of BSs showing an enhanced thermo-optic response irrespective of ambient humidity is dominated by the choice of appropriate materials with a large TOC, as well as a suitable mutual enhancement of the TOCs of the individual layers. In order to outline the influence of the TOC of the two constituent layer materials, we have analyzed the thermo-optic response of two BS configurations with different material combinations. We performed simulations for 9-bilayer 1D PCs based on TiO_2 and SiO_2 (Figure 3.2.3(a)) and on ZrO_2 and SiO_2 (Figure 3.2.3(b)). As outlined earlier, the TOC of TiO_2 is negative and equal to -3 x 10^{-4} K^{-1}, whereas the TOC of SiO_2 is positive and equal to 1 x 10^{-5} K^{-1}. In the ZrO_2/SiO_2 combination, both TOCs are positive, and the TOC of ZrO_2 ($\approx$ 4.8 x 10^{-4} K^{-1}) is roughly one

order of magnitude larger than that of SiO_2 according to Inci et al. (1997)[37]. Owing to the larger TOCs of TiO_2 and ZrO_2, the thermo-optic effect of the high-RI materials plays the dominant role in both configurations. In the TiO_2/SiO_2 BS, the stop band therefore shifts toward shorter wavelengths by 5 nm in the temperature range between 10°C and 60°C; however, the positive TOC of silica counteracts this shifting behavior to some extent. In contrast, for the ZrO_2/SiO_2 BS, the thermal behavior shows the opposite trend in the same temperature range, and hence, the stop band is shifted to longer wavelengths. In addition, the shift is larger (8 nm), which can be explained by the same sign of the TOCs for both materials that therefore add up, leading to a larger thermo-optic response. Hence, we have verified the prediction implied in Figure 3.2.2 that in order to obtain a large thermo-optic response of a BS, both constituent materials need to have individually large TOCs, and both TOCs need to have the same sign. Note, however, that the amplifying effect on the temperature response by ambient humidity that is observed in the TiO_2/SiO_2 BS is expected to be reversed in the case of ZrO_2/SiO_2 BS, as the TOC (red shift with increasing temperature) and humidity response (blue shift with increasing temperature) would counteract each other.

Figure 3.2.3. Simulated transmission spectra, demonstrating the thermal shift of the stop band in the range between 10°C and 60°C of two 9-bilayer BSs with TOCs as described in the text: (a) 90/120 nm TiO_2/SiO_2 and (b) 90/120 nm ZrO_2/SiO_2. The black arrow indicates the direction of the stop band shift toward (a) shorter wavelengths for negative (large)/positive (small) TOCs for TiO_2/SiO_2, respectively, and (b) longer wavelengths for positive (large)/positive (small) TOCs for ZrO_2/SiO_2, respectively.

Materials with large negative TOCs, such as polymers[38] and hybrid organic/inorganic materials,[39] could be of interest for tunable thermo-optic PCs. However, their thermal expansion properties have to be taken into account. Since thermal expansion and negative TOCs may cancel out each other if the

materials are assembled within a BS platform that only detects combined changes in the optical thickness, additional analysis of the influence of layer expansion would be needed.

The earlier simulations were done based on the thermo-optic response only, and humidity effects were not explicitly accounted for. However, as has been shown above (Figure 3.2.1), the environmental conditions, especially ambient relative humidity (RH), have to be taken into account for porous films when designing a thermo-optic detection platform. Hence, one needs to account for the *effective* TOC of the layers including both thermal and humidity responses that can be measured, for example, by means of spectroscopic ellipsometry.[40] Here, we analyze the influence of the bilayer lattice constant (the sum of the physical thicknesses of high-RI and low-RI materials) on the thermo-optic response of TiO_2/SiO_2 1D PCs under environmental conditions, that is, using the effective TOCs and hence RIs determined for NP-based TiO_2 and SiO_2 thin films at RH = 25%.[27] The effective TOC of the TiO_2 layer is given by $dn/dT = -1.61 \times 10^{-3}$ K^{-1} between 10°C and 30°C at 25% RH and by -2.52×10^{-4} K^{-1} above 30°C. The effective TOC of SiO_2 used for the simulations is also negative (-2.52×10^{-4} K^{-1}) over the whole temperature range and one order of magnitude larger than the literature values for dense layers. Figure 3.2.4(a) to (d) outlines the thermal shift between 10°C and 60°C for a 9-bilayer BS with the following bilayer combinations: (a) 50/80, (b) 50/90, (c) 60/90, (d) 50/110, and (e) 110/90 nm for TiO_2/SiO_2 layers, respectively, hence changing the lattice constant from (a) 130 to (e) 200 nm. It can be seen from the graphs that when detecting the shifts optically, that is, on the wavelength scale, larger shifts are observed for BSs with larger lattice constants and, hence, stop bands located at larger wavelengths. To explore the influence of the relative portions of the high-RI and low-RI materials in a bilayer with constant thickness, the ratio of the high-RI material (TiO_2) to the low-RI material (SiO_2) in a 9-bilayer BS was varied in a stepwise manner from 40/110 nm (Figure 3.2.5(a)) to 110/40 nm (Figure 3.2.5(b)) for TiO_2/SiO_2 with a constant bilayer thickness of 150 nm. A relative increase of the high-RI material portion shifts the stop band toward longer wavelengths and hence also increases the shift of the "red" edge of the stop band. In an optical detection mode, the most significant thermal response can therefore be observed for 1D PCs with a large bilayer thickness and/or a high portion of the high-RI material, as both conditions will increase the optical thickness of the BS and hence shift the position of the stop band to the red.
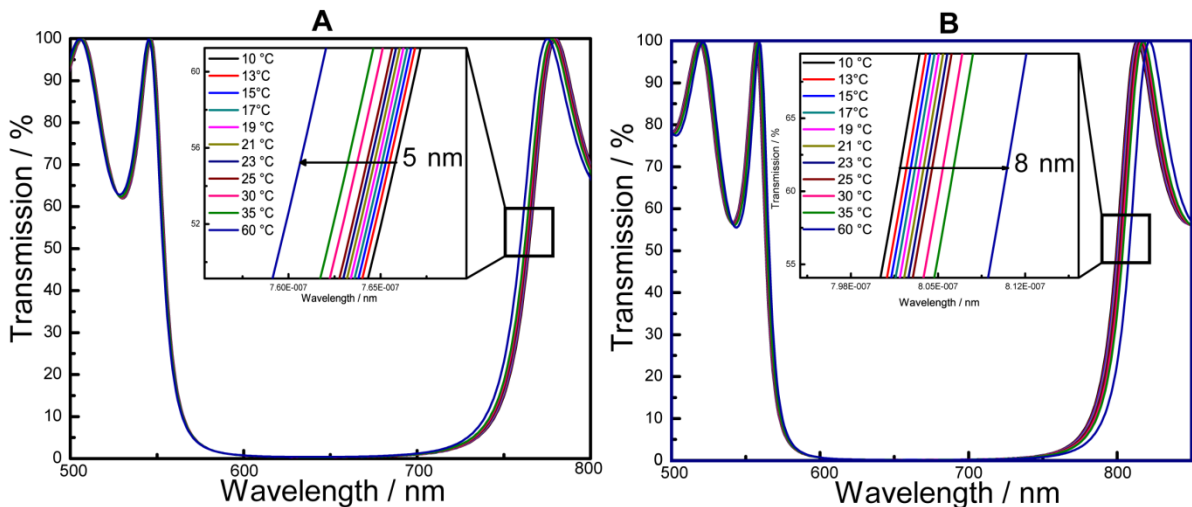
Figure 3.2.4. Simulated transmission spectra of a 9-bilayer BS, demonstrating the thermal shift of the stop band in the range between 10°C and 60°C with the experimental TOCs at 25% RH for TiO_2 and SiO_2 thin films and the following lattice parameters: (a) 50/80, (b) 50/90, (c) 60/90, (d) 50/110, and (e) 110/90 nm for the TiO_2/SiO_2 layers, respectively. The magnitude of the shift for each combination is indicated next to the black arrow.
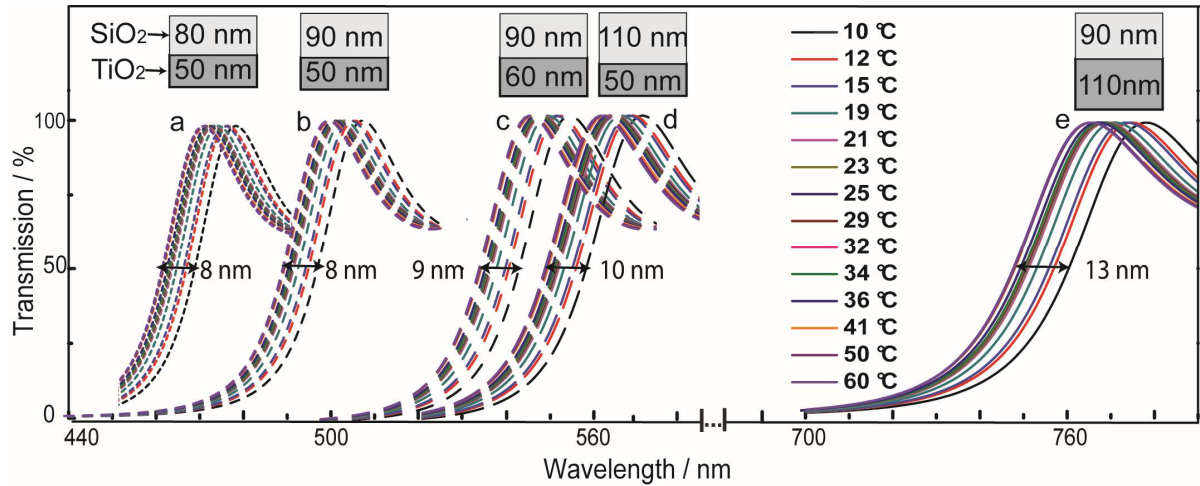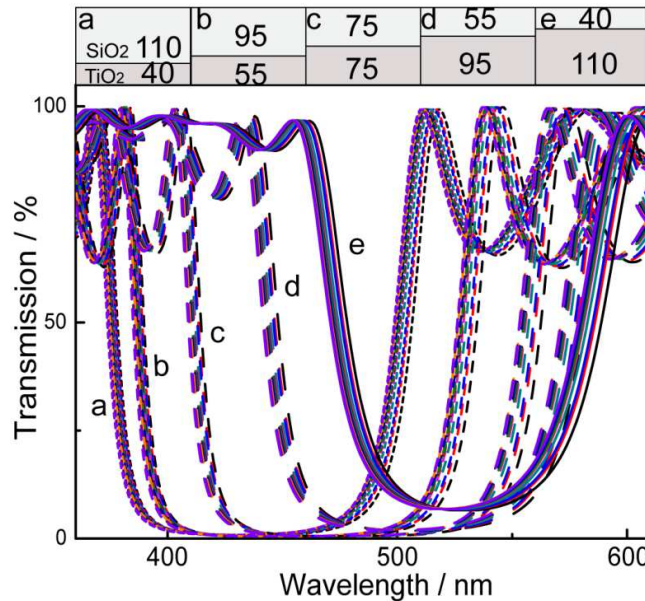

Figure 3.2.5. Simulated transmission spectra of a 9-bilayer BS, demonstrating the thermal shift of the stop band in the temperature range between 15°C and 60°C using the experimental TOCs at 25% RH for TiO_2/SiO_2 and the following layer thickness combinations at a fixed bilayer thickness of 150 nm: (a) 40/110, (b) 55/95, (c) 75/75, (d) 95/55, and (e) 110/40 nm.
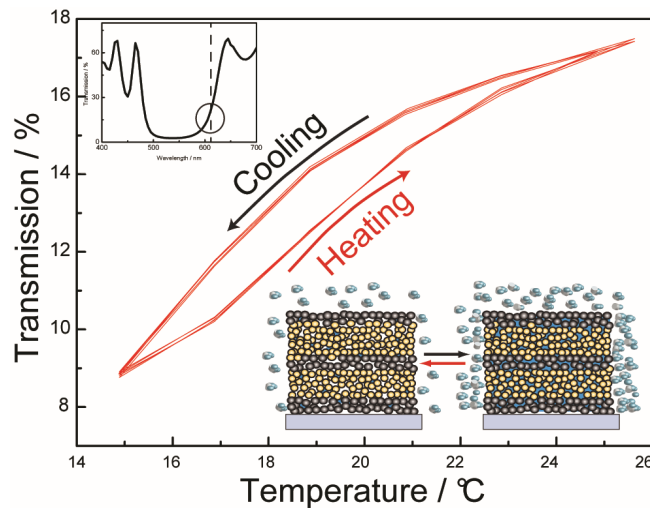
Figure 3.2.6. Heating and cooling curves recorded by monitoring the transmission at 610 nm and 25% RH between 15°C and 25°C. The stop band of the investigated BS is placed in the upper left corner. The temperature was cycled five times from 15°C to 25°C in steps of 2°C and backward with an equilibration time for each temperature of 60 s. The hysteresis may be caused by capillary condensation of ambient humidity into the mesoporous network of the BS as is schematically shown in the illustration (bottom right).

In the earlier simulations, we looked at the humidity-enhanced thermal shift (i.e. the shift induced by both TOC and ambient humidity, giving rise to an effective TOC) of the optical spectrum of the BS as a function of either cooling or heating and neglecting any affects attributable to the morphology of the BS. However, in real systems whose response is affected by processes such as water adsorption into porous layers, we would expect a hysteresis to occur when recording the optical response along a full heating–cooling cycle. Therefore, the optical response of a 9-bilayer (TiO_2 (60 nm)/SiO_2 (110 nm)) BS was studied at 25% RH by cycling the temperature up and down in steps of 2°C while measuring the transmission value at a constant wavelength (610 nm). After each set-point temperature was reached, the sample was equilibrated for another 60 s before the measurement was taken. As can be seen in Figure 3.2.6, a hysteresis is indeed observed over more than five cycles. Heating–cooling cycles recorded with longer delay times up to 900 s do not significantly change the shape of the hysteresis, thereby suggesting that the water adsorption/desorption kinetics are fast and not responsible for the observed hysteresis. On the other hand, measurements under nitrogen atmosphere with exclusion of ambient humidity show no hysteresis, thus indicating that humidity is required in order for the hysteresis to occur. We assume that the hysteresis is due to capillary condensation of water into the textural mesopores of the layers resulting from the packing of the NPs, as is observed in similar thin film systems consisting of NPs.[41] In general, however, it can be noted that the maximum opening of the hysteresis loop is only about 1.5% in transmission at 25% RH and hence results in only a moderate, yet reproducible correction of the shifts

expected for a purely thermo-optic response. A crucial aspect in designing an optical device that can detect subtle changes in RH and temperature is the average response time. The thermal response is expected to be fast if the BS is in thermal equilibrium with its environment. Therefore, although we have shown earlier that the adsorption/desorption kinetics is faster than about 60 s, we infer that the response time is still dominated by the uptake of ambient humidity into the porous BS architecture. In Figure 3.2.7, we outline an experiment that allows for a simple characterization of the response time of the multilayer system with respect to changes in ambient humidity, while keeping the temperature constant. In a typical experiment, the BS (9-bilayer TiO_2, 60 nm, 10% porosity/SiO_2, 100 nm, 25% porosity) was fixed under a microscope (20% RH at 20°C) such that the measurement spot could be constantly monitored. Then, time-resolved measurements were carried out detecting changes in transmission occurring during the external change in RH of the environment, provided by a flow setup, from 20% to 70%. Upon increasing RH, humidity is adsorbed into the textural mesopores of the BS, thus increasing the RI of the materials comprising the BS and shifting the stop band to larger wavelengths. For the BS in Figure 3.2.7(a), the transmission at 450 nm was monitored during the humidity change as shown in Figure 3.2.7(d) and (e). The response time $< \tau_1 >$ to the humidity change was ascertained to be 2 s, and the recovery time $< \tau_2 >$ after turning down the water vapor flow is approximately equal to 3.8 s, both being significantly longer than the response times of the materials due to the thermo-optic effect alone ($\sim 10^{-6} - 10^{-3}$ s).[24,42] The difference in the response and recovery times can be associated with the kinetics of the adsorption and desorption processes, where desorption is slightly more sluggish and proceeds in two steps. We also fabricated a BS (4-bilayer TiO_2, 45 nm, 10% porosity/SiO_2, 60 nm, 40% porosity) with a higher porosity of the SiO_2 layers, as can be seen in Figure 3.2.8(a) and (b). Again, the transmission change at 500 nm was monitored during abrupt changes in environmental RH from 20% to 70% (Figure 3.2.8(c) and (d)). Although the number of bilayers for this BS is almost two times less than that of the BS as shown in Figure 3.2.7 and additional porosity was introduced into the system, the response time $< \tau_1 >$ is only slightly smaller, being equal to 1.5 s (recovery time $< \tau_2 > \approx 3$ s). Colodrero et al. (2008)[21] associated this phenomenon with the fact that the sorption properties of the stack are determined by the interaction between the neighboring layers, and the response is mediated by the layer with smaller pores, which in our case is the TiO_2 NP layer in both BS configurations. Accordingly, further titania layer modification toward higher porosity would be required for even faster response times. In general, however, the observed fast response times can be of interest, for example, in medical

applications where fast sampling of a patient's breathing may be required, since human expiration contains large amounts of water vapor compared to ambient air.[43]
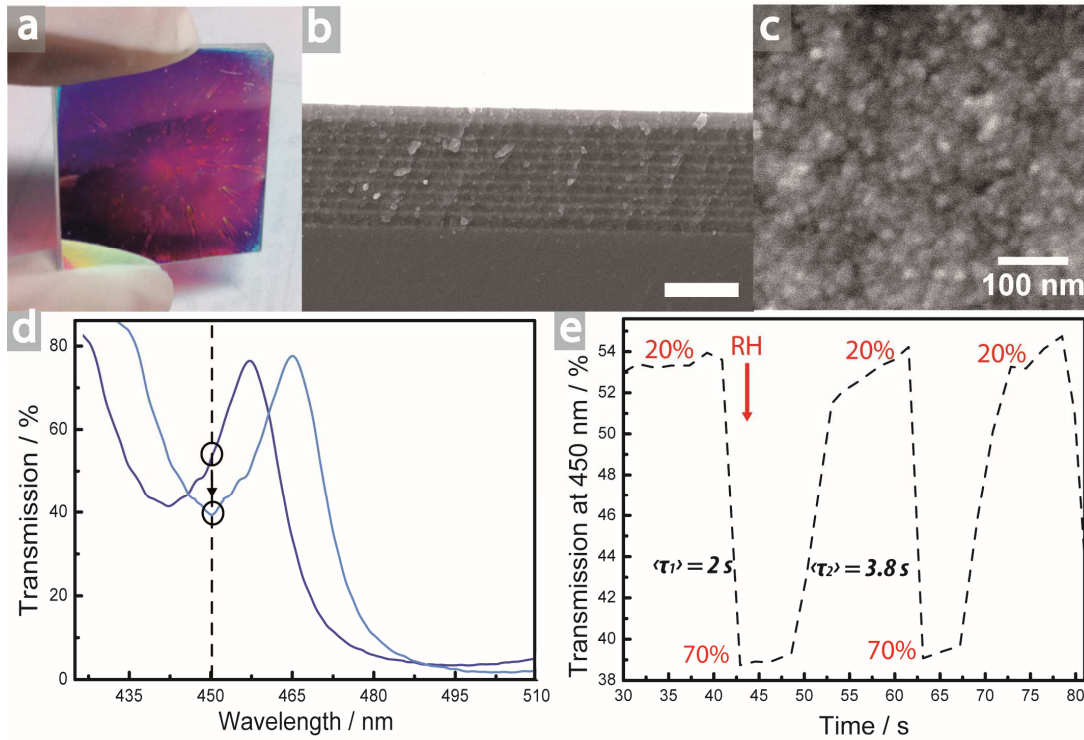
Figure 3.2.7. (a) Photograph of a 9-bilayer TiO_2 (60 nm)/SiO_2 (100 nm) 1D PC fabricated on a 2.5 x 2.5 cm^2 glass slide by multiple spin-coating, (b) SEM image of the cross section of the BS (scale bar is 1 mm), (c) SEM image showing the morphology of the TiO_2 top layer of the BS, (d) transmission spectra of the BS demonstrating the change in the transmission at 450 nm corresponding to the RH change from 20% to 70%, and (e) time-resolved transmission change in response to the change of the RH from 20% to 70%. $< \tau_1 >$ is the response time to the increase in humidity, and $< \tau_2 >$ is the recovery time after the end of the stimulus (i.e. upon decrease in humidity).
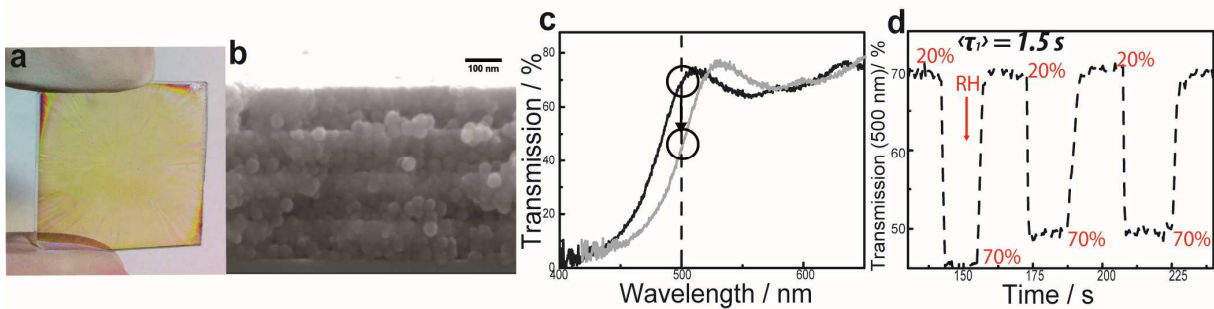
Figure 3.2.8. (a) Photograph of a 4-bilayer TiO_2 (45 nm)/SiO_2 (60 nm) 1D PC possessing higher porosity of the SiO_2 layer (40%), fabricated on a 2.5 x 2.5-cm^2 glass slide by multiple spin-coating, (b) SEM image of the cross section of the BS (scale bar is 100 nm), (c) transmission spectra of the BS demonstrating the change in the transmission at 500 nm corresponding to the RH change from 20% to 70%, and (d) time-resolved transmission

change in response to the change of the RH from 20% to 70%. $< \tau_1 >$ is the response time to the increase in humidity.

3.2.4. CONCLUSION

In this study, we present a comprehensive analysis of thermoresponsive TiO_2/SiO_2 BSs assembled by a sol–gel fabrication process. We demonstrate that due to the porous nature of the multilayer system, the temperature response of such systems is significantly enhanced in the presence of ambient humidity. In order to gain insights into the BS response to temperature and humidity, both acting on the effective RI of the multilayer system, we carried out simulations detailing the influence of RI, TOC, and layer thicknesses on the stop band position and width as well as temperature sensing characteristics. A high thermo-optic response that can be read out optically is expected for material combinations with large bilayer thicknesses, high RI contrast, and large TOCs having the same sign. As the width of the stop band is a sensitive probe of the relative RI changes of the two layer materials, it should be possible to predict the material that is affected the most by humidity-induced RI changes. The investigated BSs show an amplified thermal response when exposed to ambient humidity, suggesting that water is adsorbed in the textural mesopores, thus altering the effective RI of the constituent materials. This assumption was supported by subjecting the BS to several heating–cooling cycles, resulting in a hysteresis loop for temperatures between 15°C and 25°C with a maximum opening of 1.5% in transmission at 19°C, which is consistent with capillary condensation of water inside the mesopores. Fast response times of approximately 2–4 s upon exposure to different humidity environments are testament to a fast water adsorption/desorption kinetics that bodes well for the use of such systems as sensitive temperature and humidity detection platforms

ACKNOWLEDGEMENTS

3.2.6. BIBLIOGRAPHY

(1)   Calvo, M. E.; Colodrero, S.; Hidalgo, N.; Lozano, G.; Lopez-Lopez, C.; Sanchez-Sobrado, O.; Miguez, H. *Energ. Environ. Sci.* **2011,** *4*, 4800.

(2)   Ge, J. P.; Yin, Y. D. *Angew. Chem. Int. Edit.* **2011,** *50*, 1492.

(3)   Lotsch, B. V.; Knobbe, C. B.; Ozin, G. A. *Small* **2009,** *5*, 1498.

(4)   Puzzo, D. P.; Helander, M. G.; O'Brien, P. G.; Wang, Z. B.; Soheilnia, N.; Kherani, N.; Lu, Z. H.; Ozin, G. A. *Nano Lett.* **2011,** *11*, 1457.

(5)   Scotognella, F.; Puzzo, D. P.; Monguzzi, A.; Wiersma, D. S.; Maschke, D.; Tubino, R.; Ozin, G. A. *Small* **2009,** *5*, 2048.

(6)   Joannopoulos, J. D.; Johnson, S. G.; Winn, J. N.; Meade, R. D. Photonic Crystals: Molding the Flow of Light, 2nd Edition **2008,** 44.

(7)   Bonifacio, L. D.; Lotsch, B. V.; Puzzo, D. P.; Scotognella, F.; Ozin, G. A. *Adv. Mater.* **2009,** *21*, 1641.

(8)   Patzke, G. R.; Zhou, Y.; Kontic, R.; Conrad, F. *Angew. Chem. Int. Edit.* **2011,** *50*, 826.

(9)   Redel, E.; Mirtchev, P.; Huai, C.; Petrov, S.; Ozin, G. A. *ACS Nano* **2011,** *5*, 2861.

(10)   Hench, L. L.; West, J. K. *Chem. Rev.* **1990,** *90*, 33.

(11)   Tsuchiya, T.; Emoto, T.; Sei, T. *J. Non-Cryst. Solids* **1994,** *178*, 327.

(12)   Inui, C.; Tsuge, Y.; Kura, H.; Fujihara, S.; Shiratori, S.; Sato, T. *Thin Solid Films* **2008,** *516*, 2454.

(13)   Kobler, J.; Lotsch, B. V.; Ozin, G. A.; Bein, T. *ACS Nano* **2009,** *3*, 1669.

(14)   Nogueira, G. M.; Banerjee, D.; Cohen, R. E.; Rubner, M. F. *Langmuir* **2011,** *27*, 7860.

(15)   Macwan, D. P.; Dave, P. N.; Chaturvedi, S. *J. Mater. Sci.* **2011,** *46*, 3669.

(16)   Park, J. K.; Kim, H. K. *B. Kor. Chem. Soc.* **2002,** *23*, 745.

(17)   Lee, D.; Rubner, M. F.; Cohen, R. E. *Nano Lett.* **2006,** *6*, 2305.

(18)   Wu, Z.; Lee, D.; Rubner, M. F.; Cohen, R. E. *Small* **2007,** *3*, 1445.

(19)   Calvo, M. E.; Colodrero, S.; Rojas, T. C.; Anta, J. A.; Ocana, M.; Miguez, H. *Adv. Funct. Mater.* **2008,** *18*, 2708.

(20)   Colodrero, S.; Ocana, M.; Miguez, H. *Langmuir* **2008,** *24*, 4430.

(21)   Colodrero, S.; Ocana, M.; Gonzalez-Elipe, A. R.; Miguez, H. *Langmuir* **2008,** *24*, 9135.

(22)   Sanchez-Sobrado, O.; Calvo, M. E.; Miguez, H. *J. Mater. Chem.* **2010,** *20*, 8240.

(23) Sanchez-Sobrado, O.; Lozano, G.; Calvo, M. E.; Sanchez-Iglesias, A.; Liz-Marzan, L. M.; Miguez, H. *Adv. Mater.* **2011,** *23*, 2108.

(24) Coppola, G.; Sirleto, L.; Rendina, I.; Iodice, M. *Opt. Eng.* **2011,** *50.*

(25) Gulsen, G.; Inci, M. N. *Opt. Mater.* **2002,** *18*, 373.

(26) Ghosh, G. *J. Non-Cryst. Solids* **1995,** *189*, 191.

(27) Pavlichenko, I.; Exner, A. T.; Guehl, M.; Lugli, P.; Scarpa, G.; Lotsch, B. V. *J. Phys. Chem. C* **2012,** *116*, 298.

(28) Yadav, B. C.; Pandey, N. K.; Srivastava, A. K.; Sharma, P. *Meas. Sci. Technol.* **2007,** *18*, 260.

(29) Tai, W. P.; Kim, J. G.; Oh, J. H. *Sensor Actuat. B-Chem.* **2003,** *96*, 477.

(30) Yu, J. G.; Zhao, X. J.; Zhao, Q. N.; Wang, G. *Mater. Chem. Phys.* **2001,** *68*, 253.

(31) Zverev, G. M.; Sidoryuk, O. E.; Skvortsov, L. A. *Sov. J. Q. Elec.* **1981,** *11*, 1393.

(32) Lotsch, B. V.; Ozin, G. A. *ACS Nano* **2008,** *2*, 2065.

(33) COMSOL Multiphysics (2008) RF module model library version 3.5. Available at: http://www.comsol.com/

(34) Domash, L. H.; Ma, E.; Lourie, M.; Sharfin, W.; Wagner, M. *P. Soc. Photo-Opt. Ins.* **2003,** *4989*, 161.

(35) Hohlfeld, D.; Zappe, H. *J. Opt. A-Pure Appl. Op.* **2004,** *6*, 504.

(36) Chen, J. I. L.; von Freymann, G.; Choi, S. Y.; Kitaev, V.; Ozin, G. A. *Adv. Mater.* **2006,** *18*, 1915.

(37) Inci, M. N.; Gulsen, G.; Yaradanakul, M. A.; Kaplan, Z.; Aktas, G. *J. Phys. D - Appl. Phys.* **1997,** *30*, 517.

(38) Zhai, J. F.; Qiu, L.; Zhou, J. Y.; Zhao, Y. X.; Shen, Y. Q.; Ling, Q. D.; Yang, M. J. A*dv. Mater. Opt. Electr.* **2000,** *10*, 3.

(39) Kurata, Y.; Sugihara, O.; Kaino, T.; Komatsu, K.; Kambe, N. *J. Opt. Soc. Am. B* **2009,** *26*, 2377.

(40) Zhang, F.; Zhang, R. J.; Zhang, D. X.; Wang, Z. Y.; Xu, J. P.; Zheng, Y. X.; Chen, L. Y.; Huang, R. Z.; Sun, Y.; Chen, X.; Meng, X. J.; Dai, N. *Appl. Phys. Express* **2013,** *6*.

(41) Demessence, A.; Boissiere, C.; Grosso, D.; Horcajada, P.; Serre, C.; Ferey, G.; Soler-Illia, G. J. A. A.; Sanchez, C. *J. Mater. Chem.* **2010,** *20*, 7676.

(42) Hache, A.; Allogho, G. G. *Opt. Commun.* **2011,** *284*, 1656.

(43) Arregui, F. J.; Cooper, K. L.; Liu, Y. J.; Matias, I. R.; Claus, R. O. *IEICE T. Electron.* **2000,** *E83c*, 360.

3.3. NANOMORPHOLOGY TUNING OF THE THERMAL RESPONSE OF TiO₂/SiO₂ BRAGG STACKS

Ida Pavlichenko*, Armin T. Exner*, Gennady Logvenov, Giuseppe Scarpa, Paolo Lugli,

and Bettina V. Lotsch

* These two authors made an equal contribution

Abstract

Herein, we present a comparative study of thermo- and environmentally responsive TiO₂/SiO₂ one-dimensional photonic crystals (Bragg stacks) fabricated by different deposition methods and fabrication schemes, featuring various multilayer nanomorphologies. These include dense multilayer systems processed by physical vapor deposition and wet-chemistry protocols, as well as porous systems, namely, nanoparticle-based optical filters exhibiting textural porosity, and evaporation-induced self-assembled mesoporous Bragg stacks exhibiting predominantly structural porosity, as well as hybrid structures comprising both dense and porous layers. We investigate the spectral shift of the photonic stop band for the different Bragg stack nanomorphologies induced by the humidity-enhanced thermo-optic effect in a temperature range from 15 to 60 °C. We also demonstrate the response and recovery kinetics of the multilayer systems during external changes in ambient humidity. Notably, the choice of fabrication method plays a significant role in the thermal and humidity response of the system. Taking advantage of different material nanomorphologies we can tune the thermal shift of the photonic stop band in the range 0.2–32.9 nm for the Bragg stacks at ambient relative humidity. In addition, we can design dense

multilayer systems nonresponsive to humidity and achieve time responses of the porous systems to external changes in humidity ranging from about 1 to 3 s.

3.3.1. INTRODUCTION

The development of periodic dielectric nanostructures, i.e., photonic crystals (PCs), with tailored optical and built-in chemical properties has recently been brought to fruition by the materials science and photonics communities.[1,2] The photonic stop band, a characteristic region of high reflectivity in the optical spectrum manifesting itself in "structural color", provides ample possibilities for the design of tunable optical systems.[3] A variety of stop-band tuning mechanisms along with promising synthetic routes towards the fabrication of stimuli-responsive PCs have been reported.[4] Widespread interest in the production of tunable photonic nanostructures is due to potential applications in fields as diverse as sensor design,[5] micro-optics,[6] optofluidics,[7] medical diagnostics,[8] color displays,[9] food and water quality control,[10] and many others. One of the proposed photonic stop-band tuning scenarios employs materials featuring responsiveness to an external temperature change, such as hydrogels,[11,12] microgels,[13] polyglycidol – polystyrene core – shell particles,[14] magnetic fluids,[15] liquid-crystal elastomers,[16] or $BaTiO_3$[17] through the thermo-optic effect (TOE).[18] The principle of thermo-optic spectral tuning is based on the thermo-optic coefficient (TOC), namely, the dependence of the refractive index (n) on temperature (T) and, hence, *dn/dT*, owing to both changes of the dielectric function and thermal expansion/contraction. Thermo-optic photonic stop-band tuning has already been successfully demonstrated in microring resonators,[19] thermooptic switches,[18] and wavelength-division multiplexing.[20,21] Substantial interest has arisen from the thermo-optic tuning realized with one-dimensional systems, i.e., periodic multilayer structures with a modulation of the dielectric constant in one direction, such as thermally tunable multilayer optical filters,[22] and monolithic microcavities[23] deposited by complex physical vapor deposition (PVD) methods. Interestingly, owing to the recent progress in synthetic chemistry, sputtered and evaporated PCs may be complemented by lower cost and easier to fabricate analogues (sol–gel processed onedimensional PCs, also called Bragg stacks (BSs)) without a significant loss in the optical quality.[24,25] Although one of the main problems in the fabrication of sol– gel coatings in general and of multilayers in particular is the stress induced during heat treatment of the layers leading to defects and cracks in the films, an ample amount of recent publications

successfully dealt with the optimization of the fabrication routes to achieve better optical and mechanical quality films and BSs.[26] In contrast to the PVD-deposited PCs, synthetic BSs offer a plethora of modification possibilities towards enhancing or modifying their environmental response, for example, by varying the nanomorphology (denoted further as "morphology") of the individual layers, i.e., the texture, porosity, curvature, size, and shape of the particles or monoliths constituting the layers. [27,28] While the influence of the BSs' morphology on the stop-band tuning of wet-chemistry synthesized TiO_2/SiO_2 BSs induced by chemical stimuli has already been examined,[29–33] a comprehensive study of the interrelation between morphology and shift in thermoresponsive sol– gel processed BSs has not yet been performed.

Recently, we demonstrated the thermal tunability of nanoparticle-based TiO_2/SiO_2 BSs fabricated by a spincoating method.[34] It was shown that the shift of the stop band due to the thermo-optic effect in the constituent materials in such systems is amplified in the presence of ambient humidity: The observed enhancement of the shift is due to adsorption of water molecules into the interparticle voids in the layers, causing an increase in the effective refractive index (RI) of the layers. Therefore, one can introduce an effective thermo-optic effect including both thermal and humidity influences on the effective RI. Furthermore, we simulated the influence of the layer thickness, refractive index, and thermo-optic coefficient on the thermal response of various BS architectures to work out design criteria for optimizing the thermal tuning performance of the BSs.[35]

The general goal of our present study is to rationally design photonic crystals that are tunable by both the inherent thermooptic effect of the constitutent materials and by concurrent temperature-dependent adsorption of humidity into the multilayer system. As the latter is highly sensitive to the porosity of the layers, this aspect of the layer morphology will be central to our experimental focus. In this manuscript, we demonstrate the influence of the morphology of the constituent layers on the thermal tuning properties of various one-dimensional TiO_2/SiO_2 BSs. We show that the layer morphology is one of the key factors to be taken into account when designing tailor-made thermally tunable BSs. Towards this end, the BSs were fabricated by different sol–gel synthesis schemes, ranging from nonporous wet-chemistry-processed nanostructures to porous systems, that is, nanoparticle-based optical filters exhibiting textural porosity, and evaporation-induced self-assembled mesoporous Bragg stacks exhibiting predominantly structural porosity, as well as hybrid structures comprising both dense and porous layers. The thermo-optic response of these systems is interpreted and rationalized by comparison

with the thermal response of a nonporous, PVD-derived optical filter. We also present a comparative study of the response and recovery times of the proposed structures and demonstrate that the fabrication method can serve as a design criterion for producing tailor-made photonic crystals with desired thermal response under ambient conditions.

3.3.2. EXPERIMENTAL

Materials

Tetraethyl orthotitanate (TEOT, 99%) and tetraethyl orthosilicate (TEOS, 99%) were purchased from Merck (Darmstadt, Germany); ethanol (99%), n-butanol (99%), colloidal silica LUDOX SM-30 (30 wt % in H_2O), and Pluronic F127 and P123 were purchased from Sigma-Aldrich (Dorset, UK); HNO_3 (0.1 mol/L) was purchased from Acros Organics (Geel, Belgium); and HCl (0.1 mol/L, 2 mol/L, 37%) was obtained from Biesterfeld (Hamburg, Germany).

Titania nanoparticle (NP) suspension was prepared as described elsewhwere.[34] Particle size distribution of the precursor TiO_2 and SiO_2 suspensions was analyzed using dynamic light-scattering photocorrelation spectroscopy (Malvern Nano ZS Zetasizer) at 20 °C. Silica sol for TiO_2-NP/SiO_2-sol and TiO_2-sol/SiO_2-sol BSs was prepared by mixing TEOS, ethanol, and HCl in a ratio of 1:10:1 and 2:10:2, respectively, and subsequent ageing for 12 h. Titania sol (0.1 mol/L) for TiO_2- sol/SiO_2-sol BSs was prepared by mixing TEOT (0.228 g) in ethanol (10 mL) with subsequent ageing until the desired optical quality of spin-coated thin films was reached. To synthesize the mesoporous silica sol (meso-SiO_2), TEOS (3.12 g) was diluted in ethanol (19 mL) with the subsequent addition of surfactant Pluronic F127 (1.5 g), HCl (0.15 g, 2 mol/L), and H_2O (1.35 mL). The mixture was stirred for 5 min until it became translucent and was subsequently aged for 1 h. To prepare the mesoporous titania sol (meso-TiO_2), TEOT (2.1 g) was diluted in n-butanol (7.4 mL) with Pluronic P123 (0.65 g) and HCl (1.35 mL, 37%). The solution was stirred vigorously for 5 min and afterwards aged for at least 1 h. All suspensions were filtered prior to use (Acrodisc, GHP, 13 mm, 0.2 m). The anatase modification of the TiO_2 powder calcined at 350 °C for 1 h was confirmed by X-ray diffraction (Bruker D8 Discover).

Bragg stack fabrication

Evaporated dense TiO₂/SiO₂ BSs

The dense TiO_{2-x}/SiO_{2-x} multilayers were deposited in a Pfeiffer Vacuum Classic 500 evaporation system in vacuum ($<2 \times 10^{-6}$ mbar; 1 bar = 100 kPa) onto soda-lime glass substrates at room temperature starting from the TiO_{2-x} layer. The TiO_{2-x} layers were evaporated by using an electron gun. The SiO_{2-x} layers were evaporated by using resistive heating of SiO_2 contained in a molybdenum boat. The deposition rate for both materials was approximately 0.2 nm s^{-1}, which was monitored, as well as the layer thicknesses, in situ by a quartz crystal microbalance (QCM). The alternation of the layers was achieved by shuttering the flux of the corresponding layer. The oxygen content in the multilayers was reduced because of deposition in vacuum; therefore, further annealing in an oxygen atmosphere for 1 h at 450 °C was performed to recover the stoichiometry and optical properties of the multilayers.

TiO₂/SiO₂ BSs based on sol– gel fabrication methods

We obtained TiO_2-sol/SiO_2-sol BSs by sequential spincoating of silica sol (3000 rpm, 1500 rpm s^{-1}) and titania sol without calcination. For the titania sol (0.1 mol/L), we performed triple spin-coating (4000 rpm, 2000 rpm s^{-1}) until the necessary film thickness was achieved. Nanoparticle-based (NP-based) BSs were prepared by spin-coating as described elsewhere.[34] TiO_2-NP/SiO_2-sol BSs were prepared by sequential spin-coating of a titania NP suspension (3000 rpm, 1500 rpm s^{-1}) and silica sol (3000 rpm, 1500 rpm s^{-1}) with subsequent calcination of the films at 200 °C for 15 min. Similarly, TiO_2-sol/meso-SiO_2 BSs were fabricated by spincoating mesoporous silica (2500 rpm, 2000 rpm s^{-1}) and titania sol (0.05 mol L^{-1}, 3000 rpm, 2000 rpm s^{-1}). Mesoporosity was generally achieved by taking advantage of the evaporation induced self-assembly (EISA) method and through subsequently removing the surfactant *via* calcination of the films at 400 °C for 15 min. Meso-TiO_2/meso-SiO_2 were obtained by spin-coating mesoporous titania (5000 rpm, 2000 rpm s^{-1}) and mesoporous silica (5000 rpm, 2000 rpm s^{-1}). The single thin film thickness and refractive index were characterized by spectroscopic ellipsometry, performed on a Woollam M200D variable angle ellipsometer in the entire spectral range of 190–1000 nm at angles of incidence of 65°, 70°, and 75°. To calculate the porosity of the layers the Lorentz–Lorenz equation was

used, for which the RIs of the single films were measured first with void pores and then with the pores filled with toluene. Scanning electron microscopy (SEM, JEOL JSM-6500F operating at an accelerating voltage of 2–5 kV) was used to examine the morphology of the BSs' cross sections and flat surfaces.

Thermo-optic and humidity response characterization

To obtain transmission spectra of the BSs in the range of 400–800 nm we used a monochromator (Cornerstone260 1/4 m) with a high-pressure arc lamp as a light source and a 10 x 10 mm^2 calibrated silicon detector connected to a digital lock-in amplifier (Merlin).[34] The temperature of the BS was varied by two Peltier elements and the PT100 temperature sensor was attached to the other side of the BS above the optical axis. Peltier elements and the temperature sensor were connected to a remote-controlled source meter (Keithley). The heating and cooling of the Peltier elements were regulated by a proportional integral derivative (PID) controller. The measured deviation of the temperature during the measurement was less than 0.1 °C. For each temperature the sample was equilibrated for 60 s. The measurements in N_2 atmosphere (to mimic 0% relative humidity) were performed in a cryostat with two windows, in which the samples of interest were kept for 24 h prior to the measurements.

For the response and recovery time characterization we changed the relative humidity (RH) of the environment (20%) by introducing water vapor onto the sample surface. The tubing with the nitrogen stream carrying the water vapor was mounted above the surface of the BS. The measured RH of the vapor was 65%. Additionally, the valve located on the tubing allowed the instant turning off of the vapor stream. In a typical experiment, the BS was fixed under an optical microscope such that the measurement spot could be constantly monitored. Time-dependent spectroscopy was performed with a fiber optic spectrometer (Ocean Optics USB2000) integrated with an optical light microscope (Leica DM2500 M).

3.3.3. RESULTS AND DISCUSSION

Photonic multilayer systems fabricated by PVD feature inherently dense oxide layers (Figure 3.3.1) and can therefore be taken as a nonporous reference system for our comparative study of the thermo-optic tuning behavior. Evaporated TiO_2/SiO_2 multilayers have been extensively examined as all-dielectric

optical filters for passive optical elements [36,37] and therefore represent an excellent "classical" platform for the comparison with BSs obtained by wet-chemistry methods. Photographs of the evaporated BS samples, deposited under the same conditions, are shown in Figure 3.3.1a: The top image presents a BS on a Si wafer, captured at an angle of $\approx 45°$ with respect to the normal to the BS's surface, and the bottom image shows a BS on a glass substrate, captured normal to the BS's surface. As can be seen in Figure 3.3.1a, such BSs are almost defectless, however, their optical properties, including RI and absorption properties, are highly dependent on the deposition method and annealing conditions.[38] The cross-sectional SEM image in Figure 3.3.1b depicts a BS composed of 8.5 bilayers (BLs) of 60 nm TiO_2 ($n \approx$ 2.41) and 90 nm SiO_2 ($n \approx 1.55$). The maximum transmission of the BS annealed in air at 450 °C for 1 h to annihilate oxygen vacancies is around 50%. It is known that films deposited by PVD show a columnar microstructure with intercolumnar voids leading to inhomogeneities and roughness. [36,39] Nevertheless, the high RIs obtained for electron beam (e-beam) evaporated TiO_2 and thermally evaporated SiO_2 by spectroscopic ellipsometry are testament to their overall low porosity. Note, however, that the RI of SiO_2 may likewise be rationalized by the presence of residual substoichiometric oxide species (SiO_{2-x}) in the film. The impact of textural porosity on the thermo-optic response of the BS can be derived from the dependence of the optical shift on the environmental humidity as seen in Figures. 3.3.1c and 3.3.1d. Clearly, the magnitude of the thermal shift at 55% RH (0.49 nm) is higher than at 25% RH (0.39 nm) upon an increase in temperature from 15 to 60 °C, which can be rationalized by the effective TOC enhanced by the penetration of ambient humidity into the textural pores of the BS.

To put the humidity-enhanced thermo-optic response of the PVD-derived BS into perspective, we compare it with the response of solution-processed, spin-coated BSs with the same average layer thicknesses (the thickness of spin-coated BSs can deviate about 10%–20% on average) and number of bilayers (8.5), but composed of TiO_2 and SiO_2 NP layers. An intrinsic property of the NP-based BSs is textural porosity (porosity arising from interparticle voids in the film). With the measured NP size distributions (6–10 nm for SiO_2 and 8–20 nm for TiO_2 NPs) one can obtain films with 10% and 25% porosity for SiO_2 and TiO_2, respectively.[34] First, we investigated the thermo-optic response of the PVD-derived and porous NP-based BSs decoupled from the influence of ambient humidity. Consequently, in this experiment one can derive the shift of the stop band caused solely by the impact of the TOE. Figures 3.3.2a and 3.3.2b highlight the thermo-optic response of the samples kept in a nitrogen atmosphere for 24 h prior to the experiment. Clearly, the evaporated BS shows a small shift of 0.2 nm upon heating from

15 to 60 °C, whereas the NP-based BS shows a fairly linear thermo-optic response of 1.0 nm, which is in agreement with the theoretical value of the thermo-optic shift in this temperature range based on the TOCs reported for titania and silica, respectively.[34] We assume that the smaller shift observed for the evaporated BS is due to the TOCs of the layer materials being slightly different from the literature values for TiO_2 [40] (1.77×10^{-4} K^{-1}) and SiO_2[41] (1×10^5 K^{-1}) owing to the presence of substoichiometric oxide species (TiO_{2-x} and SiO_{2-x}) in the multilayer.
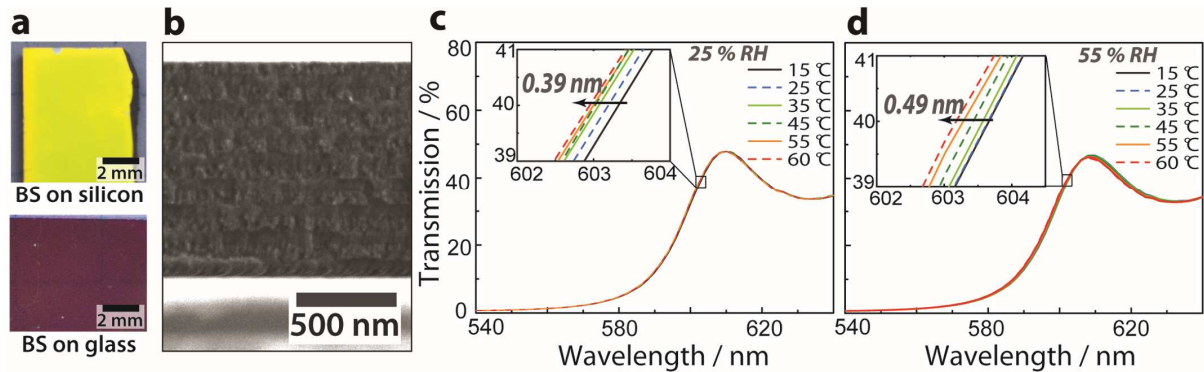

Figure 3.3.1. (a) Photographs of the electron beam (e-beam) evaporated TiO_2 (60 nm) and thermally evaporated SiO_2 (90 nm) 8.5 bilayer (BL) Bragg stack (BS) (starting from the first TiO_2 layer) deposited on a Si wafer (top image: captured at an angle) and on a glass substrate (bottom image: captured normal to the BS surface). The scale bar is 2 mm. (b) The cross-sectional SEM image of the evaporated BS from 1a (bottom). The scale bar is 500 nm. (c) Transmission spectra of the BS shown in 1a (bottom) featuring a blue shift of the stop band of ≈ 0.39 nm in a temperature range of 15 to 60 °C at 25% relative humidity (RH). (d) Transmission spectra of the same BS as in 1c demonstrating a slightly larger blue shift of the stop band (≈ 0.49 nm) in a temperature range of 15 to 60 °C at 55% RH.

To demonstrate the humidity-enhanced thermal tunability of the NP-based BS, we performed similar measurements inambient humidity (25% RH). One can discern a humidity-amplified blue shift of 4.4 nm owing to the effective TOE, which is about four times larger than in N_2 atmosphere (Figures 3.3.2c). This observation suggests a significant difference in the porosity of the solution-processed and thermally evaporated BSs. Specifically, the higher textural porosity of the NP-based BS renders it more accessible to water, thus leading to a more pronounced humidity enhancement of the thermal shift.

Having discussed two model systems with different porosities and, hence, thermal response behavior, it is instructive to explore alternative, yet solution-based routes to low-porosity BS architectures that can "mimic" the low-response thermooptic behavior of evaporated BSs. In Figures 3.3.3a, 3.3.3d, and 3.3.3g, we demonstrate the tuning properties of a BS fabricated by alternate spin-coating of titania and silica sols. As can be inferred from the SEM image (Figure 3.3.3a), the 4 BL TiO_2-sol/SiO_2-sol BS apparently

has a rather dense morphology. Low porosity of the layers is also confirmed by the thermal tuning behavior presented in Figure 3.3.3d at ambient humidity. Notably, the shift of the stop band is only 0.8 nm upon heating from 15 to 60 °C. Evidently, the magnitude of the effective thermal shift of the TiO_2-sol/SiO_2-sol BS is only slightly larger than the one of the PVD-derived BS at 25% RH (0.39 nm, Figure 3.3.1c). The low RI and at the same time the low response to temperature changes may be in part due to organic residues within the sol– gel based structure rendering the BS more hydrophobic, as no calcination was done after film deposition (see the Experimental section).
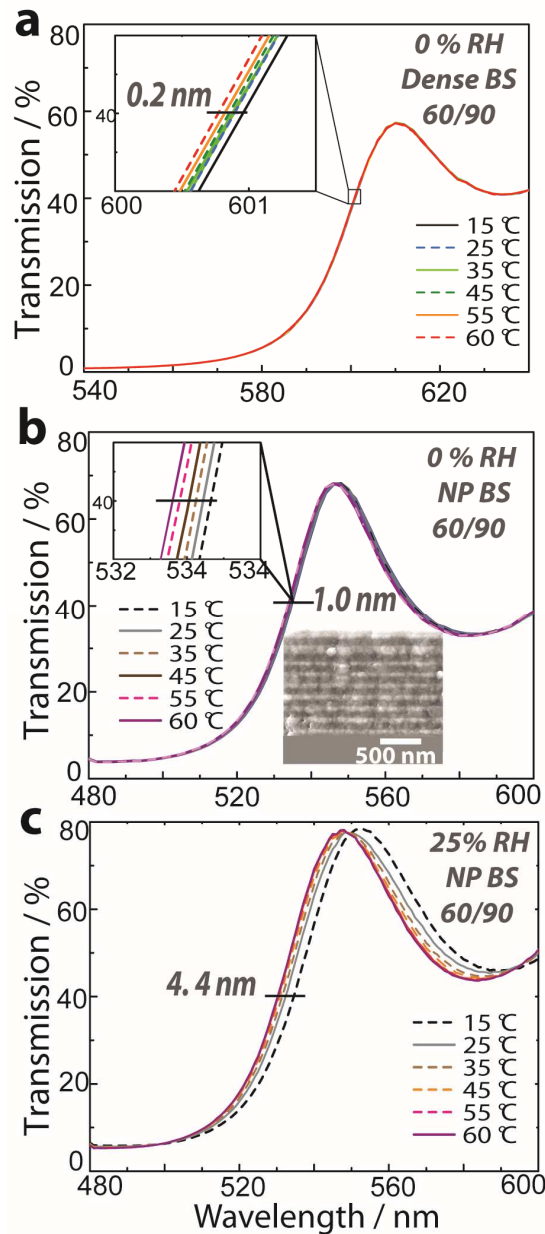
Figure 3.3.2. (a) Transmission spectra of the evaporated Bragg stack (BS) shown in Figure 3.3.1a (bottom) demonstrating a small blue shift of the stop band of ≈0.2 nm upon heating from 15 to 60 °C in N_2 atmosphere. (b) Transmission spectra of the nanoparticle (NP)- based TiO_2/SiO_2 8.5 bilayer (BL) BS featuring a blue shift of the stop band of ≈1.0 nm upon heating from 15 to 60 °C in N_2 atmosphere. The inset shows the cross-sectional

SEM image of the corresponding BS. The scale bar is 500 nm. (c) Transmission spectra of the BS from Figure 3.3.2b recorded under ambient conditions (25% RH) in the T range of 15 to 60 °C. (From Pavlichenko et al.[34] © 2012 American Chemical Society.)

In contrast, a much higher thermal response is observed for hybrid systems in which one of the layers is kept dense, while the other possesses textural or structural porosity, as is the case for NP-based and mesoporous layers, respectively (Figures. 3.3.3b and 3.3.3c, respectively). As can be seen from Figures 3.3.3e and 3.3.3f, both systems exhibit a significant response to heating under ambient conditions. The blue shift of a TiO_2-NP/SiO_2-sol is 8.9 nm for the blue and 20.0 nm for the red edge of the stop band, and the responses of TiO_2-sol/meso-SiO_2 BSs are 32.0 and 19.8 nm for the blue and red edges of the stop band, respectively. The shifting behavior of both systems is in good agreement with previous predictions relating the relative changes of the blue and red edges of the stop band to the RI changes taking place primarily in one type of layer in the bilayer system.[27,35] (i) The larger magnitude of the shift for the red edge of the stop band in the TiO_2-NP/SiO_2-sol system suggests that the high RI material TiO_2 undergoes the dominant RI changes; hence, we conclude that the water mainly adsorbs in the porous TiO_2–NP layers rather than in the dense SiO_2-sol ones. (ii) The transmission of the stop band is higher at higher T, indicative of a gradual lowering of the RI contrast of the layers with increasing T, suggesting that upon heating water desorbs mainly from the TiO_2 layers, thus reducing their RI and, hence, the overall RI contrast. These phenomena illustrate the predominant influence of TiO_2 on the thermal response. On the contrary, the change of the stop band for the TiO_2-sol/meso-SiO_2 BS is larger at the red edge and the transmission is lower at higher temperatures, highlighting the dominant influence of porous SiO_2 rather than dense TiO_2, as water seems to condense primarily into the silica layers.

Next, we compared the tuning properties of the porous hybrid systems with their nonhybrid analogues, in which both layers are comprised of either NPs or mesoporous materials, namely, with the TiO_2-NP/SiO_2-NP BS (Figure 3.3.2c) and a meso-TiO_2/meso-SiO_2 3 BL BS (Figure 3.3.4a). The thermal shift (20.1 nm for the red edge of the stop band) of the hybrid TiO_2-NP/SiO_2-sol BS in the T range between 15 and 60 °C at 30% RH is larger than for the nonhybrid TiO_2-NP/SiO_2-NP system (4.4 nm at 25% RH and 16.4 nm at 45% RH). The higher response of the hybrid system compared with the TiO_2-NP/SiO_2-NP stack may be due to more restricted moisture diffusion into the latter owing to the larger number of BLs, rendering the multilayer system more compact and less accessible to moisture. Along similar lines, for the TiO_2-sol/meso-SiO_2 BS the thermal shifts between 15 and 60 °C (32.0 and 19.8 nm for the blue and red edges, respectively) are larger than the 20.9 nm (blue edge) and 13.1 nm (red edge) shifts for the

meso-TiO$_2$/meso-SiO$_2$ BS shown in Figure 3.3.4b. The observed behavior may be rationalized by the differences in layer thicknesses and hence the relative impact of the more porous layers on the adsorption behavior: higher porosity films of SiO$_2$ were obtained with the triblock copolymer F127 used as a template (Figure 3.3.5a), resulting in nanometer-sized channels (~10 nm) organized into two-dimensional (2D) hexagonal domains parallel to the substrate, as also observed previously.[42] In contrast, P123-templated TiO$_2$ (Figure 3.3.5b) forms pores with an average size of 5 nm,[43] which is about half the size of the SiO$_2$ pores. Therefore, the larger porosity of SiO$_2$ together with the larger layer thickness of the SiO$_2$ layers in the sol−meso BS compared to the meso−meso BS is the most likely rationale for the larger thermal response observed for the sol−meso BS. Other factors may be fluctuations in ambient humidity, the mutual influence of adjacent layers (of higher and lower porosity) and their pore sizes and texture on the confinement and transport of moisture within the multilayer,[26,28] as well as other phenomena such as pore blocking at the interfaces and capillary and surface wettability effects that are naturally augmented in complex nanomorphologies.
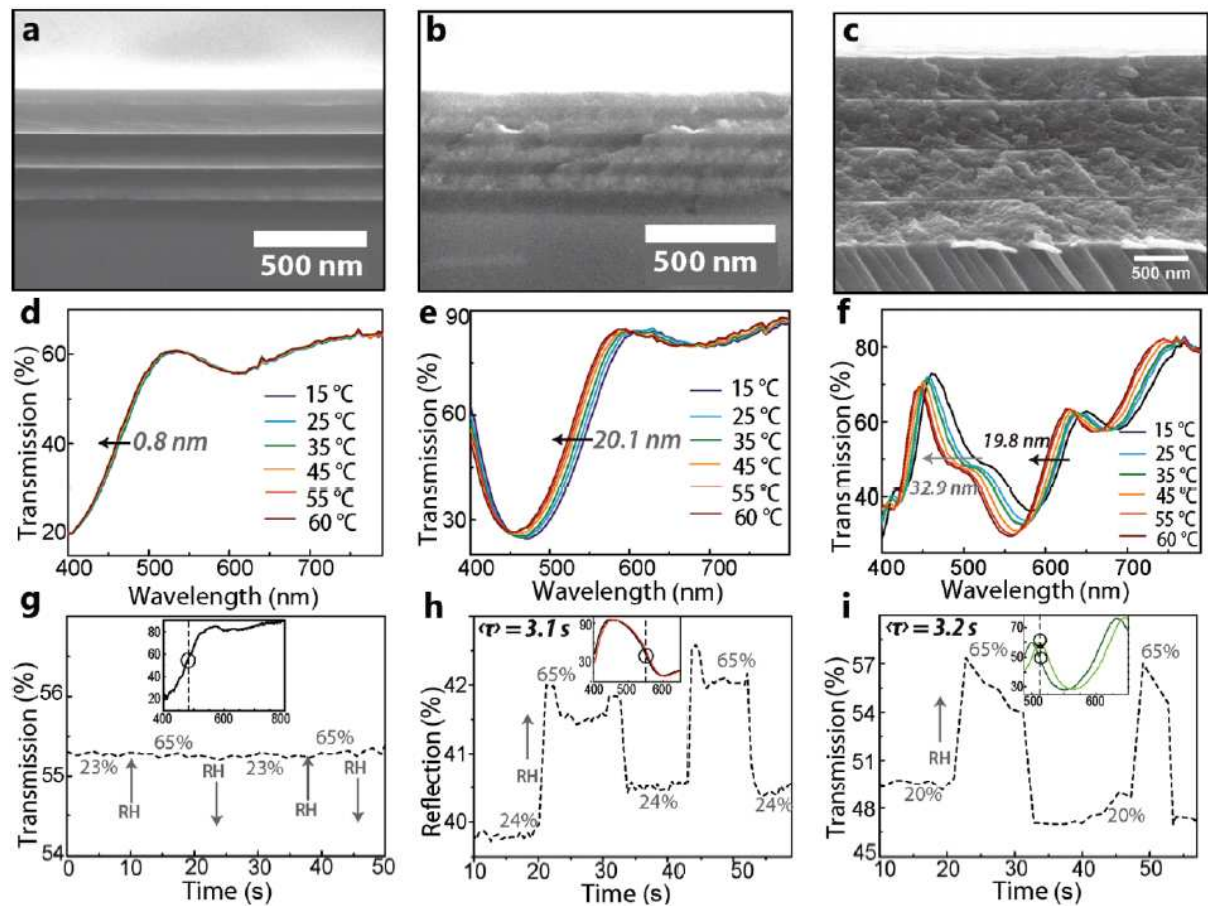

Figure 3.3.3. Cross-sectional SEM images of (a) TiO$_2$-sol (55 nm, RI 1.92)/SiO$_2$-sol (90 nm, RI 1.46) 4 BL BS, (b) hybrid TiO$_2$-NP (60 nm, RI 1.90)/SiO$_2$-sol (80 nm, 1.46) 4 BL BS, and (c) hybrid TiO$_2$-sol (55 nm, RI 1.92)/meso-SiO$_2$ (450 nm, RI 1.16) BL BS. The scale bar is 500 nm. (d)–(f) Transmission spectra corresponding to (a)–(c),

demonstrating various magnitudes of the thermal shift of the stop band in a temperature range of 15 to 60 °C at 25% RH. (g) and (i) Time-resolved transmission and (h) reflection changes in response to the change in RH from ≈20% to 65%; <τ> is the response time. The inset graphs show the reflection and transmission spectra of the BS demonstrating the change in transmission at (g) 480 nm and (i) 512 nm, and reflection at (h) 550 nm corresponding to the RH change from ≈20% to 65%.

To analyze the kinetics of the environmental response (i.e., separated from the pure thermo-optic response) and the possible impact of the layer morphology on the response time, we investigated the behavior of the multilayer systems with respect to changes in ambient humidity, while keeping the temperature constant. Time-resolved measurements were carried out by detecting changes in the reflection/transmission spectrum occurring during the instantaneous change in RH of the environment, from ≈20% to 65%. The change in reflection/ transmission was monitored at fixed wavelengths. Note that only the initial shifts right after the RH increase or decrease were recorded, while subsequent slower processes, e.g., owing to diffusion of humidity within the multilayer stacks, were neglected. Therefore, the response times only reflect the principal accessibility of the outer surfaces of the multilayer system.
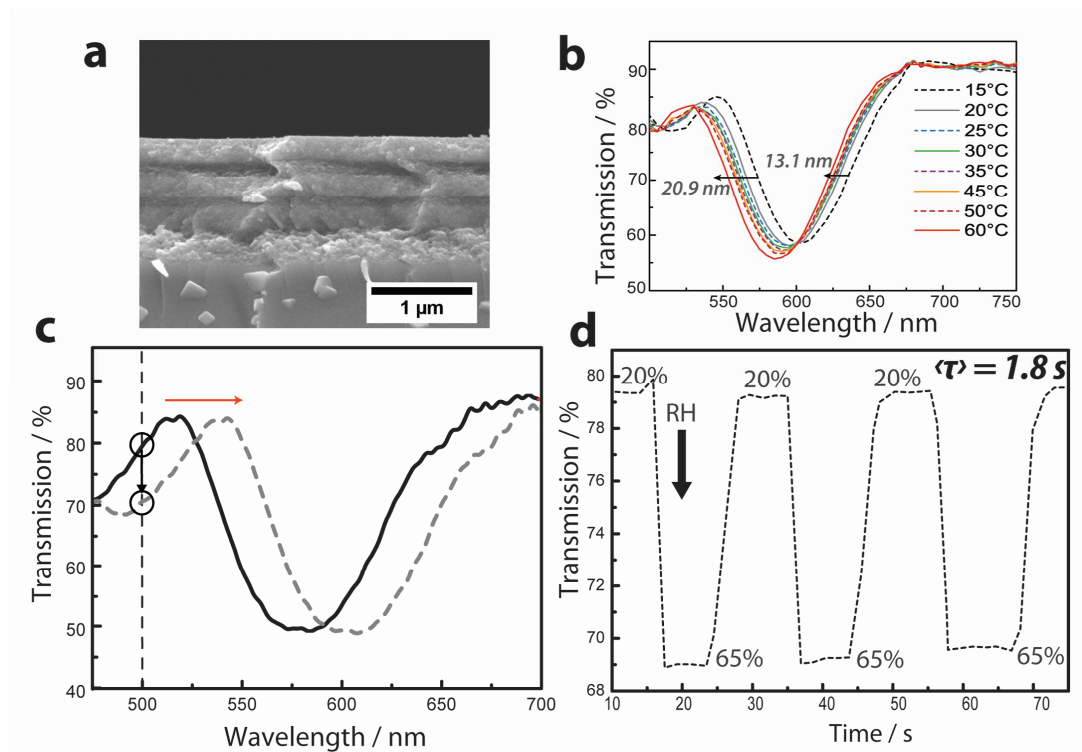
Figure 3.3.4. (a) Cross-sectional SEM images of the meso-TiO$_2$ (220 nm, RI =1.59)/meso-SiO$_2$ (140 nm, RI = 1.16) 4 BL BS. The scale bar is 1μm. (b) Transmission spectra of a BS shown in (a) showing a blue shift of the left stop band edge of ≈20.9 nm and of the right stop band edge of ≈13.1 nm in the temperature range between 15 and 60 °C at 30% RH. (c) Transmission spectra of the BS in (a) demonstrating the change in transmission at 500 nm corresponding to the relative humidity change from 20% to 65%. (d) Time-resolved transmission change in response to the change in RH from 20% to 65%; <τ> is the response time.

Comparison of the response times (given as $<\tau>$) to humidity changes for the two dense systems (TiO_2-sol/SiO_2-sol and PVD-derived BS) shows a peculiar difference: The dense sol-based BS shows a complete lack of response to humidity change (Figure 3.3.3g), whereas the response of its classical evaporated counterpart occurs promptly (1.3 s), albeit being associated with only a minor shift of 0.5 nm. The absence of response to the transient humidity changes for the sol–sol BS may be due to the larger hydrophobicity of the noncalcined layers and concomitant slow diffusion of water within the multilayer system. The porous systems with similar layer morphologies show rather fast response times, $<\tau>$, which are around 1.5–2 s for the NP–NP BS as reported earlier [35] and ≈1.8 s for the meso–meso BS (Figures 3.3.4c and 3.3.4d). The response times of the hybrid BSs are somewhat larger than those of the NP–NP, meso–meso, and dense PVD-BSs: The $<\tau>$ are around 3 s for both multilayer systems (Figures 3.3.3h and 3.3.3i). Although there is no clear trend discernible, fast response times may be triggered by (i) low accessibility of the layers to ambient humidity as seen for the PVD-BS, presumably resulting in surface rather than bulk condensation of water, and (ii) fast percolation of water within the porous layers as in the meso–meso BS. The overall shifts induced right after the humidity change are a testament to both the porosity and the connectivity of the water percolation pathways within the multilayer systems: The magnitude of the red shift increases in the order dense/sol (0 nm) < dense/PVD (≈0.5 nm) < sol–NP (≈5 nm) < NP–NP (≈8 nm) < sol–meso (≈12 nm) < meso–meso (≈25 nm), thus reflecting the increasingly porous and interconnected layer morphologies along this series, which is consistent with the observations made previously. The somewhat lower and more sluggish humidity-induced shifts observed for the hybrid systems compared with their thermal response can be rationalized by the fact that the dense layer is mediating the humidity response of the system, thus preventing fast penetration of moisture into the multilayer. In terms of BS design criteria, an optimally fast and strong effective thermo-optic response can be seen in porous multilayer systems with the same morphologies, such as fully NP-based or meso BSs.
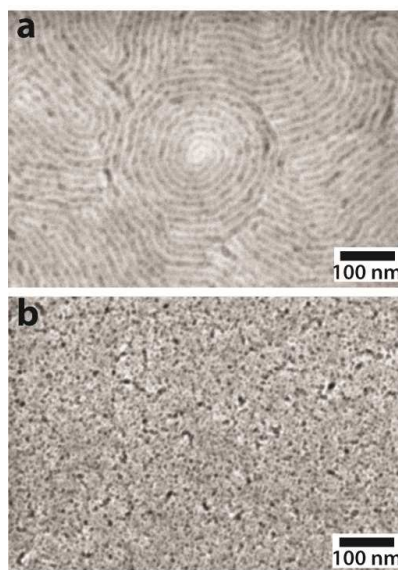
Figure 3.3.5. Top-view SEM images of mesoporous (a) silica and (b) titania films.

3.3.4. CONCLUSION

We have studied the influence of the nanomorphology on the effective, i.e., humidity-enhanced thermo-optic response of different TiO_2/SiO_2 BSs: PVD-derived and sol– gel BSs both show relatively small blue shifts of 0.39 and 0.80 nm, respectively, upon heating of the system from 15 to 60 °C at ambient relative humidity. This similarity in the optical response suggests low textural porosity in both systems, thus rendering the solution-processed sol–gel multilayer an excellent substitute for the classical low-response optical filters deposited by PVD. Alternatively, we have shown that a low thermo-optic response (1 nm as compared with 4.4 nm at 25% RH) even for porous architectures can be realized by excluding ambient humidity, equivalent to encapsulation of the system. Analysis of the effective thermo-optic response of hybrid systems composed of both dense and porous layers as well as that of an all-meso BS reveals large optical shifts attributable to a higher degree of textural porosity and accessibility of the system compared with the dense PVD and sol-based counterparts. Furthermore, the impact of morphology on the response and recovery times of the proposed systems to abrupt changes in humidity from ≈ 20% to 65% was studied. The fastest kinetics were observed for systems with the same layer morphologies (1.3 s for the evaporated, 1.5–2.0 s for the nanoparticle-based and 1.8 s for the meso BS), whereas the response of the hybrid sol–NP (3.1 s) and sol–meso (3.2 s) systems takes somewhat longer. Low or even complete insensitivity towards humidity was observed for PVD- and sol-derived BSs owing to their low degree of textural porosity, combined with larger hydrophobicity of the noncalcined layers in the sol–sol configuration. These observations point to a substantial tunability of the overall thermo-optic response

as well as the response kinetics through the choice of the fabrication method and, thus, the resulting morphology of the layers. As a perspective, the multilayers presented in this study lend themselves well as general model systems with precisely controlled porosities and types of curvatures, which can translate the adsorption of arbitrary fluids under ambient conditions into a visibly perceptible optical readout.

ACKNOWLEDGEMENT

3.3.5. BIBLIOGRAPHY

(1)   Bonifacio, L. D.; Lotsch, B. V.; Puzzo, D. P.; Scotognella, F.; Ozin, G. A. *Adv. Mater.* **2009**, *21*, 1641.

(2)   Aguirre, C. I.; Reguera, E.; Stein, A. *Adv. Funct. Mater.* **2010**, *20*, 2565.

(3)   Joannopoulos, J. D.; Villeneuve, P. R.; Fan, S. *Nature* **1997**, *386*, 143.

(4)   Ge, J.; Yin, Y. *Angew. Chem. Int. Ed.* **2011**, *50*, 1492.

(5)   Nair, R. V.; Vijaya, R. *Prog. Quantum Electron.* **2010**, *34*, 89.

(6)   Friese, C.; Werber, A.; Krogmann, F.; Mönch, W.; Zappe, H. *IEEJ T. Electr. Electr.* **2007**, *2*, 232.

(7)   Hoi, S.-K.; Chen, X.; Kumar, V. S.; Homhuan, S.; Sow, C.-H.; Bettiol, A. A. *Adv. Funct. Mater.* **2011**, *21*, 2847.

(8)   Mano, J. F. *Adv. Eng. Mater.* **2008**, *10*, 515.

(9)   Wang, H.; Kerins, F.; Kamp, U.; Bonifacio, L.; Arsenault, A. C.; Ozin, G. A. *Information Displays,* **2011**, *7-8*, 1.

(10)   Bonifacio, L. D.; Ozin, G. A.; Arsenault, A. C. *Small* **2011**, *7*, 3153.

(11)   Kang, J.-H.; Moon, J. H.; Lee, S.-K.; Park, S.-G.; Jang, S. G.; Yang, S.; Yang, S.-M. *Adv. Mater.* **2008**, *20*, 3061.

(12)   Debord, J. D.; Lyon, L. A. *J. Phys. Chem. B* **2000**, *104*, 6327.

(13)   Li, G.; Pandya, P. D.; Seo, S. S. *Int. J. Polym. Anal. Ch.* **2009**, *14*, 351.

(14)   Griffete, N.; Dybkowska, M.; Glebocki, B.; Basinska, T.; Connan, C.; Maître, A.; Chehimi, M. M.; Slomkowski, S.; Mangeney, C. *Langmuir* **2010**, *26*, 11550.

(15)   Pu, S.; Bai, X.; Wang, L. *J. Magn. Magn. Mater.* **2011**, *323*, 2866.

(16)   Wu, G.; Jiang, Y.; Xu, D.; Tang, H.; Liang, X.; Li, G. *Langmuir* **2011**, *27*, 1505.

(17)   Soten, B. I.; Miguez, H.; Yang, S. M.; Petrov, S.; Coombs, N.; Tetreault, N.; Matsuura, N.; Ruda, H. E.; Ozin, G. *A. Adv. Funct. Mater.* **2002**, *12*, 71.

(18)   Coppola, G.; Sirleto, L.; Rendina, I.; Iodice, M. *Opt. Eng.* **2011**, *50*, 071112-1 -.

(19)   Shen, X.; Han, K.; Liu, H.; Li, H.; Tang, G. *Proc. Int. Workshop on Metamaterials* **2008**, 149.

(20)   Hohlfeld, D.; Epmeier, M.; Zappe, H. *Sensor. Actuator.* **2003**, *103*, 93.

(21)   Domash, L. H.; Ma, E.; Lourie, M.; Sharfin, W.; Wagner, M. *SPIE Proc.* 2003, ***4989***, 161-167.

(22)   Hohlfeld, D.; Zappe, H. *J. Opt. A- Pure Appl. Op.* **2004**, *6,* 504.

(23)   Regoliosi, P.; Guehl, M.; Scarpa, G.; Lugli, P.; Persano, L.; Del Carro, P.; Camposeo, A.; Cingolani, R.; Pisignano, D.; Bietti, S.; Grilli, E.; Guzzi, M. *Appl. Phys. Lett.* **2008**, *92*, 253310.

(24)   Calvo, M. E.; Colodrero, S.; Hidalgo, N.; Lozano, G.; López-López, C.; Sánchez-Sobrado, O.; Míguez, H. *Energy Environ. Sci.* **2011**, *4*, 4800.

(25)   Klein, L. C. *Annu. Rev. Mater. Sci.* **1993**, *23*, 437.

(26)   Barhoum, M.; Morrill, J. M.; Riassetto, D.; Bartl, M. H. *Chem. Mater.* **2011**, *23*, 5177.

(27)   Fuertes, M. C.; Colodrero, S.; Lozano, G.; Gonzalez-Elipe, A. R.;Grosso, D.; Boissiere, C.; Sanchez, C.; Soler-Illia, G. J. A. A.;Míguez, H. *J. Phys. Chem. C* **2008**, *106*, 3157.

(28)   Illia, G. S.; Fuertes, M. C.; Angelomé, P. C.; Marchi, M. C.; Troiani, H.; Luca, V.; Míguez, H. *J. Phys. Chem.* **2007**, 4-8.

(29)   Hidalgo, N.; Calvo, M. E.; Míguez, H. *Small* **2009**, *5*, 2309.

(30)   López-López, C.; Colodrero, S.; Raga, S. R.; Lindström, H.; Fabregat-Santiago, F.; Bisquert, J.; Míguez, H. *J. Mat.Chem.* **2012**, *22*, 1751.

(31)   Hidalgo, N.; Calvo, M. E.; Bellino, M. G.; Soler-Illia, G. J. A. A.; Míguez, H. *Adv. Funct. Mater.* **2011**, *21*, 2534.

(32)   Choi, S. Y.; Mamak, M.; von Freymann, G.; Chopra, N.; Ozin, G. A. *Nano Lett.* **2006**, *6*, 2456.

(33)   Colodrero, S.; Ocaña, M.; González-Elipe, a R.; Míguez, H. *Langmuir* **2008**, *24*, 9135.

(34)   Pavlichenko, I.; Exner, A. T.; Guehl, M.; Lugli, P.; Scarpa, G.; Lotsch, B. V. *J. Phys. Chem. C* **2012**, *116, 298.

(35)   I. Pavlichenko, A. T. Exner, P. Lugli, G. Scarpa, B. V. L. *J. Intell. Mater. Struct.* **2013**, *24*, 2203.

(36)   Sagdeo, P. R.; Shinde, D. D.; Misal, J. S.; Kamble, N. M.; Tokas, R. B.; Biswas, a; Poswal, a K.; Thakur, S.; Bhattacharyya, D.; Sahoo, N. K.; Sabharwal, S. C. *J. Appl. Phys. D. Appl.Phys.* **2010**, *43*, 045302.

(37)   Macleod, H. A. *Thin-Film Optical Filters, 4ᵗʰ ed.*; Boca Raton: CRC Press, **2010**.

(38)   Duyar, Ö.; Placido, F.; Zafer Durusoy, H. *J. Phys. D: Appl. Phys.* **2008**, *41*, 095307.

(39)   Tien, C.-L. *Appl. Surf. Sci.* **2009**, *256*, 870.

(40)   Gülşen, G.; Naci Inci, *M. Opt.Mater.* **2002**, *18, 373*.

(41)   Ghosh, G. Non-Cryst. *J. Solids* **1995**, *189*, 191.

(42)   Naik, S. P.; Yamakita, S.; Ogura, M.; Okubo, T. *Micropor. Mesopor. Mat.* **2004**, *75*, 51.

(43)   Tao, J.; Shen, Y.; Gu, F.; Zhu, J.; Zhang, J. *J. Mater. Sci. Technol.* **2007**, *23*, 513.

4. THERMO-OPTIC IMAGING SENSORS BASED ON TUNABLE 1D PHOTONIC CRYSTALS

Infrared (or thermal) imaging is one of the pivotal technologies in the realm of industrial and environmental monitoring, remote sensing, contact-free biomedical diagnostics and other applications. State-of-the-art commercial infrared imagers (thermographers) can be divided into two major categories: The first group of thermographers requires cryogenic cooling for the best signal-to-noise ratio, and the second one can function at room temperature. In spite of high detection performance, the fabrication of both types of imagers involves elaborate and expensive processing steps. Hence, the development of a novel thermo-optic imaging sensing platform utilizing photonic structures and featuring low power consumption and low fabrication costs is of paramount interest for various scientific and industrial communities.

The following chapter will focus on a novel thermo-optic detection principle based on the integration of the thermally tunable mesoporous TiO_2/SiO_2 1D photonic crystals discussed in detail in the previous chapter with organic and inorganic light emitting diodes (OLEDs and LEDs, respectively), and a high-resolution imaging array.

4.1. Low-Cost Thermo-Optic Imaging Sensors: A Detection Principle Based on Tunable One-Dimensional Photonic Crystals

Armin T. Exner*, Ida Pavlichenko*, Bettina V. Lotsch, Giuseppe Scarpa, and Paolo Lugli

* These two authors made an equal contribution

Abstract

Infrared (IR) sensors employing optical readout represent a promising class of devices for the development of thermographic imagers. We demonstrate an infrared radiation detection principle based on thermally tunable one-dimensional (1D) photonic crystals acting as optical filters, integrated with organic and inorganic light emitting diodes (OLEDs and LEDs, respectively). The optical filters are composed of periodically assembled mesoporous TiO_2 and SiO_2 layers. Due to the thermal tunability of the transmission spectrum of the optical filter, the intensity of light passing through the filter is modulated by temperature. The tuned spectrum lies in the visible region and, therefore, can be directly detected by a visible-light photodetector. The thermal response of the luminance of the OLED-photonic crystal ensemble is 3.8 cd m^{-2} K^{-1}. Furthermore, we demonstrate that the local temperature profile can be time and spatially resolved with a resolution of 530 by 530 pixel, thus enabling a potential application as an infrared imaging sensor featuring low power consumption and low fabrication costs.

4.1.1. INTRODUCTION

Infrared imaging is one of the paramount tools for a contact-free temperature measurement of solid and fluid systems in industrial and environmental processes, allowing for a plethora of applications for diagnostics in material and biomedical sciences.[1,2] Hitherto, various approaches have been proposed to realize infrared sensors, among which two subcategories have won major recognition: (i) photoelectric detectors and (ii) thermal detectors.[3,4] Photoelectric detectors convert incident infrared (IR) radiation into electrical charge through the internal photoelectric effect. These detectors exhibit the best signal-to-noise ratio and a fast response; however, they require cryogenic cooling, which adds up on their size, weight, and cost.[3,5,6] Besides, the typical materials for photoelectric IR sensors include semiconductors such as PbS, PbSe, InAs, InSb, PbSnTe, InGaAs, and most prominently the ternary alloy HgCdTe, which is epitaxially grown in high vacuum with photolithographic masking and etching processing steps, which additionally makes its realization complex and expensive.[7] The second category—thermal detectors—absorb IR radiation, which in turn produces a change in a specific physical property of a material, as in, for example, resistive bolometers or pyroelectric detectors.[8] Thermal detector technology exploits semiconducting materials[9] or thermally sensitive resistors, which exhibit a temperature coefficient of resistance ($\Delta R/\Delta T$) of about 4% per degree celcius.[10] Typical representatives are transition metal oxides such as VO_2, V_2O_5,[10-12] Mn_3O_4, NiO, and CoO,[7-10] polycrystalline silicon–germanium alloy ($polySi_{0.7}Ge_{0.3}$),[13] or micromachined bimetallic cantilevers.[14] Thermal detectors do not require cryogenic cooling and, therefore, are facile to use and have lower overall system costs.[15,16] Nonetheless, thermoresistive detectors require complicated etching techniques and membrane transfer bonding techniques, which implies many processing steps.[17, 18] The sensitivity of a thermal detector is limited by the response of the active material and the overall noise of the system. In general, one needs materials where at least one parameter displays strong temperature dependence, as, for example, the electric resistance in the case of microbolometers.[19] Then, measurements *via* integrated electronics can be performed.[20]

Another possible approach exploits the changes in optical parameters of the sensitive element, e.g. its refractive index (RI), and, as a consequence, in its transmission/reflection properties. Such changes are readable by an optical setup or even by the bare eye. This principle may trigger the emergence of various IR sensor designs utilizing photonic structures, which would perform infrared thermography based on

the "wavelength conversion" of IR radiation into light intensity changes in the visible range. The development of a new thermo-optic imaging technology can significantly decrease the system cost by eliminating a dedicated electronics readout and multistep fabrication routines.[19] The price of a state-of-the-art bolometric IR camera currently reaches ≈30,000 USD (T620, FLIR IR camera) for a system with 0.3 megapixel resolution and is, therefore, a limiting factor for the application range of IR thermograpy.

Notably, the concept of optical readout for IR sensors has been proposed by several groups.[18,20-23] The demonstrated approaches rely mostly on optical deflection exhibited by temperature-sensitive microelectromechanical systems (MEMS) that are read out by constructing an interference pattern, which increases the system's cost and complexity. Another promising, yet technically challenging microphotonic IR detection principle was shown by Watts *et al.*, namely, by combining high-Q micrometer-scale resonators with extreme thermal isolation for low-noise thermal detection.[24] A further step in the improvement of the existing sensor designs toward a lower cost production and direct read out by the eye can be achieved by employing photonic crystals (PCs)—periodic dielectric nanostructures capable of manipulating light owing to strong coherent scattering interactions.[25,26] Particularly, PCs with a photonic stop band—a forbidden range of frequencies of the photons—in the visible region of the spectrum, are potentially able to "translate" IR radiation into visible color changes. This concept was recently demonstrated by Pris *et al.*[27] who presented a novel type of a miniature ultrasensitive, fast, and heat-sink-free IR thermo-optic sensor inspired by natural photonic structures present in the Morpho butterfly, in which IR absorption is enhanced by modifying the wing structures with single-walled carbon nanotubes. However, a bioinspired fabrication of artificial wing structures is far from trivial; hence, simpler approaches toward producing less complex thermally responsive structures are desirable,[28] such as one-dimensional PCs—multilayer interference-based optical filters with a periodic modulation of the RI in one dimension.[29] These so-called Bragg stacks (BSs) can be assembled from thermally responsive materials in which the RIs are temperature-dependent owing to the thermo-optic effect (TOE). Therefore, the optical properties of BSs comprising thermo-optic materials can be tuned upon varying the temperature.[30,31] Consequently, thermally responsive optical filters can be used to tune the intensity of a narrow-band visible light source, for example, when integrated with an organic light-emitting diode. For example, the coupling of an OLED with IR sensitive materials has been realized by Kim *et al.*[32] The authors investigate a hybrid "up-conversion" device based on IR sensitive PbSe nanocrystals incorporated into a green phosphorescent OLED.

In this paper, we report a route toward producing a thermo-optic imaging sensor with a ternary architecture based on the integration of sol–gel processed thermoresponsive one-dimensional photonic crystals with an OLED or LED, respectively, and a high-resolution camera. The proposed IR sensing principle is based on visualizing the changes of the intensity of light, propagating from the light source through the Bragg stack. Detecting visible light can be done in a straightforward and inexpensive fashion with low noise by using commercially available charge-coupled device (CCD) or complementary metal oxide semiconductor (CMOS) imagers. In this respect, our approach goes beyond the standard photonic crystal detection schemes based on the registration of the spectral shift of the photonic stop band.[33,34]

4.1.2. RESULTS AND DISCUSSION

As a proof of concept, we demonstrate the universality of the proposed approach by using a commercially available narrow-band blue LED as a light emitter. By detecting the light intensity transmitted through the 1D PC as a function of temperature, the thermal tunability of the PC directly translates into the intensity modulation observed at the detector. The scheme of the experimental setup is demonstrated in Figure 4.1.1a. As can be seen, the light from the LED is sent through the collimator–monochromator system and afterward through the BS and detected by the photodetector. The LED has a spectral full width at half-maximum (fwhm) of 28 nm (the spectrum of the LED light, divided by five, is plotted in Figure 4.1.1b, black dotted line). In order to match the emission spectrum of the LED, a BS thickness parameter optimization was performed to obtain a BS with 50 nm TiO_2 and 90 nm SiO_2 layers (Figure 4.1.1b, red star line). In order to provide a steep stop band, the number of bilayers was chosen to be eight (the cross section scanning electron microscopy (SEM) image of the investigated BS can be found in Figure 4.1.2i). The transmission of the BS at 25 °C and at a wavelength of 464 nm is approximately 15%. The colored lines in Figure 4.1.1b represent the spectra of the light transmitted from the LED through the BS recorded at temperatures in the range from 10 to 50 °C with a step size of 5 °C. We observed that due to the filter function of the BS in the wavelength range 450–500 nm the peak wavelength of the transmitted LED light (Figure 4.1.1, blue, green, yellow, and red curves) is shifted by ≈10 nm into the red compared to the original 464 nm peak of the LED spectrum (black dotted line). The reason for this shift can be found in the shape of the stop band of the BS (Figure 4.1.1b, red star line). However, by slightly changing the optical thicknesses of the BS layers and, hence, its transmissive

properties, the light output of the LED can be increased. The LED-BS transmission spectra in Figure 4.1.1 show a gradual increase in light intensity transmitted through the BS with rising temperature. Figure 4.1.1c shows the intensities of the emission peaks at various temperatures, namely, the value of the peak intensity increases from ≈11% for 10 °C to ≈20% for 50 °C. The intensity increase is observed due to the blue-shifting of the photonic stop band of the BS upon heating, which can be explained by considering the thermo-optic coefficients (TOCs) of the chosen materials of the BS's layers. Namely, the negative TOC of the bulk TiO_2 (equal to -1.77×10^{-4} K^{-1} between 18 and 120 °C and to -3.04×10^{-4} K^{-1} between 220 and 325 °C at 800 nm), in contrast to the lower positive TOC of bulk SiO_2 (1×10^{-5} K^{-1}) dominates the thermal response of the BS layers.[36] Consequently, the optical thickness of the TiO_2/SiO_2 bilayer decreases upon increasing temperature, and vice versa. Additionally, as pointed out elsewhere,[30] the ambient humidity also plays an amplifying role in the tuning behavior by enhancing the sensitivity of the BS. A detailed description of the dependence of the RI on temperature for nanoparticle-based silica and titania films can be found elswhere.[30] Thus, the nonlinear trend of the dependence of the intensity of the LED (see Figure 4.1.1b) on the temperature for temperatures below 20 °C originates from the effect of water adsorption/desorption into/from the BS.[30] This experiment demonstrates the easy readout of changes in the position of the stop band of an arbitrary BS by using a LED and a detector.

As a next step, we demonstrate a miniature integrated sensing platform developed by depositing the OLED and the BS on opposite sides of the same glass plate as shown in Figure 4.1.2a. The BS was fabricated *via* multiple sequential spin-coating of a high RI material—TiO_2 nanoparticles and a low RI material—commercially available SiO_2 nanoparticles (Figure 4.1.2i).[30, 35] Alternatively, a titania sol and a mesoporous silica–surfactant sol was employed, allowing the preparation of high surface area mesoporous films *via* evaporation-induced self-assembly[37] (Figure 4.1.2ii). As mentioned earlier, TiO_2 and SiO_2 have been chosen for their high RI contrast on the one hand and the high TOC of TiO_2 on the other hand. The BSs, deposited onto the indium tin oxide (ITO) glass substrates, were integrated with polymer OLEDs assembled by spin-coating. An emissive OLED polymer PDY-132 was selected because of its good stability and match with the sensitivity range of the CCD camera. A more detailed description of the synthesis and fabrication steps can be found in the Appendix 8.2. As shown in Figure 4.1.3, the transmissive properties of the BS can be precisely tuned through optimizing the deposition parameters, such as spin-coating speed and acceleration, or the concentration of the suspensions, to match the emission spectrum of the OLED. The transmission through the BS can be measured by a photodiode,

and the information about the light intensity distribution across the BS area can be obtained by, for example, a CCD or a CMOS active-pixel array camera (Figure 4.1.2b and c). The Bragg stack does not require a lithographic pixel fabrication as for most IR detectors, since the pixels are provided by the camera, recording the intensity distribution along the area of the coupled OLED-BS system.
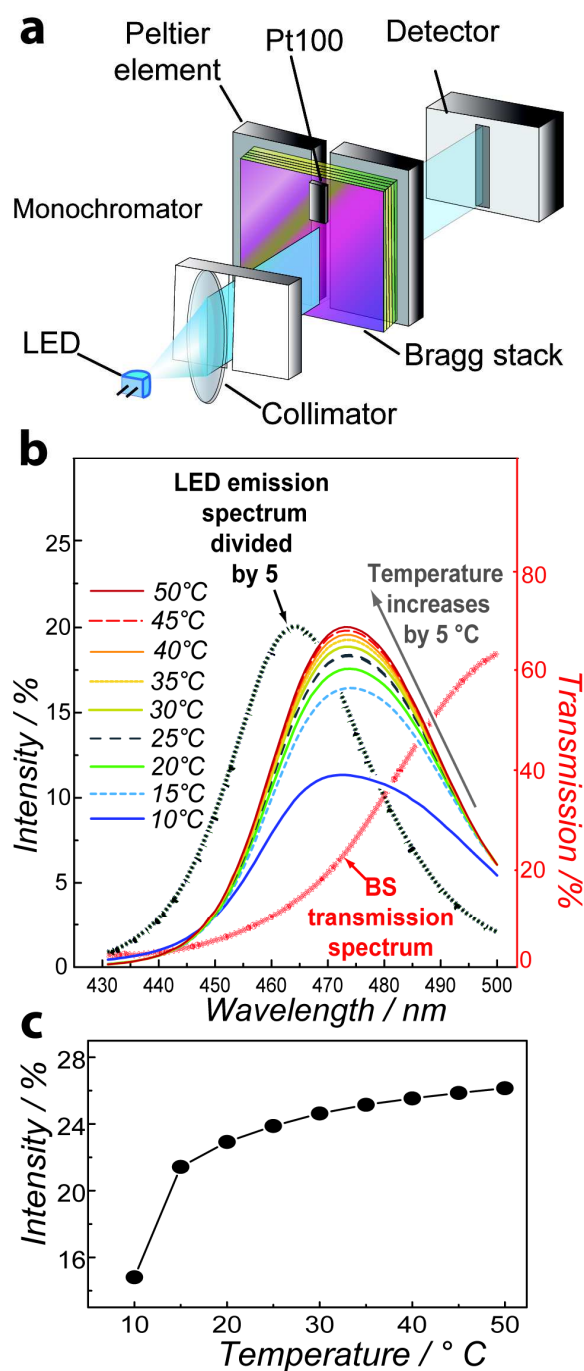
Figure 4.1.1. (a) Scheme of the experimental setup for the tuned LED light intensity. (b) Blue, green, yellow, and red lines demonstrate the intensity of light, transmitted from the blue LED through the BS with 8 TiO_2 (50 nm)/SiO_2 (90 nm) bilayers. The temperature is controlled between 10 and 50 °C in steps of 5 °C. As a reference, the LED spectrum (black dotted line) was scaled to the size of the graph ("Intensity" axis, left). The transmission

spectrum of the BS (red star line) is plotted with respect to the "Transmission" axis (right). (c) Plot showing the dependence of the peak intensity derived from the LED-BS transmission spectra in part b on the temperature.
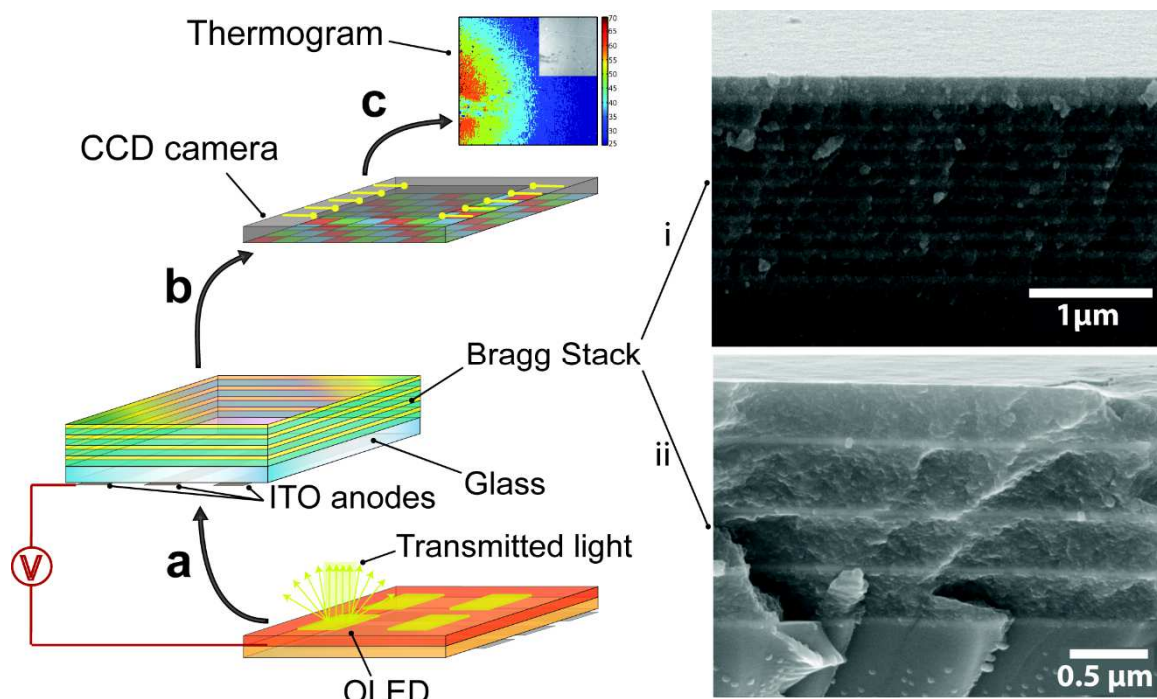
Figure 4.1.2. Scheme of the proposed thermo-optic imaging sensor featuring: (a) an OLED on the ITO-coated side of the glass substrate, (b) integration of the OLED-BS system with a CCD camera, and (c) visualization of the heat distribution on the surface of the OLED-BS ensemble. The BSs were made of (i) TiO_2 and SiO_2 nanoparticle-based layers and (ii) dense TiO_2 and mesoporous SiO_2 layers.

Due to the thermal contact of the OLED with the BS, the temperature changes of the BS and the OLED are interrelated. Therefore, we independently investigated the influence of the temperature change on the emission properties of the OLED on the one hand and the BS's spectral shift on the other hand, as well as the thermal response of the coupled OLED-BS system.

To realize the intensity tuning of the light emitted by the OLED, we assembled a Bragg stack consisting of six bilayers of nanoparticle-based TiO_2 and SiO_2 layers (Figure 4.1.5c). The optimization of the thickness of the layers (60 nm for TiO_2 with RI ≈ 1.9 and 110 nm for SiO_2 with RI ≈ 1.3) allowed us to obtain a filter with a first-order photonic stop band between 490 and 640 nm, matching the emission spectrum of the polymer OLED lying in the range between 500 and 620 nm (Figure 4.1.3a and b). In Figure 4.1.3b, we demonstrate the shifting behavior of the photonic stop band of the BS upon heating in ambient conditions. Heating induces a change in the effective RI of the employed materials due to the

combination of two phenomena operating simultaneously: The inherent thermo-optic effect and the desorption of the water molecules from the porous network of the BS lead to the change of the optical thickness of the layers and, thus, to a blue shift of the stop-band position.[30] The measurements were performed as described in the Appendix 8. 2. The reversibility of the BSs thermal tuning is proven by the fact that measurements of the transmission curves at room temperature carried out before the heating and after the cooling cycles are the same. We observe a consistent blue shift of the stop band position upon increasing temperature, equal to 25 nm for the 40% transmission level in the temperature range from 15 to 35 °C, and if we follow the transmission values at a given wavelength in Figure 4.1.3b (the vertical gray dashed line at 560 nm), we observe a variation of the optical transmission of the filter from ≈10% to ≈28% upon heating. The shift for temperatures below ≈20 °C exhibits a nonlinear behavior due to the adsorption of ambient water into the BS's textural mesopores, which is more pronounced at lower temperatures closer to the dew point. As suggested in our previous study with similar BSs, the humidity of the ambient air plays a key role in enhancing the sensor response, giving rise to an *"effective"* TOE.[30] Using BSs composed of dense layers reduces or even completely eliminates the nonlinear shifting behavior caused by the presence of ambient humidity.[38] Note, however, that reducing the humidity contribution also leads to a drop in sensitivity of the device, rendering the use of materials with a sufficiently high TOC necessary.
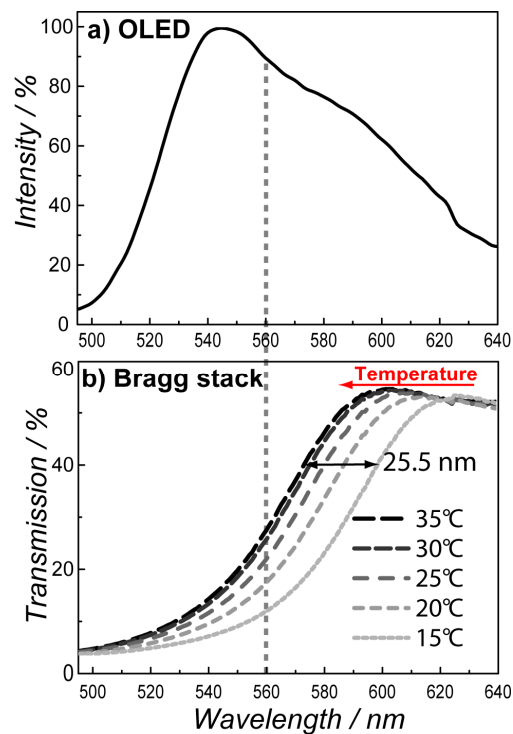
Figure 4.1.3. (a) Emission spectrum of the OLED. (b) Transmission spectra obtained upon heating a six bilayer TiO_2 (60 nm)/ SiO_2 (110 nm) BS from 15 to 35 °C with a step size of 5 °C. Note that the spectra of the BS match the OLED emission curve: the gray dashed line shows the change in the transmission from ≈10% to ≈28% at 560 nm corresponding to 90% emission of the OLED.
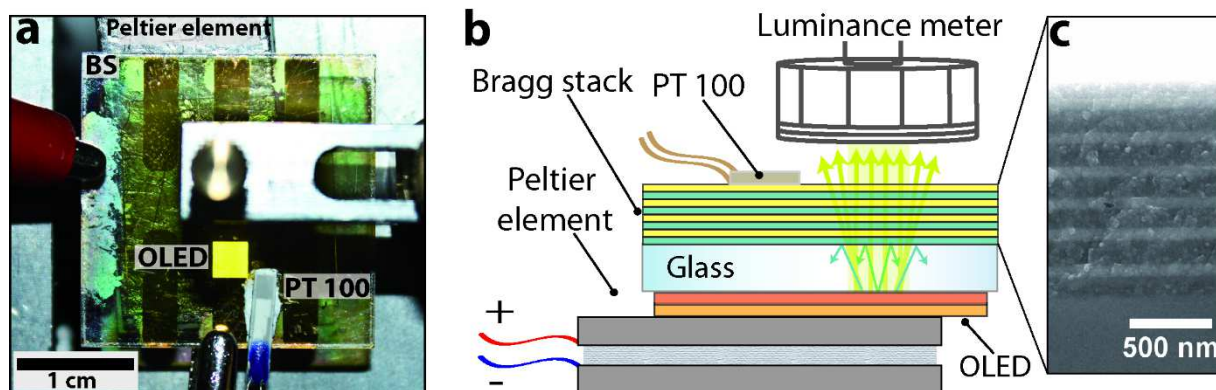
Figure 4.1.4. (a) Photograph of the sample holder with an emitting OLED-BS couple mounted onto the Peltier element. (b) Scheme of the experimental setup for the luminance measurements. (c) Cross-section SEM picture of the BS, composed of six bilayer SiO_2 (dark layers)/TiO_2 (bright layers).

In the next step, we investigate the temperature dependence of the optical emission properties of the OLED alone. As mentioned above, in the proposed setup geometry, the simultaneous heating of the OLED during the temperature increase of the BS cannot be avoided; therefore, the individual contributions of OLED and BS need to be analyzed separately. First, the OLED structure was fabricated on a glass plate and encapsulated as described in the Appendix 8.2. The active area of the OLED is equal to 3 mm × 3 mm with a light output of approximately 120 cd m^{-2}. A picture of the experimental setup is provided in Figure 4.1.4, showing a mounted OLED-BS system with a PT100 temperature sensor next to the active area. Figure 4.1.5a shows the emission spectrum of the OLED without BS for temperatures between 15 and 35 °C. In this temperature range we observe two phenomena related to the behavior of the emission spectra: (i) the intensity increases linearly upon rising temperature, and (ii) the peak intensity shifts about 1.5 nm into the blue, upon rising temperature. Both effects are fully reversible. The peak position has been determined by linear interpolation of the first derivative of the spectrum.
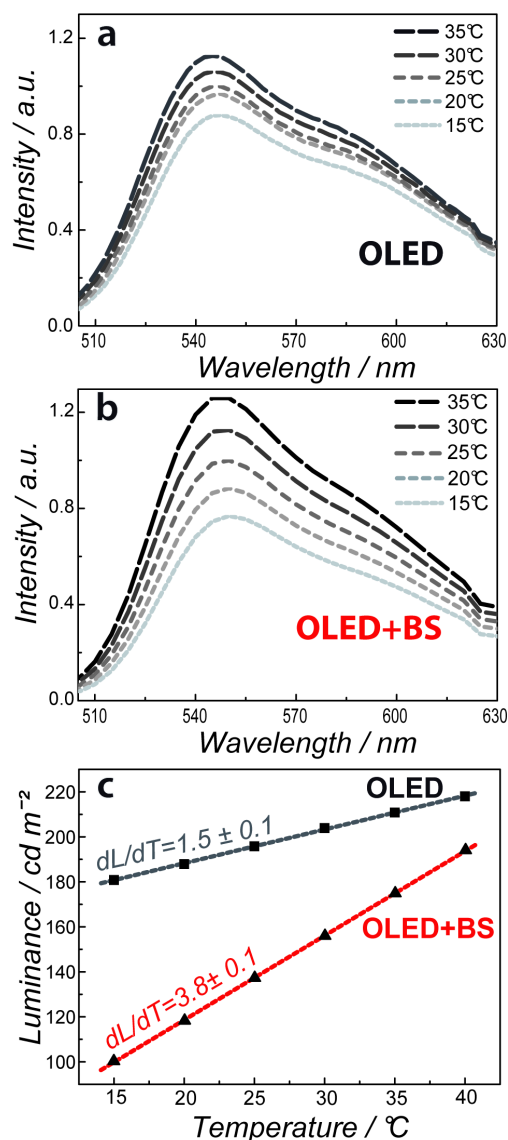
Figure 4.1.5. (a and b) The emission spectra of (a) the OLED alone and (b) the OLED-BS system recorded upon increasing the temperature from 15 to 35 °C in steps of 5 °C. For clarity, the intensities of the spectra are normalized with respect to the peak intensity at 25 °C. (c) Comparison of the luminance of the OLED alone and the OLED-BS system measured by a luminance meter. The single OLED exhibits a temperature coefficient dL/dT of 1.5 cd m^{-2} K^{-1}, whereas the combined OLED-BS device shows a 2.5 times higher sensitivity of dL/dT = 3.8 cd m^{-2} K^{-1}.

In the next step, a couple consisting of a BS and an OLED structure solution-processed on the opposite sides of a glass plate was assembled (see Figures 4.1.2 and 4.1.4). As indicated by the scheme in Figure 4.1.2a, the first step in the fabrication of the combined OLED-BS system is the fabrication of the Bragg stack on a glass substrate with the subsequent deposition of the OLED on the other, ITO-coated, surface of the glass substrate with the BS. Figure 4.1.5b shows the emission spectra of the OLED-BS at

temperatures between 15 and 35 °C with a step size of 5 °C. We observe an enhanced tuning of the intensity compared to the native OLED. The temperature response unveils two trends in the behavior of the device: (i) the increase of the peak intensity by a factor of 1.6 in a temperature range from 15 to 35 °C (notably, this effect exceeds the performance of the single OLED, which increases only by a factor of 1.3), and (ii) the shift of the emission peak toward shorter wavelengths by 3 nm upon increasing temperature. The last observation can be explained by the effect of the BS shifting behavior, namely, 25 nm per 20 °C increase, which exceeds the shift of the OLED alone being only 1.5 nm.

In order to simplify the readout apparatus, we show that the temperature changes can be detected by the integrated light going through the BS with a setup as sketched in Figure 4.1.4b. The temperature was varied using a Peltier element, between 15 and 40 °C with a step size of 5 °C. This procedure was repeated three times to check its reproducibility. Figure 4.1.5c shows the temperature-induced modulation of the luminance (L) of the OLED alone and of the OLED-BS integrated device. The luminance of the OLED-BS device changed from 100.3 to 194.1 cd m^{-2} in a range from 15 to 40 °C. It is notable that L of the combined OLED-BS system increased linearly with temperature, with a rate dL/dT derived from the linear fit of the dependence of L on temperature, equal to 3.8 ± 0.1 cd m^{-2} K^{-1} over the whole temperature range. In contrast, the single OLED, tuned in the same temperature range, showed higher luminance values from 180.8 to 218.0 cd m^{-2}; however with 2.5 times lower sensitivity of 1.5 ± 0.1 cd m^{-2} K^{-1} in comparison with the coupled OLED-BS system. Thus, it can be seen that the thermal response of the integrated OLED-BS system is higher than that of the OLED alone. The displayed resolution of the luminance meter was 0.1 cd m^{-2}, this value exceeds the noise of the system and therefore is the limiting factor in the system precision. The resolvable temperature was calculated to be 67 ± 3 mK for the OLED alone and 27 ± 3 mK for the OLED-BS system. The specifications are summarized in Table 4.1.1.

Table 4.1.1. Comparison of the temperature response and the resolvable temperature of the OLED and OLED-BS systems

	Sensitive area [mm]	Power dissipation [mW]	Temperature response [cd m^{-2} K^{-1}]	Resolvable temperature [mK]
OLED	3×3	2	1.5 ± 0.1	67 ± 3
OLED-BS	3×3	2	3.8 ± 0.1	27 ± 3

In order to demonstrate the feasibility of IR imaging we integrated the OLED-BS sensor with a camera detector array, as indicated in the scheme in Figure 4.1.2. We set up a commercial CCD camera above the device so that the light output can be recorded over the whole OLED-BS area with a resolution of 530 by 530 pixels. To detect the filter transmission in two dimensions, the light emission had to be homogeneous over the whole active filter area, a criterion verified by our OLED. The intensity of the transmitted light corresponds to the temperature of the respective point on the OLED-BS. In Figure 4.1.6a, we present a colored optical image of the OLED-BS equilibrated at 27 °C. The light intensity is relatively constant over the whole 3×3 mm large surface. The actual gray scale image as acquired from the CCD camera is shown in the upper right corner. Figure 4.1.6b shows a colored optical image of the OLED-BS under a temperature gradient induced by a hot source (here, a soldering iron at a temperature of 400 °C on the left side) generating a local temperature of less than 60 °C on the edge of the device. The increased light output shown by the monochrome image in the inset can also be seen by the naked eye. Figure 4.1.6c is taken 10 s after heating, when the device was at a temperature of 33 °C. All pictures show some irregularities in a micrometer range that originate from defects in the OLED top electrode morphology. Also slight irregularities on the surface are due to the fabrication imperfections and inhomogeneity of a BS. The inhomogeneities can be compensated by calibration and background correction, typical for IR-detectors.[39] In order to improve the readability of the image and to reduce the inhomogeneities, we subtracted the background intensity and calibrated the picture (a detailed description of the calibration procedure is given in the Appendix 8.2). The corrected image in Figure 4.1.7 outlines the gradual decrease of temperature with increased distance from the heat source position (the left edge). Figure 4.1.7 also indicates that a minimization of the thermal crosstalk has to be considered along with the device engineering. In principle, the crosstalk can be minimized by using thinner substrates or by separating the pixels by means of standard lithographic techniques. With this experiment, we prove that with the proposed thermo-optic intensity-tuning technique one can visualize the temperature changes of the integrated optical systems with a visible-light detector, such as a CCD array. Moreover, one can time and spatially resolve the kinetics of thermal equilibration and spreading of temperature fronts in the OLED-BS coupled devices. If a high temperature gradient is present, the sensor can be even be read out with the naked eye. The advantage of the introduced sensing scheme is that it involves low cost and noncomplicated fabrication methods and low power consumption (because the whole setup requires only an OLED powered at 4.5 V as the light source) and thus represents a promising candidate for potential IR imaging detectors.
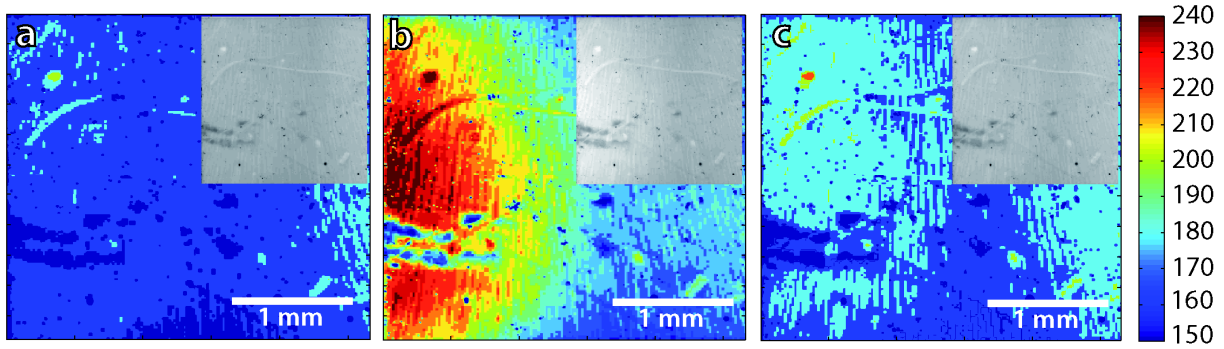
Figure 4.1.6. Colored optical images demonstrating the OLED shining through the BS in (a) thermal equilibrium at 27 °C and (b) heated on the left side. The insets show the corresponding raw image obtained by a monochrome CCD camera. (c) The OLED-BS, 10 s after heating at a temperature of 33 °C.
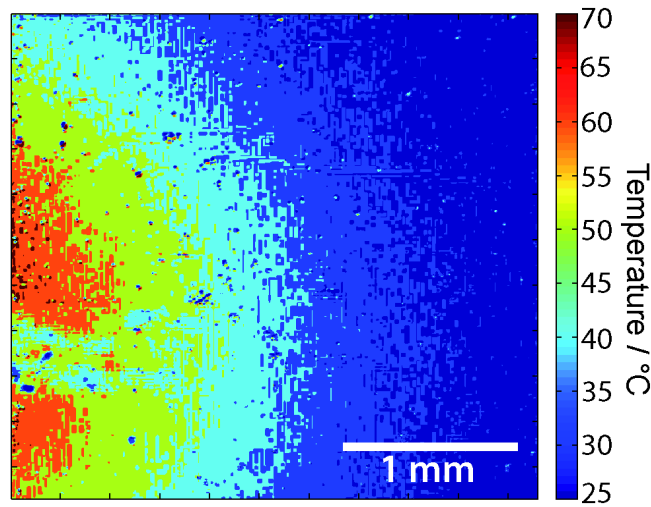
Figure 4.1.7. Calibrated thermogram, corresponding to Figure 4.1.6b, displaying the distribution of the OLED-BS temperature under the thermal gradient.

The hybrid OLED-BS device exhibits thermally tunable characteristics, thus enabling a versatile infrared imaging scheme. It should be mentioned that both OLED alone and the OLED-BS combination show pronounced thermal tunability and both are, therefore, possible candidates for IR image sensors. However, a coupled device consisting of an OLED and a Bragg stack is 2.5 times more sensitive toward temperature changes than the OLED alone. The achieved temperature sensitivity of 3.8 cd m^{-2} K^{-1}, equivalent to a temperature coefficient of luminance of 3.8%, can be compared with state-of-the-art thermoresistive detectors. For comparison, VO$_2$, which is often used in thermal detectors, has a temperature coefficient of resistance (TCR) of 4% for a single element cell.[1] We calculated the resolvable temperature to be 27 ± 3 mK for the measurement taken with the luminance meter. It is crucial to match

the OLED and the BS such that the OLEDs emission peak wavelength is at the edge of the filter's stop band. The shift of the transmission depends on the effective TOE of the materials constituting the BS. The slope is determined by the refractive index contrast of the BS materials and the number of bilayers. The tuning performance could be improved by using a narrower spectrum light source—such as a laser or an OLED with reduced spectral width as demonstrated by Puzzo *et al.*[40] Another way to improve the tuning performance is to increase the shift of the stop band of the BS, i.e. by using materials with a higher TOC.[41] The highest TOCs in inorganic materials reach up to $\pm 10^{-4}\,\mathrm{K}^{-1}$ and can be even higher in organic materials,[42, 43] which mostly possess a negative TOC around -1 to $-6 \times 10^{-4}\,\mathrm{K}^{-1}$ (it should be mentioned, however, that the thermal expansion in organic materials can have a counteracting effect on the shift of the stop band). Further improvements that need to be addressed are the device thermal capacity in order to increase device speed and thermal conductance in lateral directions. As we have seen in Figure 4.1.6, the heat conductivity across the device is fairly good which could be a problem for the image contrast. To prevent thermal crosstalk, the heat conduction in lateral dimensions can be suppressed by employing thinner substrates and a heat sink on the back side of the device. Though our active components only have a thickness of approximately 2.3 μm, the whole device measures currently 1.5 mm, which leaves room for improvement. The potentially low fabrication costs and optical readout leads to numerous possible applications. The imaging sensors can be provided by a mobile phone or a compact camera.

4.1.3. CONCLUSION

In this work we demonstrated an integrated detection platform based on an OLED and a photonic crystal, which is capable of infrared sensing *via* the temperature-induced spectral modulation of a thermoresponsive photonic crystal. On the basis of this sensing principle, the PC's thermal response translates into an intensity change in the transmitted light intensity, thus allowing for the straightforward realization of a greyscale detection scheme as opposed to the more conventional color readout schemes. Furthermore, we demonstrated time and spatially resolved temperature mapping on the device surface by interfacing the OLED-PC with a commercial CCD camera.

ACKNOWLEDGEMENTS

4.1.4. BIBLIOGRAPHY

(1)   Rogalski, A. Infrared Detectors, Second ed.; CRC Press: Boca Raton, FL, **2010**.

(2)   Meola, C.; Carlomagno, G. *M. Meas. Sci. Technol.* **2004**, *15*, R27

(3)   Rogalski, A. *Prog. Quant. Electron.* **2003**, *27*, 59.

(4)   Rogalski, A. *Infrared Phys. Techn.* **2002**, *43*, 187.

(5)   Rogalski, A. Rep. Prog. Phys. **2005**, *68*, 2267.

(6)   Dereniak, E. L.; Boreman, G. D. Infrared detectors and systems; Wiley: New York, **1996**.

(7)   Smith, E. P. G.; Winchester, K. J.; Musca, C. A.; Dell, J. M.; Faraone, L. *Semicond. Sci. Technol.* **2001**, *16*, 455.

(8)   Walcott, T. M. Bolometers: Theory, Types and Applications (Physics Research and Technology); Nova Science Publishers, Inc: Hauppage, NY, **2011**.

(9)   Ishikawa, T.; Ueno, M.; ; Nakaki, Y.; Endo, K.; Ohta, Y.; Nakanishi, J.; Kosasayama, Y.; Yagi, H.; Sone, T.; Kimata, M. *Infrared Technology and Applications XXVI*, Proceedings of SPIE, San Diego, CA, July 30, **2000**; Vol. *4130*, 152.

(10)   El Mandouh, Z. *Thin Solid Films* **2000**, *371*, 259.

(11)   Chen, C.; Yi, X.; Zhao, X.; Xiong, B. *Sens. Actuators* **2001**, *90*, 2000.

(12)   Wood, R. A.; Capper, P.; Elliott, C. T.; Willoughby, A. F. W.; Hull, R. Infrared Detectors and Emitters: Materials and Devices; Capper, P.; Elliott, C. T., Eds.; Springer US: Boston, MA, **2001**; Vol. *8*, 149.

(13)   Sedky, S.; Fiorini, P.; Caymax, M.; Verbist, A.; Baert, C. *Sens. Actuators A-Phys*. **1998**, *66*, 193.

(14) Lavrik, N. V.; Grbovic, D.; Rajic, S.; Datskos, P. G.; Forrai, D.; Nelson, E.; Devitt, J.; McIntyre, B. *Infrared Technology and Applications XXXII*, Proceedings of SPIE, Orlando, FL, April 17, **2006**; Vol. *6206*, 62061K.

(15) Emmons, R. B.; Hawkins, S. R.; Cuff, K. F. *Opt. Eng.* **1975**, *14*, 21.

(16) Smith, R. A. *Detection and Measurement of Infrared Radiation (Monographs on the Physics & Chemistry of Materials);* Oxford University Press: New York, **1968**.

(17) Niklaus, F.; Kälvesten, E.; Stemme, G. *J. Micromech. Microeng.* **2001**, *11*, 509

(18) Jones, C. D. W.; Bolle, C. A.; Ryf, R.; Simon, M. E.; Pardo, F.; Aksyuk, V. A.; Lai, W. Y.-C.; Bower, J. E.; Miner, J. F.; Klemens, F. P.; Cirelli, R. A.; Sorsch, T. W.; Ferry, E. J.; Fetter, L. A.; Pai, C.-S.; Taylor, J. A.; Vyas, B.; Watson, G. P.; Stekas, B.; Baker, M. R.; Papazian, A. R.; Basavanhally, N. R.; Mansfield, W. M.; Kornblit, A.; Keller, R. C.; Gates, J. V.; Ramirez, A. P. *Sens. Actuators A-Phys.* **2009**, *155*, 47.

(19) Ostrower, D. *III-Vs Rev.* **2006**, *19*, 24.

(20) Lavrik, N.; Archibald, R.; Grbovic, D.; Rajic, S.; Datskos, P. *Infrared Technology and Applications XXXIII*, Proceedings of SPIE, Orlando, FL, April 9, **2007**; Vol. *6542*, 65421E.

(21) Grbovic, D.; Lavrik, N. V.; Datskos, P. G.; Forrai, D.; Nelson, E.; Devitt, J.; McIntyre, B. *Appl. Phys. Lett.* **2006**, *89*, 073118

(22) Salerno, J. P. *Infrared Technology and Applications XXXIII*, Proceedings of SPIE, Orlando, FL, April 9, **2007**; Vol. *6542*, 65421D.

(23) LeMieux, M. C.; McConney, M. E.; Lin, Y.-H.; Singamaneni, S.; Jiang, H.; Bunning, T. J.; Tsukruk, V. V. *Nano Lett.* **2006**, *6*, 730.

(24) Watts, M. R.; Shaw, M. J.; Nielson, G. N. *Nature Photon.* **2007**, *1*, 632.

(25) Joannopoulos, J. D. Photonic Crystals: Molding The Flow Of Light; 2nd ed.; Princeton University Press: Princeton, NJ, **2008**.

(26) Calvo, M. E.; Colodrero, S.; Hidalgo, N.; Lozano, G.; López-López, C.; Sánchez-Sobrado, O.; Míguez, H. *Energy. Environ. Sci.* **2011**, *4*, 4800

(27) Pris, A. D.; Utturkar, Y.; Surman, C.; Morris, W. G.; Vert, A.; Zalyubovskiy, S.; Deng, T.; Ghiradella, H. T.; Potyrailo, R. A. *Nature Photon.* **2012**, *6*, 195.

(28) Sambles, J. R. *Nature Photon.* **2012**, *6*, 141.

(29) Macleod, H. A. Thin-film optical filters; Hilger: Bristol, U.K., **1986**.

(30) Pavlichenko, I.; Exner, A. T.; Guehl, M.; Lugli, P.; Scarpa, G.; Lotsch, B. V. *J. Phys. Chem. C.* **2012**, *116*, 298.

(31) Regoliosi, P.; Guehl, M.; Scarpa, G.; Lugli, P.; Persano, L.; Carro, P. D.; Camposeo, A.; Cingolani, R.; Pisignano, D.; Bietti, S.; Grilli, E.; Guzzi, M. *Appl. Phys. Lett.* **2008**, *92*, 2008.

(32)   Kim, D. Y.; Choudhury, K. R.; Lee, J. W.; Song, D. W.; Sarasqueta, G.; So, F. *Nano Lett.* **2011**, *11*, 2109.

(33)   Takeoka, Y.; Watanabe, M. *Adv. Mater.* **2003**, *15*, 199.

(34)   Weissman, J. M.; Sunkara, H. B.; Tse, A. S.; Asher, S. A. *Science* **1996**, *274*, 959.

(35)   Colodrero, S.; Ocaña, M.; Míguez, H. *Langmuir* **2008**, *24*, 4430.

(36)   Gülşen, G.; Naci Inci, M. *Opt. Mater.* **2002**, *18*, 373.

(37)   Lee, Y.-F.; Chang, K.-H.; Chu, C.-Y.; Chen, H.-L.; Hu, C.-C. *RSC Adv.* **2011**, *1*, 401.

(38)   Pavlichenko, I.; Exner, A. T.; Logvenov, G.; Scarpa, G.; Lugli, P.; Lotsch, B. V. *Can. J. Chem.* **2012**, *90*, 1069.

(39)   Minkina, W.; Dudzik, S. Infrared Thermography: Errors and Uncertainties; John Wiley and Sons: New York, **2009**; p 212.

(40)   Puzzo, D. P.; Helander, M. G.; O'Brien, P. G.; Wang, Z.; Soheilnia, N.; Kherani, N.; Lu, Z.; Ozin, G. A. *Nano Lett.* **2011**, *11*, 1457.

(41)   Kang, E.-S.; Lee, T.-H.; Bae, B.-S. *Appl. Phys. Lett.* **2002**, *81*, 1438.

(42)   Ballato, J.; James, A. *J. Am. Ceram. Soc.* **1999**, *82*, 2273.

(43)   Zhang, Z.; Zhao, P.; Lin, P.; Sun, F. *Polymer* **2006**, *47*, 4893.

5. ELECTROPHOTONIC CHEMOSENSING PLATFORM BASED ON TUNABLE ONE-DIMENSIONAL PHOTONIC CRYSTALS

Currently the demand for fast and reliable ubiquitous monitoring systems is propelled by a growing number of potentially hazardous contaminants released to the environment. In the recent past, sensors utilizing "smart" stimuli-responsive photonic crystals have offered cutting-edge solutions in the realm of emerging sensor technologies. However, despite numerous advantages provided by the colorimetric read-out schemes, a facile and unambiguous signal-transduction mechanism allowing to convert the optical response (color change) of the tunable photonic crystals into an electronic signal with a high sensitivity and a high signal-to-noise ratio is of great interest.

In chapter 5.1 we report a route towards the bottom-up assembly of an innovative fully functional, integrated "all-in-one" *electrophotonic* sensing platform based on the integration of a TiO_2/SiO_2 1D photonic crystal with an organic light-emitting diode (OLED) and an organic photodetector (OPD). The conceptually novel electrophotonic sensor demonstrated in this chapter exceeds the capabilities of most commercial spectrometers and has potential for the development of highly sensitive low-cost and low power consumption "electrophotonic nose" detection platforms.

5.1. A STEP TOWARDS THE ELECTROPHOTONIC NOSE: INTEGRATING 1D PHOTONIC CRYSTALS WITH ORGANIC LIGHT-EMITTING DIODES AND PHOTODETECTORS

Armin T. Exner*, Ida Pavlichenko*, Daniela Baierl, Morten Schmidt, Gerald Derondeau, Bettina V. Lotsch, Paolo Lugli, and Giuseppe Scarpa

* These two authors made an equal contribution

Abstract

An innovative integrated sensing platform for the detection of various chemical analytes *via* translating the photonic stop-band shift of a one-dimensional photonic crystal (PC) into an electrical current change is proposed. The miniaturized sensing platform features an organic light-emitting diode (OLED) as a light source and an organic photodetector (OPD) as a light sensor and allows for the detection of ethanol vapor concentrations down to ≈ 10 parts per million (ppm) in nitrogen, which corresponds to a stop-band shift of ≈ 27 pm. The resolution of the proposed platform exceeds the capabilities of most commercial spectrometers and by far the human eye, while, at the same time, such a sensor is less expensive and less power consuming than a spectrometer. The presented setup is generic and can detect optical changes in the transmission of PCs, which can be induced by both vapor adsorption or by a liquid analyte, as demonstrated with a microfluidic setup.

5.1.1. INTRODUCTION

Nowadays, the active development of ubiquitous environmental sensors is being facilitated by a wide range of applications devoted to the engineering of a convenient interface between the real and digital worlds, such as for air-quality monitoring, detection of hazardous chemicals and health-care diagnostics. The demand for fast and reliable monitoring systems is ever increasing, and due to the general trend towards automatization and at the same time aggravation of environment-protecting legal constraints, the market of environmental sensors is expected to expand in the future and to reach $15.3 billion in 2016, growing with an annual rate of 6.5%, including remote sensing, atmospheric measurements and monitoring services.[1] For a practical use the sensor must convert the environmental change into an electrical signal *via* a transduction scheme that can be processed in a small integrated circuit. Current requirements for mass-produced environmental sensors are, besides low cost, low energy consumption and small dimensions, a noncomplex read-out that can be easily processed, and, at the same time, high sensitivity with a high signal-to-noise ratio (SNR). Currently, a variety of structures, assembled on the nanometer scale, enable the detection of the smallest traces of pollutants, and their relatively fast response time renders such systems suitable for integration into electronic devices.[2] Another interesting option for the analysis of environmental changes is being offered by a promising class of nanostructures, called photonic crystals (PCs). Hereby, a colorimetric read-out scheme has been adopted and investigated during the last two decades.[3,4] Colorimetric sensors, well known ever since the litmus pH paper, glucose and pregnancy color tests have successfully entered the market, are currently undergoing a revival in the area of stimuli-responsive PCs. A color change of the PC is usually read out by a spectrometer or by the naked eye, which may give rise to ambiguities. Therefore, the signal-transduction mechanism allowing to convert the optical response of a tunable PC into an electronic signal is in high demand.

A photonic crystal is a periodic optical nanostructure typically composed of two or more alternating materials with different refractive indices (RI) that can be manufactured in one, two or three dimensions.[5-8] In a PC a photonic stop-band is formed due to the interference of light at the interfaces between the high- and low-RI materials. In a 1D PC, which is also often called a Bragg stack (BS) or a Bragg mirror, the maximum reflection for normal incidence can be observed if the optical thickness of

each layer is a quarter wavelength. The maximum reflection for normal incidence is given by the following approximate Equation (1):

$$m\lambda_{Bragg} = 2(n_1 d_1 + n_2 d_2) \ , \quad (1)$$

where m is the order of the stop-band maximum, d_i is the thickness of the respective layer and n_i their RIs.[9] As can be derived from Equation (1), if one of the PC materials exhibits a change in either RI or in the physical dimensions when exposed to the target analyte, the PC can act as a sensor with an optical read-out. An example of structures that change their physical dimensions (i.e. d_i) upon exposure to certain analytes is offered by polymeric layers, which may dramatically swell by adsorbing the analytes.[10,11] On the other hand, one can consider a second group of PCs based on inorganic porous materials, where pore filling by the analyte induces a RI change and, hence, an optical thickness change, while at the same time the physical dimensions of the structure remains largely constant.[9]

In order to achieve a high sensitivity and uniform optical response, the photonic structure must be accessible to the analyte *via* the pore system, e.g. the textural pores in nanoparticle-based materials or structural mesopores and micropores. For a robust sensor design three major challenges shall be addressed: (i) sensitivity, (ii) selectivity in order to distinguish different analytes, and (iii) response speed. The sensitivity, as we have demonstrated in former studies [12], can be tuned by the level of porosity of the material. The selectivity is generally low in most porous PCs, since the infiltration process works for every molecule that is small enough to fit in the pores. Approaches to gain high selectivity have been demonstrated by Burgess *et al.* and Raymond *et al.* using surface modification to selectively detect, e.g., alcohols, aliphatic compounds and different grades of gasoline.[13-15] Alternative approaches have been demonstrated by us by employing cation-selective clays [16] or inherently porous coordination frameworks with structurally well-defined pore sizes as active layers in 1D PCs [17], and by the time-domain analysis of the PC response.[18] The response time, i.e. the time from the start of exposure until the sensor delivers a readable output is a key parameter for a sensor. In our previous study we have demonstrated that a 1D-PC composed of porous SiO_2/TiO_2 with a total thickness of less than 2 μm obtained response times as low as 2 s for exposure to air with relative humidities of 20% and 70%.[19] In the case of liquids the response can be as low as 0.1 s, for example by taking advantage of capillary forces in an electrochemically etched 700-nm thick PC.[20]

The PC-based optical sensors discussed above indeed represent suitable candidates for sensing devices, which can be read out by a spectrometer, which is available in most laboratories. However, the laboratory approach is too bulky, expensive and power consuming for mobile applications. The alternative read-out with the naked eye is hampered in terms of resolution, leading to considerable inaccuracies. As a consequence, there is a missing link between the optical response and a low-cost electric read-out that demands to be closed, as most sensor data must be transmitted and processed digitally, while the sensor must be cheap and low in power consumption. So far, sensors involving a photonic crystal and featuring simplified colorimetric read-out schemes have been demonstrated by several groups.[21,22] However, these detection schemes typically require beam alignment, lenses and a laser. Another versatile principle for the detection of the photonic stop-band position has been demonstrated by Fang *et al.* using a porous polymeric photonic bandgap sensor integrated with a color-sensitive CMOS detector, which has the advantage of detecting the stop-band position in a broad wavelength range from 425 nm to 700 nm.[23] A further step towards low-cost integration has been provided by Nazirizadeh *et al.* who detected the polarization rotation of a photonic crystal slab biosensor by using a light-emitting diode (LED) and a photodetector (PD) and two crossed polarizers.[24] It is noteworthy that hybrid devices, based on combining organic light-emitting diodes (OLEDs) with various photodetectors were successfully applied in fluorescence detection [25] and in oxygen and pH sensing.[26] An elegant solution based on employing a smartphone as a spectrometer for measuring the transmission of the PC handheld biosensor was proposed by Gallegos *et al.*[27]

Following this route, we aim to take the next step by further reducing the dimensions of the device and simultaneously the required alignment effort and device complexity. Our proposed sensor platform is a stack of three devices: an OLED, a 1D PC as a tunable filter, and an organic photodetector (OPD) that realizes the electrical output. The components can be solution processed, which makes them compatible with mass-production techniques and possibly low-cost fabrication. With this platform we demonstrate a high sensitivity down to parts per million (ppm) concentration of ethanol in nitrogen at room temperature. Furthermore, the proposed setup is compatible with every PC exhibiting a change of stop-band position and/or transmission in the visible range, demonstrating the versatility of the proposed concept.

5.1.2. EXPERIMENTAL

PC fabrication

The photonic crystals were assembled by sequential deposition of TiO_2 and SiO_2 nanoparticle suspensions on a clean, uncoated side of an ITO-coated glass slide (2.5×2.5 cm^2) previously activated by air-plasma treatment (Femto, Diener Electronic). TiO_2 nanoparticles (hydrodynamic diameter 7–20 nm) were synthesized by the method described elsewhere.[28] SiO_2 colloids (hydrodynamic diameter 6–10 nm) were purchased (LUDOX SM-30, 30 wt% in H_2O, Sigma-Aldrich) and diluted with distilled water using a ratio of 2:5. Both suspensions were filtered using syringe filters (SPARTAN 13, 0.2 and 0.45 μm) to remove aggregates. Thin layers of TiO_2 and SiO_2 were produced by using the spin-coating technique (Laurell WS-650SZ-6NPP/LITE) at 25 °C and relative humidity of the spin-coating chamber between 36% and 45%. The glass slides were alternatingly covered by 200–250 μl of TiO_2 and SiO_2 suspensions and accelerated at 1500 rpm s^{-1} to final rotation speeds ranging from 3500 to 4000 rpm. The total spin-coating process for each layer was completed in 60 s. Afterwards, the sample was put into a muffle furnace (Nabertherm, L3/11/B810) for calcination at 400 °C for 15 min. The same procedure was applied to deposit the desired number of 6 bilayers. The refractive indices of single thin films at various ethanol saturation pressures were characterized by spectroscopic ellipsometry (performed on a Woollam M200D variable-angle ellipsometer in the entire spectral range of 250–1000 nm at an angle of incidence of 75°) by using the Cauchy model. The SEM micrograph was recorded with a JEOL JSM-6500F scanning electron microscope at 5 kV.

OLED and OPD fabrication

OLEDs were fabricated on a glass substrate covered with a structured indium tin oxide (ITO) transparent electrode (40 Ω sq^{-1}). The substrates were cleaned in an ultrasonic bath, in isopropanol. Then, the samples where transferred into a glovebox with N_2 atmosphere where the OLED fabrication was performed. First, a 20-nm thick PEDOT:PSS (Clevios) layer was deposited using the spin-coating technique to smoothen the surface and to improve the injection of holes into the active polymer. Subsequently, the poly(para-phenylene vinylene) copolymer Super Yellow (Merck PDY-132, 0.5 wt.%) dissolved in toluene was spin coated onto the sample, with the layer thickness of ∼80 nm. The solution

was prepared 24 h prior to use and kept at room temperature. Subsequently, the samples were transferred into a high-vacuum chamber (Leybold) at a pressure of $\approx 10^{-6}$ mbar to deposit the top electrodes through a shadow mask. The electrodes were evaporated by means of a thermal physical vapor deposition method in the following sequence: first, a 25-nm Ca layer, and, afterwards, a 125-nm Ag layer. The OLEDs were encapsulated with a microscope glass coverslip glued (Araldite 2011, Huntsman) on top of the device. The OLEDs were biased with a voltage source at 4.5 V, which resulted in a current of about 2 mA, giving a power dissipation of 9 mW. The OLEDs were switched on 30 min before each experiment was started to ensure a good thermal equilibration.

An OPD was fabricated, first, by spin coating a layer $\approx$ 20 nm of PEDOT:PSS 4083 (Clevios) onto the ITO-coated side of a glass slide used for the BS fabrication described above, followed by a 300-nm thick layer of the active polymer P3HT:PCBM blend with a mixing ratio of 1:1, dissolved in 1,2-dichlorobenzene and stirred overnight at 60 °C. Subsequently, a 150-nm top aluminum electrode was deposited *via* PVD and encapsulated by gluing a glass coverslip on top of the layer stack. We applied a reverse bias of –4 V for one hour to stabilize the device before the first measure. The OPD biased at –2 V shows high photosensitivity between 350 and 650 nm.

Chemical analyte sensing

To prepare a miniature PDMS flow chamber for the OLED-1D PC-OPD stack we used the Sylgard 184 elastomer kit (Dow Corning). First, PDMS was combined with the curing agent in the Petri dish in the ratio of 10:1, respectively, filling the dish to approximately 4–5 mm, and was vigorously mixed to ensure a good intermixing. Then, the mixture was covered with a Parafilm for around 30 min to allow the gas bubbles to dissipate; the mixture was cured in the oven at 120 °C for 1 h. Afterwards, in a 2.5 × 2.5 cm² square piece of the PDMS mold a window of $\approx$ 2 × 2 cm² was cut out, providing the chamber for the vapor. Additionally, we made an inlet for the gas tube by piercing a syringe needle through one side of the chamber and then inserting the µL pipette tip, which was connected with the external flow controllers, the outlet for the gas chamber was provided by cutting out a $\approx$1 × 1 mm hole in the neighboring side of the chamber. The surface of the PDMS flow chamber was first activated in the plasma cleaner and then sandwiched between the OLED and BS to ensure a tight contact and a chamber of 20 × 20 × 4 mm³ volume for the gas measurement. Two different gas-flow setups where used to mix

ethanol vapor with N_2 with the respective concentration, a gas–liquid setup and a gas–gas setup. For the range between 0 and 260 ppm we used a gas–gas setup employing two gas mass-flow controllers (Bronkhorst) for controlled mixing of the N_2 carrier gas and the ethanol calibration gas mixture (Dräger). The gas–liquid setup (Bronkhorst) utilized a liquid mass-flow controller and a vaporizer with a subsequent mass-flow-controlled carrier-gas flow for ethanol concentrations above 260 ppm. To deliver the vaporized analyte of interest into the chamber under the desired relative pressure, digital mass-flow controllers (EL-FLOW F201CV-500RAD-33-V and μ-FLOW L01-RAD11–0–80S, Bronkhorst High-Tech) were used. The carrier gas nitrogen (flow rate 200 ml/min) and the liquid ethanol (flow rate was varied between 0 and 1.5 g/h) were dosed into the heated CEM (controlled evaporation and mixing) system (W101A-130-K, Bronkhorst High-Tech), where ethanol was vaporized at 110 °C and mixed with the carrier gas, and further delivered into the test chamber. During the delivery of the vaporized analyte into the chamber, the digital mass-flow controllers provide an oscillating flow pattern, which results in a measurement error during recording of the spectra, which tends to increase at higher relative pressures. The ethanol relative pressure was calculated using the software FLUIDAT in the subsection "CEM calculation" [29], which takes into account the atmospheric pressure, temperature and pressure of the individual components to determine the relative ethanol pressure p/p_0 (i.e. the fraction of partial ethanol pressure (p) and saturation pressure (p_0)) which ranges from 0 – for 100% nitrogen – to 1 for ethanol-saturated nitrogen vapor. The ratio p/p_0 can also be expressed on the percentage scale from 0 to 100%. A similar setup with the digital mass-flow controllers (EL-FLOW F201C and μ-FLOW L01–70S, Bronkhorst High-Tech) was used for recording the dependence of the refractive index on the relative pressure of ethanol *via* spectroscopic ellipsometry.

5.1.3. RESULTS AND DISCUSSION

The scheme of the proposed miniaturized sensing platform shown in Figure 5.1.1a features a chemically sensitive, optically responsive element – the 1D photonic crystal – sandwiched between an OLED and an OPD. This sandwich architecture acts like a transducer, translating the optical response of the 1D PC into an electrical signal. Specifically, exposure of the environmentally sensitive 1D PC to an analyte leads to a shift of the photonic stopband, which is translated into an intensity change of the OLED transmission through the PC, resulting in a change of the OPD current. Figures 5.1.1b–d depict a

photographic image of the sensor and its individual components, respectively. The test gas is led into a small polydimethylsiloxane (PDMS) chamber between the PC and the OLED, which isolates the system from ambient air and guides the analyte gas mixture over the surface of the BS through an in- and outlet hole. The PC consists of 6 bilayers of porous nanoparticle-based TiO_2 and SiO_2 featuring a pronounced photonic stop-band due to the high RI contrast of the layers. Figure 5.1.1e outlines a SEM micrograph of the layer composition, showing the TiO_2 as bright stripes and the SiO_2 as dark stripes.
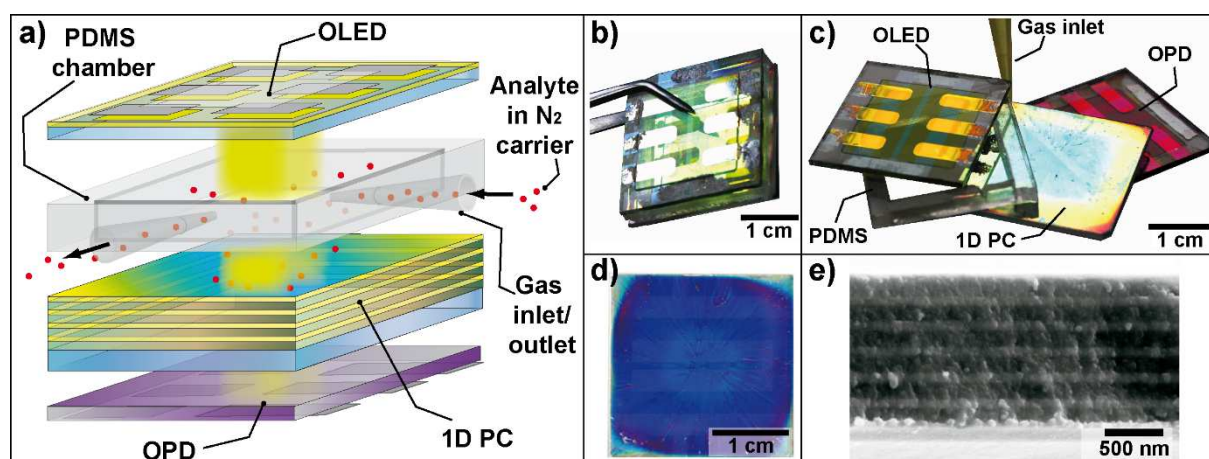
Figure 5.1.1. (a) The scheme of the proposed electrophotonic sensor: An OLED emits through the PDMS chamber, which is continuously purged with the analyte of interest mixed with a gas carrier, and through the responsive 1D PC, which is being infiltrated through the top layer with the analyte at various relative pressures. The modulated intensity of light is detected by an OPD, which translates the decrease/increase of the light intensity into a current change. (b) Photograph of the integrated sensing platform shown in Scheme 5.1.1a. (c) Photograph of the individual components of the sensor shown in Scheme 1a. (d) Photograph of the 1D PC deposited on the ITO-coated glass. (e) Cross-sectional SEM image of the 1D PC, composed of 6 nanoparticle-based SiO_2 (dark layers)/TiO_2 (bright layers) bilayers.
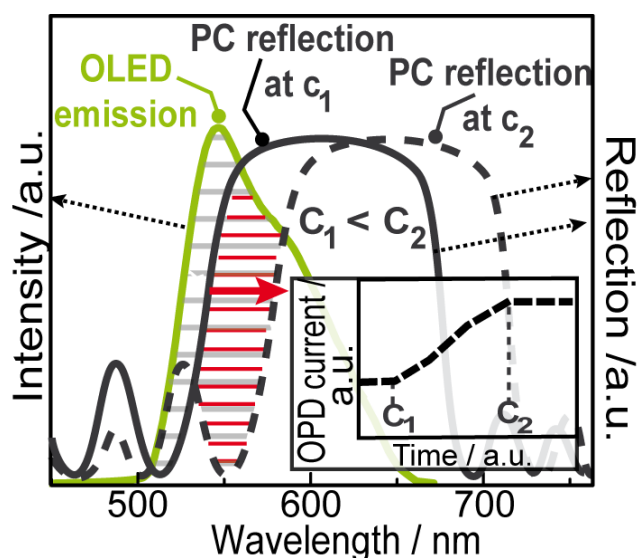
Figure 5.1.2. Schematic illustration of the detection principle, showing the photonic stop-band positions corresponding to two different gas concentrations ($C_1 < C_2$) and the emission spectrum of the OLED: A PC at concentration C_1 transmits less incident OLED light compared to the PC at a higher concentration C_2. The inset schematically shows the corresponding change of OPD current, resulting from the increase in the intensity of the transmitted light.

The choice of the individual layer thicknesses was dictated by the emissive properties of the fabricated OLED, which has an emission intensity maximum of 550 nm and emits photons in the range of 500–650 nm. The chosen layer thicknesses were the result of an optimization procedure towards a maximised response of transmitted light for a given stop-band shift, thus, the fabricated stack of 6 bilayers composed of nanoparticle-based TiO_2 (thickness ≈70 nm, with RI ≈ 1.7) and SiO_2 (thickness ≈130 nm, with RI ≈ 1.3) thin films allows for the optimal tuning of the OLED intensity exactly in the required range of frequencies. For the design of a sensitive PC-based sensor two main criteria are important: (i) the position and (ii) the shape of the stop-band. The position of the stop-band should be chosen such that the steepest slope lies in the peak wavelength of the emission spectrum of the light source. The shape should be designed such that the slope is constant over the whole wavelength range of the emitted light. Besides these criteria it is still a major challenge to fabricate a PC that exhibits large shifts of the stop-band position when exposed to analytes, which, in turn, gives rise to a high sensitivity. In our device, the TiO_2 and SiO_2 nanoparticle layers both feature high textural porosities, rendering the PC sensitive for the detection of various analytes, as we have previously demonstrated.[12]
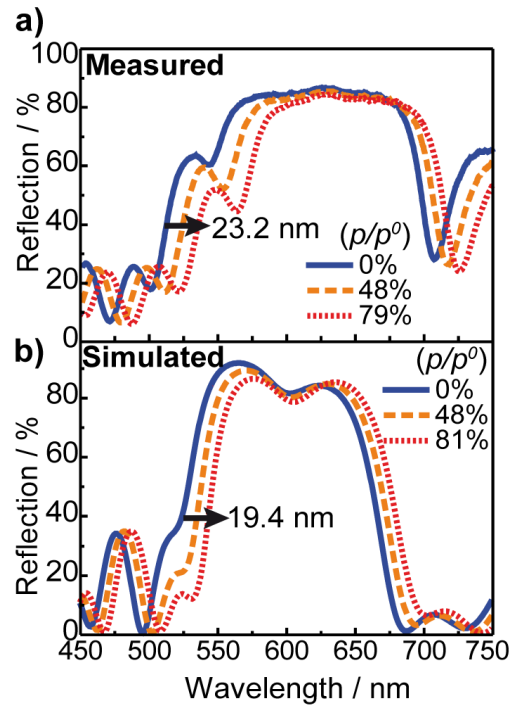
Figure 5.1.3. (a) Reflection spectra of the 1D PC shown in Figure 5.1.1d, taken under normal incidence of light, demonstrate a red shift (23.2 nm) for relative ethanol pressures (p/p_0) from 0 to 79%. (b) Simulated reflection spectra of the photonic stop-band shift of the 1D PC with 6 SiO_2/TiO_2 bilayers. Simulations are based on the thickness information for the individual TiO_2 and SiO_2 layers in the multilayer stack (obtained by SEM on the PC shown in Figure 5.1.1e) and the refractive indices of SiO_2 ($n_{0\%} = 1.3249$, $n_{47\%} = 1.3535$, $n_{81\%} = 1.3845$) and TiO_2 ($n_{0\%} = 1.7180$, $n_{47\%} = 1.7339$, $n_{81\%} = 1.7584$) thin films at ethanol vapor saturations of 0%, 47% and 81%.

For the optical read-out we have chosen an organic light emitter and an organic photodetector, which can be processed from solution over large areas, thus opening the way to low-cost, possibly disposable sensors. The fabrication of the OPD and PC on the same substrate greatly reduces the system complexity. The resulting output signal, a DC current from the OPD representing the light intensity, is coupled with the stop-band position of the PC. The impact of the photonic stop-band position on the light intensity is illustrated in Figure 5.1.2, which schematically shows the photonic stop-band positions corresponding to two different gas concentrations ($C_1 < C_2$) and the emission spectrum of the OLED. The stop-band shift – a measure of the analyte concentration – is then derived by comparing the initial OPD current without analyte exposure to the value that is measured during exposure. From the ratio of the current response to the initial current we can calculate the normalized response (NR) of the sensor according to the following Equation (2):

$$NR = \frac{I_r - I_i}{I_i} \cdot 100\% \quad , \quad (2)$$

where I_i is the initial OPD current as a reference measured in a N_2 atmosphere, and I_r is the OPD current after analyte exposure.

The optical reflection spectrum upon exposure to ethanol vapor in nitrogen gas has been recorded at various ethanol concentrations, as outlined in Figure 5.1.3a. As predicted, the photonic stop-band shifts to the red as the pores that were formerly filled with nitrogen (RI = 1) are filled with ethanol (RI = 1.36) instead, hence giving rise to an increased effective RI and, thus, optical thickness. From Equations (1) and (2) we can deduce that an increase in optical thickness results in a stop-band shift to longer wavelengths. The measured overall shift between the two extreme cases, nitrogen atmosphere and a $\approx$ 80% saturated ethanol–nitrogen gas mixture, is 23.2 nm. It can be observed in Figure 5.1.3a that the reflectivity decreases with the ethanol content in the gas. The decrease of reflectivity originates from a decreasing RI contrast between the TiO_2 and SiO_2, as the simulation suggests (Figure 5.1.3a, bottom). From ellipsometry measurements we know that the RI of SiO_2 increases more pronouncedly compared to that of TiO_2, thus decreasing the RI contrast. In order to verify the measured result with our assumption that all layers are equally infiltrated, we simulated the reflection spectrum using the ComSol Multiphysics software.[30] The RI values of SiO_2 ($n_{0\%}$ = 1.3249, $n_{47\%}$ = 1.3535, $n_{81\%}$ = 1.3845) and TiO_2 ($n_{0\%}$ = 1.7180, $n_{47\%}$ = 1.7339, $n_{81\%}$ = 1. 7584) thin films at ethanol vapor saturations of 0%, 47% and 81%, respectively, were determined by spectroscopic ellipsometry and the thickness information for the individual TiO_2 and SiO_2 layers in the multilayer stack (38 and 114 nm in bilayer #1, 70 and 139 nm in #2, 74 and 127 nm in #3, 74 and 135 nm in #4, 74 and 122 nm in #5, 74 and 143 nm in #6) has been obtained from the SEM micrograph shown in Figure 5.1.1e. Figure 5.1.3b shows the simulation of a 6-bilayer SiO_2/TiO_2 structure on a glass substrate providing a shift of 19.4 nm for an ethanol saturation (p/p_0) of 81%. The value is comparable to the shift of 23.2 nm we measured for an ethanol saturation of 79%. The measurements were taken under slightly different process conditions, which resulted in slightly different saturation ratios for the same mass flow. However, from these results we can state that all layers are fully infiltrated by ethanol within less than 60 s of exposure. Further simulations show that a partial infiltration of the layer decreases the shift to an extent roughly linearly proportional to the number of infiltrated layers.
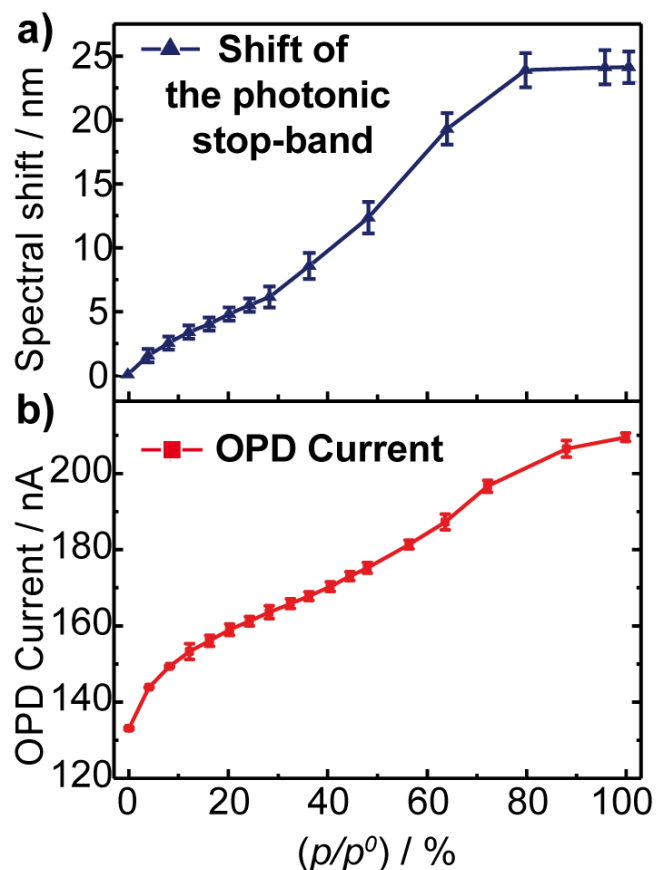
Figure 5.1.4. (a) The spectral shift of the stop-band when exposed to relative ethanol pressures (p/p_0) varying from 0 to 100%, as measured with a spectrometer. (b) The OPD current as a function of the relative ethanol pressure demonstrates the correlation between the stop-band shift and the OPD response. The measurement error results from an oscillating flow pattern provided by the digital mass-flow controllers.

After this basic characterization of the stop-band shift we moved to a simplified read-out using the proposed setup shown in Figure 5.1.1a with an OLED-PC-OPD system translating the ethanol concentration into an electric current. The OLED-PC-OPD setup was exposed to an ethanol saturation between 0 and 100%, such that the stop-band of the PC was tuned by 23.2 nm shown in Figure 5.1.4a and the OPD photocurrent followed accordingly with an increase from 133 nA to almost 210 nA, as shown in Figure 5.1.4b. We obtained a normalized response value (NR) of $\approx 60\%$ for the relative pressure change of ethanol vapor from 0 to 100%, calculated according to Equation (2).

Figure 5.1.5. (a) Response curve of the proposed sensor to changes in the concentration of the ethanol vapor, ranging from 0 to 260 ppm. The sensor was exposed to the gas mixture for 1 min and afterwards flushed with pure nitrogen for another minute. (b) Normalized response (NR) of the sensor calculated from Eq. (2) showing a linear behavior of the OPD current for low concentrations of ethanol and a response of 0.9% at an ethanol concentration of 260 ppm. (c) The response t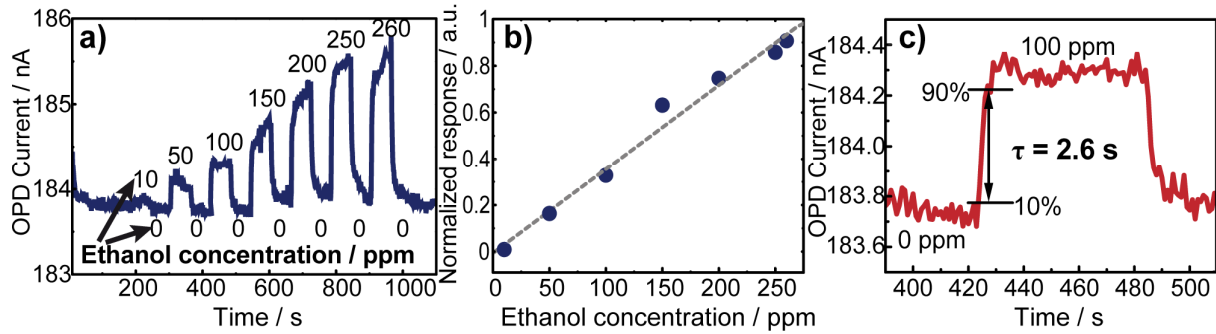ime of the sensor for a change of ethanol concentration from 0 to 100 ppm was measured to be 2.6 s for the response from 10% to 90% of the final value.

As mentioned above, in gas-sensing applications one is often interested in detecting very small traces of a gas. We were interested in the minimum shift that can be detected with this setup. As shown in Figure 5.1.4b the OPD current for low concentrations (0 to 4% ethanol saturation) changes at 7.4 nA nm⁻¹. We know from statistical noise analysis that the root-mean-square (RMS) noise lies around 0.2 nA. Thus, we can extract a signal-to-noise-ratio (SNR) of 1 for a shift of only 27 pm. This very high precision, which indeed exceeds the performance of most spectrometers by one order of magnitude, needs of course to be demonstrated in a practical detection of an analyte. We therefore took a response curve for ethanol concentrations in nitrogen from 10 to 260 ppm and an exposure time of 60 s for each interval as shown in Figure 5.1.5a. After the exposure interval the chamber was flushed with nitrogen for another 60 s to show the reversibility of the ethanol response. The response of the OPD current to ethanol originates solely from the adsorption of ethanol molecules in the PC and the resulting stop-band shift, as experiments with the same setup but without PC do not show a response. The response curve plotted in Figure 5.1.5a shows a steady increase of the OPD current with rising ethanol concentration. The nitrogen flush cycles after exposure to ethanol clearly show the fast desorption of the ethanol molecules from the PC pores. For this response curve the normalized response (NR) has been calculated according to Equation (2) and plotted in the inset of Figure 5.1.5b. It can be observed that the response increases fairly linearly to more than 0.9% for a concentration of 260 ppm ethanol vapor in nitrogen, implying that the measured current under ethanol exposure was 0.9% higher than the initial current of roughly

183.8 nA. An important parameter besides the NR is the response time of the sensor that, as for all sensors controlled by diffusion processes, can be very long. We have therefore measured the response time after which 90% of the maximum response has been reached. The response time for a change in the ethanol concentration from 0 to 100 ppm has been determined to be $\tau = 2.6$ s, as illustrated in Figure 5.1.5c, which is among the fastest for reported sensors, and at the same time a heater or an active recovery phase are not required.[31,32]

5.1.4. CONCLUSION AND OUTLOOK

In conclusion, we demonstrate a miniaturized photonic sensing platform that utilizes an OLED and an OPD to convert the color shift of a stimuli-responsive 1D PC into a current signal. The capabilities of this integrated, miniaturized detection platform based on a porous TiO_2/SiO_2 stack was exemplified by using an ethanol–nitrogen gas mixture, showing a response down to 10 ppm ethanol at room temperature. The photonic stop-band shift was simulated based on the measured thickness and RI of the single layers, suggesting that all the layers of the PC are infiltrated by the analyte after 60 s of exposure. The relation between photocurrent and stop-band shift for low concentrations was determined to be 7.4 nA nm^{-1}, which translates into a sensitivity of as small as 27 pm without signal processing at an integration time of 100 ms. Longer integration times and the use of low-noise amplifiers such as lock-in amplifiers could even lower the detectable shift. It should be emphasized that the proposed sensing platform is generic and can be used in combination with virtually any environmentally responsive photonic crystal to electronically detect minute optical shifts without requiring an expensive spectrometer. Further investigation of the response time and ad- and desorption behavior of the sensing device points out several advantages compared to existing sensors. The low power consumption renders the device also suitable for wireless and battery-driven devices. The selectivity can be tuned and enhanced by surface functionalization of the layers and by the intrinsic structure of the active PC layers.[15, 17, 33, 34]

ACKNOWLEDGEMENTS

5.1.5. BIBLIOGRAPHY

(1a)   Walt, D. R. *ACS Nano,* **2009***, 3*, 2876.

(1b)   BCC Research LLC, Environmental Sensing and Monitoring Technologies: Global Markets – Report Code: IAS030B, Wellesley, MA (**2011**), http://www.bccresearch.com.

(2a)   Arregui, F. J. *Sensors Based on Nanostructured Materials,* Springer Science, USA, **2009**.

(2b)   Stewart, M. E.; Anderton, C. R.; Thompson, L. B.; Maria, J.; Gray, S. K.; Rogers, J. A.; Nuzzo, R. G. *Chem. Rev.* **2008**, *108*, 494.

(3)   Von Freymann, G.; Kitaev, V.; Lotsch, B. V; Ozin, G. A. *Chem. Soc. Rev.* **2013**, *42*, 2528.

(4)   Kim, E.; Kim, S. Y.; Jo, G.; Kim, S.; Park, M. J. *ACS Appl. Mater. Interfaces* **2012**, *4*, 5179.

(5)   Joannopoulos, J. D. *Photonic Crystals: Molding The Flow of Light* (Princeton University Press, Princeton, NJ, USA, **2008**) 2nd edn.

(6)   Colodrero, S.; Ocaña, M.; Míguez, H.; *Langmuir* **2008**, *24*, 4430.

(7)   Chow, E.; Lin, S. Y.; Johnson, S. G.; Villeneuve, P. R.; Joannopoulos, J. D.; Wendt, J. R.; Vawter, G. A.; Zubrzycki, W.; Hou, H.; Alleman, A. *Nature* **2000**, *407*, 983.

(8)   Ren, K.; Li, Z.-Y.; Ren, X., Feng, S.; Cheng, B.; Zhang, D.; *Phys. Rev. B* **2007**, *75*, 115108.

(9)   Calvo, M. E.; Colodrero, S.; Hidalgo, N.; Lozano, G.; López-López, C.; Sánchez-Sobrado, O.; Míguez, H.; *Energy Environ. Sci.* **2011**, *4*, 4800.

(10)   Alexeev, V. L.; Das, S.; Finegold, D. N.; Asher, S. A. *Clin. Chem.* **2004**, *50*, 2353.

(11)   Arsenault, A. C.; Míguez, H.; Kitaev, V.; Ozin, G. A.; Manners, I. *Adv. Mater.* **2003**, *15*, 503.

(12)   Pavlichenko, I.; Exner, A. T.; Logvenov, G.; Scarpa, G.; Lugli, P.; Lotsch, B. V. *Can. J. Chem.* **2012**, *90*, 1069.

(13)   Burgess, I. B.; Koay, N.; Raymond, K. P.; Kolle, M.; Lončar, M.; Aizenberg, J. *ACS Nano* **2012**, *6*, 1427.

(14)   Burgess, I. B.; Mishchenko, L.; Hatton, B. D.; Kolle, M.; Lončar, M.; Aizenberg, J. *J. Am. Chem. Soc.* **2011**, *133*, 12430.

(15)   Raymond, K. P.; Burgess, I. B.; Kinney, M. H.; Lončar, M. Aizenberg, *J. Lab Chip* **2012**, *12*, 3666.

(16)   Lotsch, B. V.; Knobbe, C. B.; Ozin, G. A. *Small* **2009**, *5*, 1498.

(17)   Hinterholzinger, F. M.; Ranft, A.; Feckl, J. M.; Rühle, B.; Bein, T.; Lotsch, B. V. *J. Mater. Chem.* **2012**, *22*, 10356.

(18)   Kelly, T. L.; Garcia Sega, A.; Sailor, M. *J. Nano Lett.* **2011**, *11*, 3169.

(19)   Pavlichenko, I.; Exner, A. T.; Lugli, P.; Scarpa, G.; Lotsch, B. V *J. Intell. Mater. Struct.* **2012**, *24*, 18.

(20)   Chan, C. T.; Yeh, J. A. *Proceedings of the 16th International Solid-State Sensors, Actuators and Microsystems Conference, IEEE,* **2011**, 1531.

(21)   Snow, P. A.; Squire, E. K.; Russell, P. S. J.; Canham, L. T. *J. Appl. Phys.* **1999**, *86*, 1781.

(22)   Shi, J.; Hsiao, V. K. S.; Walker, T. R.; Huang, T. *J. Sens. Actuators B Chem.* **2008**, *129*, 391.

(23)   Fang, X.; Hsiao, K. S.; Chodavarapu, V. P.; Titus, A. H.; Cartwright, A. N. *IEEE Sens. J.* **2006**, *6*, 661.

(24)   Nazirizadeh, Y.; Bog, U.; Sekula, S.; Mappes, T.; Lemmer, U.; Gerken, M. *Opt. Exp.* **2010**, *18*, 19120.

(25)   Shin, K. S.; Kim, Y. H.; Paek, K. K.; Park, J. H.; Yang, E. G.; Kim, T. S.; Kang, J. Y.; Ju, B. K. *IEEE Electron Device Lett.* **2006**, *27*, 746.

(26)   Kraker, E.; Haase, A.; Lamprecht, B.; Jakopic, G.; Konrad, C.; Köstler, S. *Appl. Phys. Lett.* **2008**, *92*, 033302.

(27)   Gallegos, D.; Long, K. D.; Yu, H.; Clark, P. P.; Lin, Y.; George, S.; Nath, P.; Cunningham, B. T. *Lab Chip* **2013**, *13*, 2124.

(28)   Pavlichenko, I.; Exner, A. T.; Guehl, M.; Lugli, P.; Scarpa, G.; Lotsch, B. V. *J. Phys. Chem. C* **2012**, *116*, 298.

(29)   http://www.fluidat.com/, FLUIDAT on the Net.

(30)   http://www.comsol.com/, COMSOL Multiphysics.

(31)   Mei, L.; Deng, J.; Yin, X.; Zhang, M.; Li, Q.; Zhang, E.; Xu, Z.; Chen, L.; Wang, T. *Sens. Actuators B Chem.* **2012**, *7*, 166.

(32)   Delaunay, J.-J. Kakoiyama, N. Yamada, I. *Mater. Chem. Phys.* **2007**, *104*, 141.

(33)   Bonifacio, L. D.; Puzzo, D. P.; Breslav, S.; Willey, B. M.; McGeer, A.; Ozin, G. A. *Adv. Mater.* **2010**, *22*, 1351.

(34)   Xie, Z.; Cao, K.; Zhao, Y.; Bai, L.; Gu, H.; Xu, H.; Gu, Z. *Adv. Mater.* **2014**, *26*, 2413.

6. CHEMICAL DIFFUSION VISUALISATION AND CELL ADHESION DETECTION WITH TUNABLE ONE-DIMENSIONAL PHOTONIC CRYSTALS

In chapter 6.1 we discuss the different sensing functionalities and design modes of a generic electrophotonic detection platform based on one-dimensional stimuli-responsive photonic crystals modularly integrated with various light emitting devices and detectors. Specifically, we demonstrate the quantitative real-time analysis of the diffusion kinetics and spatial distribution of the adsorbed analyte within porous TiO_2/SiO_2 1D photonic crystals. Moreover, we report a non-invasive, real-time optical monitoring approach for evaluating the confluency, viability and proliferation rate of adhesive cells. The proposed platform can potentially be employed for medical screening applications, and point-of-care diagnostics.

6.1.   BRINGING ONE-DIMENSIONAL PHOTONIC CRYSTALS TO A NEW LIGHT: AN ELECTROPHOTONIC PLATFORM FOR CHEMICAL DIFFUSION VISUALISATION AND CELL ADHESION DETECTION

Ida Pavlichenko, Ellen Broda, Yoshiyuki Fukuda, Katalin Szendrei, Anna Katharina Hatz, Giuseppe Scarpa, Paolo Lugli, Christoph Bräuchle and Bettina V. Lotsch

Abstract

Photonic sensor technologies represent an important milestone in monitoring complex physical, chemical and biological systems. We present an integrated chemo- and bio-photonic sensing scheme drawing on the integration of one-dimensional (1D) stimuli-responsive photonic crystals (PCs) with an electrophotonic visualisation platform. We demonstrate various *modi operandi,* including the real-time mapping of spatial concentration distribution of a chemical analyte and the *ex vivo* monitoring of adhesive cell cultures, enabled by the modular combination of stimuli-responsive 1D PCs with various light emitters and detectors.

Conceptual insights

Recent progress in the development of numerous photonic crystal (PC) architectures along with a variety of state-of-the-art organic and inorganic light emitting devices and photodetectors covering a broad range of wavelengths has opened up new avenues in the photonic sensor technologies. In particular, one-dimensional (1D) PCs provide facile yet effective optical label-free detection schemes for a broad range of applications including environmental monitoring, industrial process control, food safety and others. In this work we endeavour to further expand the scope of integrated, 1D-PC-based sensing schemes and present an innovative electrophotonic sensing platform based on tunable 1D PCs, aiming for reduced cost and energy consumption, miniaturisation, high sensitivity, straightforward data processing and fast response times. By combining different types of light sources and detection schemes, we realize "smart" photonic crystals acting as optical transducers for spatially resolved refractive index

changes and as platforms to probe macroscopic bio-objects on photonic surfaces. We reveal the previously unexplored possibility to perform quantitative real-time analysis of lateral diffusion kinetics and spatial distribution of analytes adsorbed within porous multilayers, which can be of fundamental interest for studying diffusion processes in photonic multilayer systems. Additionally, a non-invasive, real-time optical monitoring approach for evaluating the confluency and viability of unlabelled fibroblast- and tumorigenic hepatocyte-type cells adhered to a biocompatible 1D PC surface is presented, which can be of interest for future cancer progression studies and for drug toxicity and pathogenicity tests.

6.1.1. INTRODUCTION

Since their conception in 1987, photonic crystals have transformed into one of the most versatile class of optical materials, particularly in the realm of sensing.[1,2,3,4] PCs are artificial nanostructures capable of molding the flow of light in one, two or three dimensions due to their unique ability to guide, restrict or block the motion of photons, which originates from the periodic variation of the dielectric constant of the media comprising the PC.[5] Well-defined physical properties together with tailored chemical functionalities of the PCs have empowered their use in label-free colorimetric sensing platforms capable of fast and reliable ambient monitoring.[6,7] Devices that spotlight facile coupling to the photonic nano- and microstructures aim for a simplified read-out, robust *modus operandi*, large-scale and low-cost production and straightforward and accurate data processing recipes.[8,9] Electrophotonic sensing devices utilize the integration of PCs with an optoelectronic detection scheme, thus transforming the optical response of a stimuli-responsive PC into an electronic signal.[10] This concept does not only provide a highly sensitive and compact read-out, but simultaneously allows for interfacing the detection panel with micro- and nanofluidic dosing or sequencing systems for the development of integrated, portable "lab-on-a chip" platforms.[11,12,13] Furthermore, implementing the electrophotonic transduction scheme in the development of compact visualisation platforms capable of time and spatially resolving dynamic processes such as thermal mapping, vapour and liquid diffusion, cellular adhesion and proliferation, and others can be key for enhanced environmental sensing, point-of-care diagnostics and biosecurity technologies.

En route with the advancement of PC-based sensors meeting the aforesaid requirements, a myriad of colorimetric and fluorometric platforms for vapour and liquid analysis have been designed, which are referred to as artificial noses.[2,14,15] Such platforms allow for a better discrimination between individual compounds in mixtures as compared to the traditional costly gas chromatography–mass spectrometry tandems.[16] An optofluidic nose based on the combinatorial "wetting in colour kit" (WICK) comprising 3D PCs - surface-modified silica inverse-opal films – has been introduced recently by Burgess *et al.*[17] WICK allows for encoding chemical information *via* unmasking visible patterns by exposure to substances with various surface tensions.[18] Photonic porous silicon (PSi) nanostructures have also proven versatile tools for chemo- and biosensing.[19,20,21,22,23] A single component optical "nose" based on stacked PSi rugate photonic crystals capable of identifying organic vapours at parts-per-million (ppm) concentrations *via* time-resolved diffusion drift analysis was suggested by Kelly *et al.*[24] In terms of cell monitoring, a number of photonic crystal-inspired visualisation platforms have been developed recently.[25] The need for quantitative, time-resolved analysis of a multitude of vital cellular processes, such as cell differentiation, chemotaxis, apoptosis, metastasis, wound healing, cell surface attachment and others without sample pre-fixing has sparked the development of an imaging technique known as photonic crystal enhanced microscopy (PCEM).[26,27] Cunningham and co-workers showed that label-free imaging of cell attachment on low-refractive-index sub-wavelength guided mode resonant (GMR) gratings is possible with 0.61 μm^2 resolution.[26] Likewise, Nazirizadeh *et al.* have demonstrated that the combination of GMR spectral mapping of a 1D photonic crystal slab with finite-difference time-domain (FDTD) simulations of the GMR allows translating the 2D real-time bright-field images into 3D topography of the adhered cells in a non-invasive fashion.[28]

Among the various PC architectures for sensing applications, 1D PCs – multilayer structures with a periodic modulation of the refractive index (RI) in one dimension referred to as Bragg stacks – are of particular practical relevance due to their low complexity as well as straightforward and inexpensive wet-chemistry-based fabrication methods. A facile optical read-out is provided by the photonic band gap (PBG), a forbidden frequency range between the air and dielectric bands, which is analogous to a band gap between the conduction and valence

bands in electronic semiconductors. Favorably, the position and shape of the PBG can be modulated by changing the lattice constant and/or the dielectric contrast of the materials constituting the PC by various external stimuli, which facilitates their application in physical, chemical and biological sensors.[29,30,31,32] In spite of the abundance of material combinations available for the fabrication of 1D PCs, the prototype materials titanium dioxide and silicon dioxide offer a range of advantages for the assembly of high-quality multifunctional multilayers, including high RI contrast, nanomorphology and surface chemistry modification possibilities, high chemical and mechanical stability, biocompatibility and self-cleaning properties of TiO_2.[33,34,35] Along these lines, Bonifacio *et al.* have realized a photonic nose biosensor by chemically "pixelating" nanoparticle-based (NP-based) TiO_2/SiO_2 stacks capable of displaying the optical fingerprints of various bacteria strains.[36,37] To address the demand for label-free, fast and reliable monitoring systems featuring an optical read-out, we have recently demonstrated an integrated "electrophotonic nose" sensing platform based on a stimuli-responsive NP-based TiO_2/SiO_2 1D PC as a sensing element integrated with an organic light-emitting diode (OLED) as light source and an organic photodetector (OPD) as light detector, which is capable of detecting ppm concentrations of organic solvents.[13]

In this work we aim to further expand the scope of integrated, 1D-PC-based sensing schemes, discuss important aspects of sensor design, and present new operational modes of the electrophotonic sensing approach in chemo- and biosensing, with a particular focus on chemical diffusion mapping and cell monitoring. The promising novel sensing applications arising from the integration of stimuli-responsive NP-based TiO_2/SiO_2 1D photonic crystals with various light emitting devices and photodetectors represent a central "three-in-one" motif of our study. We discuss possible advantages of the electrophotonic signal transduction scheme, namely the translation of the PBG position/transmittance (or reflectance) changes into an electric signal based on the judicious choice of the light source bandwidth - broadband, narrowband or monochromatic. We demonstrate the possibility to perform quantitative real-time analysis of the diffusion kinetics and spatial distribution of analytes adsorbed within porous multilayers with micrometre resolution by combining a 1D PC with broadband and narrowband light emitters and imaging arrays. Lateral diffusion of analytes into the porous multilayer has not been investigated yet based on a photonic read-out in a spatially resolved fashion to the best of our

knowledge and is of a great importance in many applications including photovoltaics, (barrier) membranes, efficient drug delivery systems and others.[38,39] Furthermore, by measuring the change in the light power signal of a monochromatic light source modulated by a 1D-PC-cell hybrid structure, we demonstrate a non-invasive, real-time, optical monitoring approach for evaluating the confluency and viability of unlabelled cells adhered to a 1D PC surface. We show the possibility to rapidly test cytotoxic effects induced by certain chemicals of interest by using the example of fibroblast surfactant-induced lysis. Furthermore, we highlight the potential of the electrophotonic platform in assessing cell proliferation on the PC surface, by monitoring the coverage of human hepatocarcinoma cells.

6.1.2. RESULTS AND DISCUSSION

A comprehensive overview of the functionalities provided by the proposed sensing platform is schematically shown in Figure 6.1.1. As can be seen, the sensing platform is composed of three major components: a *stimuli-responsive* optical element – *the 1D photonic crystal –*, *a photodetector* (spectrometer, organic/inorganic photodiode or an imaging array), and *a light source* (LS). Importantly, the latter is categorized into three classes of light emitters based on their bandwidth - namely, broadband (e. g. incandescent lamp), narrowband (e. g. LED and OLED), and monochromatic (e. g. laser) LSs. Depending on the LS used, the presented "sandwich-like" sensing setup allows for the three modes of read-out referred to in Figure 6.1.1 as "spectral tuning", "intensity tuning" and "imaging". Specifically, in the "spectral tuning" mode the classical spectroscopic read-out of the optical response of a color-tunable PC is realized – the spectral shift of the PBG induced by an external stimulus is recorded by a spectrometer in the chosen wavelength range. The next mode is "intensity tuning", in which one can tune the initial emission intensity of the light source by tuning the band gap of a responsive 1D PC and register the optical response with a photodiode or radiometer. This transduction scheme can, in principle, be realized with all three types of the above-named LSs, however, it is more straightforward to tune the intensity of narrowband and monochromatic LSs: One can deliberately design a 1D PC with tailor-made optical properties for the optimal tuning of a LS in a specific (narrow) range of wavelengths, matching the responsivity range of the chosen detector. The position of the central wavelength (λ_c) of the PBG should be chosen such that the "blue" or

"red" PBG slope corresponds with the maximum emission wavelength of the LS (as shown in the schematic insets in Figure 6.1.1). Finally, the third mode – "imaging" – is realized by integrating the 1D PC with an imaging array, such as a charge-coupled device (CCD) or a complementary metal-oxide semiconductor (CMOS) camera, and either reading out the color of the PC with a color camera, or recording the intensity change with a grayscale camera, using the "spectroscopic" or "intensity" tuning approaches mentioned afore. Below we will provide a comparative study of the presented measurement modes as well as shed light on the new application possibilities enabled by integrating 1D PCs with various light sources and detectors.
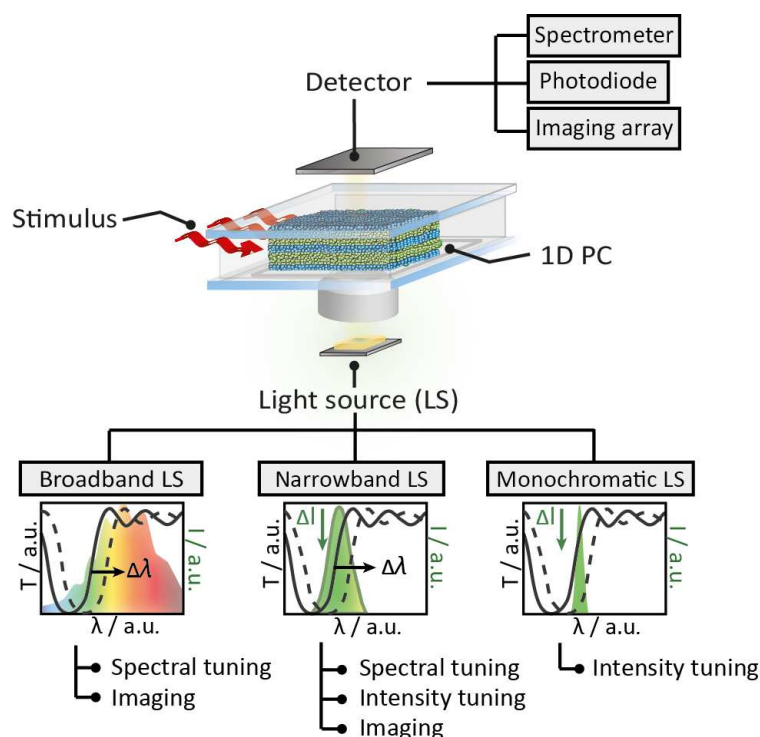
Figure 6.1.1. Schematic illustration of the suggested sensing platform featuring a stimuli-responsive 1D PC as the sensitive element, and overview of the different measurement modalities enabled by various light sources (broadband, narrowband and monochromatic LSs) and photodetectors (spectrometer, photodiodes and imaging arrays).

Firstly, we discuss previously unexplored prospects of interfacing the responsive 1D PCs with a spectrometer and imaging array to enable temporal and spatial observation of chemical diffusion processes within the 1D PC. We combine the stimuli-induced spectral tuning of the PBG, enabled by illumination with a broadband halogen lamp light source, with the quantitative analysis of the true-color images of the 1D PC obtained with an imaging array, to gain information about the spatial concentration of the analyte during the diffusion process. To

perform the above-mentioned spectral characterisation of the chosen 1D PC (as shown in Figure 6.1.2), the ethanol vapour was mixed with a N_2 carrier gas at various concentrations to achieve relative vapour pressures from 0 to 100% and continuously delivered to a polydimethylsiloxane (PDMS) chamber sandwiched between the 1D PC surface and the glass slide window (see the Supporting Information for a description of the experimental procedure). The 1D PC surface was exposed to a vapour volume of $\approx$ 2x2x0.4 cm^3 provided by the chamber. The 1D PC was composed of 9 bilayers of porous TiO_2 ($\approx$ 90 nm) and SiO_2 ($\approx$ 135 nm) nanoparticle layers, starting with a SiO_2 layer and finishing with TiO_2. Figure 6.1.2a depicts a SEM cross-section micrograph of the multilayer system, showing the TiO_2 layer as bright stripes and the SiO_2 as dark stripes (the fabrication routine is provided in the Supporting Information). The refractive index (n_D^{20}) of porous single films was determined *via* spectroscopic ellipsometry at room temperature of 20 °C as a function of ethanol relative pressure for TiO_2 ($n_D^{20}(0\%)$ = 1.875, $n_D^{20}(100\%)$ = 1.915) and SiO_2 ($n_D^{20}(0\%)$ =1.325, $n_D^{20}(100\%)$=1.385) films placed into the closed chamber. As can be seen in Figure 6.1.2b, the PBG shifts towards longer wavelengths by $\approx$ 55 nm without a loss in reflectivity ($\approx$ 95%) upon increasing the relative pressure of the ethanol vapour from 0 to 100%. By extracting the wavelength values corresponding to 60% of the reflectance for various p/p^0 (shown with a red arrow in Figure 6.1.2b) we obtain the optical isotherm of the vapour adsorption - the spectral shift as a function of the relative vapour pressure - as shown in Figure 6.1.2c. The shape of the optical adsorption isotherm corresponds to a type IV isotherm, indicating capillary condensation of the gas molecules in the textural mesopores of the material.[40] In parallel with the spectral acquisition, photographs of the 1D PC surface in RGB color space were captured with the CMOS image sensor covered with a RGB Bayer mosaic filter. Images were taken for the corresponding relative pressure values after 120 s of equilibration; p/p^0 values are indicated in the upper right corner of the individual image, as shown in Figure 6.1.2c. The photographs shown in Figure 6.1.2d were further converted into grayscale color space for calibration purposes. To perform the calibration, the relative luminance (Y) depending on the spectral sensitivity of human visual perception of brightness was calculated by using Equation 6.1, which includes the weighing of the three stacked colour channels – red (R), green (G) and blue (B):
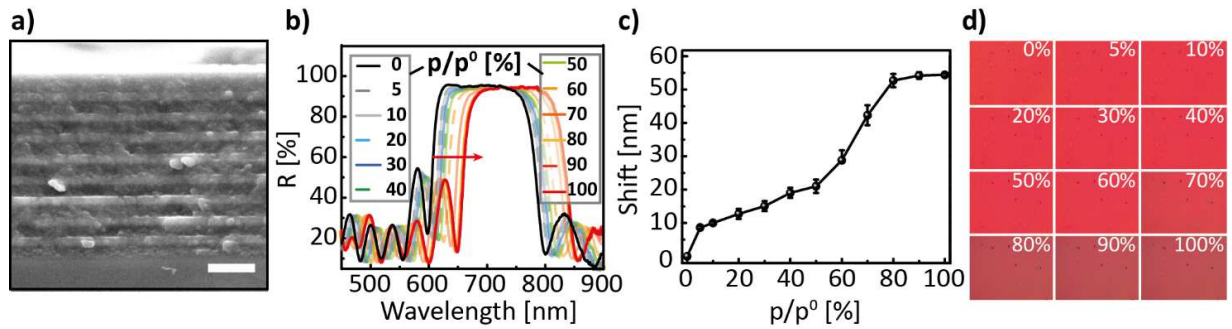
$$Y = 0.299 \cdot R + 0.587 \cdot G + 0.114 \cdot B \,. \qquad (6.1)$$

Figure 6.1.2. a) Cross-section SEM image of the investigated 1D PC, composed of 9 nanoparticle-based SiO$_2$ (darker layers $\approx$ 135 nm)/TiO$_2$ (brighter layers $\approx$ 90 nm); b) reflectance spectra of a TiO$_2$/SiO$_2$ 1D PC at normal incidence show a red shift ($\approx$ 55 nm) upon infiltration with ethanol vapour at p/p0 from 0 to 100%; c) optical isotherm for the adsorption branch of the ethanol vapour; d) photographs of the 1D PC surface captured during the acquisition of the spectra shown in Figure 6.1.2b at various p/p^0.

For a clear and fast visual representation of the diffusion process occurring in the porous multilayer systems we used a model experiment, schematically illustrated in Figures 6.1.3 a-d. At the beginning of the experiment a 3 µL droplet of liquid ethanol was carefully placed on the surface of the porous 1D PC, whose sorptive properties were already discussed in Figures 6.1.2b-d; note that for the experiment the 1D PC was also placed into the closed PDMS chamber with a glass window as in the previous experiment (Figure 6.1.2b-d). To keep the experimental conditions the same, the chamber was ventilated by a slow laminar N$_2$ gas flow of (50 mL min^{-1}). The contact angle of the ethanol droplet on the top layer of the 1D PC - the nanoparticle-based TiO$_2$ film - is 21.5 ± 1°, signifying a high wettability of the investigated multilayer for ethanol (see Supporting Information, Figure 8.1.6). During the experiment ethanol was evaporating from the surface of the 1D PC and concurrently also from the porous network of the multilayer, as schematically shown in the cross-section views of the NP-based 1D PC (see Figures 6.1.3a-d), – this dynamic diffusion process was recorded on the video by using the CMOS image sensor with the same settings as in the previous experiment to enable the correct post-processing. Figures 6.1.3e-h show the true-color photographs taken at normal incidence and depicting a 300 µm^2 area of the 1D PC (with an area of 0.1 mm^2) during the evaporation of the ethanol droplet at 0 s (e), 1.5 s (f), 2.5 s (g), 3.5 s (h), after the start of the acquisition. The obtained RGB images (Figures 6.1.3e-h) were converted into the grayscale relative luminance matrices by using Equation 6.1. Taking into account that the images in Figure 6.1.2d allowed for establishing

a calibration relation (Y (p/p^0)) between the relative luminance value and the known relative pressure, the true-color photographs in Figures 6.1.3e-h can be transformed into the two-dimensional calibrated pseudocolor maps of the ethanol relative pressure distribution during the evaporation process shown in the Figures 6.1.3i-l. Specifically, by comparing the values of the relative pressure in the pseudocolor maps in Figures 6.1.3i-l one can see that in the beginning of the evaporation process the vicinity of the droplet (an annular sector with an area of ≈0.075 mm²) is fully impregnated with ethanol (green tints corresponding to p/p^0 of ≈90-100%), while already after 1.5 s a smaller sector of the 1D PC (area of ≈ 0.038 mm²) corresponds to relative pressures of 75-90%; after 2.5 s ethanol approximately 0.010 mm² of the area of the observation was at p/p^0 of ≈ 45-65%), and after 3.5s ethanol has fully desorbed from ≈ 95% of the area of observation (as derived from the red coloration). With this experiment, we have quantitatively visualized, in a time-resolved fashion, the diffusion processes in a multilayer 1D PC system based on a photonic read-out for the first time and revealed the spatial concentration distribution of the analyte condensed in the pores.

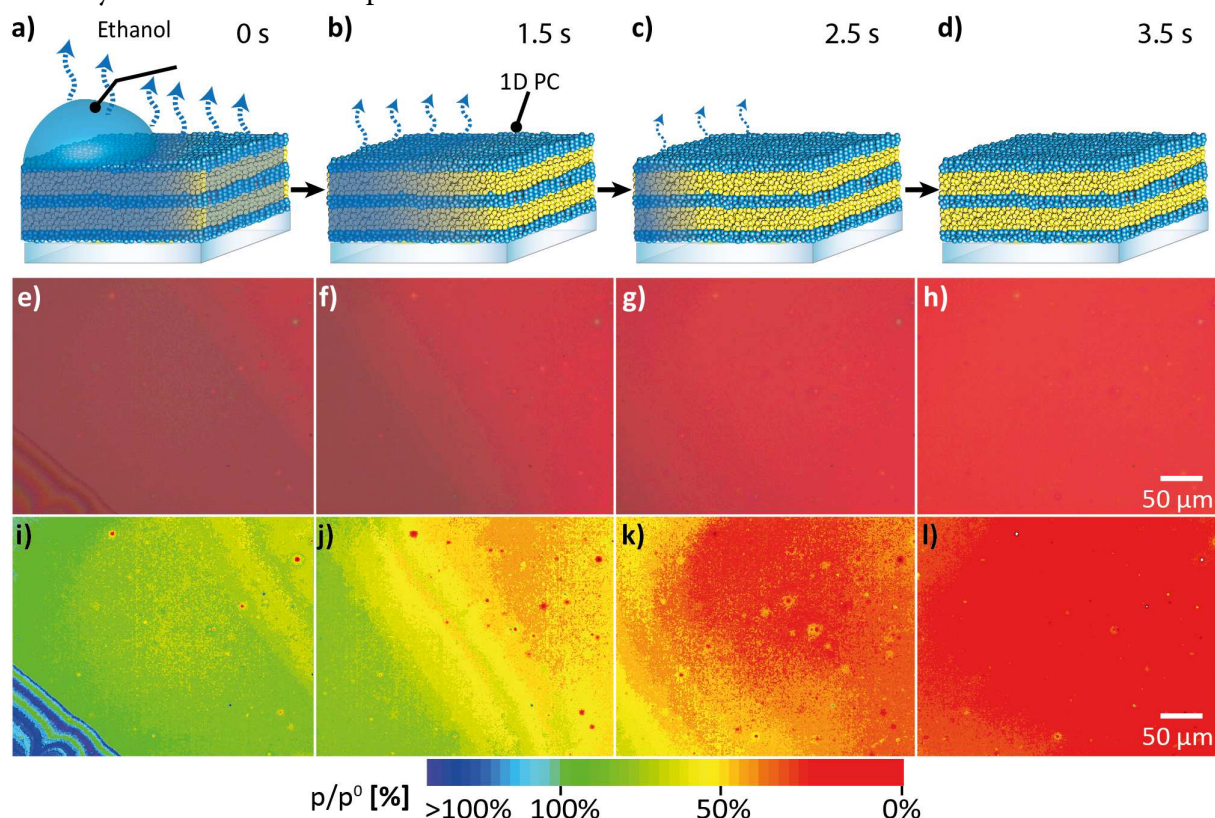**Figure 6.1.3.** Visualization of the chemical analyte diffusion in a 1D PC. Schematic illustration of the analyte droplet (e.g. ethanol) evaporating from the surface of the 1D PC, followed by evaporation of the analyte from the porous network of the multilayer at a) 0 s, b) 1.5 s, c) 2.5 s and d) 3.5 s after the start of the acquisition. Figures 6.1.3e-h show the CMOS true-colour photographs taken normally to the 1D PC surface

during ethanol evaporation at e) 0 s, f) 1.5 s, g) 2.5 s and h) 3.5 s. Figures 6.1.2i-l show the corresponding calibrated time-resolved pseudocolour maps of the ethanol relative pressure distribution during the evaporation process.

Having demonstrated the possibility to perform a quantitative analysis of diffusion maps *via* spectral tuning and imaging, in the next step we extend the capabilities of our sensing platform by introducing the second read-out mode, namely intensity tuning through an "electrophotonic nose" array (see Figure 6.1.1). To this end, we have replaced the broadband LS used in the previous measurements in Figure 6.1.2 by its narrowband analogue with a bandwidth of ≈100 nm. The experimental setup for the electrophotonic sensing platform is schematically depicted in Figure 6.1.3a, and the photograph of a prototype setup is shown in Figure 6.1.3b. The platform encompasses a tunable 1D PC placed into the closed PDMS chamber with a glass window and a volume of 1.6 cm^3, with built-in inlet and outlet for the analyte of interest (in gaseous and liquid phases), a narrowband LS (≈100 nm wide green LED centered at 550 nm) and the photodetector (e. g. a power sensor and/or the CMOS imaging array).
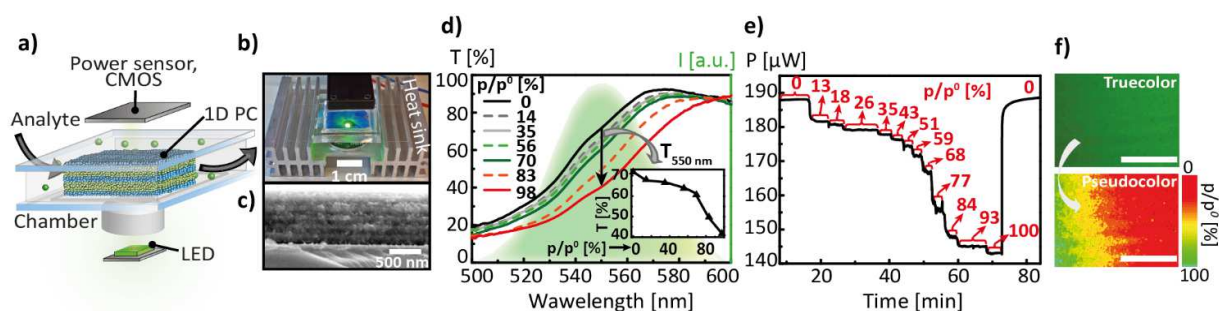

Figure 6.1.4. a) Schematic illustration of the electrophotonic platform for chemo-sensing depicts a narrowband light source shining through the tunable 1D PC located in the closed chamber, to which an analyte of interest is being delivered; b) photograph of a prototype platform based on a green LED with a wavelength band centered at 550 nm as a light source and a slim Si photodiode power sensor as a detector; c) cross-section SEM image of the 1D PC, composed of 6 nanoparticle-based SiO$_2$ (of ≈ 90 nm)/TiO$_2$ (≈ 60 nm) bilayers, the scale bar is 500 nm. The response of 1D PC to the external stimulus can be measured *via* d) the classical spectral analysis of the photonic stop band shift in the narrow range of wavelengths between 500 and 600 nm (provided by the LED), induced by the infiltration of the PC porous network with analyte (ethanol) at relative pressures (p/p^0) from 0 to 100%; the inset shows the dependence of the transmission values extracted at 550 nm on p/p^0, or *via* e) the photonic-to-electronic transduction path by measuring the modulated power of light versus time for various p/p^0 by means of a power sensor, the p/p^0 values are indicated with the red arrows for each plateau region. f) Visualization of the chemical analyte diffusion. Top: true-colour photograph of the gradient concentration distribution of ethanol in the 1D PC illuminated by green light, bottom: the corresponding calibrated pseudo-colour map of the ethanol relative pressure distribution, the scale bar is 50 μm.

For the chemical adsorption and diffusion experiments shown in Figure 6.1.4 we have modified the architecture of the 1D PC from the one used in Figure 6.1.2, to align the photonic bandgap with the emission band of the LED. As mentioned previously[13], optimisation of the layer thicknesses and RI contrast of the layers is needed in order to maximize the response of the 1D PC integrated with the LS of interest. The position of the PBG was chosen such that the steepest slope of the longer wavelength side (dielectric band) of the PBG lies in a range of 540-560 nm. To meet this criterion, we have fabricated the 1D PC with 6 bilayers of SiO_2 (of $\approx$ 90 nm)/TiO_2 ($\approx$ 60 nm) nanoparticle films, as can be seen in the cross-section SEM image shown in Figure 6.1.4c. The RIs of the single films measured for 0 and 100% relative ethanol pressure are $n_D^{20}(0\%)$ = 1.839 and $n_D^{20}(100\%)$ 1.923 for TiO_2 and $n_D^{20}(0\%)$ = 1.301 and $n_D^{20}(100\%)$= 1.355 for SiO_2. Due to the nature of the experimental setup (see Figures 6.1.4a,b)– the light from the LED is shone through the 1D PC from the bottom and analysed on the opposite side by a power sensor – we have collected the spectra in transmission mode for the spectral characterisation of analyte sorption. The response of the 1D PC to the change in relative ethanol pressure from 0 to 100% was first measured *via* the classical spectral tuning approach, see Figure 6.1.4d: The PBG red shift ($\approx$ 25 nm) was recorded in the wavelength range between 500 and 600 nm upon increasing the p/p^0 from 0 to 100%. The inset in Figure 6.1.4d displays the corresponding optical adsorption isotherm, i.e. the dependence of the transmittance values extracted at 550 nm ($T_{550\ nm}$) on p/p^0. As seen in the inset of Figure 6.1.4d, the convolution of the spectral properties of the LED and the tunable PC leads to a *decrease* in the intensity of the used LS: As the "red" PBG edge shifts towards longer wavelengths (due to the increased effective refractive index of the infiltrated layers) in the range between 500 and 600 nm, the transmittance ($T_{550\ nm}$) corresponding to the LED emission peak (at 550 nm) is decreasing, thus reducing the output LED intensity. This constellation was also independently proven in the photonic-to-electronic transduction ("electrophotonic nose") experiment shown in Figure 6.1.4e. For this, the modulated power of light was measured by means of a power sensor for various p/p^0. The measured values of the power range from 140 μW to 190 μW for the LED driven at 8 mA. Similar to the experimental routine described in Figure 6.1.2d, in parallel with the spectra acquisition we have captured the photographs of the multilayer surface with a CMOS imaging array at $0 < p/p^0 < 100\%$ and performed a relative luminance analysis of the individual photographs (see Supporting Information, Figure 8.1.5) for calibrating the diffusion gradient and mapping the spatial

concentration of the analyte in the multilayer, as demonstrated in Figure 6.1.4f. In the top part of Figure 6.1.4f one can see the true-color photograph of the gradient concentration distribution of ethanol, depicted in transmission mode after 2 s from the start of the acquisition. The image appears green to the viewer due to the color of the LED. The corresponding calibrated pseudo-colour 110×81 μm² map of the ethanol relative pressure distribution is displayed in the bottom part of Figure 6.1.4f. It can be seen that after 2 s ethanol has evaporated from more than 60% of the observed PC area. Summarising the above experiments, one can conclude that in contrast to the broadband-LS-illuminated sensors featuring a colorimetric read-out as shown in Figure 6.1.2, the use of narrowband LSs such as LEDs (and OLEDs) can enhance the sensing capabilities of the 1D PC platform by additionally providing an electrophotonic read-out that allows for the design of highly compact, integrated sensors with high sensitivity in the whole range of relative pressures of the volatile analytes ($0 < p/p^0 < 100\%$). Besides, the analysis of sorption kinetics in 1D PCs integrated with narrowband light sources can also be performed with less expensive CMOS arrays without a RGB Bayer mosaic filter.

Hereafter, we address the last of the proposed read-out modes of our sensing platform – integration of the 1D PC with a monochromatic light source - to show the potential applicability of the electrophotonic platform for *ex vivo* cell monitoring. Monochromatic light is advantageous for its robustness against chromatic aberrations as well as long-term intensity stability and its collimated light beam. A schematic illustration of the cell analysis platform in Figure 6.1.5a shows the 1D PC with the cell layer, placed into a Petri dish with the buffer. The input power of the monochromatic light source (for the presented experiments we used a 532 nm laser) is first modulated by the 1D PC, and then recorded by the Si photodiode power sensor. The photographs of the employed 1D PC taken normally and at an angle of ≈ 45° are shown in Figures 6.1.5b,c (note that the ring defect in the middle of the substrate indicates a spin-coater chuck mark; this area was not used for the measurements). The large round samples were then divided into smaller pieces of about 5 mm². The PC was fabricated out of 6 NP-based bilayers starting with SiO_2 (≈ 90 nm) and finishing with a top TiO_2 (≈ 60 nm) layer, as displayed in the cross-section SEM micrograph in Figure 6.1.5d. The thickness of the layers was optimized in order to match the position of the central wavelength of the PBG with the laser emission wavelength (532 nm). By applying the intermediate calcination routine to the individual NP-

based SiO_2 and TiO_2 layers (see Supporting Information), we have obtained durable 1D PCs, possessing excellent mechanical stability upon long term exposure to fluids – the durability of the samples placed in water was up to three months and up to one month in the cell culture medium. For preliminary studies of the optical PC properties modified with adhesive cell lines we have used BHK-21 fibroblasts. In order to obtain the cell thickness distribution, we have investigated a topography of the fixed BHK-21 fibroblast monolayer on the 1D PC surface by AFM, as shown in Figure 6.1.5f. 4% paraformaldehyde was chosen as an optimal fixative enabling good optical quality of the BHK-21 cells, preserving the fibroblastic morphology and preventing the presence of debris on the substrate.[41] The measured thickness of the cells fixed after 24 h of incubation ranges between 50 and 900 nm. Furthermore, the overlay fluorescence image of the fixed BHK-21 cells attached to the 1D PC after 24 h of incubation in Figure 6.1.5g shows the distribution of TRITC-phalloidin dye ($\lambda_{emission}$ at $\approx$ 573 nm) in F-actin filaments, indicated by red color, and Hoechst-33342 ($\lambda_{emission}$ at $\approx$ 497 nm) in the double stranded DNA, indicated by blue color, proving that the cells remained adherent and viable on the PC surface. To estimate the impact of the adhered cell layer on the optical properties of the 1D PC, we have carried out simulations in *Comsol Multiphysics RF Module*.[42] Figure 6.1.5g represents a comparison of the simulated transmittance spectra of the PBG of the 6 bilayer 1D PC (SiO_2 thickness of 90 nm; TiO_2 thickness of 60 nm) without the cell monolayer (black curve) and the PC covered with a 100% confluent cell layer with an effective thickness of 200 nm (the average cell thickness value determined from the AFM topographic map in the Figure 6.1.5f) and a refractive index of 1.40[43] (gray curve). The simulation was performed based on the assumption that the pores of the multilayer are filled with cell medium liquid ($RI_{eff/titania}$ = 1.35, $RI_{eff/silica}$ = 1.90). As a result, a significant decrease in transmittance by 7% measured at 532 nm (from 18% to 11%), due to the introduction of the cellular monolayer onto the PC, was predicted by our simulations. Consequently, one should expect a decrease in the laser signal shining through the PC covered with cells compared to the bare PC. Noteworthy, a similar decrease of 7.5% in the reflectance was reported for a porous SiO_2 Fabry–Pérot thin film upon immobilisation of an *E. coli* bacterial layer.[44] The experimental transmittance spectra of the used 1D PC with (gray line, "+") and without (black line, "-") the fixed BHK-21 cell layer are shown in Figure 6.1.5h. The spectra were obtained for the PC immersed into 2 mL of transparent CO_2-independent cell medium (dashed lines, "M") and for the PC without cell medium (in ambient air) at relative

humidity of 21 % (solid lines, "NM"). Figure 6.1.5h gives a visible explanation for the above-discussed choice of the lattice parameter and the morphology of the 1D PC. It can be clearly seen that upon filling the pores of the layers with the cell medium the effective refractive index of SiO_2 and TiO_2 increases and, thus, the spectrum (black solid and dashed lines) shifts by ≈ 55 nm towards longer wavelengths, such that the PBG matches with the emission peak of the laser at 532 nm. By comparing the spectra in Figures 6.1.5g and 6.1.5h for the PC placed in the cell medium (dashed lines) with and without a cell layer, one can see a clear correlation between the simulated and the experimental plots. Similarly as the simulated curves, the experimental results demonstrate a decrease of 8% in the transmittance at 532 nm upon introducing the cell layer. Hence, we have shown that adding an additional "defect" cell layer on the surface of a 1D PC leads to a decrease in the output light intensity of the monochromatic light source.
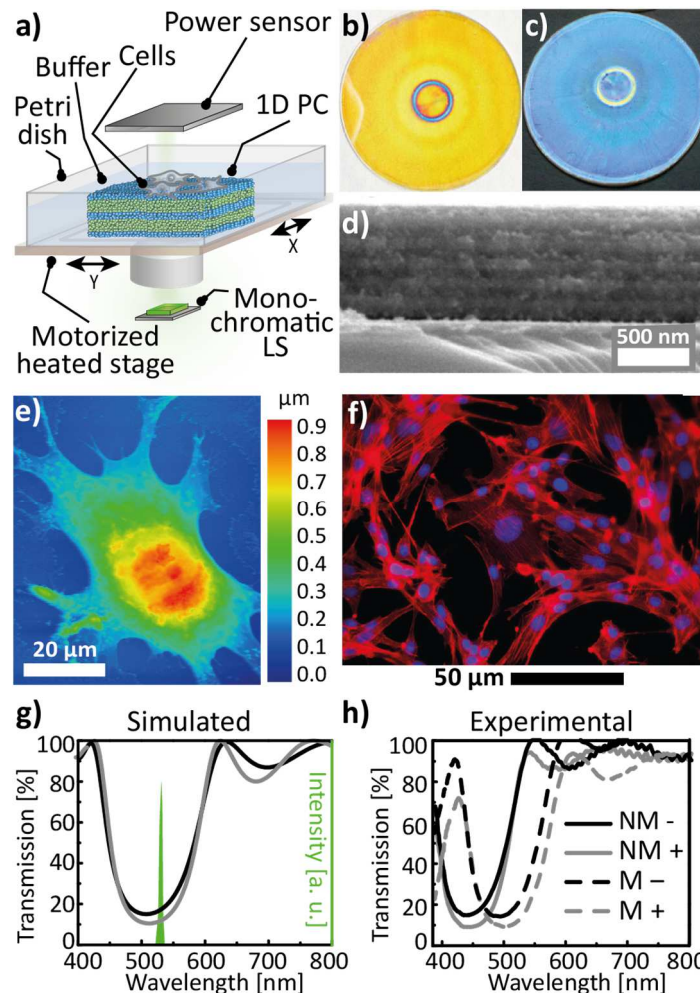

Figure 6.1.5. a) Schematic illustration of the electrophotonic platform for cellular sensing: A 1D PC is placed into a buffer solution in the Petri dish and covered with cells, and the modulated power of the monochromatic LS is recorded by the power sensor. The photographs of the employed 1D PC taken

normally (b) and approximately at 45° (c) to the PC surface (the diameter of the round substrate is 5 cm); d) cross-section SEM image of a 1D PC composed of 6 nanoparticle-based SiO_2 ($\approx$ 90 nm)/TiO_2 ($\approx$ 60 nm) bilayers. e) AFM topography of the fixed BHK-21 fibroblast cell on a 1D PC, and f) fluorescence image of BHK-21 attached to the 1D PC after 24 h of incubation showing the distribution of F-actin and nuclear DNA inside the cells. g) Simulated transmission spectra of the 1D PC PBG show a decrease in transmission by 8% from a PC with no cells on top (black curve) to a PC covered with a 200 nm thick cell layer (gray curve), leading to a decrease in the emission intensity of a 532 nm laser (green spectrum). h) Experimental transmission spectra of the 1D PC PBG measured in various milieus: in air (solid lines indicated by "NM"), in cell medium (dashed lines indicated by "M"), without a cell layer (indicated by "-") and with a 100% confluent cell layer (indicated by "+").

Cell adhesion is known for playing a substantial role in progression and metastasis of cancer cells and is crucial for establishing new tumors in the body, hence methods for visualising proliferation or apoptosis/necrosis of cancer cells is of great interest. Therefore, we have tested the 1D-PC-based electrophotonic platform for studying the behaviour of a common liver cancer - a human hepatocellular carcinoma HuH7. Hepatocytes represent an established *in vitro* cell culture system for studies of drug metabolism, drug–drug interactions, enzyme induction and others. Our electrophotonic platform was used first for monitoring the HuH7 cell death induced by the addition of a detergent. Sodium dodecyl sulphate (SDS) is known for its ability to provide a fast (of the order of seconds) cell lysis due to the denaturation of the cell proteins and membranes.[45] The platform was integrated with the 532 nm laser and the power sensor as a detector. We have tested the robustness of the setup by measuring a low laser power baseline drift ($\approx$ 1%) by a Si power meter for a bare 1D PC upon illumination with the laser (output power of 94.5 $\pm$ 0.2 μW) for several hours. Herein, the settling time of the power meter (on the order of 10-20 s) - the time difference between the moment of opening the laser shutter and the time of achieving the steady state – was also taken into account. In Figure 6.1.6a we show the power response for a "control" 1D PC (without a HuH7 cell monolayer placed into the cell medium) to the addition of 100 μL of 1.5% aq. SDS three times at intervals indicated by the vertical arrows. The drops of the laser power seen on the curves are due to the momentary turbulence of the medium upon adding the SDS dose at 162, 231 and 300 s with a micropipette after the starting point of the experiment. As can be seen, the initial power signal of 94.5 $\pm$ 0.2 μW does not significantly change throughout the control test. On the contrary, a distinct behavior was

observed for the 1D PC with a confluent HuH7 cell monolayer incubated for 48 hours (see Figure 6.1.6b) for the same experimental procedure as for the "control" measurement (the stages of the SDS-induced cell lysis are schematically illustrated in Figure 6.1.6c). Firstly, it is noteworthy that the initial laser power (before adding SDS) for the 1D PC with a cell layer is 6% smaller than the "control" value, and is equal to 88.7 ± 0.2 μW. Upon adding apiece 100 μL of 1.5% aq. SDS three times in the instants indicated by the vertical arrows (60, 150 and 210 s) in Figure 6.1.6b, the signal gradually increases until it reaches the plateau value of 94.3 ± 0.2 μW. Notably, this output laser power value is identical to the one corresponding to the bare 1D PC in the "control" experiment, as indicated by the red dashed arrow in Figure 6.1.6b, and, moreover, is in agreement with the simulation prediction of 7% decrease in transmittance due to the addition of a cell layer (see Figure 6.1.5g). Additional characterisation of the 1D PC by widefield light microscopy in the transillumination mode, done before and after the treatment of the sample with SDS, is shown in Figures 6.1.6d and e. Clearly, these two photographs also confirm the detachment of the cell monolayer due to the SDS-induced lysis.
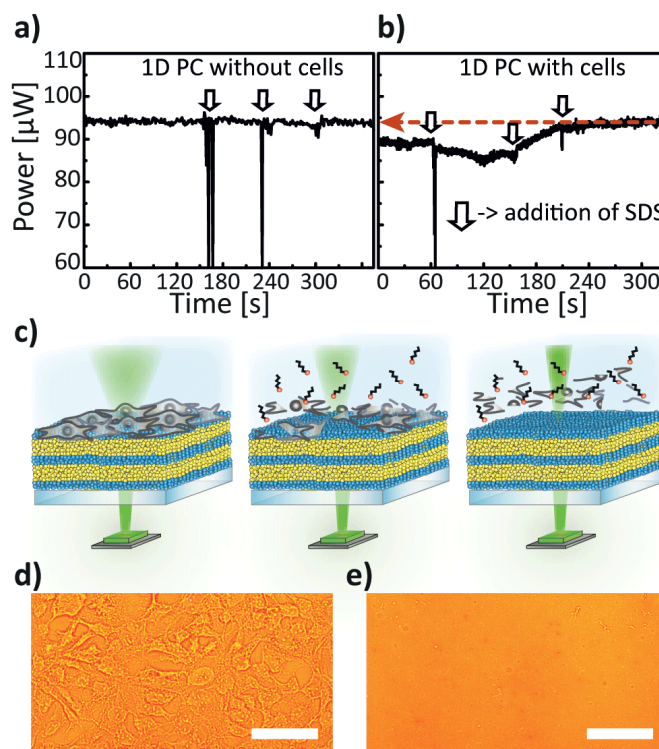

Figure 6.1.6. a and b) Monitoring of SDS-induced cell lysis with the 1D-PC-platform integrated with a 532 nm laser as LS and a power sensor as a detector: Measurement of the power response for a laser shining through a) a control 1D PC without a cell monolayer and b) the 1D PC with modified on top with a 100% confluent HuH7 cell layer upon adding to both systems 100 μL of 1.5%

aq. SDS three times (as indicated by vertical arrows in Figures 6.1.6a and b). c) Schematic illustration of the SDS-induced cell lysis electrophotonic experiment shown above in the Figure 6.1.6b. Left: the PC covered with cells before adding SDS, middle: 0.5 min after adding SDS, right: 2.5 min after the SDS addition. d) Photograph of the HuH7 cell monolayer, adhered to a 1D PC surface, captured in the transillumination mode before adding SDS and e) after adding SDS (100 μL, 1.5%) three times; scale bar = 20 μm.

Another demonstration of a non-invasive cell monitoring by our 1D-PC-based electrophotonic platform was performed *via* the real-time "visualisation" of the cell coverage on a PC surface. A schematic illustration of the performed experiment is depicted in Figure 6.1.7a: A change in the power signal of a 532 nm laser was recorded during a slow scanning of a 1D PC hybrid with a partial cell coverage in buffer with the motorized XY-stage. The laser signal was measured by means of a power meter. The 1D PC partially covered with adhered HuH7 cells, incubated in a Petri dish in a cell medium for 24 hours, was scanned in the positions (P) 1-8 in a "snake-like" fashion: P8 → P1 → P2 → P3 → P4→ P5→ P6 → P7 and back to the initial position P8. The insets in the Figure 6.1.7b show the corresponding widefield microscope images taken in the positions 1-8 with 60x magnification. Evidently, positions 1 through 4 can be characterized by a 100% confluent cell state, positions 5 and 6 by ≈ 50%, and positions 7 and 8 by 0% confluency. The corresponding laser power signal displays a behavior consistent with the microscope images (Figure 6.1.7b): In the beginning of the P8 scan the power value of 90.6 ± 0.1 μW is in agreement with the previously obtained value (94.5 ± 0.2 μW) for the PC without the cell layer from the "control" measurement (see Figure 6.1.6a). Subsequently, when the stage is brought to fully-covered P(1-4), the corresponding power value drops, and for each position it is equal to 82.1 ± 0.1 μW (decreases by 9.4%); then, in the half-covered P(5-6) the value again increases to 88.0 ± 0.1 μW, and by bringing the laser to the bare area of the PC (P7 and P8) the signal returns to the initial value of 90.6 ± 0.2 μW. Hence, we see an agreement between the confluency state of the cell monolayer and the laser power signal. The demonstrated electrophotonic analysis of the cell cluster coverage can be of interest for cancer progression studies and for drug toxicity and pathogenicity tests.
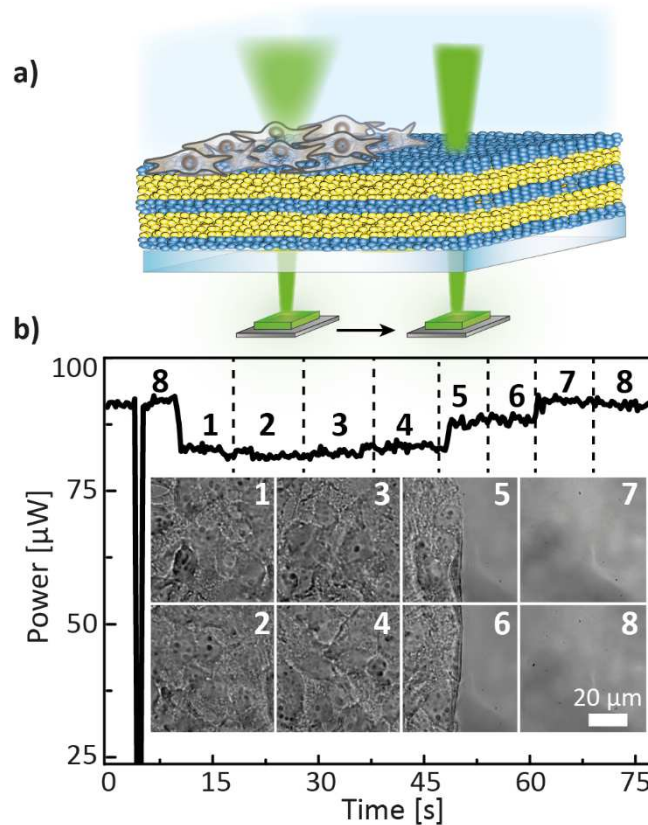
Figure 6.1.7. a) Schematic illustration of the cell coverage experiment, b) Laser power signal obtained during scanning the partially covered 1D PC with a HuH7 cell monolayer in the positions 1-8 with a microscope stage; the black dashed lines mark the time instants of the stage position change; the inset of Figure 6.1.5 e shows the corresponding widefield microscope images taken in the positions 1-8.

6.1.3. CONCLUSIONS

In this contribution we have presented a comprehensive study harnessing the capabilities of distinct sensing functionalities and design modes of a generic 1D-PC-based electrophotonic detection platform incorporating various light emitting and detecting devices. We have demonstrated that integrating 1D PCs with narrowband light sources allows for a maximum diversity of sensing modes including the combination of spectral and intensity tuning with image processing and a straightforward photonic-to-electronic transduction scheme. We have shown the capability of the "electrophotonic nose" platform to spatially map the relative pressure distribution of a volatile analyte during the diffusion process on the surface of a PC porous network with micrometre resolution, enabling potential applications as imaging sensors with low power consumption, straightforward assembly methods and low fabrication costs. Furthermore, based on the integration of a 1D PC with a monochromatic LSs we have proposed

a label-free, non-invasive platform for *ex vivo* cell observation, which provides a complementary technique for monitoring changes in the cell motility and viability, important for applications such as the analysis of cell proliferation and differentiation, wound healing, cytotoxicity and drug screening.

ACKNOWLEDGEMENT

6.1.4. BIBLIOGRAPAHY

(1)   Zhao, Y.; Zhao, X.; Gu, Z. *Adv. Funct. Mater.* **2010**, *20*, 2970.

(2)   Burgess, I. B.; Lončar, M.; Aizenberg, J. *J. Mater. Chem. C* **2013**, *1*, 6075.

(3)   Xu, H.; Wu, P.; Zhu, C.; Elbaz, A.; Gu, Z. Z. *J. Mater. Chem. C* **2013**, *1*, 6087.

(4)   Luchansky, M. S.; Bailey, R. C. *Anal. Chem.* **2012**, *84*, 793.

(5)   Joannopoulos, J. D.; Villeneuve, P. R.; Fan, S. *Nature* **1997**, *386*, 143.

(6)   Fenzl, C.; Hirsch, T.; Wolfbeis, O. S. *Angew. Chem. Int. Ed.* **2014**, *53*, 3318.

(7)   Raymond, K. P.; Burgess, I. B.; Kinney, M. H.; Lončar, M.; Aizenberg, J. *Lab Chip* **2012**, *12*, 3666.

(8)   Walt, D. R. *ACS Nano* **2009**, *3*, 2876.

(9)   Gallegos, D.; Long, K. D.; Yu, H.; Clark, P. P.; Lin, Y.; George, S.; Nath, P.; Cunningham, B. T. *Lab Chip* **2013**, *13*, 2124.

(10)   Exner, A. T.; Pavlichenko, I.; Lotsch, B. V; Scarpa, G.; Lugli, P. *ACS Appl. Mater. Interfaces* **2013**, *5*, 1575.

(11)   Psaltis, D.; Quake, S. R.; Yang, C. *Nature* **2006**, *442*, 381.

(12)   Estevez, M. C.; Alvarez, M.; Lechuga, L. M. *Laser Photon. Rev.* **2012**, *6*, 463.

(13)   Exner, A. T.; Pavlichenko, I.; Baierl, D.; Schmidt, M.; Derondeau, G.; Lotsch, B. V.; Lugli, P.; Scarpa, G. *Laser Photon. Rev.* **2014**, 8(5), 726.

(14)   Dickinson, T. A.; White, J.; Kauer, J. S.; Walt, D. R. *Nature* **1996**, *382*, 697.

(15)   Oh, J.-W.; Chung, W.-J.; Heo, K.; Jin, H.-E.; Lee, B. Y.; Wang, E.; Zueger, C.; Wong, W.; Meyer, J.; Kim, C.; Lee, S.-Y.; Kim, W.-G.; Zemla, M.; Auer, M.; Hexemer, A.; Lee, S.-W. *Nat. Commun.* **2014**, *5*, 3043.

(16)   Yildirim, A.; Ozturk, F. E.; Bayindir, M. *Anal. Chem.*, **2013**, *85(13)*, 6384.

(17)   Burgess, I. B.; Mishchenko, L.; Hatton, B. D.; Kolle, M.; Lon, M.; Aizenberg, J. *J. Am. Chem. Soc.*, **2011**, *133* (32), 12430.

(18)   Burgess, I. B.; Koay, N.; Raymond, K. P.; Kolle, M.; Lončar, M.; Aizenberg, J. *ACS Nano* **2012**, *6*, 1427.

(19)   Dhanekar, S.; Jain, S. *Biosens. Bioelectron.* **2013**, *41*, 54.

(20)   Bonanno, L. M.; Segal, E. *Nanomedicine* **2011**, *6*, 1755.

(21)   Pacholski, C.; Sartor, M.; Sailor, M. J.; Cunin, F.; Miskelly, G. M. *J. Am. Chem. Soc.* **2005**, *127*, 11636.

(22)   Schwartz, M. P.; Derfus, A. M.; Alvarez, S. D.; Bhatia, S. N.; Sailor, M. J. *Langmuir* **2006**, *22*, 7084.

(23)   Ivanov, I. I.; Skryshevsky, V. a.; Serdiuk, T.; Lysenko, V. *Sensors Actuators B Chem.* **2012**, *174*, 521.

(24)   Kelly, T. L.; Garcia Sega, A.; Sailor, M. J. *Nano Lett.* **2011**, *11*, 3169.

(25)   Shamah, S. M.; Cunningham, B. T. *Analyst* **2011**, *136*, 1090.

(26)   Lidstone, E. a; Chaudhery, V.; Kohl, A.; Chan, V.; Wolf-Jensen, T.; Schook, L. B.; Bashir, R.; Cunningham, B. T. *Analyst* **2011**, *136*, 3608.

(27)   Chen, W.; Long, K. D.; Lu, M.; Chaudhery, V.; Yu, H.; Choi, J. S.; Polans, J.; Zhuo, Y.; Harley, B. a C.; Cunningham, B. T. *Analyst* **2013**, *138*, 5886.

(28)   Nazirizadeh, Y.; Reverey, J.; Geyer, U.; Lemmer, U.; Selhuber-Unkel, C.; Gerken, M. *Appl. Phys. Lett.* **2013**, *102*, 011116.

(29)   Calvo, M. E.; Colodrero, S.; Hidalgo, N.; Lozano, G.; López-López, C.; Sánchez-Sobrado, O.; Míguez, H. *Energy Environ. Sci.* **2011**, *4*, 4800.

(30)   Hinterholzinger, F. M.; Ranft, A.; Feckl, J. M.; Rühle, B.; Bein, T.; Lotsch, B. V. *J. Mater. Chem.* **2012**, *22*, 10356.

(31)   Pavlichenko, I.; Exner, A. T.; Guehl, M.; Lugli, P.; Scarpa, G.; Lotsch, B. V. *J. Phys. Chem. C*, **2012**, *116 (1),* 298**.**

(32)   Lotsch, B. V; Knobbe, C. B.; Ozin, G. A. *Small* **2009**, *5*, 1498.

(33)   Choi, S. Y.; Mamak, M.; von Freymann, G.; Chopra, N.; Ozin, G. A. *Nano Lett.* **2006**, *6*, 2456.

(34)   Colodrero, S.; Ocaña, M.; González-Elipe, a R.; Míguez, H. *Langmuir* **2008**, *24*, 9135.

(35)   Sio, C.; Bragg, T.; Wu, Z.; Lee, D.; Rubner, M. F.; Cohen, R. E. *Small* **2007**, *3(8),*1445.

(36)   Bonifacio, L. D.; Ozin, G. A.; Arsenault, A. C. *Small* **2011**, *7*, 3153.

(37)   Bonifacio, L. D.; Lotsch, B. V.; Puzzo, D. P.; Scotognella, F.; Ozin, G. A. *Adv. Mater.* **2009**, *21*, 1641.

(38)   López-López, C.; Colodrero, S.; Raga, S. R.; Lindström, H.; Fabregat-Santiago, F.; Bisquert, J.; Míguez, H. *J. Mater. Chem.* **2012**, *22*, 1751.

(39)   Anglin, E. J.; Cheng, L.; Freeman, W. R.; Sailor, M. J. *Adv. Drug Deliv. Rev.* **2008**, *60*, 1266.

(40)   Sing, K.S.W.; Everett, D.H.; Haul, R.A.W.; Moscou, L.; Pierotti, R.A.; Rouquerol, J.; Siemieniewska T. *Pure Appl. Chem.* **1985**, *57*, 603.

(41)   Moloney, M.; McDonnell, L.; O'Shea, H. *Ultramicroscopy* **2004**, *100*, 153.

(42)   COMSOL Multiphysics. *HTTP://www.comsol.com/.*

(43)   Bereiter-Hahn, J. *J. Cell Biol.* **1979**, *82*, 767.

(44)   Massad-Ivanir, N.; Shtenberg, G.; Zeidman, T.; Segal, E. *Adv. Funct. Mater.* **2010**, *20*, 2269.

(45)   Brown, R. B.; Audet, J. *J. R. Soc. Interface* **2008**, *5 (2)*, S131.

7. Conclusion and outlook

Rapid advancements in the photonic technologies over the last decades have remarkably amended the field of photonic physical, chemical and biological sensors.[1,] Recent progress in the development of numerous stimuli-responsive photonic crystals (PCs) along with a variety of state-of-the-art organic and inorganic light emitting devices and photodetectors covering a broad range of wavelengths has opened up new avenues in the photonic sensor technologies.[2] Photonic sensors have the potential to provide effective label-free solutions for a broad range of applications including the industrial process control, environmental monitoring, clinical diagnostics, drug screening, food safety and others. Modern sensing platforms aim for reduced costs and energy consumption, miniaturisation, high sensitivity and selectivity, straightforward data processing and fast response times.[3] Besides, new optimal signal transduction mechanisms should facilitate the wider application of sensors.

To address the above-stated opportunities, this dissertation presents a comprehensive study based on harnessing "smart" tunable optical properties of 1D photonic structures as well as opportunities enabled by synthetic chemistry and nanotechnology. The design, fabrication, and characterization of biocompatible thermo-, hygro- and chemoresponsive one-dimensional (1D) TiO_2/SiO_2 photonic crystals are reported. Furthermore, the work emphasizes a route towards the bottom-up assembly of a fully functional, high resolution, miniature 1D PC platform, integrated with organic and inorganic narrowband light emitting diodes and photodetectors/imaging arrays and their possible applications. The platform utilizes scalable easy-to-fabricate wet-chemistry processing techniques that allow to significantly reduce the required production costs. The following Section 7.1 provides a summary of principal contributions and conceptual insights presented in the individual chapters that can benefit the design and performance of future label-free temperature, humidity, chemical and biological sensors. Section 7.2 sheds light on future research directions that can be fostered by the results discussed in this work, and gives an outlook on potential improvements and applications of the proposed detection concept.

7.1. SUMMARY

Thermo- and hygroresponsive TiO₂/SiO₂ one-dimensional photonic crystals

The results presented in Chapter 3 shed light on the reversible thermo-optic tuning of TiO_2/SiO_2 one-dimensional photonic crystals with various degrees of porosity and pore accessibility of the individual layers. A key finding of these studies emphasizes a strong amplification (fourfold) of the thermal response of the investigated 1D PC at higher relative humidities of the ambient environment. Remarkably, the effective thermo-optic response of the PCs can be modified through the choice of the PC fabrication method and thus the morphology of the layers, featuring different morphologies of the constituent layers (dense layers obtained by physical vapor deposition or sol-gel spin-coating, nanoparticle-based layers with textural mesoporosity and evaporation-induced self-assembled layers with structural mesoporosity). Photonic simulations performed to rationalize the influence of refractive index, thermo-optic coefficient and layer thicknesses on the thermal tunability of the multilayer reveal peculiar trends for the tailor-made sensor design strategies. Utilizing the interplay between temperature- and humidity-based effects enabled the development of sensitive photonic crystal temperature and humidity sensors with fast humidity response and recovery kinetics on the order of 2-4 s, as shown in Chapter 4.

Thermo-optic imaging sensors based on tunable porous one-dimensional photonic crystals

Chapter 4 highlights the development of thermo-optic imaging sensors with a ternary architecture based on wet-chemistry processed mesoporous thermoresponsive TiO_2/SiO_2 1D PCs integrated with inorganic and organic light emitting diodes and a high-resolution camera. The proposed grayscale detection approach based on the transduction of IR radiation into light intensity changes in the visible range goes beyond the classical photonic crystal colorimetric detection scheme and enables time and spatially resolved temperature mapping with a temperature coefficient of luminance of 3.8%, which is comparable with the performance of state-of-the-art thermoresistive detectors.

Electrophotonic sensing platforms based on one-dimensional photonic crystals

Chapter 5 presents a low-cost and easy-to-fabricate miniature, integrated sensing platform, christened "electrophotonic nose", for the sensitive detection of volatile and fluid analytes. The 2.5×2.5×1 cm³

platform consists of a chemoresponsive TiO_2/SiO_2 1D photonic crystal sandwiched between a solution-processed spin-coated organic light-emitting diode, an organic photodetector and the polydimethylsiloxane fluidic chamber. Contrary to the existing works, the platform proposed in this thesis provides an excellent sensitivity also for small vapor concentrations (down to $\approx$ 10 parts per million in nitrogen). Notably, the resolution ($\approx$ 27 pm) of the electrophotonic sensor exceeds the capabilities of most commercial spectrometers and by far the human eye.

Chemical diffusion visualization and cell adhesion detection.

The electrophotonic sensing platform characterized in Chapter 5 was further modified in order to demonstrate a broader scope of operation and various *modi operandi* to address the possibility of multimodal sensing. Namely, Chapter 6 highlights various sensing schemes (spectral tuning, intensity tuning and imaging) enabled by the modular combination of responsive TiO_2/SiO_2 1D PCs with various light emitters and detectors. For the first time, the possibility to perform quantitative real-time analysis of lateral diffusion kinetics and spatial distribution of analytes adsorbed within porous multilayers with micrometre resolution was demonstrated. Furthermore, a non-invasive, real-time optical monitoring approach for evaluating the confluency and viability of unlabelled fibroblast- and tumorigenic hepatoblastoma-type cells adhered to a biocompatible 1D PC surface is presented, which can be of interest for future cancer progression studies and for drug toxicity and pathogenicity tests.

7.2. OUTLOOK

The results and conceptual insights presented in this thesis highlight various directions for future advancements in the realm of detection and monitoring technologies. The cost- and power-effectiveness together with multi-modal capabilities and straightforward readout schemes of the presented proof-of-concept 1D photonic crystal sensing platform have the potential to improve existing environmental sensors available on the market. The proposed sensing platform provides the advantage of combining real-time, continuous sensing and imaging modes, which is of great importance for environmental sensing and accurate portable "point-of-care" diagnostics. Additional benefits can be associated with the use of low-cost and simple, yet versatile one-dimensional photonic crystals as the sensitive components. A variety of fabrication methods and numerous combinations of organic, inorganic and composite

materials together with tailored surface functionalization and morphology tuning can further improve the underlying sensing technology. For example, introducing new families of nanoporous materials[4] such as metal-organic frameworks (MOFs)[5], covalent organic frameworks (COFs)[6] and others, or novel two-dimensional (2D) materials[7] such as nanosheets of oxides and hydroxides,[8,9] or implementing plasmonic nanostructures[10] into photonic-crystal-based sensing elements can open up new avenues towards sensing platforms with an amplified sensitivity and specificity towards chemo- and bioanalytes of interest. An intelligent optimization of geometry and optical parameters of the employed photonic crystals and optoelectronic devices done with computer simulations can further enable the design of more efficient sensors. Furthermore, an enhanced performance of the "electrophotonic nose" platform can be achieved by fabricating an array of specifically functionalized photonic crystals with a microfluidic setup for the simultaneous multiplexed "lab-on-a-chip" sensing. Along these lines, exploiting inexpensive materials enabling organic light emitting and detecting devices with longer lifetime and slower degradation rate, and improved signal-to-noise ratio is crucial for the upscaling of reliable and long-lasting electrophotonic sensors. The use of low-noise amplifiers (such as lock-in amplifiers) for the optoelectronic components can further lower the detectable photonic band gap shift. In terms of thermal imaging, further research addressing the effective pixelation of the sensitive area of the responsive photonic crystals and minimization of thermal crosstalk in order to increase the resolution of the imager is of great interest. A possibility to add a wireless transmission of the obtained sensor measurements into a cloud-computing network to perform on- and offline analysis of data streams from the remote resource-limited areas lacking powerful processing tools is desirable. This option can be, in principle, provided by implanting miniaturized cartridge-like photonic sensor arrays into modern smartphones and portable cameras. And last but not least, introducing other types of tunable photonic crystals, for example, photonic slabs,[11,12] colloidal 2D and 3D crystals[13,14] and their inversed replicas[15,16] and many others may enable distinct functionalities and further boost the performance of the suggested platform.

7.3. BIBLIOGRAPHY

(1)   Fenzl, C.; Hirsch, T.; Wolfbeis, O. S. *Angew. Chem. Int. Ed.* **2014**, *53*, 3318.

(2)   Sensors for Environment, Health and Security. In *Proceedings of the NATO Advanced Study Institute on Sensors for Environment, Health and Security: Advanced Materials and Technologies*; Baraton, M.-I., Ed.; Vichy, France, **2007**; Vol. XXIII.

(3)   Walt, D. R. *ACS Nano* **2009**, *3*, 2876.

(4)   Zhao, X. S. *J. Mater. Chem.* **2006**, *16*, 623.

(5)   Rowsell, J. L. C.; Yaghi, O. M. *Microporous Mesoporous Mater.* **2004**, *73*, 3.

(6)   Doonan, C. J.; Tranchemontagne, D. J.; Glover, T. G.; Hunt, J. R.; Yaghi, O. M. *Nat. Chem.* **2010**, *2*, 235.

(7)   Mas-Ballesté, R.; Gómez-Navarro, C.; Gómez-Herrero, J.; Zamora, F. *Nanoscale* **2011**, *3*, 20.

(8)   Ma, R.; Sasaki, T. *Adv. Mater.* **2010**, *22*, 5082.

(9)   Osada, M.; Sasaki, T. *Adv. Mater.* **2012**, *24*, 210.

(10)   Anker, J. N.; Hall, W. P.; Lyandres, O.; Shah, N. C.; Zhao, J.; Van Duyne, R. P. *Nat. Mater.* **2008**, *7*, 442.

(11)   Johnson, S.; Fan, S.; Villeneuve, P.; Joannopoulos, J.; Kolodziejski, L. *Phys. Rev. B* **1999**, *60*, 5751.

(12)   Nazirizadeh, Y.; von Oertzen, F.; Plewa, K.; Barié, N.; Jakobs, P.-J.; Guttmann, M.; Leiste, H.; Gerken, M. *Opt. Mater. Express* **2013**, *3*, 556.

(13)   Takeoka, Y. *J. Mater. Chem. C* **2013**, *1*, 6059.

(14)   Mishchenko, L.; Hatton, B.; Kolle, M.; Aizenberg, J. *Small* **2012**, *8*, 1798.

(15)   Schroden, R. C.; Al-Daous, M.; Blanford, C. F.; Stein, A. *Chem. Mater.* **2002**, *14*, 3305.

(16)   Aguirre, C. I.; Reguera, E.; Stein, A. *Adv. Funct. Mater.* **2010**, *20*, 2565.

8. APPENDIX

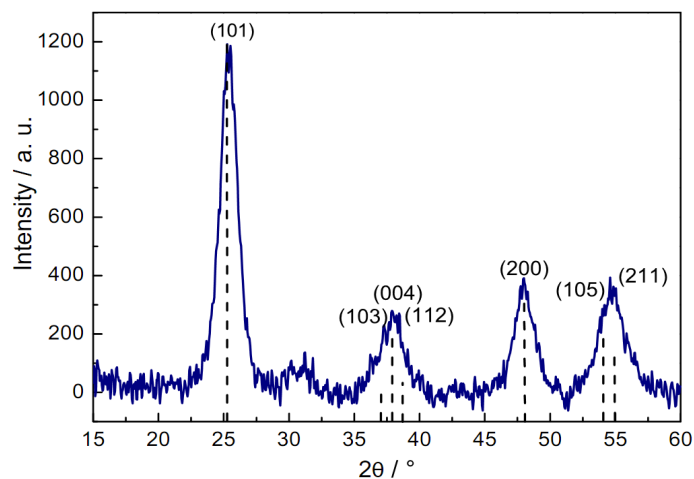## 8.1. SUPPORTING INFORMATION FOR CHAPTER 3.1

Figure 8.1.1. X-ray diffraction pattern of the TiO_2 powder calcined for 1 h at 350 °C.
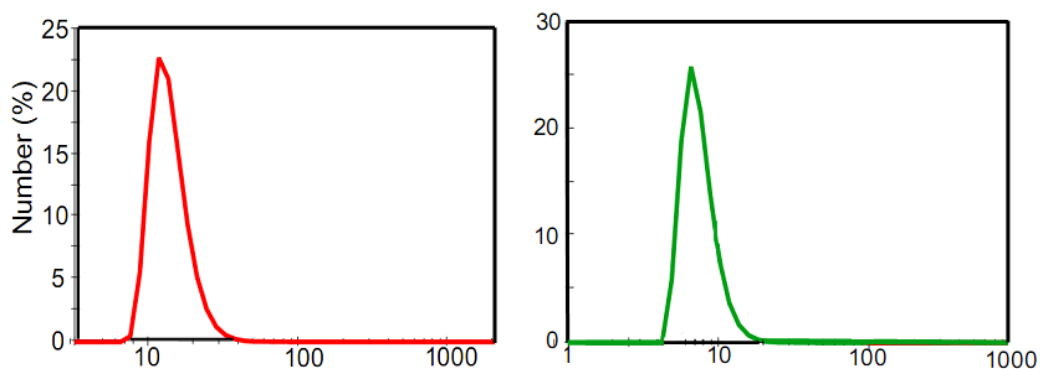

Figure 8.1.2. Number-size distributions of the TiO_2 and SiO_2 measured by dynamic light scattering.
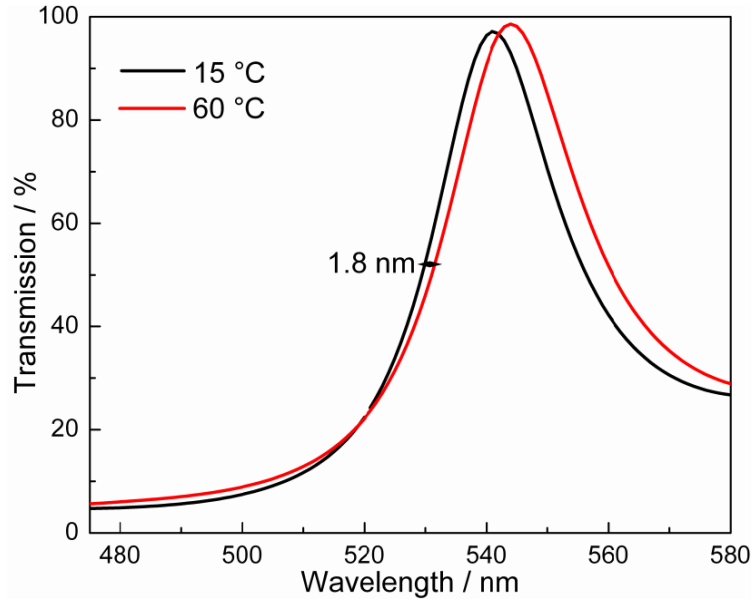
Figure 8.1.3. Simulation of the spectral shift of a BS with 8.5 60 nm TiO_2 and 93 nm SiO_2 bilayers based on the assumption that the thickness of the thin films increases by 0.02 nm from 15° to 60°C.

Relative humidity versus temperature

To determine the dew points corresponding to the relative humidities 25, 45, 55% at 20 °C we first calculated the actual water vapor pressure at 20 °C using the following ratio (Equation 8.1):

$$RH \equiv \frac{P_w^a}{P_w^s} 100\% \,, \tag{8.1}$$

where P_w^a - actual water vapor pressure, P_w^s- saturated water vapor pressure, RH – relative humidity.

The expression for the saturated water vapor pressure P_w^s is valid for temperatures (T) 123 < T < 332K (Equation 8.2):

$$\ln(P_w^s) \approx 54.842763 - \frac{6763.22}{T} - 4.210 \ln(T) + 0.000367T +$$

$$+\tanh\{0.0415(T - 218.8)\}(53.878 - \frac{1331.22}{T} -$$

$$-9.44523 \ln(T) + 0.014025T) \,, \tag{8.2}$$

was used as in the paper of Murphy and Koop.[1] The dew point was extracted from the equation P_w^s ($T_{\text{dew point}}$) = P_w^a. For the simulation of the dependence of RH on the temperature we assumed that the actual water pressure is constant.
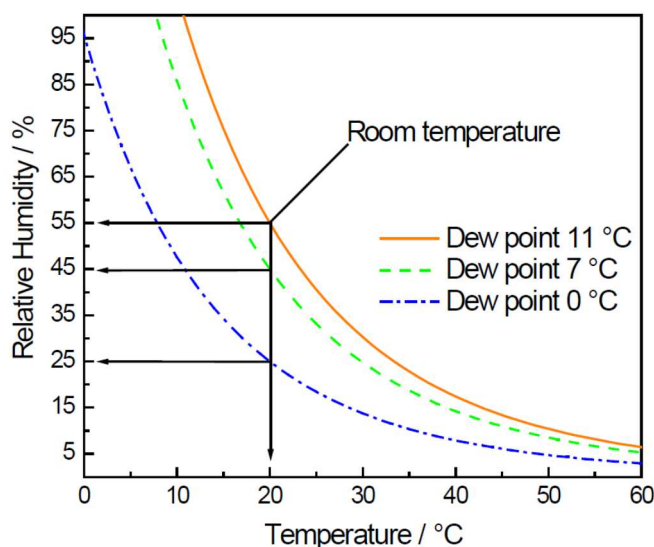
Figure 8.1.4. The simulation of the dependence of relative humidity of air on temperature for the dew points of 0 °C, 7 °C and 11 °C made in MATLAB.

(1) Murphy, D. M.; Koop, T. *Q. J. Roy. Meteor. Soc.* **2005**, *131(608)*, 1539.

8.2. SUPPORTING INFORMATION FOR CHAPTER 4.1

Bragg stack fabrication

Thermoresponsive photonic crystals for Figures 4.1.2, 4.1.3, 4.1.5 were assembled by sequential deposition of TiO_2 and SiO_2 nanoparticle suspensions on a clean glass slide (2.5×2.5 cm^2) previously activated by air plasma treatment (Femto, Diener Electronic). TiO_2 nanoparticles (hydrodynamic diameter 7-20 nm) were synthesized by the method described elsewhere.[1] To improve the TiO_2 film quality, polyethylene glycol (PEG, 2.5 wt. %, $M_w = 8000$ g mol^{-1}) was added. SiO_2 colloids (hydrodynamic diameter 6-10 nm) were purchased from Sigma-Aldrich (LUDOX SM-30, 30 wt % in H2O) and diluted with distilled water using a ratio of 1:5. Both suspensions were filtered using syringe filters (SPARTAN 13, 0.2 μm) to remove aggregates. Thin layers of TiO_2 and SiO_2 were produced by using the spin-coating technique (Laurell WS-650SZ-6NPP/LITE). The glass slides were covered by 200-250 μl of TiO_2 suspension and accelerated at 1500 rpm s^{-1} to final rotation speeds ranging from 2500 to 5500 rpm. The total spin-coating process for each layer was completed in 60 s. Afterwards the sample was put into a muffle furnace (Nabertherm, L3/11/B810) for calcination at 350˚C for 30 min. The same procedure was

applied to deposite the desired number of bilays from 6 to 10. The film thickness of the individual layers was characterized by spectroscopic ellipsometry (performed on a Woollam M200D variable angle ellipsometer in the entire spectral range of 190-1000 nm at angles of incidence of 65°, 70°, 75°). Thermoresponsive photonic crystals for Figures 4.1.6 and 4.1.7 were obtained by spin-coating the suspensions of mesoporous silica and titania-sol. To synthesize mesoporous silica (mp-SiO$_2$) films, tetraethyl orthosilicate (TEOS, 3.12 g) was diluted in ethanol (19 mL) with subsequent addition of the surfactant Pluronic F127 (1.5 g), HCl (0.15 g 2 M) and H$_2$O (1.35 mL). We stirred the mixture for 5 minutes to turn the initailly milky white suspension to a transparent one and aged the mixture for at least one hour. The substrate covered with 200-250 µl of filtered solution (Acrodisc, GHP, 13mm, 0.2 µm) was spin-coated for 40 s (3000 rpm, 4000 rpm s^{-1}). Mesoporous films of ≈ 450 nm we obtained by evaporation-induced self-assembly (EISA) method, namely, by removing the surfactant *via* calcination of the films at 400 °C for 15 minutes. Titania films were spin-coated from the filtered titania-sol suspension (0.05 M), synthesized by diluting tetraethyl orthotitanate (TEOT, 0.231 g) in ethanol (20 mL). To obtain homogeneous films, the substrate was spin-coated for 40 s (3000 rmp, 4000 rmp s^{-1}).

OLED fabrication

OLEDs were fabricated on a glass substrate covered with a structured indium tin oxide (ITO) transparent electrode. The substrates were cleaned in an ultrasonic bath, in isopropanol and acetone. Then, the samples where transferred into a glovebox with N$_2$ atmosphere where the OLED fabrication was performed. First, a 40 nm thick PEDOT:PSS layer was deposited using the spin-coating technique to smoothen the surface and to improve the injection of holes into the active polymer. Subsequently, the poly(para-phenylene vinylene) copolymer Super Yellow (Merck PDY-132, 0.5 wt.%) dissolved in toluene was spin-coated onto the sample, with a layer thickness of ≈ 80 nm. The solution was prepared 24 hours prior to use and kept at room temperature. Subsequently, the samples where transferred into a high vacuum chamber (Leybold) at a pressure of ≈10^{-6} mbar to deposit the top electrodes. The electrodes were evaporated by means of the thermal physical vapor deposition method in the following sequence: first, a 25 nm Ca layer, and then a 125 nm Ag layer. The OLEDs were encapsulated with a microscope glass coverslip glued (Araldite 2011, Huntsman) on top of the device. The OLEDs were biased with a voltage source at 4.5 V, which resulted in a current of about 2 mA giving a power dissipation of 9 mW.

The OLED and the BS exhibit a satisfactory thermal stability – both systems showed the same degree of thermal tunability after approximately ten temperature heating/cooling cycles.

Thermo-optical analysis

We used two different mechanisms of heat transfer to change the temperature of the devices. Firstly, *via* heat conductance by using two Peltier elements placed on the sample (BS) and arranged with a 4 mm gap in-between to provide the optical axis for the transmission measurements of the Bragg stack. A PT100 temperature sensor was attached to the other side of the sample above the optical axis. To thermally tune the light intensity of an OLED and OLED-BS, we used using only one Peltier element, as shown on the photograph in Figure 4.1.4 (a) in the main manuscript. Peltier elements and temperature sensor were connected to a remote-controlled sourcemeter (Keithley). A software proportional-integral controller regulated the heating and cooling of the Peltier elements. The standard deviation from the set-point temperature during the measurement was 7 mK. For each temperature the sample was equilibrated for 60 sec. For all measurements the light source (high pressure Hg arc-lamp, LED) and the detector where placed in a sufficient distance from the sample to ensure thermal decoupling. Alternatively, (Figure 4.1.6 and 4.1.7), we transferred heat *via* IR radiation from the tip of a hot (400 °C) soldering iron.

Spectra from Figures 4.1.1, 4.1.3 and 4.1.5 (a, b) were obtained by using a monochromator (Cornerstone260 1/4 m) with a 10 x 10 mm calibrated silicon photodetector connected to a digital lock-in amplifier (Merlin). As light source in Figure 4.1.2(b) we used the broad spectrum high pressure Hg arc-lamp and for Figure 4.1.3 - standard blue LED (LL-504BC2E-009, Lucky Light) with a spectral width (FWHM) of 28 nm and the emission peak at 464 nm. The LED was driven at a current of 2 mA and switched on 30 minutes prior to starting the experiment to ensure a constant light output and to achieve constant emission. Transmission curves were measured with a thermal equilibration of one minute at temperatures in the range from 15 °C to 35 °C with a step size of 5 °C. The luminance measurements for the Figure 4.1.5 (c) were performed using a "MAVO SPOT 2" luminance meter placed at a distance of about 25 cm orthogonal to the sample surface. The measured area was a circle with a diameter of ≈ 3mm. For the measurements in Figure 4.1.6 a CMOS camera (uEye 2240-M) with CCD sensor was used.

The BS was mounted on thermoelectric heaters, controlled by a remote source meter, while the actual temperature was measured by a PT100 sensor. Transmission curves were measured with a thermal equilibration of one minute at temperatures in the range from 15 °C to 35 °C with a step size of 5 °C. In this setup, the BS modifies the spectrum of the incident light (a high-pressure arc lamp light source) as a function of temperature by acting as a thermoresponsive optical filter. This procedure was repeated for all measurements shown in this work, unless stated differently.

Thermogram analysis

The thermogram on the Figure 4.1.7 was created by using the following two-step calibration procedure:

1) The slope of a linear calibration line has been determined using the average light intensity at two different temperatures using Formula S1:

$$\frac{dT}{dI} = \frac{T_2 - T_1}{\bar{I}_2 - \bar{I}_1} = \frac{33°C - 27°C}{\bar{I}_{33} - \bar{I}_{27}} = 0.58°C , \tag{8.3}$$

where $\bar{I}_{27} = 1684$ and $\bar{I}_{33} = 1788$ are the average pixel intensities of the two calibration measurements at 27 °C and 33 °C (Figure 4.1.6 a and c), respectively.

2) The respective temperature of each pixel (T_{pixel}) has been calculated using Formula S2:

$$T_{pixel} = 27°C + (I_{pixel} - I_{27})\frac{dT}{dI} , \tag{8.4}$$

I$_{pixel}$ and *I*$_{27}$ are the intensities of the single pixels at 27 °C and under a temperature gradient (from Figure 4.6.1 b).

(1) Pavlichenko, I.; Exner, A. T.; Guehl, M.; Lugli, P.; Scarpa, G.; Lotsch B. V. *J. Phys. Chem. C*, **2012**, *116 (1)*, 298

8.3. SUPPORTING INFORMATION FOR CHAPTER 6.1

PC fabrication

The photonic crystals were assembled by sequential deposition of TiO_2 and SiO_2 nanoparticle suspensions on a clean glass slide (VWR microscope slides, 2.5×2.5 cm^2) or a round cover glass (Thermo scientific, ø = 5 cm) previously activated by air plasma treatment (Femto, Diener Electronic). TiO_2 nanoparticles (hydrodynamic diameter 7-20 nm) were synthesized by the method described elsewhere.[28] Briefly, tetraethyl orthotitanate (12.50 mL, Sigma-Aldrich) was added dropwise to HNO_3 (75 mL, 0.1 M) under vigorous stirring, and heated for 8 h at 80 °C; subsequently, the obtained product was sonicated (Elmasonic S10) at 25°C for 10 hr. To wash the synthesized nanoparticles, first, acetone (40 mL) was added to the suspension to initiate particle flocculation. After centrifugation of the suspension at 23000 rpm (Sigma 3-30K) at 15 °C for 20 min, the precipitate was redispersed in methanol (75 mL), providing a concentration of around 20 mg mL^{-1}. SiO_2 colloids for the PCs presented in the Figures 6.1.2, 6.1.3 (LUDOX SM-30, 30 wt % in H_2O, Sigma-Aldrich) with a hydrodynamic diameter of 6-10 nm were diluted with distilled water using a ratio of 2:5, and the colloids for the PCs shown in Figures 6.1.4, 6.1.5, 6.1. 6, 6.1.7 (LUDOX TMA, 34 wt % in H_2O, Sigma-Aldrich) with a hydrodynamic diameter of 20-30 nm were diluted with methanol (Merck) using a ratio of 1:20. Both suspensions were filtered using hydrophilic syringe filters (SPARTAN 13, 0.2 and 0.45 μm, regenerated cellulose membrane). Thin layers of TiO_2 and SiO_2 were produced by using the spin-coating technique (Laurell WS-650SZ-6NPP/LITE) at 25 °C and relative humidity of the spin-coating chamber between 36% and 45%. The glass slides were alternatingly covered by 200-250 μl of TiO_2 and SiO_2 suspensions and accelerated at 1500 rpm s^{-1} to final rotation speeds ranging from 3500 to 4000 rpm. The total spin-coating process for each layer was completed in 60 s. Afterwards, the sample was put into a muffle furnace (Nabertherm, L3/11/B810) for calcination at 400˚C for 15 min. The same procedure was applied to deposit the desired number of 6-9 bilayers. The refractive indices of single thin films at various ethanol saturation pressures were characterized by spectroscopic ellipsometry (performed on a Sopra Semilab PS-100 ellipsometric porosimeter

in the spectral range of 300-900 nm at angle of incidence of 75°) by using the Cauchy model. Scanning electron microscopy (SEM) micrograph was recorded with JEOL JSM-6500F at 5 kV.

Chemical analyte sensing

The PDMS chamber was prepared with the Sylgard 184 Elastomer Kit (Dow Corning) as described elsewhere.[11] First, PDMS was combined with the curing agent in 10:1 ratio and the dish was filled to a height of approximately 4-5 mm. Then the mixture was covered with a Parafilm for around 30 min to allow the air bubbles to disappear, and then cured in the oven at 120 °C for 1 h. Afterwards, in a 2.5 x 2.5 cm^2 square piece of the PDMS mold a window of $\approx$ 2x2 cm^2 was cut out, providing the chamber for the vapor. An inlet for the gas tube was constructed by piercing a syringe needle through one side of the chamber and then inserting a pipette tip, which was connected with the external flow controllers. The outlet for the gas chamber was provided by cutting out a $\approx$1x1 mm hole in the neighboring side of the chamber. To deliver the vaporized analyte of interest into the chamber under the desired relative pressure (p/p^0), digital mass flow controllers (EL-FLOW F201CV-500RAD-33-V and μ-FLOW L01-RAD11-0-80S, Bronkhorst High-Tech) were used. The carrier gas nitrogen (flow rate 200 ml min^{-1}) and the liquid ethanol (flow rate was varied between 0 and 1.5 g h^{-1}) were dosed into the heated CEM (Controlled Evaporation and Mixing) system (W101A-130-K, Bronkhorst High-Tech), where ethanol was vaporized at 100 °C and mixed with the carrier gas, and further delivered into the test chamber (note that during the delivery of the vaporized analyte into the chamber, the digital mass flow controllers provide an oscillating flow pattern, which results in a measurement error during recording of the spectra, which tends to increase at higher relative pressures). The ethanol relative pressure p/p^0 (i.e. the ratio of partial ethanol pressure (p) and saturation pressure (p^0)) was calculated using the software *FLUIDAT* in the subsection "CEM calculation".[39] Contact angle of the ethanol droplet on the surface of the 1D PC was measured with an optical tensiometer (Theta Lite, TL100). The samples were investigated with a light microscope (Leica DM 2500M with 12 V halogen lamp) combined with a 3-megapixel CMOS camera (DFC295, Leica) and interfaced with a miniature UV-Vis spectrometer (Ocean Optics USB2000+) and an optical fiber (Ocean Optics, QP400-2-UV-BX). A narrow-band light source - a green LED (M530D1, Thorlabs) - was fixed to an 8x5 cm^2 aluminium heat sink and powered by a sourcemeter at 8 mA

(Keithley 2636A System). The slim Si photodiode power sensor (S130C, Thorlabs) operating in the wavelength range of 400-1000 nm was connected to the power meter interface (PM 100USB, Thorlabs) and aligned above the measurement chamber. For the analysis of the solvent diffusion described in Figure 6.1.3, a closed PDMS chamber was pierced with a syringe needle through one side, while the chamber was ventilated with a N_2 gas at a low flow speed of 50 mL min^{-1}. Afterwards an approximately 3 µL droplet of ethanol was injected to the area of observation avoiding stage vibrations. The evaporation process accompanied by the color change of the 1D PC was recorded using the Leica LAS 3.8 software, and subsequently the film frames were extracted by using the software VirtualDub 1.9.11 and analyzed with ImageJ plugins.

Cell monitoring

For the cell experiments 1D PCs were sterilized in 70% ethanol for 1 h. Subsequently, the samples were allowed to dry in a sterile laminar flow hood under ultra-violet illumination. For the experiments shown in Figure 6.1.5 the BHK-21 (syrian hamster kidney fibroblasts, ATCC (CCL 10)) cell culture medium composed of 500 mL minimum essential medium (MEM) with Earls's salt and L-Glutamine (Gibco® 31095-029), 50 mL FBS (fetal bovine serum, Gibco®, 16000-044), 5.5 mL non-essential amino acids (Gibco® 11140-035, 100x) and 5.5 mL Penicillin and Streptomycin (Gibco® 15140-122, Pen 10000 µU mL^{-1}, Str 10000 µg mL^{-1}) was used. The BHK-21 cell density on the seeding day was 6 x 10^4 cells per ø35 mm Petri dish (Falcon 35/3001, polystyrene). The culture was incubated at 37 °C with 7% CO_2 gas. For analysis purposes the BHK-21 cells were fixed onto the 1D PC with 4 % paraformaldehyde in 0.1 M PBS (phosphate buffered saline) for 30 min, and afterwards washed three times with PBS at room temperature (r.t.). Atomic force microscopy (AFM) measurement of the cell topography shown in Figure 6.1.5e was performed on a MFP-3D AFM (Asylum Research, Santa Barbara) in air, in tapping mode. For the fluorescent staining the 1D PC was soaked with Buffer G (0.1 % Triton X-100, 5% normal goat serum in PBS) for 10 min at r. t., then it was washed three times with PBS for 10 min at r. t. and incubated with Buffer G containing 1/1000 dilution of phalloidin–tetramethylrhodamine B isothiocyanate (phalloidin-TRITC, 0.5 mg mL, Sigma-Aldrich) for actin staining, and again washed three times in PBS. Hoechst 33342 (1 µl, 1 mg mL^{-1}, Sigma-Aldrich) in PBS was added for nuclear staining. Figure 6.1.5f was captured on an Axiovert 200M

(Zeiss) epifluorescence microscope with ZEISS LD Achroplan objective 40x/NA 0.6, equipped with a motorized stage (DC 120100, Märzhäuser, Wetzlar, Germany), CCD camera (AxioCam MRm, Zeiss), a short-wavelength mercury lamp, and fluorescent filter sets (Zeiss filter set 01 and AHF F46-005). The BHK-21-covered 1D PCs shown were investigated with a light microscope (Leica DM 2500M) integrated with a miniature UV-Vis spectrometer (Ocean Optics USB2000+) and an optical fiber (Ocean Optics, QP400-2-UV-BX). For the experiments shown in the Figures 6.1.6, 6.1.7 HuH7 cells (Human hepatocellular liver carcinoma, wildtype) were cultured in Dulbecco's Modified Eagle Medium: Nutrient Mixture F-12 (DMEM/F-12, Gibco®, life technologies, Carlsbad, SA) supplemented with 10% FBS (Gibco®) in a 5% CO_2-containing atmosphere at 37 °C. The cells were seeded into a sterile Petri dish (Falcon 35/3001, polystyrene) onto a small piece of a 1D PC with a cell density of 1.3×10^5 and incubated for 24 and 48 h. For the measurements, the 1D PC with adhered HuH7 cells was transferred into a Petri dish with a glass bottom (Mat Tek P356-0-14-C, glass #0, ø = 35 mm) and covered with 2 mL of CO_2-independent medium (Gibco®) supplemented with 10% FBS. A custom-built wide-field microscope, based on a Nikon Ti Eclipse microscope with an oil immersion objective CFI Plan Apochromat TIRF 60x/ NA 1.45 integrated with a motorized XY scanning stage (MAC 6000, Ludl Electronic Products), 532 nm laser (DLTS 200 Soliton) and EM-CCD camera chip (iXon+ DV884, Andor Technology) was used for the optical experiments with the HuH7 cells. The cell lysis observed in Figure 6.1.6 a-d was achieved by adding 100-400 µL of sodium dodecyl sulfate (SDS, 1.5% aq., Sigma-Aldrich) to a glass bottom Petri dish containing the 1D PC in 2 mL of CO_2-independent medium. The power signal was monitored with a Si Photodiode Power Sensor (S130C, Thorlabs) mounted 5 mm above the Petri dish. Cell coverage estimation (see Figure 6.1.7) was done by scanning the 1D PC surface in a phase-contrast transillumination mode with a motorized stage in a "COMB" (snake-like) fashion in 8 adjacent positions with the area of 64 µm² (60x magnification).
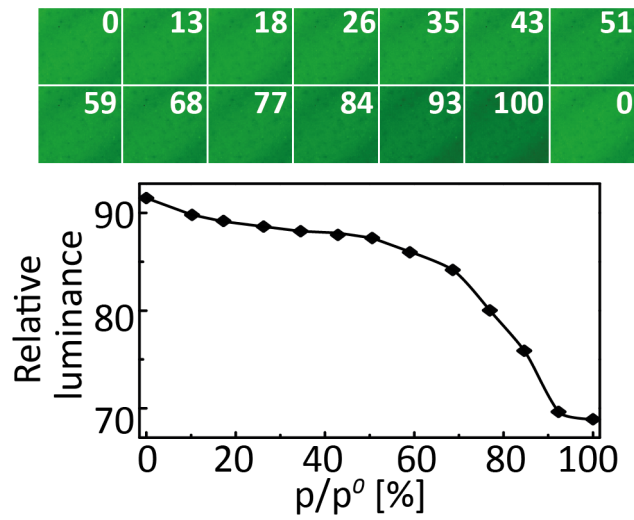
Figure 8.1.5. Top: photographs of the PC surface captured with a CMOS imaging array, taken at 0 < *p/p⁰* < 100% (*p/p⁰* values are indicated in the corner of each image), bottom: relative luminance analysis of the top photographs used for the calibration of the image in the Figure 6.1.4f.
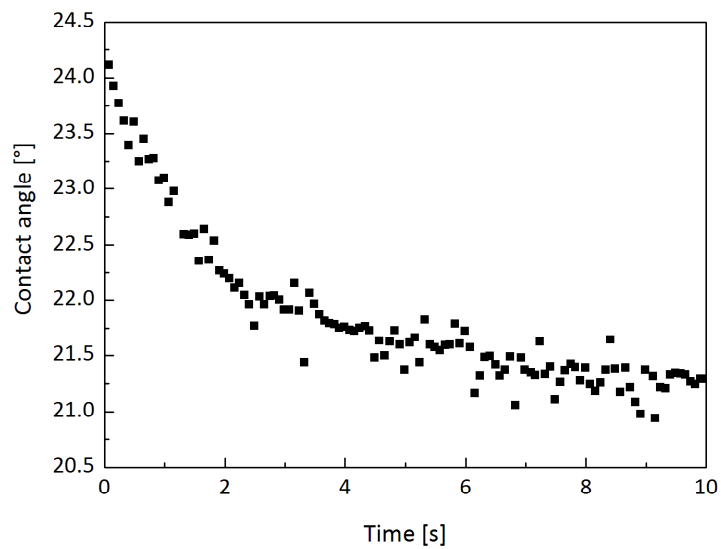

Figure 8.1.6. Evolution of the mean contact angle of a 3 μL water droplet applied onto the surface of the 1D PC with time.

8.4. LIST OF PUBLICATIONS

PUBLISHED AS PART OF THIS THESIS

The authors with (*) made an equal contribution:

5. **A step towards the electrophotonic nose: Integrating 1D photonic crystals with organic emitting diodes and photodetectors,** A. T. Exner*, **I. Pavlichenko***, D. Baierl, M. Schmidt, G. Derondeau, B. V. Lotsch, P. Lugli, G. Scarpa, *Laser Photon. Rev.* **2014,** 8(5), 726.

4. **A Low-Cost Thermo-Optic Imaging Sensors: A Detection Principle Based on Tunable 1D Photonic Crystals,** A. T. Exner*, **I. Pavlichenko***, B. V. Lotsch, G. Scarpa, P. Lugli, *ACS Appl. Mater. Interface* **2013**, *5(5),* 1575. **Cover image:**
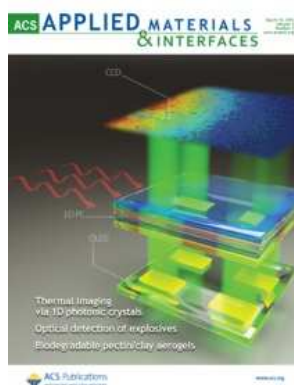
3. **Tunable Thermoresponsive TiO_2/SiO_2 Bragg Stacks Based on Sol-Gel Fabrication Methods,** I. **Pavlichenko***, A. T. Exner*, P. Lugli, G. Scarpa, B. V. Lotsch, *J. Intell. Mater. Struct.* 2013, 24, 2203.

2. **Nanomorphology Tuning of the Thermal Response of TiO_2/SiO_2 Bragg Stacks,** I. **Pavlichenko***, A. T. Exner*, G. Logvenov, G. Scarpa, P. Lugli, B. V. Lotsch, *Can. J. Chem.* **2012**, 90, 12, 1069.

1. **Humidity-Enhanced Thermally Tunable TiO_2/SiO_2 Bragg Stacks,** I. **Pavlichenko***, A. T. Exner* , M. Guehl, P. Lugli, G. Scarpa, B. V. Lotsch, *J. Phys. Chem. C,* **2012**, *116*, 298.

PUBLISHED NOT AS PART OF THIS THESIS

1. **Ultra-Thin Titanium Oxide,** M. Bareiß, D. Kälblein, C. Jirauschek, A. Exner, **I. Pavlichenko**, B. Lotsch, U. Zschieschang, H. Klauk, G. Scarpa, B. Fabel, W. Porod, P. Lugli, *Appl. Phys. Lett.* **2012**, *101*, 083113.

2. **Multiarm Polydimethylsiloxane Stars Based on High Generation Dendrimers**, O. V. Novozhilov, **I. V. Pavlichenko**, N. V. Demchenko, A. I. Buzin, N. G. Vasilenko, A. M. Muzafarov *Russ Chem B+*, **2010**, *59*, 1909.

8.5. CONTRIBUTIONS TO CONFERENCES

ORAL PRESENTATIONS

June 15-18, 2014, Washington DC, USA	**TechConnect World 2014. Nanotech 2014**, Talk. I. Pavlichenko, A. T. Exner, P. Lugli, G. Scarpa, B. V. Lotsch. Low-Cost Sensing Platforms Based on Tunable 1D Photonic Crystals Integrated with Organic Light-Emitting Diodes and Photodetectors
January 31, 2013, Munich, Germany	**LS-Nano Hauptseminar at the** Institute for Nanoelectronics, TUM. Invited Talk. I. Pavlichenko, A. T. Exner, P. Lugli, G. Scarpa, B. V. Lotsch. Towards Low-Cost Sensors: A Detection Principle Based on Tunable Photonic Crystals
July 27-29, 2012 Munich, Germany	**IDK Final Symposium 2012**, Invited Talk. I. Pavlichenko, A. T. Exner, P. Lugli, G. Scarpa, B. V. Lotsch. Towards integrated sensing platform based on 1D photonic crystals
February 20-24,2012, Schloss Ringberg, Germany	**Ringberg Meeting** Talk. I. Pavlichenko, A. T. Exner, P. Lugli, G. Scarpa, B. V. Lotsch. Stimuli-responsive photonic crystals for sensing applications.
September 12-15,2011 Montpellier, France	**Euromat 2011.** Talk. European Congress and Exhibition on Advanced Materials and Processes. I. Pavlichenko, A. T. Exner, P. Lugli, G. Scarpa, B. V. LotschIntegrated sensing platform based on stimuli-responsive photonic crystals.
August 2-4, 2011 Aiterbach, Germany	**IDK-NBT Summer School 2011**, Talk. I. Pavlichenko, B. V. Lotsch Photonic crystals for sensing applications.

POSTER PRESENTATIONS

October 30, 2013, Munich, Germany	**NIM Area II Meeting "Materials and Assemblies"** I. Pavlichenko, A. T. Exner, P. Lugli, G. Scarpa, B. V. Lotsch. The electrophotonic nose: Integrating 1D photonic crystals with organic emitting diodes and photodetectors
April 1-5, 2013, San Francisco, USA	**MRS Spring Meeting 2013,** I. Pavlichenko, A. T. Exner, P. Lugli, G. Scarpa, B. V. Lotsch. Towards Low-Cost Miniature Sensing Platforms: A Detection Principle Based on Tunable Photonic Crystals
November 6, 2012, Stuttgart, Germany	**Max Planck Institute for Solid State Research Evaluation Day.** I. Pavlichenko, A. T. Exner, P. Lugli, G. Scarpa, B. V. Lotsch. Poster: Towards Low-Cost Sensors: A Detection Principle Based on Tunable Photonic Crystals
June 13-16, 2011 Boston,USA	**TechConnect World 2011. Nanotech 2011.** I. Pavlichenko, A. T. Exner, M.Guehl, P. Lugli, G. Scarpa, B. V. Lotsch: Thermo- and Hygrotunable Nanoparticle-Based TiO_2/SiO_2 Bragg Stacks.
March 27–April 2, 2011 St. Christoph, Austria	**NIM-CeNS Winter School 2011,** I. Pavlichenko, A. T. Exner, M.Guehl, P. Lugli, G. Scarpa, B. V. Lotsch. Poster: Integrated sensing platform based on stimuli-responsive photonics crystals.

8.6. CURRICULUM VITAE

EDUCATION

10/2010-present	**Ludwig Maximilian University of Munich, Department of Chemistry and** **Max Planck Institute for Solid State Research, Stuttgart** **Group of Prof. Dr. Bettina V. Lotsch** PhD Student • Research topic: Development of multifunctional sensing platforms based on stimuli-responsive photonic crystals Member of the graduate programs: • Nanosystems Initiative Munich (NIM) Graduate Program • International Doctorate Program NanoBioTechnology (IDK-NBT) by Center for NanoScience Munich and the Elite Network of Bavaria
09/2004 01/2010	**M. Sc. in Physics, Lomonosov Moscow State University, Department of Physics** **Division of Physics of Polymers and Crystals** Graduated *summa cum laude ("Red Diploma")* Diploma title: The investigation of physico-chemical properties of methylsiloxane polymers with various molecular architecture. Supervisor: Prof. Dr. A. M. Muzafarov
2004	**Moscow High School № 1931** *Graduated with highest honors (Gold Medal Honor Roll)*

AWARDS AND SCHOLARSHIPS

03/2013	CeNS Travel Award
12/2011	e-Fellows.net fellowship
10/2010	Elite Network of Bavaria Scholarship for the International Doctorate Program NanoBioTechnology (IDK-NBT) 2010-2013
11/2009	Best Poster award on Macromolecular nanoobjects and polymer nanocomposites conference in Russia
12/2009	Nominee of R.V. Khokhlov competition for best M. Sc. Thesis in MSU
08/2009	Nanosystems Initiative Munich Student Research Award
08/2009	Best Poster Award on the INASCON Conference in Switzerland
04/2009	The Vladimir Potanin Foundation Scholarship for Excellent Students in MSU
03/2009	S.I. Vavilov MSU Scholarship for the students with outstanding undergraduate records (100% rating)